2019

Advanced anode materials for sodium ion batteries

Xiu Li
University of Wollongong

UNIVERSITY OF WOLLONGONG

Institute for Superconducting & Electronic Materials

Advanced anode materials for sodium ion batteries

Xiu Li

This thesis is presented as part of the requirements for the

Award of the Degree of Doctor of Philosophy

University of Wollongong

Otc. 2019

CERTIFICATION

I, Xiu Li, declare that this paper submitted in the request for the award of Doctor of Philosophy, in the Institute for Superconducting & Electronic Materials (ISEM), Faculty of Engineering, University of Wollongong, NSW, Australia, is original and finished by myself unless otherwise referenced or acknowledged. This paper has never been submitted to any other academic institution for higher education.

Xiu Li

Oct. 2019

ACKNOWLEDGEMENTS

Firstly, I want to express my heartiest gratitude to my supervisor, Dr Xun Xu, for his financial support, and professional and kindly supervision during my PhD period. I also want to give sincere thanks to my co-supervisors, Professor Shi-xue Dou and Shu-lei Chou, for their invaluable encouragement to pursue my PhD degree. Furthermore, I am deeply grateful to Prof. Hua-kun Liu, for her care about my study and life during my whole PhD period.

Moreover, I would like to give grateful thanks to Prof. An-min Cao and Prof. Rui Wen from Institute of Chemistry, the Chinese Academy of Science (CAS), and Prof. Libao Chen from Central South University for their supports to carry out some experiments. Special thanks should be given to Dr. Tania Silver for critical reading of manuscripts, and also Dr. Yunxiao Wang, Dr. Fang Li, Dr. Haipeng Guo, Dr. Weihong Lai, Dr. Yuejiao Chen and Dr. Yutao Li for discussion on the relationship between electrochemical performance and the structures and compositions of materials.

Furthermore, I wish to express my thanks to Miss. Chen Wu, Mr. Chao Cui, Mr. Qingwang Lian, Miss. Yuehua Wei, Mr. Weiwei Ning, Mr. Lin Zhou, Mr. Weiyi Lu, Mr. Tao Liu, Mr. Hao Yang, Dr. Xincheng Hu, Dr. Yonggang Sun, Miss.Yueli Hu and Miss Suting Weng for their kindly help during my PhD research. They have given me much help and enjoyment in my studies and in my life.

Finally, I would like to give deep thanks to my family, especially to my parents, my husband, my lovely son and my sisters. They have given me great encouragement to study hard for a bright future.

This work is supported by the Australian Research Council Discovery Project (DP160102627).

ABSTRACT

Sodium-ion batteries (SIBs) have received extensive attention as promising, cost-effective energy storage devices for the large-scale energy storage due to the abundance and low cost of sodium resources in the earth's crust (2.83% for Na *vs.* 0.0065% for Li), and the similar working mechanism with lithium-ion batteries. Nevertheless, the severe volumetric expansion of most reported anodes during the sodiation/desodiation processes affects the cycling stability of SIBs due to the larger radius of sodium ion than that of lithium ion. Moreover, the reported anodes usually show limited specific capacity, which also inhibits the commercial application of SIBs. Therefore, designing high-performance anode materials is urgently needed and remains a major challenge for SIBs. In this thesis, the mesoporous sulfur and nitrogen co-doped carbon (S/N-C) nanofibers are firstly designed as the anode materials for SIBs based on the doping effect on improving the capacity. Then, WS_2 nanosheets embedded in the lotus rhizome-like heteroatom-doped carbon nanofibers with abundant hierarchical tubes inside are designed for further improving the capacity. Last, the Fe_7S_8 modified sulfur, nitrogen-doped carbon (S/N-C) nanofibers are prepared to improve the capacity and cycling stability of SIBs.

The mesoporous S/N-C nanofibers doped with amounts of N and S atoms (S/N-C) are fabricated by electrospinning technique. The contents of N and S in the S/N-C are 12.59% and 27.95%, respectively. Owing to the high contents of N and S in the

S/N-C, the electrode delivered a high reversible capacity of 552.5 and 355.3 mA h g^{-1} at 0.1 and 5 A g^{-1}, respectively. The excellent performance is attributed to the introduction of N and S in carbon nanofibers. It increases the active sites for Na^+ storage and facilitate Na^+ transfer, which is confirmed by *in-situ* Raman spectra and density functional theory (DFT) calculations. Moreover, the mesoporous S/N-C nanofibers can be wetted by the liquid electrolyte, which also facilitates the Na^+ transport for increasing the rate performance. These indicate the as-synthesized S/N-C is a promising anode material for SIBs.

Layered WS_2 exhibits larger layer spacing with weak van der Waals interaction and higher electrical conductivity. Benefiting from its structural characteristics and conductive nature, the WS_2 anode material exhibits high rate capability；however, the long-term cycling performance of WS_2 as anode for SIBs is not satisfactory. In order to improve its property, the WS_2 nanosheets are embedded into lotus rhizome-like heteroatom-doped carbon nanofibers with abundant hierarchical tubes inside, to obtain the WS_2@S/N-C. The as-synthesized WS_2@S/N-C nanofibers exhibite a discharge capacity of 381 mA h g^{-1} at 0.1 A g^{-1}, excellent rate capacity of 108 mA h g^{-1} at 30 A g^{-1}, and a superior cycling lifespan of 1000 cycles at 5 A g^{-1} with the capacity of 175 mA h g^{-1}, which is ascribed to the synergistic effects of WS_2 nanosheets with larger interlayer spacing, and the stable lotus rhizome-like S/N-C nanofiber frameworks to alleviate the mechanical stress. In addition, the WS_2@S/N-C electrode shows an obvious pseudocapacitance property at 1 mV s^{-1} with a capacitive

contribution of 86.5%. DFT calculations demonstrated that WS_2@S/N-C electrode was favorable for Na storage due to the effect of S/N-C on WS_2. The design strategy for synthesizing WS_2@S/N-C is expected to prepare other electrode materials for rechargeable batteries.

Graphite is a low-cost material; however, it could not accommodate sodium ion effectively in carbonate-based electrolytes. Therefore, low-cost anode materials are highly desired. Iron sulfides are attractive due to the rich stoichiometries and high capacity. Nevertheless, they usually exhibit poor cycling performance due to the large volume change during cycling process. Therefore, the Fe_7S_8@S/N-C nanofibers are synthesized through electrospinning/sulfurization processes with easily synthesized Fe_2O_3 particles as the precursor. The as-synthesized Fe_7S_8@S/N-C nanofibers sustain a reversible capacity of 347 mA h g^{-1} after 150 cycles at 1 A g^{-1} and a high rate capacity of 220 mA h g^{-1} at 5 A g^{-1}. The excellent performance is attributed to its structural characteristics with high-capacity, low-cost Fe_7S_8 particles and high-conductivity of S/N-C nanofibers.

TABLE OF CONTENTS

CERTIFICATION.....I

ACKNOWLEDGEMENTS.....II

ABSTRACT.....IV

TABLE OF CONTENTS.....VII

LIST OF FIGURES.....XI

LIST OF TABLES.....XVII

LIST OF ABBREVIATIONS.....XVIII

LIST OF SYMBOLS.....XXI

LIST OF ORGANIZATIONS..... XXII

1 Chapter 1 Introduction.....1

1.1. Research Background.....1

1.2. The Problem Statement..... 2

1.3. Objectives of the Research..... 2

1.4. Thesis Outline.....3

2 Chapter 2 Literature Review..... 6

2.1 Mechanism of Sodium-ion Batteries.....7

2.2 Cathode Materials.....8

2.3 Electrolyte Systems..... 9

2.4 Anode Materials..... 10

2.4.1. Carbon-based anode materials..... 11

2.4.2 Alloying anodes..... 18
2.4.3 Metal oxides.....28
2.4.4 Metal sulfides.....40
2.4.5 Metal selenides.....56
2.4.6 Metal phosphides..... 65
3 Chapter 3 Experimental Procedure.....70
3.1 Chemicals and Materials..... 71
3.2 Materials Preparation.....73
3.2.1 Electrospinning method..... 73
3.2.2 Hydrothermal method..... 75
3.3 Characterization Techniques..... 76
3.3.1 X-ray diffraction.....76
3.3.2 Raman spectroscopy.....77
3.3.3 Fourier transform infrared spectroscopy.....78
3.3.4 X-ray photoelectron spectroscopy.....78
3.3.5 Thermogravimetric analysis.....79
3.3.6 BET measurement.....79
3.3.7 Scanning electron microscopy..... 80
3.3.8 Transmission electron microscopy.....81
3.4 Electrode Preparation and Coin-cell Assembly.....82
3.5 Electrochemical Measurements.....83
3.5.1 Cyclic voltammetry tests.....83
3.5.2 Galvanostatic charge-discharge..... 84
3.5.3 Electrochemical impedance spectroscopy.....84
3.6 Calculation Methods.....85

4 Chapter 4 S/N-doped High-Capacity Mesoporous Carbon Anode for Na-ion Batteries....86
4.1 Introduction....86
4.2 Experimental Section....88
4.3 Results and Discussion....90
4.3.1 Structure and morphology....90
4.3.2 Electrochemical characterization....95
4.3.3 Theoretical calculations....101
4.3.4 *In situ* Raman analysis....102
4.4 Conclusion....103
5 Chapter 5 Lotus Rhizome-like S/N-C for Strengthening WS_2 with Superior Sodium Storage....105
5.1 Introduction....105
5.2 Experimental Section....108
5.3 Results and Discussion....112
5.3.1 Structure and morphology....112
5.3.2 Electrochemical performance....120
5.3.3 Theoretical calculations....128
5.4 Conclusion....130
6 Chapter 6 S/N-doped Carbon Nanofibers Affording Fe_7S_8 Particles with Superior Sodium Storage....132
6.1 Introduction....132
6.2 Experimental Section....134
6.3 Results and Discussion....136

6.3.1 Structure and morphology.....136
6.3.2 Electrochemical characterization..... 143
6.4 Conclusion.....150
7 Chapter 7 Conclusions and Outlook.....151
7.1 General Conclusion..... 151
7.2 Outlook.....153
7.2.1 Large-scale preparation of nanofibers.....153
7.2.2 Pre-sodiation of the as-obtained nanofibers.....154
7.2.3 Detailed Na storage mechanism study..... 154
7.2.4 Optimizing electrolyte formulations..... 155
REFERENCES.....156
APPENDIX A: LIST OF PUBLICATIONS.....177

LIST OF FIGURES

Figure 2.1 Schematic illustration of a sodium-ion battery.[1] 8

Figure 2.2 Chemical compositions of the organic electrolytes for SIBs.[17] 10

Figure 2.3 Schematic illustration of sodium storage in (a) graphite, (b) graphite oxide, and (c) expanded graphite.[20] 12

Figure 2.4 Proposed scheme of Na storage in natural graphite with different electrolyte systems.[22] 13

Figure 2.5 Schematic illustrations of graphite and HC accommodating sodium.[29] 16

Figure 2.6 Proposed formation scheme for HC at different temperatures.[32] 17

Figure 2.7 (a) Schematic illustration of the synthesis process for Sn@N-C nanofibers; (b) photograph of the integrated precursor and electrode; (c) scanning electron microscope (SEM) image and (d) element mapping of Sn@N-C nanofibers.[42] 20

Figure 2.8 (a) Schematic illustration of the chemical dealloying process to produce the porous Sb structure; (b) $Al_{30}Sb_{70}$ and its dealloyed products; (f-i) $Al_{20}Sb_{80}$ and its dealloyed products.[51] 22

Figure 2.9 Schematic illustrations of (a) the synthesis of 3D interconnected NiSb hollow nanospheres; and (b) the sodiation/desodiation of 3D interconnected NiSb hollow nanospheres.[54] 23

Figure 2.10 Schematic illustration of the synthesis of Sb/graphene composite.[55] 24

Figure 2.11 Synthesis process for red P/carbon nanotube composite.[73] 27

Figure 2.12 (a) Schematic illustration of the preparation of highly ordered 3D Ni-TiO_2 nanoarrays using the AAO templating technique. SEM images of (b and e) the AAO template, (c and f) Ni nanopillar arrays, and (d and g) 3D Ni-TiO_2 nanoarrays.[81] 29

Figure 2.13 Schematic diagram of Na storage in Nb_2O_5.[84] 31

Figure 2.14 (a) Schematic illustration of the synthesis of S-Nb_2O_5@S-rGO; (b) the Na^+/e transportation process in Nb_2O_5/rGO composite; (c) the hollow

nanosphere/graphene structure can buffer the volume expansion during the sodiation/desodiation processes.[86]....32
Figure 2.15 Schematic illustration of the synthesis of hollow carbon@NiO composite.[103]....35
Figure 2.16 The synthesis process for CuO@C nanofibers.[107]....36
Figure 2.17 The synthesis process for MoS_2@SnO_2@C.[112]....37
Figure 2.18 Schematic diagram of the characteristics of the alloying reaction and conversion reaction.[113]....38
Figure 2.19 Schematic illustration of charge transfer in Bi_2S_3-Bi_2O_3 heterostructures.[117]....39
Figure 2.20 (a-d) Synthesis of the 3D MoS_2-graphene-MoS_2 structure; (e) Mechanism of MoS_2 growth on both sides of the 3D graphene. (f) Photograph of the lightweight, free-standing MoS_2-graphene foam.[127]....42
Figure 2.21 Synthesis of MoS_2@HfO_2 nanosheets.[128]....43
Figure 2.22 Synthesis of WS_2/CNT-rGO aerogel.[132]....44
Figure 2.23 Synthesis of of FeS/C fibers.[146]....46
Figure 2.24 Synthesis of Co_9S_8@C hollow microspheres.[164]....49
Figure 2.25 Synthesis of NiS@C nanofibers.[177]....50
Figure 2.26 (a) SEM image; (b) TEM image; (c) scanning TEM (STEM) image; (d) high resolution TEM (HRTEM) image of multi-shell Sb_2S_3.[198]....54
Figure 2.27 Synthesis of Bi_2S_3/rGO composite.[207]....55
Figure 2.28 (a and c) Charge–discharge profiles; (b and d) *In situ* XRD patterns at different charge-discharge states of $MoSe_2$@C/N,P-rGO; (e) Schematic illustration of the proposed energy storage mechanism of $MoSe_2$@C/rGO at different stages.[217]....58
Figure 2.29 Synthesis process for $FeSe_2$ hollow nanocubes.[229]....61
Figure 2.30 Synthesis route for SnSe/NC.[246]....64
Figure 2.31 Two-step synthesis of Bi_2Se_3/G.[252]....65
Figure 2.32 (a and b) Synthesis and reversible reactions with Na^+ ions of the composite and bare CuP_2.[263]....69

Figure 3.1 Outline of the experimental procedures and characterization techniques used in this thesis..... 70
Figure 3.2 Schematic diagram of the electrospinning device..... 74
Figure 3.3 Hydrothermal autoclave (left) with a cross-sectional view (right)..... 75
Figure 3.4 Fundamental principles of XRD..... 77
Figure 3.5 Stacking sequence of components of a coin cell..... 82
Figure 4.1 (a) XRD patterns and (b) Raman spectra of sulfur, N-C and S/N-C samples. 90
Figure 4.2 (a) XPS spectra of N-C and S/N-C samples; high-resolution XPS spectra of (b) C 1s, (c) N 1s, and (d) S 2p for the S/N-C sample; high-resolution XPS spectra of (e) C 1s, and (f) N 1s for the N-C sample.....91
Figure 4.3 FT-IR spectra of the N-C and S/N-C samples..... 93
Figure 4.4 (a and b) SEM images of S/N-C nanofibers and N-C nanofibers; (c) high-magnification SEM image of S/N-C nanofibers; (d) low-magnification and (e) high- magnification TEM images of S/N-C nanofibers; (f) element mapping of the part of a S/N-C nanofiber.....94
Figure 4.5 Nitrogen adsorption/desorption isotherms of N-C and S/N-C nanofibers.95
Figure 4.6 Electrochemical performance of N-C and S/N-C electrodes. (a-b) The first three CV curves at 0.1 mV s^{-1}; (c-d) The charge-discharge profiles at 0.1 A g^{-1}; (e) Cycling performance at 0.1 A g^{-1}; (f) Rate capability at various current densities; (g) Long cycling performance of S/N-C at 5 A g^{-1}.....96
Figure 4.7 Nyquist plots of EIS data for N-C and S/N-C nanofiber electrodes. The inset is the equivalent circuit diagram.....98
Figure 4.8 CV curves of (a) N-C and (d) S/N-C electrodes at different scan rates; linear fitting of peak current dependence (normalized by $v^{1/2}$) on the square root of the scan rate ($v^{1/2}$) for the (b) N-C and (e) S/N-C electrodes; capacitive and diffusive contributions to the current density of (c) N-C and (f) S/N-C electrodes at 1.0 mV s^{-1}; percentage of the capacitive contribution to the current density of the (g) N-C and (h) S/N-C electrodes at different scan rates.....99

Figure 4.9 Optimized structure and charge density difference of (a) N-C, (b) S^1/N-C, and (c) S^2/N-C; (d) Na^+ diffusion energy and the related migration path for (e) N-C, (f) S^1/N-C, and (g) S^2/N-C. Grey, red, orange, blue, and purple spheres represent C, H, S, N, and Na atoms, respectively.....101

Figure 4.10 (a-b) *In situ* Raman spectra of S/N-C electrode in the first cycle with a scan rate of 1.0 mV s^{-1} in discharge and charge processes..... 102

Figure 5.1 Schematic illustration of the synthetic route to prepare the porous WS_2@S/N-C nanofibers.....108

Figure 5.2 (a) Low-resolution SEM image of WO_3 nanosheets; (b) low-resolution and (c) high-resolution SEM images, (d) low-resolution TEM image, (e) electron diffraction pattern, (f) high-resolution TEM image, and (g) element mappings of WS_2@ S/N-C.....112

Figure 5.3 (a) The SEM and (b) TEM images of synthesized WS_2; (c) SAED images and (d) high-resolution TEM images of WS_2..... 114

Figure 5.4 (a) XRD patterns of WO_3, WS_2, and WS_2@S/N-C; (b) Raman spectra, (c) FT-IR spectra, and (d) TGA curves of WS_2 and WS_2@S/N-C.....115

Figure 5.5 Nitrogen adsorption and desorption isotherms of WS_2@S/N-C nanofibers and pure WS_2.....117

Figure 5.6 Characterizations of S/N-C nanofibers: (a) XRD pattern; (b) SEM image; (c) TEM image and (d) HR-TEM image.....117

Figure 5.7 EDS spectra of (a) WS_2@S/N-C nanofibers and (b) S/N-C nanofibers.. 118

Figure 5.8 (a) XPS full survey spectra of WS_2@S/N-C nanofibers and pure WS_2; (b-e) High-resolution XPS spectra of WS_2@S/N-C: (a) W; (b) S; (c) N; (d) C; (f and g) High-resolution XPS spectra of W and S elements for pure WS_2..... 119

Figure 5.9 CV curves of (a) WS_2@S/N-C, (b) WS_2 and (c) S/N-C electrodes in the voltage range of 0.01-3 V at a scan rate of 0.1 mV s^{-1}; Charge-discharge profiles of (d) WS_2@S/N-C, (e) pure WS_2 and (f) S/N-C electrodes at a current density of 0.1 A g^{-1}. 120

Figure 5.10 Rate capability of the (a) WS_2@S/N-C, (b) WS_2 and (c) S/N-C electrodes at various current densities; Cycling performance of the (d) WS_2@S/N-C, (e) WS_2 and (f) S/N-C electrodes at a current density of 0.1 A g^{-1}; (g) Long-term cycling performance and Coulombic efficiency of WS_2@S/N-C electrode at a current density of 5 A g^{-1}..... 122

Figure 5.11 Low-resolution SEM images of WS_2@S/N-C electrode: (a) fresh electrode and (b) cycled electrode after 100 cycles; low-resolution SEM images of WS_2 electrode: (c) fresh electrode and (d) cycled electrode after 100 cycles.....124

Figure 5.12 EIS spectra of WS_2@S/N-C and pure WS_2 after 1st cycle at 0.1 A g^{-1}. The inset is the equivalent circuit.....125

Figure 5.13 (a) CV curves of WS_2@S/N-C electrodes at different scan rates; (b) log i *vs.* log v plots of WS_2@S/N-C electrodes; (c) Ratio of diffusion and capacitive contributions to the capacity at various scan rates for WS_2@S/N-C electrodes; (d) Capacitive charge storage contribution (pink region) for WS_2@S/N-C electrode at 1.0 mV s^{-1}..... 126

Figure 5.14 Adsorption sites for of I, II and III Na on (a) pure WS_2 and (b) the WS_2 in WS_2@S/N-C; Differences of charge density (charge accumulation: green, charge depletion: blue) with an isosurface level of 0.001 e/Å3 for Na on (c) pure WS_2 and (d) the WS_2 in WS_2@S/N-C in the most stable adsorption configuration.....128

Figure 6.1 Illustrative synthesis scheme of Fe_7S_8@S/N-C nanofibers.....133

Figure 6.2 (a) SEM image of α-Fe_2O_3 nanoparticles; (b) SEM image of Fe_7S_8@S/N-C nanofibers; (c) Low-resolution and (d) high-resolution TEM images of a Fe_7S_8@S/N-C nanofiber; (e) Element mapping of a Fe_7S_8@S/N-C nanofiber.....137

Figure 6.3 (a) SEM image and (b) HR-TEM image of Fe_7S_8; (c) SEM image and (d) HR-TEM image of S/N-C..... 139

Figure 6.4 (a) XRD patterns of as-prepared α-Fe_2O_3, Fe_7S_8, S/N-C and Fe_7S_8@S/N-C samples; (b) Raman spectra, (c) N_2 adsorption-desorption isotherms and (d) TGA data of as-prepared Fe_7S_8, Fe_7S_8@S/N-C and S/N-C samples..... 140

Figure 6.5 High-resolution XPS spectra of Fe_7S_8@S/N-C: (a) Fe 2p; (b) S 2p; (c) C 1s; (d) N 1s..... 142

Figure 6.6 CV curves of (a) Fe_7S_8@S/N-C, (b) Fe_7S_8 and (c) S/N-C electrodes at 0.2 mV s^{-1}. The charge-discharge profiles of (d) Fe_7S_8@S/N-C, (e) Fe_7S_8 and (f) S/N-C electrodes at 0.1 A g^{-1}. (g) Rate capability of Fe_7S_8@S/N-C, Fe_7S_8 and S/N-C electrodes at various current densities. (h) Cycling performance of Fe_7S_8@S/N-C, Fe_7S_8 and S/N-C electrodes at 1 A g^{-1}..... 143

Figure 6.7 Nyquist plots of the Fe_7S_8 and Fe_7S_8@S/N-C electrodes (a) before and (b) after 10 cycles..... 147

Figure 6.8 (a) CV curves at various sweep rates from 0.2 to 5 mV s^{-1}, (b) relationship between the peak currents and scan rates in logarithmic format, (c) capacitive contribution at a scan rate of 0.5 mV s^{-1} and (d) contribution ratio of the capacitive and diffusion-controlled capacity of Fe_7S_8@S/N-C electrode..... 149

Figure 6.9 (a) CV curves at various sweep rates from 0.2 to 5 mV s^{-1} and (b) contribution ratio of the capacitive and diffusion-controlled capacity of Fe_7S_8@S/N-C electrode..... 150

LIST OF TABLES

Table 3.1 Chemicals employed in this thesis..... 71

Table 5.1 The adsorption behaviour of Na on pristine WS_2.....130

Table 5.2 The adsorption behaviour of Na on WS_2@S/N-C**.**.....130

Table 6.1 Comparisons of electrochemical performances of this work with the reported Fe_7S_8 for Sodium ion batteries……145

LIST OF ABBREVIATIONS

Abbreviation	Full name
1D	One-dimensional
2D	Two-dimensional
3D	Three-dimensional
PAN	Polyacrylonitrile
PMMA	Polymethylmethacrylate
DMF	N, N–dimethylformamide
CNFs	Carbon nanofibers
CNTs	Carbon nanotubes
GO	Graphene oxide
rGO	Reduced graphite oxide
EVs	Electric vehicles
CV	Cyclic voltammetry
EDS	Energy dispersive X-ray spectroscopy
EIS	Electrochemical impedance spectroscopy
DFT	Density functional theory
FE-SEM	Field emission scanning electron microscopy
HR-TEM	High-resolution transmission electron microscopy
FT-IR	Fourier transform infrared spectroscopy
XRD	X-ray diffraction

XPS	X-ray photoelectron spectroscopy
BET	Brunauer-Emmett-Teller
TGA	Thermogravimetric analysis
EIS	Electrochemical impedance spectroscopy
LIBs	Lithium-ion batteries
SIBs	Sodium-ion batteries
a.u.	Arbitrary unit
cm	Centimeter
um	Micrometer
nm	Nanometer
WS_2	Tungsten disulfide
Fe_7S_8	Pyrrhotite
EG	Expanded graphite
CMC	Carboxymethyl cellulose
PC	Propylene carbonate
EC	Ethylene carbonate
DEC	Diethyl carbonate
FEC	Fluoroethylene carbonate
DME	Dimethoxyethane
CF_3SO_3Na	Sodium trifluoromethanesulfonate
NaFSA	Sodium bis (fluorosulfonyl) amide
SN	Succinonitrile

PEDOT	Poly(3,4-ethylenedioxythiophene)

LIST OF SYMBOLS

Symbol	Name	Unit
2θ	Detection angle in XRD	Degree
d	Lattice spacing	nm
C-rate	Charge or discharge rate	mA g^{-1}
S_{BET}	Specific BET surface area	m^2 g^{-1}
p	Relative pressure	Pa
P^0	Saturation pressure	Pa
I	Current	A
T	Temperature	K or °C
t	Time	h or s
wt.%	Weight percent	-
λ	X-ray Wavelength	Å
R_{ct}	Charge transfer resistance	Ω
f	Frequency in the EIS test	Hz
W	Warburg impedance	Ω
η	Coulombic efficiency	%
σ	Ionic conductivity	S cm^{-1}

LIST OF ORGANIZATIONS

Abbreviation	Full name
ISEM	Institute for Superconducting and Electronic Materials
AIIM	Australian Institute for Innovative Materials
EMC	Electron Microscopy Centre
UOW	University of Wollongong

CHAPTER 1 INTRODUCTION

1.1. Research Background

The limited lithium resources in the earth's crust will be likely to deplete, as lithium-ion batteries (LIBs) are being used for electric vehicles (EVs) and electronic portable devices on a large scale.[1, 2] The low-cost sodium-ion batteries (SIBs) are considered to be a promising alternative for the future.[3, 4] Since there are many similarities between the properties of sodium and lithium, SIBs share the same working principle with LIBs, i.e., the "rocking-type" battery. Compared with LIBs, SIBs have their own unique advantages, such as the abundance and wide distribution of sodium in the earth's crust and its higher standard reduction potential. Thus, SIBs are the potential substitute for LIBs as next-generation energy storage systems. Despite these advantages of SIBs, there is still a long way to go for realizing SIBs commercialization due to its relatively low capacity and inferior long-term cycling stability. The worldwide researchers have been devoted into SIBs for decades and many innovations in the materials have been obtained, such as for electrodes, electrolytes, and the separators.[5-8] However, the present anode materials are still not able to meet the requirements for practical application, because the existing anode materials are suffering from either large volume expansion or relatively low capacity. Therefore, designing novel anode materials is extremely urgent. The good news is the rapid development of nanotechnologies for high-performance LIBs could give some hints for searching ideal anode materials for SIBs with similar synthesis methods.[9, 10]

For obtaining anode materials with low-cost and good capability, in this thesis, three anode materials, i.e., N, S-co-doped carbon nanofibers, WS_2@carbon nanofibers and Fe_7S_8@carbon nanofibers, have been synthesized by electrospinning techniques and sulfidation process, and investigated as anodes for SIBs.

1.2. The Problem Statement

Although SIBs have obvious advantages in terms of the low cost and high abundance of sodium resource, there are also some limits on anode materials, i.e., low capacity, and poor cycling performance and rate capability. WS_2 and Fe_7S_8 could provide relatively high capacity for Na storage, although, these materials also suffer from poor cycling performance during the conversion process. These problems can be attributed to the volume change during the sodiation/desodiation process for SIBs, which is larger than that for the lithiation/delithiation process in LIBs. The inherent reason is the fact that the radius of the sodium ion is larger than that of the lithium ion. Therefore, it is important to develop novel technologies to obtain high-performance anode materials for SIBs.

1.3. Objectives of the Research

The main goal of this research is to develop the high-performance anode materials for SIBs. Three anode materials are included in this work, N, S-co-doped carbon nanofibers, WS_2@carbon nanofibers and Fe_7S_8@carbon nanofibers. This research was also dedicated to revealing the electrochemical sodium storage mechanisms based on

these materials and uncovering the relationship between these materials and their corresponding electrochemical performance.

1.4. Thesis Outline

The scope of this thesis consists of seven chapters, which are summarized as follows:

Chapter 1 introduces the research background, existing challenges for the anode development of sodium-ion batteries, the objectives of this research, and the thesis outline.

Chapter 2 provides a comprehensive literature review on the basic concepts, and recent advances in anode materials for sodium-ion batteries.

Chapter 3 includes information on the chemicals used in my experiments, the synthetic methods for the targeted anode materials in my research, and the corresponding characterization techniques.

Chapter 4 describes an electrospinning method to successfully fabricate mesoporous S/N-doped carbon nanofibers (S/N-C) as the anode for SIBs. Firstly, the introduction of N and S in S/N-C nanofibers can increase the active sites for Na^+ storage and reduce the energy required for Na^+ transfer. Moreover, the mesoporous S/N-doped carbon nanofibers are easily wetted by liquid electrolyte, which facilitates the Na^+ transport and increases the rate performance. As a result, the as-synthesized S/N-C

nanofibers deliver a high reversible capacity of 552.5 and 355.3 mA h g^{-1} at 0.1 and 5 A g^{-1}, respectively.

Chapter 5 reports a delicate method to embed WS_2 nanosheets into lotus rhizome-like heteroatom-doped carbon nanofibers with abundant hierarchical tubes inside, forming WS_2@sulfur and nitrogen-doped carbon nanofibers (WS_2@S/N-C). Firstly, the embedding of WS_2 nanosheets in carbon nanofibers could enhance the overall electrode conductivity, offering high reversible capacity. Moreover, the formation of lotus rhizome-like carbon nanofibers could facilitate electron transfer and prevent the pulverization of the electrode structure, resulting in a stable long-term cycling lifespan. As a result, the WS_2@S/N-C nanofibers exhibit a large discharge capacity of 381 mA h g^{-1} at 0.1 A g^{-1}, excellent rate capacity of 108 mA h g^{-1} at 30 A g^{-1}, and a superior capacity of 175 mA h g^{-1} at 5 A g^{-1} after 1000 cycles.

Chapter 6 describes a synthesis method for synthesizing Fe_7S_8@sulfur, nitrogen-doped carbon (S/N-C) nanofibers through electrospinning/sulfurization processes with Fe_2O_3 particles as the precursor. Owing to the unique structural characteristics, Fe_7S_8@S/N-C exhibited stable cycling performance of 347 mA h g^{-1} after 150 cycles at 1 A g^{-1} and superior rate capability of 220 mA h g^{-1} at 5 A g^{-1}. The improved performance of Fe_7S_8@S/N-C is ascribed to the enhanced Na adsorption provided by the heteroatom doped carbon nanofibers.

Finally, Chapter 7 provides a conclusion for the research work in this thesis. In addition, some comments on the present work are included, and future research directions in this field are also presented.

CHAPTER 2 LITERATURE REVIEW

Sodium batteries have been studied for electrochemical energy storage since the late 1970s, when TiS_2 was found to intercalate Na^+ ions reversibly at room temperature. The Na/TiS_2 battery was not comparable with Li/TiS_2 batteries, however, in terms of in energy density.[11, 12] Moreover, Prof. Goodenough discovered the potential of $LiCoO_2$ as the cathode material of choice for lithium ion batteries (LIBs) in 1980, while Prof. Yazami found that graphite could intercalate Li^+ ions reversibly and could be used as the anode for LIBs in 1982. These two important milestones promoted the rapid development of LIBs and most researchers focused their attention on the area of LIBs, which hindered the development of sodium ion batteries (SIBs). After they were commercialized by Sony in 1991, LIBs came to be widely used in portable electronics, and began to be used as power sources for electric vehicles (EVs) and hybrid electric vehicles (HEVs) in the subsequent three decades. Nevertheless, the scarcity of lithium resources means that they will not be able to meet the requirements of large-scale applications of LIBs in EVs and HEVs in the future, which directed researchers' attention onto the SIBs again, because the sodium is much more abundant than lithium. Yet there was no suitable electrode material for sodium insertion for a long period. In 2000, Stevens and Dahn found that hard carbon could deliver a high reversible capacity of 300 mA h g^{-1} for Na^+ ion storage, although its cycle life could not meet the demands of battery applications. In 2009, $NaFeO_2$ was found to be reversible for Na^+ insertion/de-insertion based on the redox couple of

Fe^{3+}/Fe^{4+}, which could offer an opportunity for the development of high-energy and low-cost SIBs. Since 2010, the research on SIBs has regained its initial rapid development due to the driving force of the large-scale applications in EVs and HEVs. In this chapter, the mechanism of sodium-ion batteries and recent developments related to the cathode, electrolyte, and anode will be summarized, with the main focused on anode materials because my research works are all related to anode materials for SIBs.

2.1 Mechanism of Sodium-ion Batteries

SIBs are mainly composed of the cathode (negative electrode), anode (positive electrode), separator, and electrolyte. The cathode and anode are separated by the separator, which is immersed in the electrolyte. The anodes usually consist of hard carbon or intercalation compounds for Na storage, while the cathodes consist of layered transition metal oxides, Prussian blue materials, or polyanionic cathode materials for hosting Na^+ ions. The SIBs share almost the same working principle with the "rocking-chair-type" LIBs, as shown in **Figure 2.1**. On charge, the cathode is oxidized due to the increase of the metal valence, with the de-intercalation of Na^+ ions into the electrolyte while the anode intercalates sodium and undergoes reduction. On discharge, they undergo the reverse process.

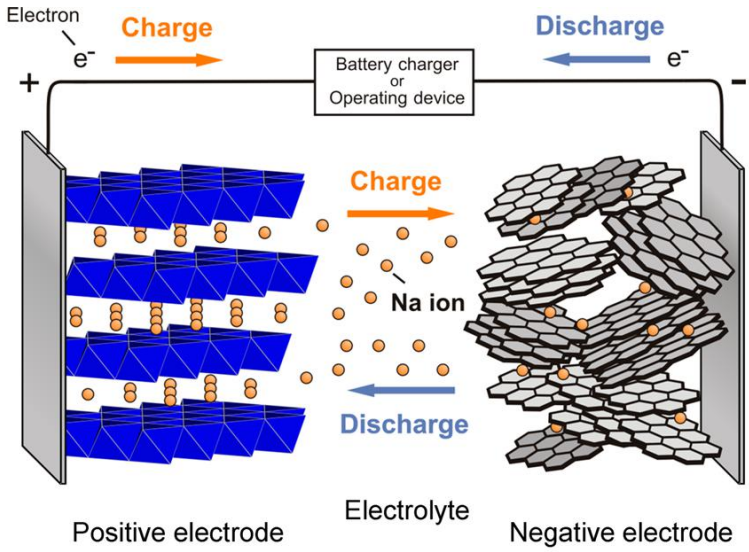

Figure 2.1 Schematic illustration of a sodium-ion battery.[1]

2.2 Cathode Materials

The cathode material is one of the important components that determine energy density. Great efforts have been made to search for suitable cathode materials with reversible capacity, resulting in excellent cycling stability. To date, many kinds of materials have been studied as potential cathode materials for SIBs, such as layered transition metal oxides,[13] Prussian blue materials,[14] and polyanionic cathode materials.[15] In the case of layered transition metal oxides (Na_xMO_2), many metal elements (M = Fe, Mn, Ni, Co, Cr, Ti, or V) are available as promising cathode candidates for SIBs due to their advantages of feasible synthesis and high operating potential. Nevertheless, their structural instability is an obstacle to their large-scale practical application in SIBs. As one class of important cathodes, Prussian blue materials ($Na_2M[Fe(CN)_6]$, M = Fe, Co, Mn, Ni, or Cu) have attracted great attention due to their open channel structure and compositional tunability. Moreover, their low

cost is also an important factor driving us to study them. However, the low energy density of Prussian blue cathodes will limit their applications at higher energy density, such as EVs and grid-scaled energy storage systems. The polyanionic cathode materials are a big group of cathode materials for SIBs, including phosphates, sulfates, mixed polyanionic compounds, silicates, molybdates, etc. They have obvious structural stability, but they exhibit low electronic conductivity, which limits their rapid development.

2.3 Electrolyte Systems

Electrolytes play crucial roles in the performance and characteristics of SIBs. At present, there are five kinds of electrolytes, e.g., aqueous electrolytes, organic electrolytes, ionic liquids, ceramic electrolytes, and polymer electrolytes.[16] The aqueous electrolytes possess high ionic conductivity, low effective cost, and good safety, but they have low energy density due to their limited voltage window. Compared to aqueous electrolytes, organic electrolytes have obvious advantages in terms of the voltage window. As shown in **Figure 2.2**, organic electrolytes are composed of sodium salts, solvents, and additives. Some additives could improve the performance of SIBs in some situations. Owing to the low cost of the sodium salts and solvents used in organic electrolytes, organic electrolytes can be used in large-scale practical application, which is cost-effective. Ionic liquids and ceramic electrolytes can tolerate high voltage and high temperature, so they can be used in some harsh environments. Their synthesis is complicated, however, and the cost is unaffordable

for practical applications at present. Polymer electrolytes possess moderate conductivity, safety, and good stability compared with organic electrolytes and ceramic electrolytes. In addition, the cost of polymer electrolytes is acceptable, which indicates that polymer electrolyte is a promising electrolyte in the future. Therefore, it is very important for us to choose suitable electrolytes for certain targeted purposes.

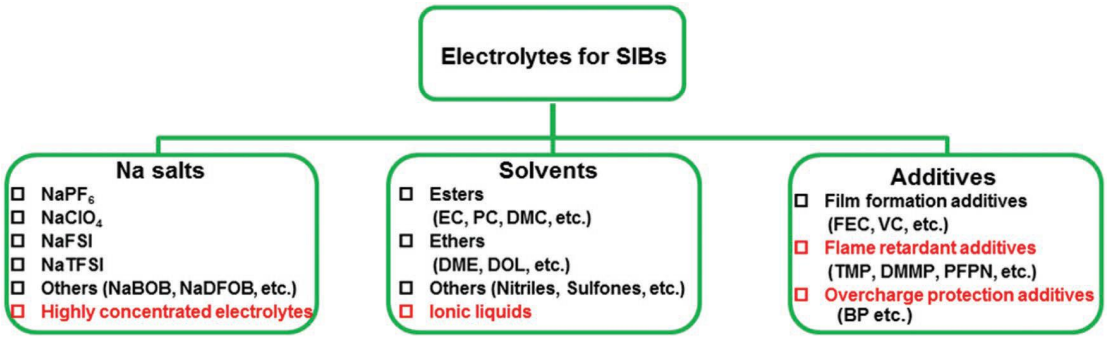

Figure 2.2 Chemical compositions of the organic electrolytes for SIBs.[17]

2.4 Anode Materials

In view of the current state of sodium ion batteries, a huge number of researchers are paying attention to exploring anode material. Some of them have already shown excellent specific capacity and stable cycling performance. Generally, these anode materials can be classified into the following six main groups: carbon-based materials, alloying materials, metal oxides, metal sulfides, metal selenides, and metal phosphides. In the following part, I will introduce some representative works in detail.

2.4.1. Carbon-based anode materials

2.4.1.1. Graphite

Metal Na anode can exhibit a theoretical capacity of 1165 mA h g^{-1}, although its theoretical operating voltage is the lowest among the various anode materials. This would lead to the formation of Na dendrites, causing serious safety problems. This has prompted us to look for other anode materials. Graphite, with its long-range-ordered layered structure, has been successfully commercialized and widely studied as an anode material due to its reversible capacity of 372 mA h g^{-1} in LIBs. Graphite could not well work in SIBs, however, because the interlayer distance (0.34 nm) between graphite layers is too small to allow the insertion of Na^+ (0.37 nm). Therefore, it is necessary to adjust the lattice spacing of the graphite to accommodate Na^+ insertion and extraction.

Expanded graphite (EG) is considered to be effective for storing more Na^+ due to the enlarged lattice spacing of the graphite. Dou's group synthesized thermally reduced graphene oxide (rGO) with an interlayer lattice spacing of 3.71-3.65 Å, and found that it could sustain a reversible capacity of 141 mA h g^{-1} at 40 mA g^{-1} in the electrolyte of 1 M $NaClO_4$ in propylene carbonate (PC) after 1 000 cycles.[18] There is a large irreversible capacity, however, which arises from the formation of a solid-electrolyte interphase (SEI) film due to the decomposition of electrolyte. Matsuo and Ueda synthesized carbon with a interlayer distance of 4.22 - 3.34 Å through the pyrolysis of

graphite oxide at 300 - 1000 °C.[19] The optimized expanded carbon (300 °C) could maintain a reversible capacity of 252 mA h g^{-1} at 20 mA g^{-1} in an electrolyte consisting of 0.5 M $NaClO_4$ in ethylene carbonate/diethyl carbonate (EC/DEC, 1:1 v/v) after 250 cycles. Wang's group realized the synthesis of expanded graphite (EG) with a interlayer lattice distance of 4.3 Å through the oxidation/partial reduction of graphite.[20] The as-synthesized EG could maintain a highly reversible capacity of 284 mA h g^{-1} at 20 mA g^{-1}, which is attributed to its enlarged interlayer lattice spacing with reduced oxygen-containing groups, as shown in **Figure 2.3**. The above examples indicate that it is effective to store Na^+ ions in graphite with a widened interlayer lattice distance.

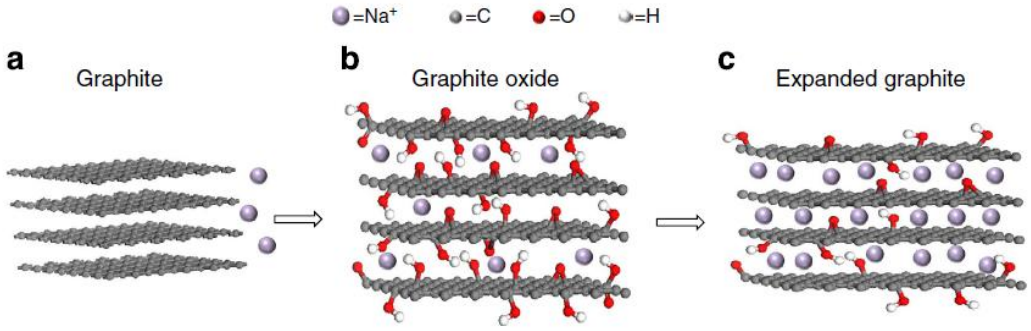

Figure 2.3 Schematic illustration of sodium storage in (a) graphite, (b) graphite oxide, and (c) expanded graphite.[20]

Electrolytes play important roles in the formation of stable graphite intercalation compounds (GICs), which makes graphite a promising anode for SIBs. Therefore, co-intercalation reactions can be employed to improve the performance of graphite. Previously, we thought that graphite could not be properly used as the anode for SIBs, since no binary graphite intercalation compound can be formed due to mismatch of

the structure of graphite and the size of Na^+ ions . Ternary graphite intercalation compounds of graphite and sodium, however, offer a great opportunity to store sodium with the proper electrolytes. Jache and Adelhelm found that the ternary GICs $Na(diglyme)_2C_{20}$ ($Na(DGM)_2C_{20}$) could be formed in electrolyte consisting of 1 M $NaPF_6$ in EC/DMC (1:1, w%), and the graphite could sustain a reversible capacity of ~ 100 mA h g^{-1} after 1000 cycles with high Coulombic efficiency.[21] Moreover, ~ 15 % expansion of the interlayer lattice spacing of graphite was observed. Kang's group found that natural graphite could present a reversible capacity of ~150 mA h g^{-1} after 2500 cycles in ether-based electrolytes.[22] The high capacity is attributed to the Na^+-solvent co-intercalation and pseudocapacitive behaviour, which were further confirmed by Chen's group.[23] The effect of electrolytes is schematically shown in **Figure 2.4**.

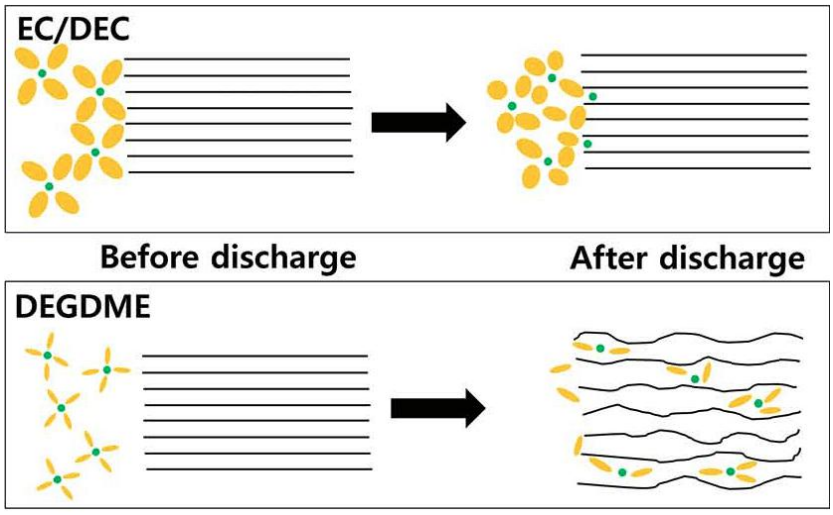

Figure 2.4 Proposed scheme of Na storage in natural graphite with different electrolyte systems.[22]

Since the first use of co-intercalation in graphite anode for SIBs, some work has been done along this direction, and some progress has been achieved. Tirado's group further studied sodium co-intercalation in the thermally synthesized EG with a interlayer lattice distance of 3.388 Å in 1 M $NaCF_3SO_3$/DGM electrolyte, and found that solvated sodium ions intercalated into the EG based on a two-stage sodium storage process, as identified by *ex-situ* X-ray diffraction (XRD) patterns.[24] Adelhelm's group used certain techniques, such as *in-situ* electrochemical dilatometry, online electrochemical mass spectrometry (OEMS), and other structural and compositional characterizations to clearly help us to understand the co-intercalation reaction,[25] and they found that there was no SEI film in graphite for the co-intercalation reaction. Gotoh's group further investigated the effect of the active motion of sodium-DGM complexes on Na^+ diffusion via the dynamics and the coordination structure of DGM-d14 molecules using 2 H solid-state nuclear magnetic resonance (NMR).[26]

Based on their understanding of the nature of electrolytes and graphite, Hassoun's group designed the first full sodium-ion cell, which consisted of graphite anode and $Na_{0.7}CoO_2$ cathode with 1 M $NaClO_4$ with tetraethylene glycol dimethyl ether (TEGDME) as the electrolyte.[27] The as-designed cell could deliver a high energy density of 30 W h kg^{-1} at 10 C, which demonstrated the promise for high rate application. Then, Kang's group further optimized the full sodium-ion cell with

graphite anode, $Na_{1.5}VPO_{4.8}F_{0.7}$ cathode, and a designed ether-based electrolyte.[28] The cell presented an energy density of as high as 149 W h kg^{-1} at 0.1 A g^{-1}..

2.4.1.2. Hard carbon

Compared to graphite, non-graphitizable hard carbon (HC) can be considered not to transform into graphite even above 3000 °C. It is composed of randomly aligned small graphene layers, which exhibit a porous structure that well accommodates Na^+.[29] The detailed structure is shown in **Figure 2.5**. In this structure, there are some sites that can store sodium, i.e., through intercalation between small graphene layers, in the porous structure, and by defect and surface adsorption. In addition, the sodium storage mechanism in HC has also been confirmed to be a three-step process: i) Na^+ ions are adsorbed at defect sites in the sloping voltage range; ii) Na^+ ions are intercalated into the hard carbon lattice; and iii) Na^+ ions are adsorbed at the porous surface in the plateau range. The unique structure offers many advantages for sodium storage. The clear mechanism of Na storage helps us to develop enhanced HC materials.

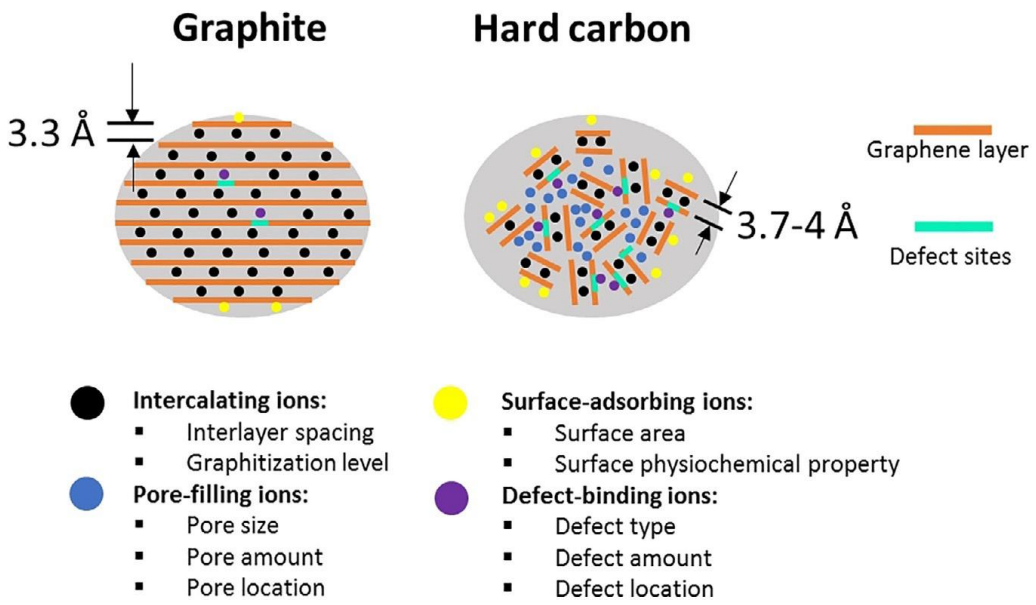

Figure 2.5 Schematic illustrations of graphite and HC accommodating sodium.[29]

HC has been usually synthesized from biomass precursors for SIBs.[30] Commonly, it is thought that the carbonization is accompanied by some concurrent reactions, e.g., dehydrogenation, condensation, hydrogen transfer, and isomerization (**Figure 2.6**). Yuan et al. synthesized a 3D hard carbon matrix through carbonizing sodium polyacrylate at 1100 °C for 10 h.[31] The porous structure could present a discharge capacity of 116 mA h g^{-1} at 4 A g^{-1} after 3000 cycles, which is attributed to the structural characteristics of the 3D porous matrix, which could effectively store sodium and accommodate the volume changes.

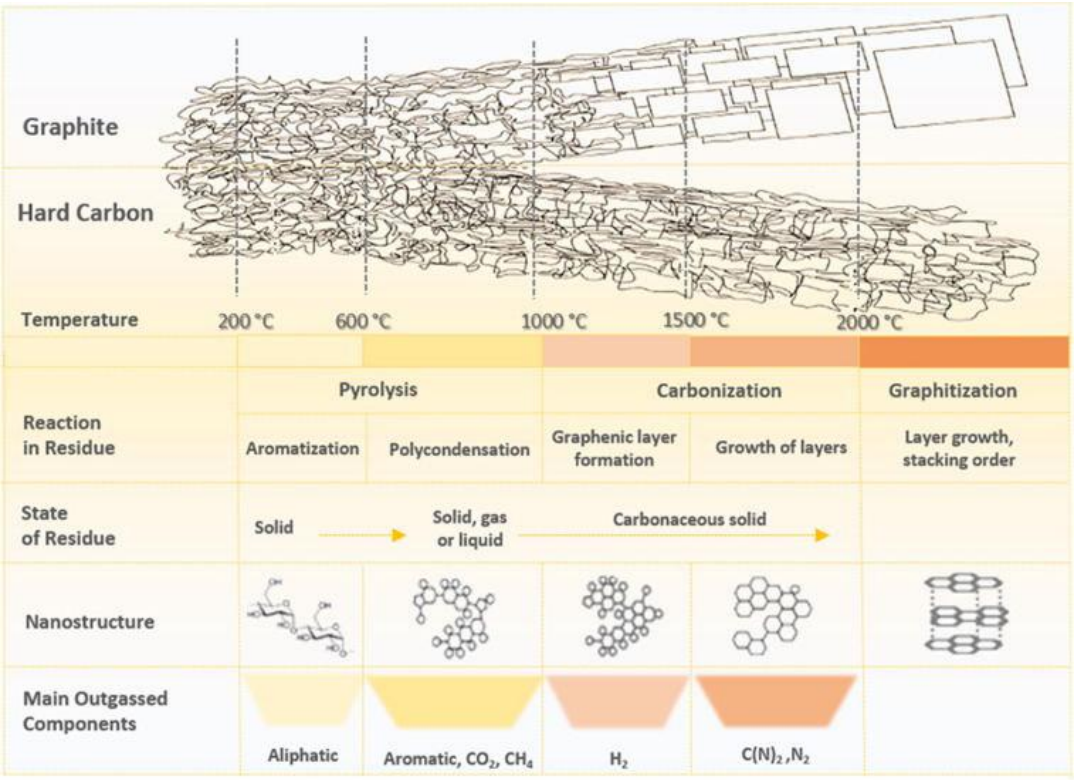

Figure 2.6 Proposed formation scheme for HC at different temperatures.[32]

Moreover, some other strategies are employed to enhance the electrochemical performance of hard carbon, such as optimizing electrolytes and binders. Komaba's group found that sodium carboxymethyl cellulose helps hard carbon to deliver good performance.[33] Yamada's group found that 50 mol % sodium bis(fluorosulfonyl)amide (NaFSA)/succinonitrile (SN) electrolyte could facilitate reversible Na^+ insertion into hard carbon.[34] This demonstrates that the electrolyte plays an important role in the electrochemical performance of hard carbon.

2.4.1.3 Soft carbon

Soft carbon exhibits a semi-graphitic, fewer-defect structure with high/low strain regions (disordered and graphitic parts). This structure endows soft carbon with good

electronic conductivity. Little research on soft carbon anode for SIBs has been reported, however, due to the small interlayer spacing of graphite.[35] Alcántara *et al.* synthesized soft carbon through the calcination of petroleum coke and firstly found that it could offer a discharge capacity of above 100 mA h g^{-1}.[36] Recently, Song's group found that mesoporous soft carbon obtained through the carbonization of mesophase pitch with $CaCO_3$ as the template could retain a sustainable capacity of 103 mA h g^{-1} after 3000 cycles at 500 mA g^{-1},[37] which could be due to its mesoporous structure and well-balanced disordered and graphitic parts. Feng's group found that soft carbon fibers obtained through the calcination of wet-spun polyacrylonitrile (PAN) fibers could sustain a discharge capacity of 190 mA h g^{-1}.[38] More attention should be paid to soft hard research in the future.

2.4.2 Alloying anodes

Carbon-based materials have been successfully used for Na storage in SIBs, delivering reasonable capacity during the charge/discharge processes. The specific capacity of carbon-based materials is obviously low, however, owing to its intrinsic structural constraint. Alloy materials are attractive for storing Na^+ ions in the host structure below 1.0 V to achieve a high specific capacity. To date, some alloying metal anode materials have been reported, *i.e.*, Sn, Bi, Si, Ge, Sb, P, *etc.* The large Na^+ ion could cause severe volume changes during the electrochemical reactions, however, leading to their fracture or pulverization. To overcome these problems, structural design of the electrode materials is particularly crucial.

2.4.2.1 Sn anode

Sn has attracted great attention as a high-capacity anode (847 mA h g^{-1} for $Na_{15}Sn_4$ alloy), although it also suffers from severe volume change of ~ 400% during the sodiation process.[39] To overcome this obstacle, many strategies have been used for obtaining good electrochemical performance from the cycling and rate aspects.[40]

In 2012, Wang's group designed mesoporous C/Sn composites to stabilize Sn nanoparticles via the mesoporous carbon matrix during sodiation/desodiation processes.[41] The as-synthesized samples showed very poor cycling performance, however, due to the large interfacial resistance to the sodiation of Sn. Since then, some progress has been achieved. Chen's group synthesized Sn nanodots@porous N-doped carbon nanofibers to form an integrated electrode by the electrospinning method (**Figure 2.7 a** and **b**).[42] The as-synthesized integrated electrode (**Figure 2.7 c** and **d**) could deliver a high capacity of 483 mA h g^{-1} after 1300 cycles at 2000 mA g^{-1}. Its excellent performance could be attributed to the small Sn particle size, the porous carbon matrix for Sn, and the interlinked 3D carbon network. Wang's group prepared core–sheath Sn nanorods@carbon nanotubes on carbon paper through a soaking-chemical vapour deposition process, which could maintain a high capacity of ~ 887 μAh·cm^{-2} after 50 cycles at 50 mA g^{-1}.[43] The integrated Sn@carbon nanotube (CNT) arrays facilitated fast ion/electron transfer, and provided enough room for volume change during the sodiation process. Moreover, other Sn/carbon hybrids were also reported, such as Sn@C nanospheres/carbonized filter paper,[44] yolk-shell Sn@C

nanostructures,[45] Sn/graphene composites,[46] and so on. These researchers could obtain superior anodes with good performance through taking the advantages of the structure and the high conductivity of the carbon matrix.

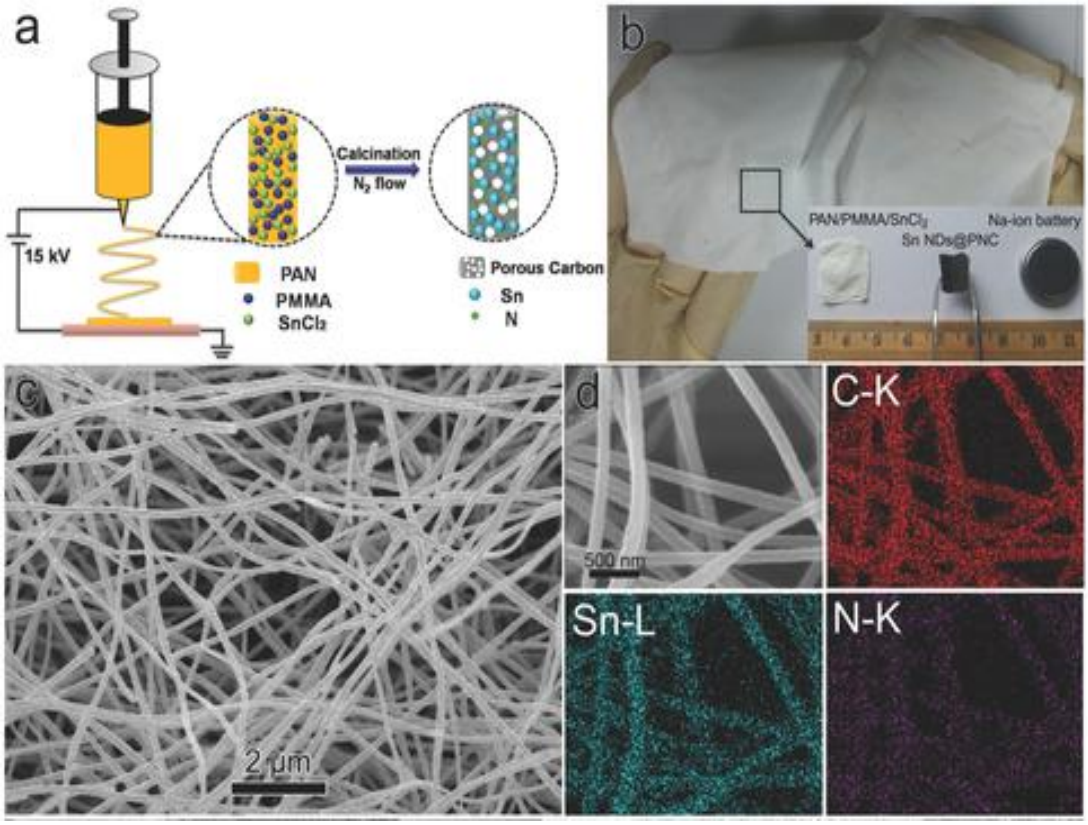

Figure 2.7 (a) Schematic illustration of the synthesis process for Sn@N-C nanofibers; (b) photograph of the integrated precursor and electrode; (c) scanning electron microscope (SEM) image and (d) element mapping of Sn@N-C nanofibers.[42]

Furthermore, Sn intermetallic compounds, i.e., $Sn_{0.9}Cu_{0.1}$,[47] $Na_xSb_ySn_{100-x-y}$,[48] etc., have been reported for Na^+ storage in SIBs. These intermetallic compounds can be catalogued into two kinds, alloying with inactive metals and alloying with active metals. On the one hand, in the case of alloying with inactive metals, the inactive metals play two important roles in buffering the volume expansion of Sn and

improving the conductivity. On the other hand, active metals can contribute extra capacity and buffer the volume expansion in hybrids.

2.4.2.2 Sb anode

As a potential anode for SIBs, Sb has relatively high theoretical capacity (Na_3Sb, 660 mA h g^{-1}) and working voltage of about 0.5-0.8 V vs. Na^+/Na. These two characteristics endow Sb with high energy-density and safety. There is a ~390% volume change in Na_3Sb during electrochemical processes, however, which will lead to poor electrochemical performance due to the pulverization of the electrode. The following part will discuss the progress of the Sb anode for SIBs.

Xie's group was the first to synthesize the Sb/graphene (Sb/G) nanocomposite using the solvothermal method in 2014,[49] which could deliver 211 mA h g^{-1} after 30 cycles at 20 mA g^{-1}. To further improve the performance, Ji's group designed hollow structural Sb by galvanic replacement, using nickel nanoparticles as the precursor, and employed the unique structure to realize a high capacity of 627.3 mA h g^{-1} after 50 cycles at 100 mA g^{-1}.[50] Feng's group employed the chemical dealloying technique to synthesize porous Sb particles, and the optimized sample could deliver a sustainable capacity of 573.8 mA h g^{-1} after 200 cycles at 100 mA g^{-1},[51] which is ascribed to the interconnected porous structure of integrated Sb, which might provide easy electrolyte access and excellent electron/ion transport. They selectively etched Al from the Al-Sb alloy using NaOH to form porous Sb, as shown in **Figure 2.8**. Apart from the

above-mentioned structural control, Yang's group exfoliated Sb particles from antimony nanosheets in isopropyl alcohol solution containing sodium hydroxide, and combining the as-exfoliated Sb nanoplates with graphene to assemble hybrid films, which demonstrated a high volumetric capacity of 1226 mA h cm^{-3}.[52] The sample's high volumetric sodium storage should be attributed to the high capacity and high density of antimony along with the high conductivity of graphene.

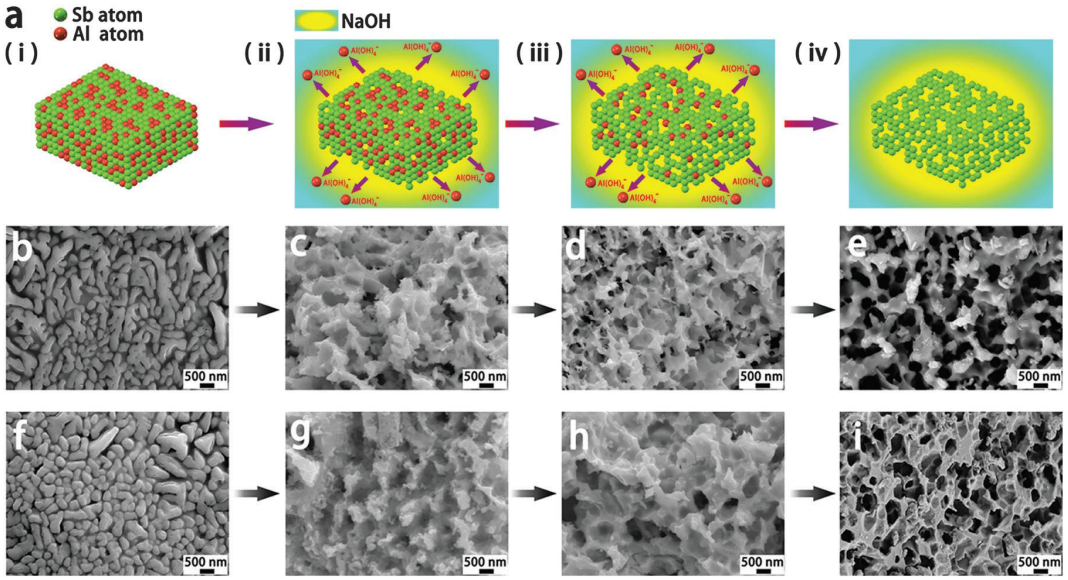

Figure 2.8 (a) Schematic illustration of the chemical dealloying process to produce the porous Sb structure; (b) $Al_{30}Sb_{70}$ and its dealloyed products; (f-i) $Al_{20}Sb_{80}$ and its dealloyed products.[51]

Compared to their pure counterparts, intermetallic compounds have some advantages, i.e., improved capacity retention, faster kinetics, etc. From these considerations, some Sb-based intermetallic compounds have been synthesized, such as Cu_2Sb, NiSb, etc. Baggetto *et al.* synthesized Cu_2Sb thin films, and tested their performance with fluoroethylene carbonate (FEC) as the electrolyte additive, finding that they could largely sustain a discharge capacity of ~ 250 mA h g^{-1} after 200 cycles.[53] Yu's group

designed 3D interconnected NiSb hollow nanospheres by a galvanic replacement reaction using 3D interconnected Ni nanospheres and Sb^{3+} ions as the precursors, as shown in **Figure 2.9 a**.[54] The as-synthesized hybrid structures exhibited a discharge capacity of 230 mA h g^{-1} after 150 cycles at 10 C. Both the unique structure and the Ni matrix could improve the rate capability of the 3D interconnected NiSb nanospheres, as shown in **Figure 2.9 b**. The above examples demonstrate that the intermetallic compounds are promising anode materials for SIBs.

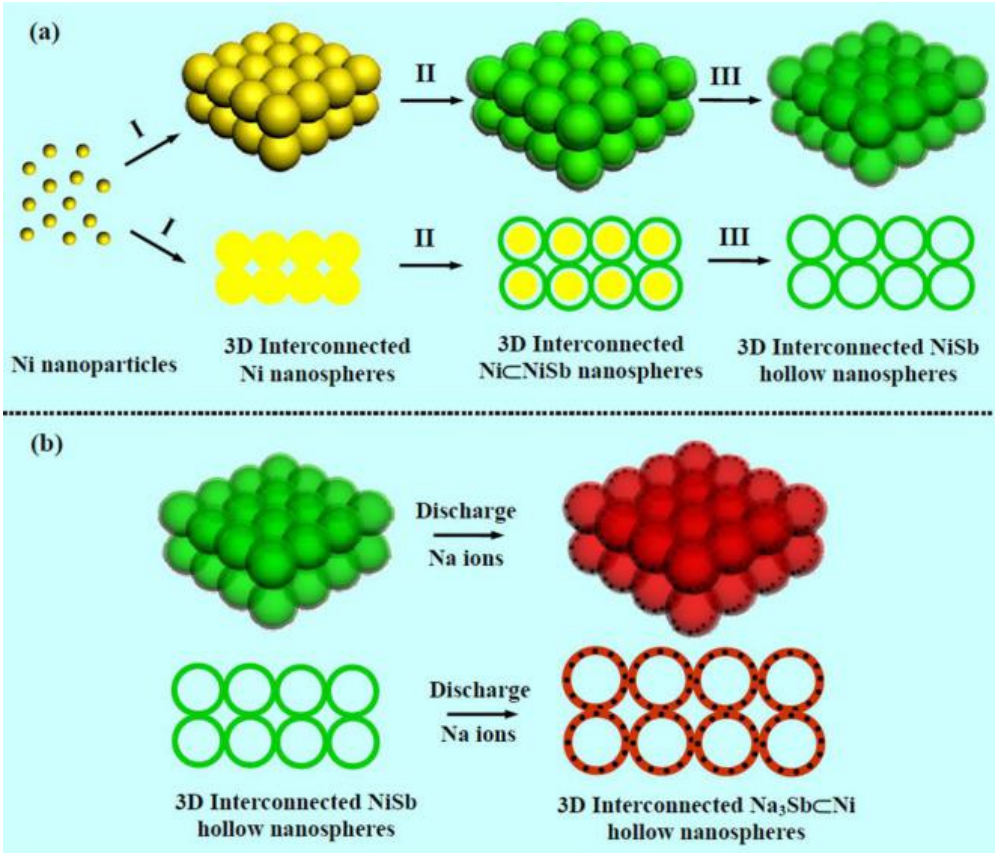

Figure 2.9 Schematic illustrations of (a) the synthesis of 3D interconnected NiSb hollow nanospheres; and (b) the sodiation/desodiation of 3D interconnected NiSb hollow nanospheres.[54]

To alleviate the stress during the sodiation process for Sb, it is an effective strategy to hybridize the Sb with various kinds of carbon, such as graphene,[55] carbon nanofibers,[56] etc. Bao's group designed the Sb/G composites through confined vapour deposition with the Sb particles and freeze-dried graphene oxide located at the lower and upper parts of a sealed tube,[55] as shown in **Figure 2.10**. The as-synthesized Sb/graphene composite could deliver a high rate capability of 210 mA h g^{-1} at 5000 mA g^{-1}, which was attributed to the graphene, which could enhance sodium ion/electron diffusion and electronic transport, and possibly stabilize the SEI layer.

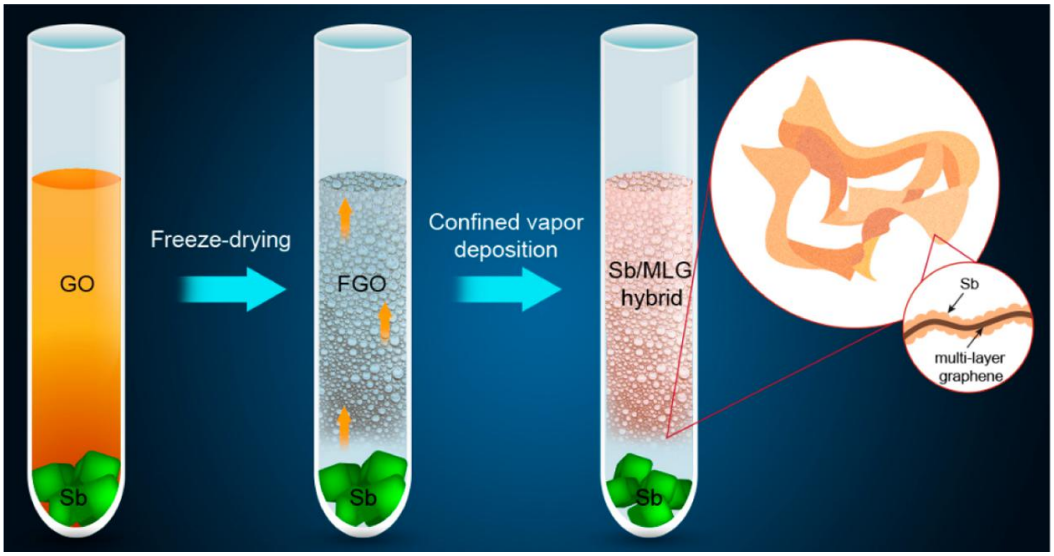

Figure 2.10 Schematic illustration of the synthesis of Sb/graphene composite.[55]

2.4.2.3 Ge anode

Ge presents a theoretical capacity of 369 mA h g^{-1} via alloying with sodium (NaGe) and has its potential range from 0.15 to 0.6 V.[57] Veith's group was the first to report the Na storage behavior of Ge thin films, and found that the as-synthesized thin films

could offer a capacity of 110 mA h g^{-1} at 125.46 A g^{-1}.[58] Lu's group designed and prepared the core-shell Ge@rGO@TiO_2 nanofibers by electrospinning/atomic layer deposition processes, which exhibited a capacity of 182 mA h g^{-1} after 250 cycles at 100 mA g^{-1} owing to the graphene/TiO_2 double protection.[59] Yin's group designed a carbothermal reduction method for encapsulating Ge nanoparticles in hollow carbon boxes, with a reversible capacity of 346 mA h g^{-1} after 500 cycles at 100 mA h g^{-1}.[60]

2.4.2.4 Bi anode

As one of the potential anode materials, Bi exhibits a theoretical capacity of 385 mA h g^{-1} for Na_3Bi, with 250 % volumetric expansion during the charge/discharge processes. Owing to its high volumetric capacity and relatively low volume change, Bi has attracted some attention as an anode material for SIBs.[61]

Wang's group found that the Bi@G composite could demonstrate a highly reversible capacity of 561 mA h g^{-1},[62] which was attributed to the unique structure of Bi for Na intercalation. Feng's group prepared Bi nanorod bundles by chemically dealloying $Al_{30}Bi_{70}$ alloy, and found that it exhibited 301.9 mA h g^{-1} after 150 cycles at 50 mA g^{-1}, which was due to high Na^+ /electron accessibility and transport in the structure.[63] Liang's group grew Bi nanosheets on carbon fiber cloth. The integrated Bi electrode showed a reversible capacity of 240 mA h g^{-1} after 300 cycles at 200 mA g^{-1}, which is attributed to the integrated electrode design.[64] Yin et al. embedded Bi in carbon nanofibers through the electrospinning method. The 1D hybrid structure endowed the sample with a sustainable

capacity of 273.2 mA h g^{-1} after 500 cycles at 100 mA g^{-1}.[65] Yu's group prepared Bi nanorods@N-doped carbon nanotubes through the reduction of Bi_2S_3 and the carbonization of a polymer coating layer. The as-synthesized Bi@C electrode delivered a reversible capacity of 410 mA h g^{-1} at 50 mA g^{-1} for SIBs.[66] The unique structure could account for its excellent performance. The hybridization with various carbon materials is demonstrated to be effective to improve the performance of Bi-based anodes. Moreover, Li's group found that bulk Bi could also present a sustainable capacity of 400 mA h g^{-1} in $NaPF_6$-DGM electrolyte with a high retention rate of 94.4% after 2000 cycles.[67] They found that both the porous integrity of the bulk Bi and the wettability of DGM towards Bi contributed to the formation of a stable SEI film for achieving excellent performance.

2.4.2.5 P anode

Phosphorus is considered to be a cost-effective anode material with a theoretical capacity of 2590 mA h g^{-1} (Na_3P) for SIBs.[68] Due to severe volume changes during alloying/dealloying processes, however, P anode usually exhibits poor cycling performance, so it is necessary to find new strategies to overcome this.

Yang's group was the first to report an amorphous phosphorus/carbon (P/C) composite as anode for SIBs.[69] It could sustain a reversible capacity of 1764 mA h g^{-1}, but it exhibited disappointing cyclability due to its weak ion/electron conductivity. Oh's group found that their amorphous red P/carbon composite could maintain a

sustainable capacity of 1890 mA h g^{-1} at 143 mA g^{-1}.[70] Song et al. prepared a chemically bonded phosphorus/graphene composite, which sustained a capacity of 1700 mA h g^{-1} after 60 cycles with relatively good cyclability.[71] Following these pioneering works, more and more work has been done in this field. They mainly focused on the design and synthesis of P/C composites and ranged from physical hybrids to chemically bonded hybrids.[72] Wang's group found that their red P/CNT composite fabricated by the vaporization–condensation method (**Figure 2.11**) could present a reversible capacity of ~240 mA h g^{-1} after 2000 cycles at 2 A g^{-1}.[73] This excellent cycling performance was ascribed to the conductive carbon nanotube network surrounding the red P. Amine's group further synthesized a black phosphorus/Ketjenblack–carbon nanotubes composite by ball milling, and found that it could exhibit 1700 mA h g^{-1} after 100 cycles at 1.3 A g^{-1}, which was attributed to nanostructuring of the phosphorus particles and the carbon matrix.[74]

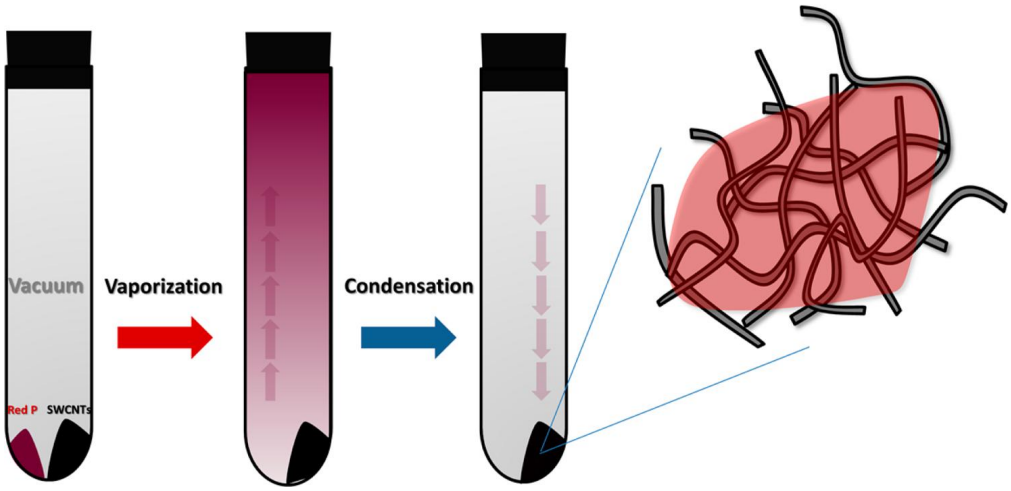

Figure 2.11 Synthesis process for red P/carbon nanotube composite.[73]

2.4.3 Metal oxides

Metal oxides have the advantages of abundance and high theoretical capacity as anode materials for SIBs. Metal oxides can be classified into three groups according to their electrochemical reaction mechanisms in SIBs: i) intercalation/de-intercalation materials (TiO_2, Nb_2O_5), ii) conversion materials (Fe, Cu, Ni, or Co-based oxides), and iii) conversion and alloying materials (SnO_2, Sb_2O_3, and Bi_2O_3). Nevertheless, the metal oxides suffer from unsatisfactory cycling stability and rate capability, which are ascribed to low conductivity and large volumetric changes during the charge/discharge processes. To date, a great number of efforts have been made to solve these issues via designing new composite structures and combining them with carbonaceous substrates.

2.4.3.1 TiO_2 anode

TiO_2 is considered to be able to store Na with some advantages, *i.e.,* natural abundance, non-toxicity, high chemical stability, *etc.*[75] Yet, there are also the disadvantages of low electronic conductivity and the inferior Na^+ diffusion of TiO_2.[76] Xiong et al. synthesized amorphous TiO_2 nanotubes (NTs) on Ti foil as the substrate that demonstrated a reversible capacity of ~150 mA h g^{-1} at 50 mA g^{-1} with poor cycling performance.[77] In order to solve these problems, various strategies have been employed, such as nanostructured designs,[78] hybridization with carbon,[76] hybridization with other materials,[79] and defect engineering.[80]

Nanostructure design is important for the development of TiO_2 anode. Lei's group designed 3D Ni-TiO_2 core-shell nanoarrays by the nanoimprinted anodic aluminium oxide (AAO) templating method, and they sustained a reversible capacity of ~200 mA h g^{-1} after 100 cycles at 50 mA g^{-1},[81] which is attributed to their good ion/electron transport and electrode integrity. The fabrication process for highly ordered 3D Ni-TiO_2 nanoarrays is shown in **Figure 2.12** using the AAO templating technique. Ji's group synthesized anatase TiO_2@C "olives" composed of tiny crystalline grains with a sustainable capacity of 267 mA h g^{-1} at 33.6 mA g^{-1}, which is associated with the existence of subtle loose structure that can facilitate Na^+ transportation.[82]

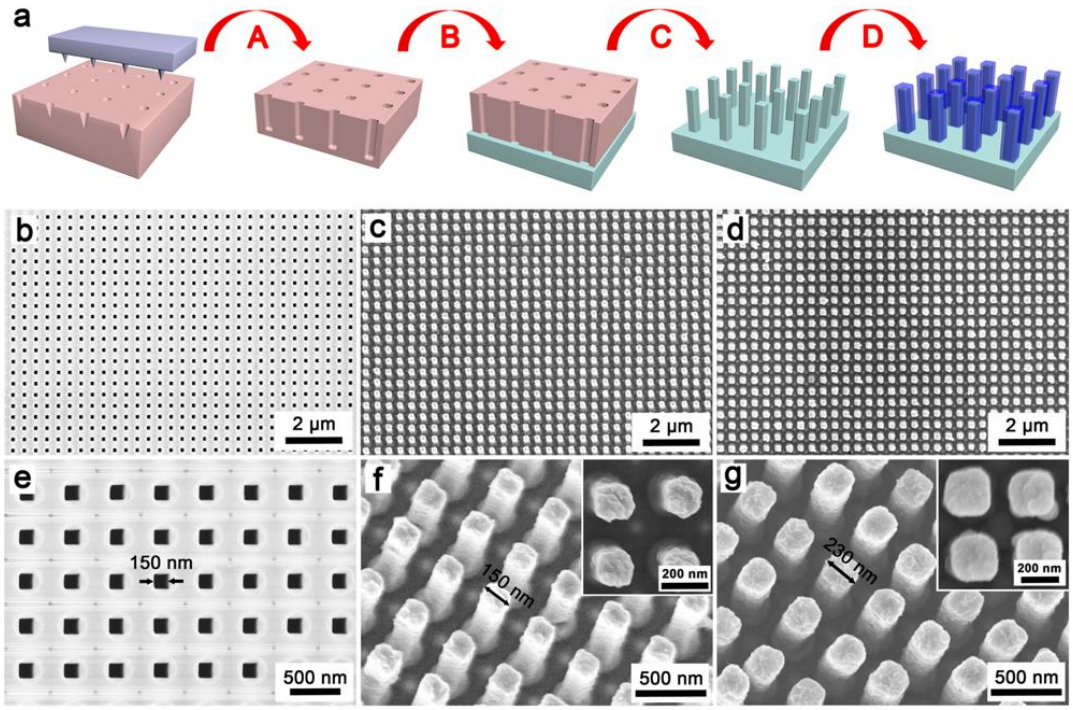

Figure 2.12 (a) Schematic illustration of the preparation of highly ordered 3D Ni-TiO_2 nanoarrays using the AAO templating technique. SEM images of (b and e) the AAO template, (c and f) Ni nanopillar arrays, and (d and g) 3D Ni-TiO_2 nanoarrays.[81]

2.4.3.2 Nb_2O_5 anode

Recently, Nb_2O_5 has attracted tremendous attention due to its advantages of unique chemical stability under acid conditions, wide potential window and rich redox chemistry (Nb^{5+}/Nb^{4+}, Nb^{4+}/Nb^{3+}). Orthorhombic Nb_2O_5 features the largest interplanar lattice spacing of 0.39 nm for (001) planes, which could possibly promote the fast diffusion and storage of Na^+. Nevertheless, the low electronic conductivity of Nb_2O_5 has greatly hindered its application in high performance SIBs. Much effort has been made to address this problem by structure optimization.[83]

Kang's group reported an ordered mesoporous Nb_2O_5/C composite with a discharge capacity of ~175 mA h g^{-1}, which could be achieved because the mesoporous structure could accommodate the large volume changes. They also found that the Na storage in Nb_2O_5 is *via* Na intercalation/deintercalation reactions and surface capacitive reactions,[84] as shown in **Figure 2.13.** Lee's group designed core-shell Nb_2O_5@C nanoparticles supported by rGO, which delivered ~ 285 mA h g^{-1} at 25 mA g^{-1}.[85]

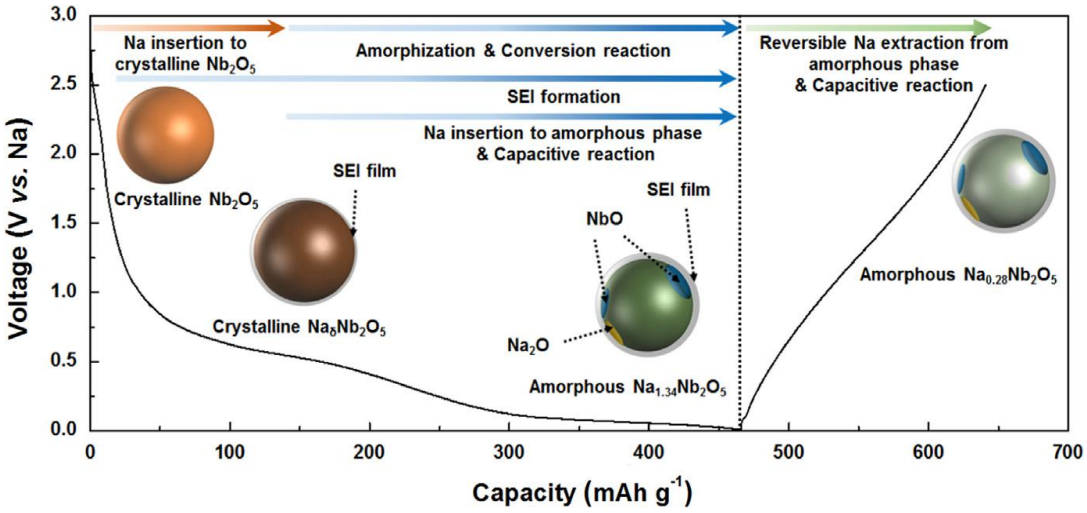

Figure 2.13 Schematic diagram of Na storage in Nb_2O_5.[84]

Yu's group encapsulated S-doped Nb_2O_5 hollow nanospheres in S-doped graphene networks to form a S-Nb_2O_5@G composite with outstanding rate capability due to the combined effects of the 3D hollow structure and heteroatom doping,[86] as shown in **Figure 2.14**. Wang and his co-workers proposed a nanocasting approach to synthesize a mesoporous Nb_2O_5 nanosheets/graphene (Nb_2O_5/G) composite, which could present a capacity of 230 mA h g^{-1} after 30 cycles at 0.25 C.[87] This high performance was attributed to its unique thin mesoporous structure and crystalline characteristics.

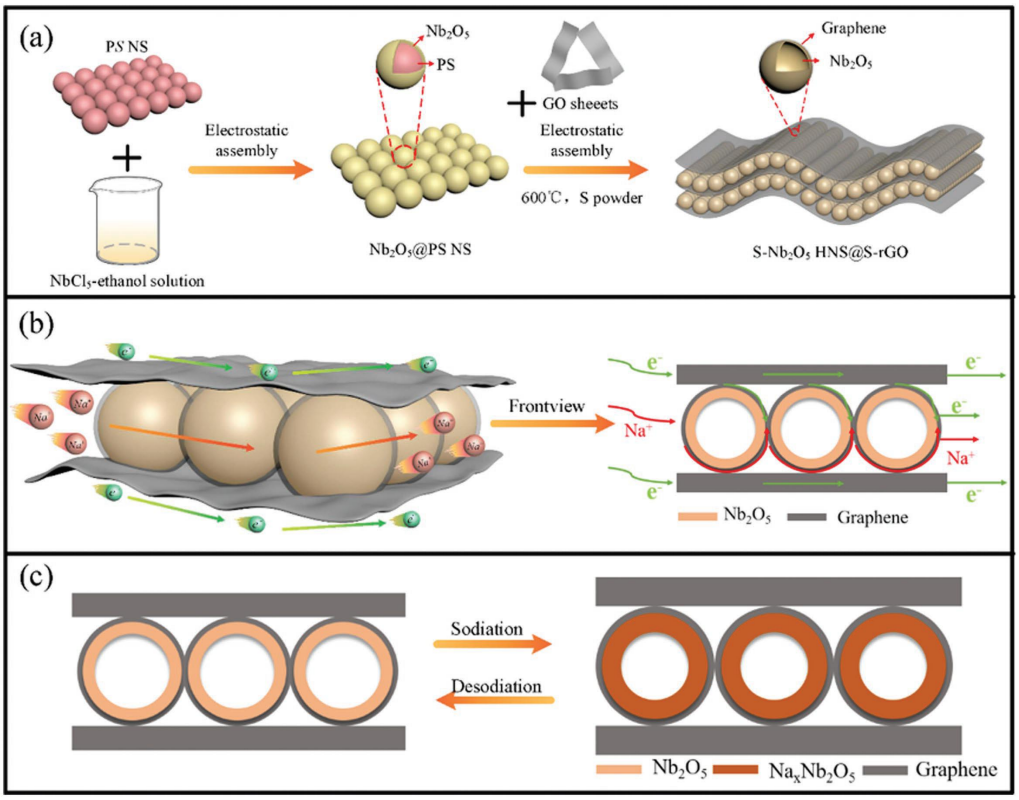

Figure 2.14 (a) Schematic illustration of the synthesis of S-Nb_2O_5@S-rGO; (b) the Na^+/e transportation process in Nb_2O_5/rGO composite; (c) the hollow nanosphere/graphene structure can buffer the volume expansion during the sodiation/desodiation processes.[86]

2.4.3.3 Fe_2O_3 and Fe_3O_4 anodes

Fe_2O_3 and Fe_3O_4 have high theoretical capacities (~1007 mA h g^{-1} for Fe_2O_3 and 926 mA h g^{-1} for Fe_3O_4) and are considered as promising anodes for SIBs,[88, 89] although their poor intrinsic electronic conductivity and severe volume changes during the cycling process would cause pulverization and capacity fading. In order to solve these problems, nanostructuring and hybridizing with carbon were investigated and found to alleviate expansion of the structure and improve the conductivity.[90]

Zhou's group found that their Fe_2O_3@graphene composite could sustain ~ 400 mA h g^{-1} after 200 cycles at 100 mA g^{-1}.[91] Inspired by this idea, some works on a variety of Fe_2O_3/graphene composites as anodes for Na storage were reported . For example, Yang's group anchored ~ 300 nm Fe_2O_3 single crystallites on rGO nanosheets to form a Fe_2O_3/graphene composite, which exhibited ~ 500 mA h g^{-1} after 100 cycles at 50 mA g^{-1} due to the existence of the conductive matrix.[92] Moreover, other carbon materials have been also used as supports for Fe_2O_3 to improve its performance.[93]

Fe_3O_4/C composites have been employed as models for improving the electrochemical performance of Fe_3O_4.[90, 94] Wang's group reported that Fe_3O_4/rGO composite exhibited a sustainable capacity of 210 mA h g^{-1} for 250 cycles at 200 mA g^{-1}.[95] Xu's group synthesized an Fe_3O_4/rGO composite composed of Fe_3O_4 quantum dots and 3D rGO by the hydrothermal method, which presented a capacity of 312 mA h g^{-1} after 200 cycles at 50 mA g^{-1}.[96] This performance was attributed to the 3D structure of graphene, which could accommodate the volume changes during the cycling process, and the small size of the Fe_3O_4 particles. In addition, Fe_3O_4-based heterostructures,[97,98] i.e., Fe_3O_4/MoS_2, Fe_3O_4@FeS, and Fe_3O_4/$Fe_{1-x}S$@C@MoS_2, have also achieved excellent performance due to their multi-component effects.

2.4.3.4 Co_3O_4 anode

Co_3O_4 undergoes a multi-electron transfer reaction process with a theoretical capacity of ~ 890 mA h g^{-1}. Some strategies should be undertaken for improving its

performance, however, e.g., accommodating the volume changes during sodiation/desodiation and enhancing its electrical conductivity. Rahman et al. reported that Co_3O_4 nanoparticles could sustain a capacity of 447 mA h g^{-1} after 50 cycles at 25 mA g^{-1}.[99] Li et al. demonstrated that Co_3O_4/3D graphene composite could exhibit a capacity of ~523.5 mA h g^{-1} after 50 cycles,[100] which is attributed to the ability of 3D graphene to accommodate the volume change of Co_3O_4 during the cycling process. Inspired by these results, other Co_3O_4/C composites have been studied, i.e., CNTs, carbon nanofibers (CNFs), carbon hollow spheres, etc.[101]

2.3.4.5 NiO anode

NiO has a theoretical capacity of 718 mA h g^{-1} for Na storage.[102] Wang and his coworkers realized the growth of NiO nanosheets on the surface of hollow carbon microspheres to form the HC@NiO composite (**Figure 2.15**), which maintained a capacity of 309 mA h g^{-1} after 50 cycles at 0.1 A g^{-1}.[103] Zhu's group synthesized NiO/Ni/graphene from nickel metal-organic frameworks (Ni-MOFs), which had a sustainable capacity of 300 mA h g^{-1} at 200 mA g^{-1}, which is attributed to the facilitation of faster charge transfer by the conductive matrix.[104]

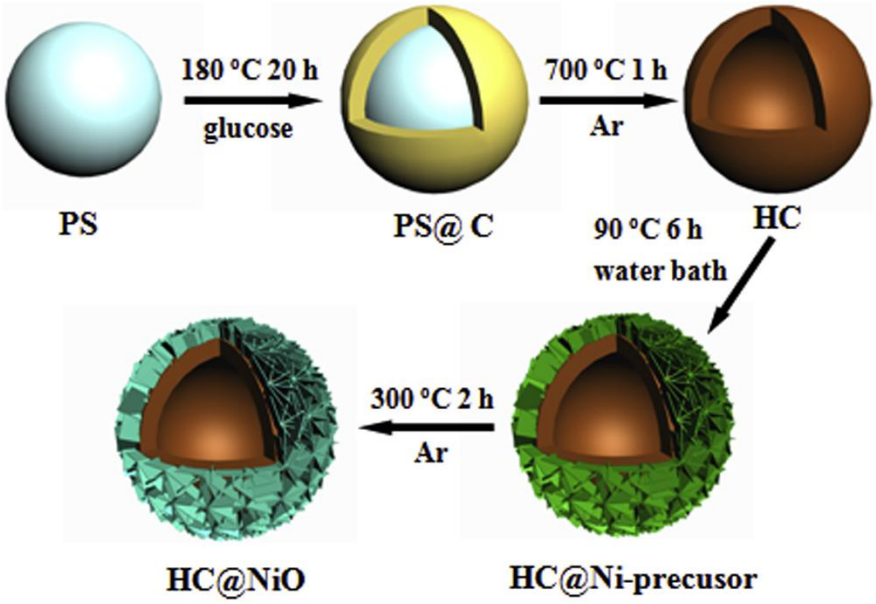

Figure 2.15 Schematic illustration of the synthesis of hollow carbon@NiO composite.[103]

2.4.3.6 CuO anode

CuO follows a conversion reaction mechanism for Na storage and has a high theoretical capacity (674 mA h g^{-1}), which has attracted some attention due to the abundant global reserves and environmental compatibility of Cu, although its poor electronic conductivity and severe volume expansion have limited its application in SIBs.

Zhang's group designed CuO nanoarrays on Cu foil as anode for SIBs, which could sustain ~640 mA h g^{-1} at 200 mA g^{-1} due to its structural characteristics.[105] Wang's group prepared 3D CuO on Cu foil, which maintained a reversible capacity of 280 mA h g^{-1} at 1.0 A g^{-1}.[106] Jiao's group further synthesized CuO@C nanofibers

(**Figure 2.16**) with a specific capacity of 401 mA h g^{-1} after 500 cycles at 500 mA g^{-1}, which was attributed to the integration of CuO with the conductive carbon matrix.[107]

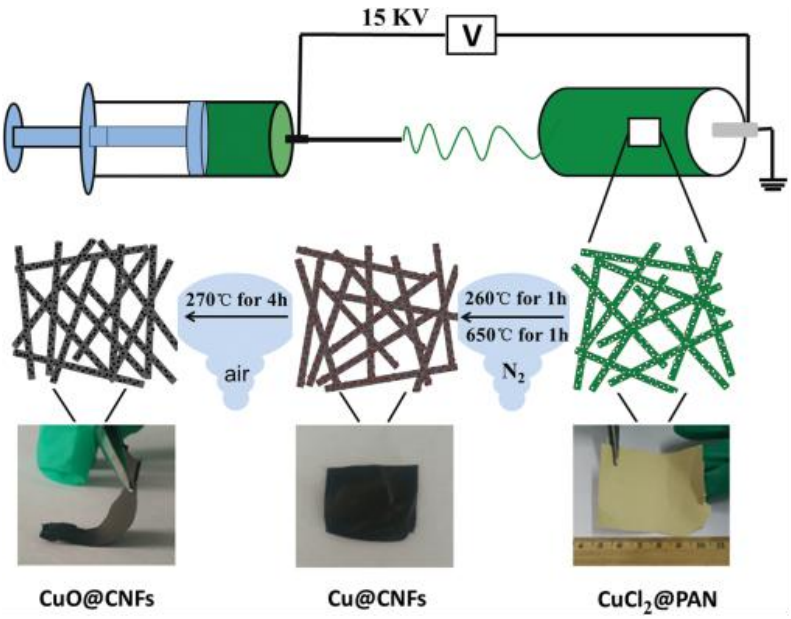

Figure 2.16 The synthesis process for CuO@C nanofibers.[107]

2.4.3.7 SnO_2 anode

SnO_2 has a theoretical capacity of 667 mA h g^{-1}, and follows the conversion/alloying reaction mechanism,[108] although SnO_2 has low conductivity and suffers huge volume variation during the cycling process. To explore the potential of SnO_2, several strategies have been used.

The hybridization of SnO_2 with graphene is considered to be a useful method to obtain high performance. Wang et al. synthesized an ultrasmall SnO_2/rGO composite that could sustain a capacity of 330 mA h g^{-1} after 150 cycles at 50 mA g^{-1}.[109] Other carbon materials were also used to support SnO_2 to form composites. Zhang's group

reported the use of carbon coated SnO_2/C nanofibers to form C@SnO_2@C nanofibers, which delivered ~374 mA h g^{-1} after 100 cycles at 50 mA g^{-1}.[110] Zhang's group constructed SnO_{2-x}@C nanofibers with a reversible capacity of 565 mA h g^{-1} after 2000 cycles at 1 A g^{-1}, which was attributed to the enhanced reaction kinetics and less volume expansion due to the integration of the electrode structure.[111] Moreover, Zhang's group reported that sandwich-like MoS_2@SnO_2@C (**Figure 2.17**) exhibited a capacity of 396 mA h g^{-1} after 150 cycles at 0.1 A g^{-1} due to the combined effect of MoS_2 and SnO_2.[112]

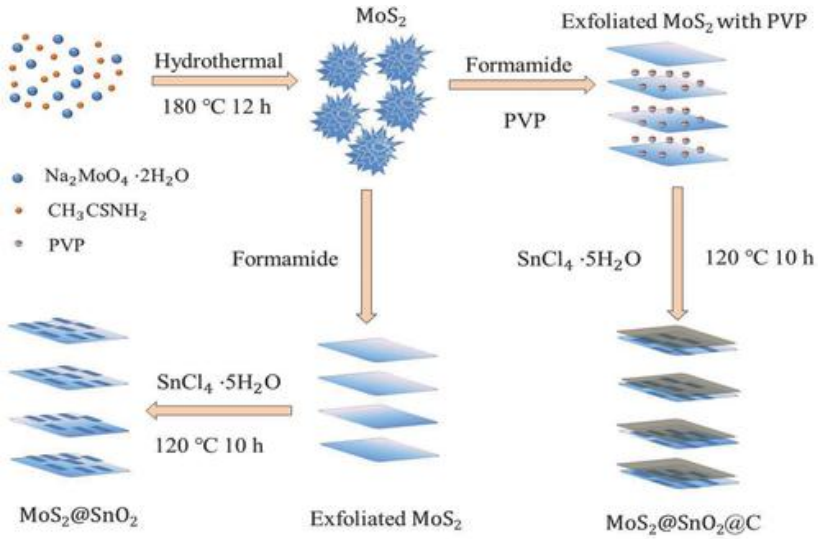

Figure 2.17 The synthesis process for MoS_2@SnO_2@C.[112]

2.4.3.8 Sb_2O_3 and Bi_2O_3 anodes

Sb_2O_3 and Bi_2O_3 have attracted some attention for Na storage due to their high gravimetric specific capacity and abundant resources, although they inevitably suffer from huge volume expansion during the sodiation/desodiation process and low

electrical conductivity (**Figure 2.18**).[113] To address these issues, several strategies have been proposed.

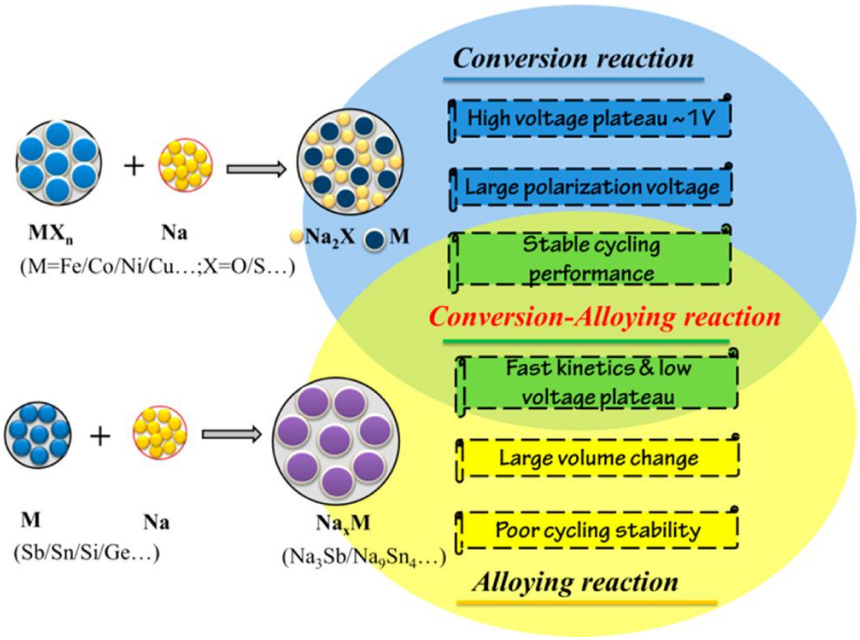

Figure 2.18 Schematic diagram of the characteristics of the alloying reaction and conversion reaction.[113]

Yan's group investigated an Sb_2O_3 film fabricated by the electrostatic spray deposition (ESD) method that could sustain capacity of 414 mA h g^{-1} after 200 cycles at 0.5 A g^{-1} through a reversible conversion-alloying process.[113] Wang's group fabricated a $Sb_2O_3/Ti_3C_2T_x$ composite with a capacity of 472 mA h g^{-1} after 100 cycles at 100 mA g^{-1} due to the high capacity of Sb_2O_3 and the conductive $Ti_3C_2T_x$ network.[114]

Nithya reported the synthesis of a Bi_2O_3/rGO composite with 70.2 % capacity retention after 200 cycles at 350 mA g^{-1}.[115] Zhu's group prepared Bi_2O_3@C nanofibers with capacity of as high as 430 mA h g^{-1} after 200 cycles at 100 mA g^{-1},

which was attributed to the small Bi_2O_3 particle size and the conductive CNFs.[116] Mai's group constructed sheet-like Bi_2S_3-Bi_2O_3 heterostructures with a built-in electric field (**Figure 2.19**), which could effectively facilitate the charge transport to yield a reversible capacity of ~630 mA h g^{-1} at 100 mA g^{-1}.[117]

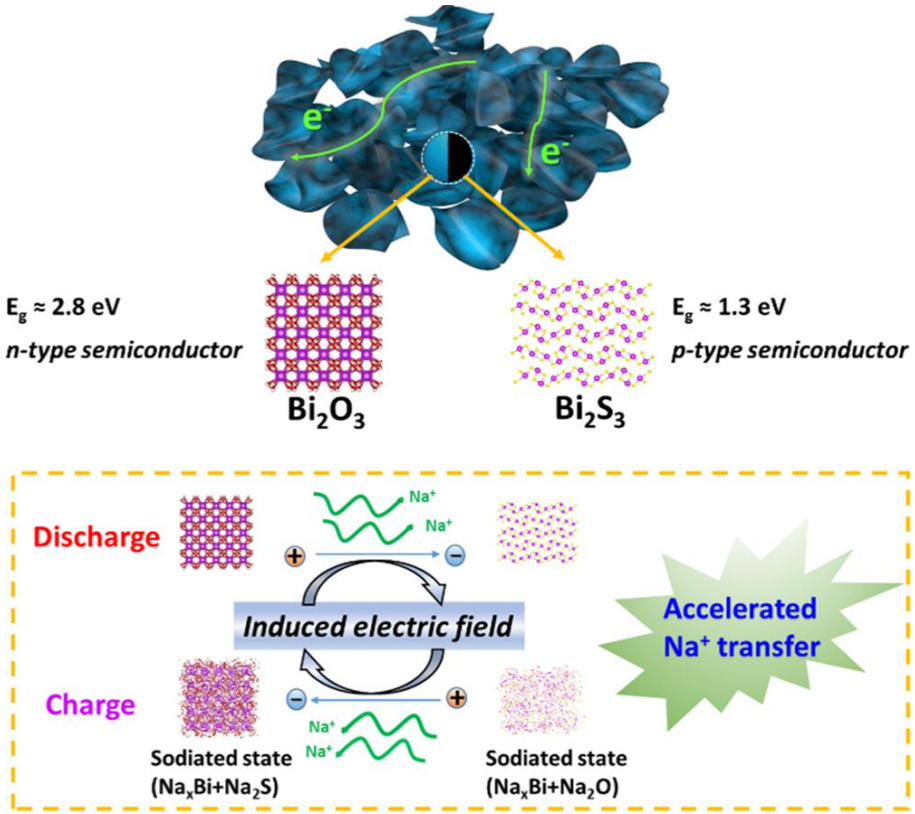

Figure 2.19 Schematic illustration of charge transfer in Bi_2S_3-Bi_2O_3 heterostructures.[117]

2.4.3.9 MoO_2 and MoO_3 anodes

Molybdenum oxides, including MoO_3 and MoO_2, have been considered as promising anodes due to their layered structure and environmental friendliness, although they still suffer from poor capacity retention and ion transfer kinetics. To date, enormous attempts have been devoted to solving these critical problems.

Xu's group investigated a MoO_2/rGO composite that delivered 276 mA h g^{-1} after 1000 cycles at 100 mA g^{-1}.[118] Xia *et al.* reported vertical graphene/MoO_2 core-shell arrays synthesized by plasma-enhanced chemical vapor deposition–electrodeposition (PECVD-ED).[119] The core-shell arrays demonstrated superior Na storage capability with ~554 mA h g^{-1} after 500 cycles at 100 mA g^{-1} due to the improved electrical conductivity.

Balaya's group was the first to report α-MoO_3 as anode, sustaining 100 mA h g^{-1} after 500 cycles at 1.117 A g^{-1}.[120] Sreedhara and his coworkers reported the synthesis of a MoO_3/rGO composite by the oxidation of few-layer MoS_2 nanosheets.[121] The hybrid demonstrated superior electrochemical stability, which was ascribed to the Mo-O-C linkages between MoO_3 and rGO. Moreover, MoO_3/MoS_2 and MoO_3/$MoSe_2$ heterostructures have been reported to achieve enhanced performance.[122, 123]

2.4.4 Metal sulfides

Metal sulfides have the following advantages for Na storage: i) they have high theoretical capacity; ii) the weak M-S bonds in metal sulphide are favourable for conversion reactions with Na^+ ions; and iii) they have comparable mechanical stability to the oxides. Most of them usually follow the conversion reaction mechanism or the conversion/alloying reaction mechanism. To date, some sulfides, including MoS_2, WS_2, SnS, NbS_2, TiS_2, FeS, Fe_3S_4, Fe_7S_8, FeS_2, CoS, Co_3S_4, Co_9S_8,

CoS_2, NiS, Ni_3S_2, NiS_2, SnS, SnS_2, Sb_2S_3, and Bi_2S_3, have been reported as anode materials for SIBs.

2.4.4.1 MoS_2 anode

MoS_2 consists of S-Mo-S sandwich layers with 0.62 nm interlayer spacing, which is beneficial for the migration of Na^+ ions,[124] although the aggregation and collapse of this structure during sodiation/desodiation processes and its low electronic conductivity are obstructing its practical application in SIBs. To explore its potential as anode, some strategies have been used to enhance MoS_2 anode performance.

Singh's group prepared a paper assembled from acid-exfoliated MoS_2 and rGO, which showed superior Na storage with a capacity of ~230 mA h g^{-1} after 20 cycles at 25 mA g^{-1}.[125] Inspired by this example, more than 40 examples of MoS_2/G composites have been explored for obtaining optimized performance up to August 2019.[126] From this, we can conclude that graphene can be explored as a support for MoS_2 with enhanced electrochemical performance. Zhu's group designed the growth of metallic 1T MoS_2 on graphene tubes to form a free-standing MoS_2 anode (**Figure 2.20**),[127] which exhibited a capacity of 313 mA h g^{-1} after 200 cycles at 50 mA g^{-1}. In addition, other carbon materials were well considered as excellent supports for MoS_2, such as CNTs, CNFs, carbon paper, carbon fabrics, graphite paper, etc.[97]

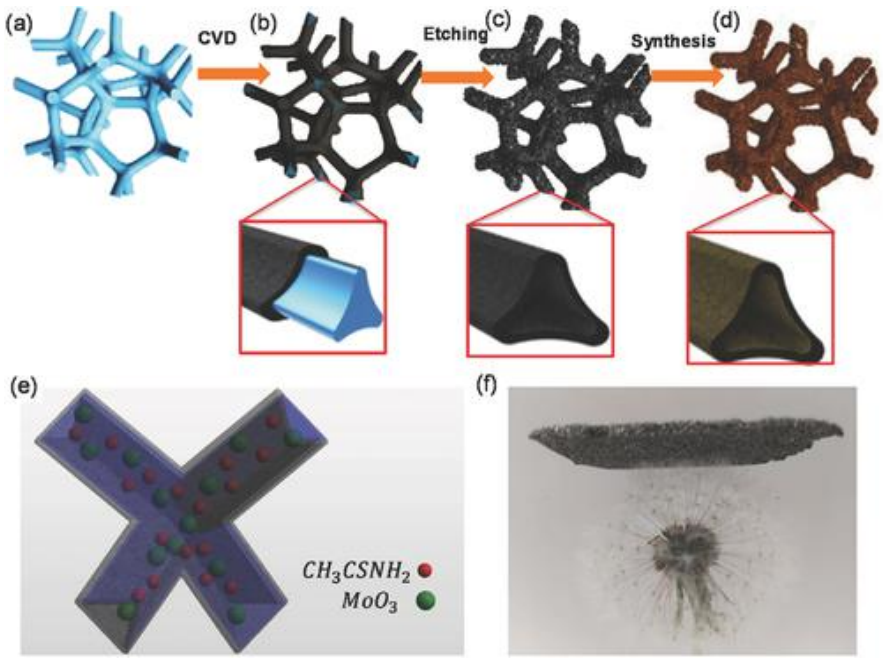

Figure 2.20 (a-d) Synthesis of the 3D MoS_2-graphene-MoS_2 structure; (e) Mechanism of MoS_2 growth on both sides of the 3D graphene. (f) Photograph of the lightweight, free-standing MoS_2-graphene foam.[127]

It is considered effective to construct heterostructures with MoS_2 to boost their Na storage performance. Ahemd et al. prepared MoS_2@HfO_2 nanosheets through a hydrothermal process, followed by atomic layer deposition (ALD), as shown in **Figure 2.21**, in which HfO_2 strongly enhances the cycling performance, with a capacity of 435 mA h g^{-1} after 50 cycles at 100 mA g^{-1}.[128] Chen's group modified MoS_2 nanosheet arrays on carbon cloth by TiO_2 layers by ALD, and they exhibited a capacity of 891 mA h g^{-1} after 150 cycles at 200 mA g^{-1}.[129] Moreover, other heterostructures, i.e., Sn/MoS_2, Fe_3O_4/MoS_2, SnS_2/MoS_2, MoS_2/MoO_3, MoS_2/Fe_2O_3, Co_9S_8/MoS_2, and $NiCo_2S_4$/MoS_2, have been explored for enhanced electrochemical performance.[97]

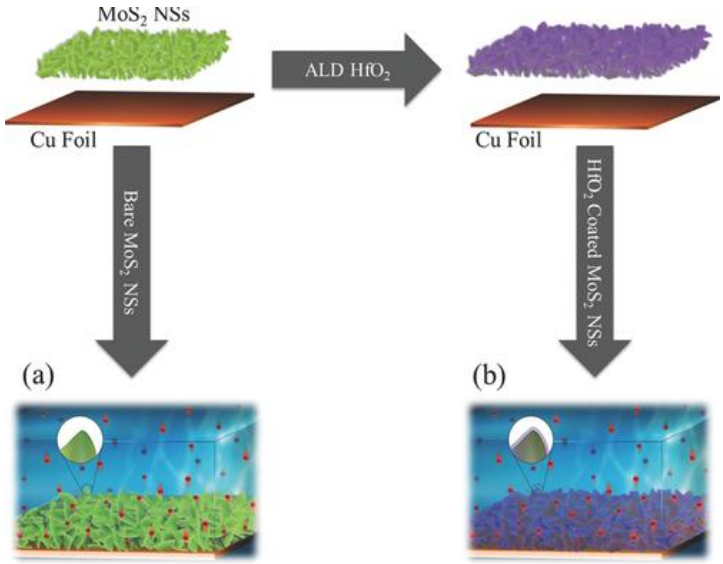

Figure 2.21 Synthesis of MoS_2@HfO_2 nanosheets.[128]

2.4.4.2 WS_2 anode

WS_2 has a theoretical capacity of 432 mA h g^{-1} for Na storage, which is relatively lower than that of MoS_2.[130] In addition, it also suffers from similar problems to those of MoS_2. Therefore, there are few reports on WS_2 anode for SIBs. Yu's group synthesized a 3D WS_2/C composite by electrostatic spray deposition (ESD) technique with WS_2 particles, rGO, and CNTs as precursors.[131] The as-synthesized composite could deliver a capacity of 219 mA h g^{-1} after 300 cycles at 432 mA g^{-1}, which was due to the conductive pathways provided by the structure and the composite's ability to accommodate the volume change during cycling. Wang et al. further developed a WS_2/CNT-rGO composite to form an aerogel through a three-step method including solvothermal treatment and freeze-drying/post annealing techniques (**Figure 2.22**).[132] The aerogel could sustain 252.9 mA h g^{-1} after 100 cycles at 200 mA g^{-1}. Moreover,

there are some high-performance WS_2/C composites that have been due to their superior structural design.[133]

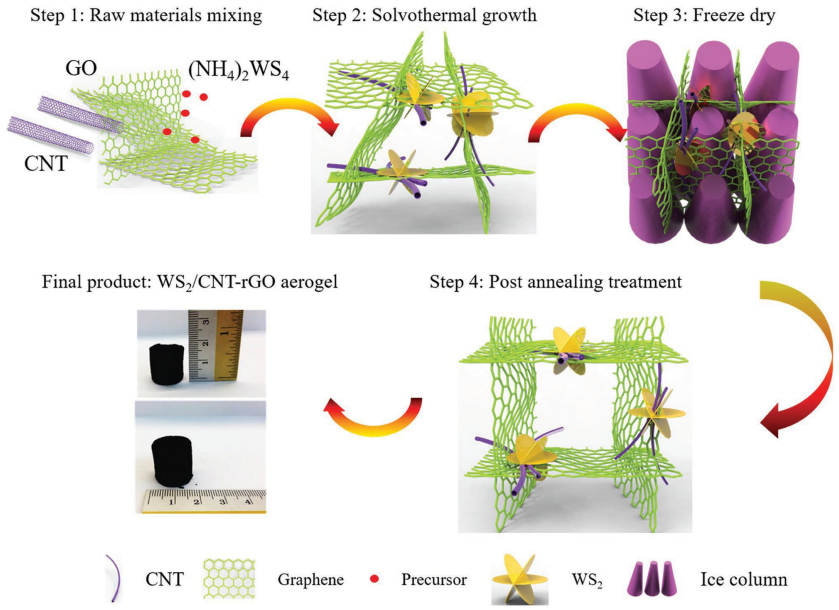

Figure 2.22 Synthesis of WS_2/CNT-rGO aerogel.[132]

2.4.4.3 TiS_2 anode

As early as the 1980s,[134] a room-temperature Na/TiS_2 cell was reported. There has been little progress on TiS_2, however, which has attracted less attention as an anode material for SIBs due to its low theoretical capacity of 239 mA h g^{-1}, capacity loss, and low ion diffusion rate. To more deeply understand the reason for the capacity decay, Han et al. investigated the Na^+ intercalation behaviour by *in situ* transmission electron microscope (TEM) measurements,[135] and found that the structure broke into nanosized domains with a diameter of ~3 nm, which accounts for the capacity decay during the charge/discharge processes. Li's group found that TiS_2 nanoplates could show a capacity of ~100 mA h g^{-1} at 2.39 A g^{-1} due to the low dimensions and large

surface area.[136] In addition, Chou's group prepared ultrathin TiS_2 nanosheets by the shear-mixing method, which exhibited 386 mA h g^{-1} after 200 cycles at 0.2 A g^{-1}.[137] Hawkins and Whittaker-Brooks prepared TiS_2 arrays with a discharge capacity of 224 mA h g^{-1} after 100 cycles at 23.9 mA g^{-1},[138] which was related to the short ion diffusion paths and the good electrical conductivity offered by the structure.

2.4.4.4 NbS_2 anode

Metallic NbS_2 consists of the S-Nb-S layers,[139, 140] and has a theoretical capacity of 683 mA h g^{-1}. There have only been a few research works on NbS_2, however. Lepienski's group was the first to report the Na storage behaviour of NbS_2 in a saturated $Na_2S_2O_4$ aqueous solution.[141] Liu *et al.* employed *in situ* XRD to research the phase transformation of NbS_2 during sodiation/desodiation through the intercalation and conversion processes.[142]

2.4.4.5 FeS, Fe_3S_4, Fe_7S_8, and FeS_2 anodes

Iron sulfides feature low cost, environmental-friendliness, and high capacities for Na storage. They also have some disadvantages like other sulfides, undergoing severe volume changes during electrochemical processes, which lead to poor cycling performance. Thus, some strategies should be used to overcome these problems.

Ferrous sulfide (FeS) has a theoretical capacity of 609 mA h g^{-1} for Na storage.[143, 144] Yu's group designed the growth of FeS@C on carbon cloth to form FeS@C/carbon

cloth for Na storage, with the composite sustaining a capacity of 365 mA h g^{-1} after 100 cycles at 91 mA g^{-1}.[145] The good conductivity of carbon cloth and its porous structure endowed FeS with good performance. Following this example, some FeS/C composites have been designed as anodes for SIBs. For example, Yang's group prepared porous FeS/C fibers through the pyrolysis of Fe-carrageenan fibers, as shown in **Figure 2.23**.[146] The as-synthesized FeS/C fibers exhibited a capacity of 283 mA h g^{-1} after 400 cycles at 1 A g^{-1} due to their structural advantages. In addition, FeS/Fe_3C and FeS/Fe_3O_4 heterostructures were reported to improve the FeS behavior.[98,147]

Figure 2.23 Synthesis of of FeS/C fibers.[146]

Jung's group synthesized Fe_7S_8@C nanoparticles with ~10 nm in size by colloidal synthesis, and the composite achieved a capacity of 447 mA h g^{-1} after 1000 cycles at 180 mA g^{-1},[148] which was ascribed to the small size of Fe_7S_8 and the carbon shell. Under the guidance of this example, much effort has recently been made to the

synthesis of various kinds of Fe_7S_8/C composites to obtain high-performance results.[149] In addition, as another kind of iron sulphide, Fe_3S_4 has been employed as an active material through hybridization with carbon to form Na storage composites.[150, 151]

Pyrite FeS_2 has a theoretical capacity of 894 mA h g^{-1} for Na storage. Walter et al. reported that FeS_2 nanoparticles sustained a capacity above 500 mA h g^{-1} after 400 cycles at 1.0 A g^{-1} due to the small size of FeS_2.[152] Chen's group found that their optimized Co-doped FeS_2 could exhibit 220 mA h g^{-1} after 5000 cycles at 2 A g^{-1} due to its pseudocapacitive behaviour.[153] To improve the reversibility of FeS_2, some strategies have been undertaken to synthesize FeS_2/C composites with various functions.[154,155]

2.4.4.6 CoS, Co_3S_4, Co_9S_8, and CoS_2 anodes

Cobalt sulfides are promising as anode materials for SIBs due to their high conductivity and high capacities. Similar problems to those of other sulfides still exist, however, such as volume changes during the charge/discharge process and relatively low conductivity. Thus, some strategies have been adopted to deal with these issues and improve their electrochemical performance.

Peng et al. synthesized a CoS nanoplates/rGO composite to form CoS/rGO composite as an advanced anode, which exhibited 420 mA h g^{-1} after 1000 cycles at 1 A g^{-1} due to their synergetic effects.[156] Then, Wang's group and Wei's group also employed

graphene as the support for buffering the volume changes of CoS during the charge/discharge processes.[157] Moreover, in order to enhance the performance of CoS, a carbon coating strategy was used to improve the conductivity of CoS/C composites, resulting in excellent electrochemical behaviour.[158, 159] Compared with CoS, there have been few reports on Co_3S_4 for Na storage. The Liu group reported Co_3S_4@polyaniline nanotubes that sustained a capacity of 252.5 mA h g^{-1} after 100 cycles at 200 mA g^{-1}.[160] In addition, to enhance the performance of Co_3S_4, hybridization strategies with carbon were also used by Hou's group.[161, 162]

Hybridizing Co_9S_8 with carbon is considered to be one of the most effective methods to improve its electrochemical performance. Kang's group synthesized a Co_9S_8/carbon composite by the spray pyrolysis method, which exhibited a capacity of 404 mA h g^{-1} after 50 cycles at 0.5 A g^{-1}.[163] Jiao's group reported Co_9S_8@C hollow microspheres synthesized by a solvothermal/thermal treatment process,[164] as shown in **Figure 2.24**. The carbon layers played an important role in boosting charge transfer for obtaining the excellent performance of 492 mA h g^{-1} after 100 cycles at 0.5 A g^{-1}. In addition, to boost the charge-transfer kinetics, some Co_9S_8-based heterostructures were proposed as advanced anodes for SIBs,[165] *i.e.*, Co_9S_8/MoS_2, Ni_3S_2/Co_9S_8, Co_9S_8/Co, *etc*.

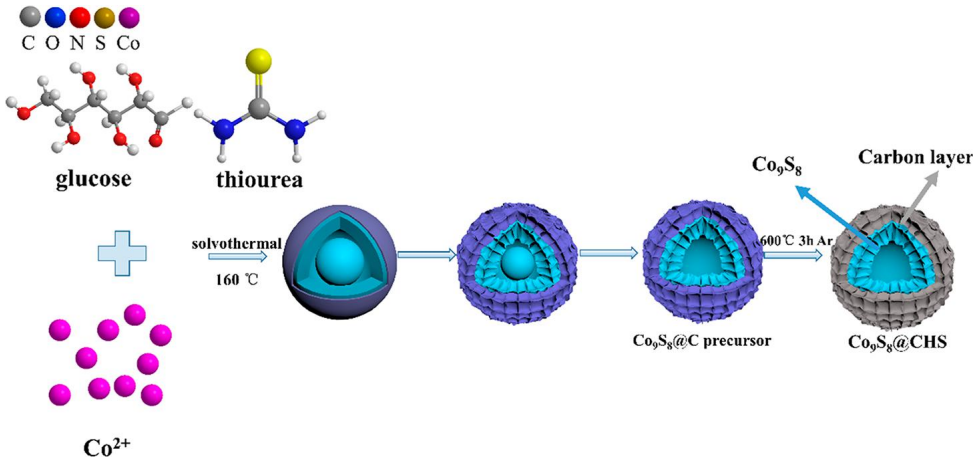

Figure 2.24 Synthesis of Co_9S_8@C hollow microspheres.[164]

CoS_2 is another important cobalt sulphide investigated as anode for SIBs,[166] and has been mainly studied through incorporating carbon into composites. Fu's group was the first to investigate such composites and found that CoS_2/CNTs exhibited 568 mA h g^{-1} after 100 cycles at 100 mA g^{-1} in ether-based electrolyte.[167] Graphene and CNFs were also used as the support for CoS_2 by some groups.[168] In addition, the hybridization of CoS_2 with other types of functional carbon has been also employed to improve its Na storage behaviour.[169]

2.4.4.7 NiS, Ni_3S_2 and NiS_2 anodes

Nickel sulfides are promising anode materials for Na storage due to their low cost, rich chemical formulas, and high electrical conductivity. Ni_3S_2, NiS, and NiS_2 have theoretical capacities of 446, 591 and 870 mA h g^{-1}, respectively,[170, 171] although they suffer from poor cycling performance due to structural collapse during sodiation/disodiation processes.[172] Some work has been done to overcome this obstacle.

Cui's group constructed a composite of Ni_3S_2-poly(3,4-ethylenedioxythiophene) (PEDOT) on Ni foam,[173] which delivered 280 mA h g^{-1} after 30 cycles at 280 mA g^{-1}. Sun's group further prepared Ni_3S_2 nanosheets/carbon tubes on Ni foam.[174] The composite sustained capacity of 212 mA h g^{-1} after 260 cycles at 50 mA g^{-1}, which was attributed to the free space provided by the arrays for buffering volume changes.

Yan's group prepared NiS nanosheets by the MOF-template method, which could sustain 166 mA h g^{-1} over 100 cycles at 1 A g^{-1}.[175] Zhao's group was the first to report NiS/rGO composite as an anode with sustained capacity of 446 mA h g^{-1} over 50 cycles at 200 mA g^{-1}.[176] Yang's group designed the synthesis route of NiS@C nanofibers, as shown in **Figure 2.25**. The optimized hybrid exhibited a reversible capacity of 320.5 mA h g^{-1} after 100 cycles at 1.0 A g^{-1} due to the hollow structure of NiS and conductive CNFs.[177]

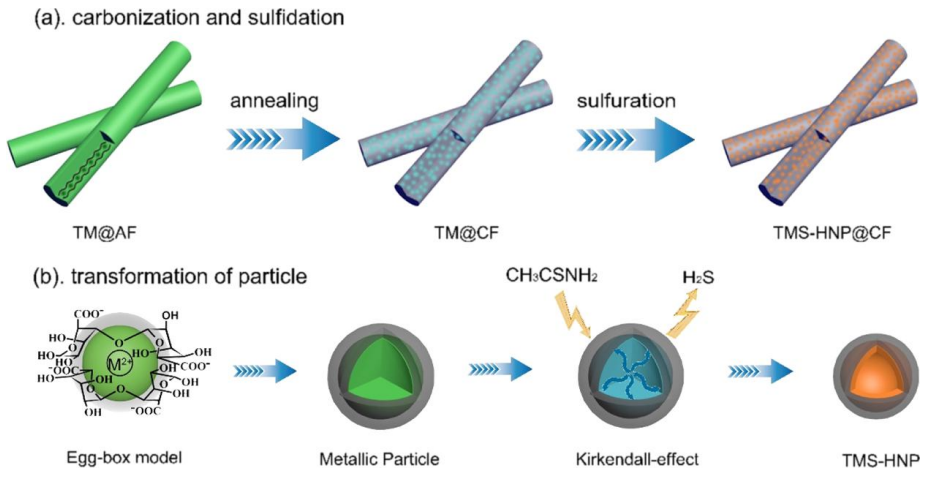

Figure 2.25 Synthesis of NiS@C nanofibers.[177]

In addition, much effort has been made to enhance the cycling performance of NiS_2 through combining it with carbon materials. Hou's group encapsulated NiS_2 in bifunctional carbon to form NiS_2@C rods wrapped in S/N-co-doped carbon,[178] which delivered ~580 mA h g^{-1} after 100 cycles at 0.1 A g^{-1}. Wen *et al.* prepared NiS_2@CNFs by the electrospinning method with a capacity of 200 mA h g^{-1} at 2 A g^{-1}.[179] Zhu and co-workers reported NiS_2@CoS_2@N-doped CNTs synthesized by a co-precipitation method, which offered a capacity of 560 mA h g^{-1} over 250 cycles at 5 A g^{-1} due to the interconnected porous structure[180].

2.4.4.8 SnS and SnS_2 anodes

Low-cost tin-based sulfides are regarded as promising anodes for Na storage due to their high capacity (1022 mA h g^{-1} for SnS and 1136 mA h g^{-1} for SnS_2).[181] During the sodiation process, the interlayer spacing of SnS_2 can accommodate the transfer of Na^+ ions with a three-phase conversion from hexagonal SnS_2 to orthorhombic-$Na_{15}Sn_4$ via tetragonal Sn.[182] In the case of SnS, the same multiple-phase reaction pathway was also proved from orthorhombic SnS to orthorhombic $Na_{15}Sn_4$ via cubic Sn.[183] To date, great efforts have been made to explore its potential as anode for SIBs.

Mitra's group was the first to investigate SnS nanoparticles and found that they exhibited ~500 mA h g^{-1} at 125 mA g^{-1}.[184] Guo's group found that SnS@graphene composite, originating from the annealing treatment of SnS_2/graphene in argon, exhibited 492 mA h g^{-1} over 250 cycles at 810 mA g^{-1}, which was ascribed

to the fact that there was a two-structural-phase transformation mechanism for SnS.[185] This facilitated the structural stability of SnS@graphene composite. Following this, many examples of SnS/C composites were reported,[186] such as with graphene, CNTs, and others. In addition, some SnS-based heterostructures, i.e., SnS/SnS_2, SnS/SnO_2, SnS/ZnS, SnS/SnSb, etc., have also been studied to boost the electrochemical performance through their built-in driving force for charge-transfer kinetics.[187]

Layered SnS_2 has 0.5899 nm interlayer spacing for Na storage.[188] Qu et al. reported that a SnS_2/rGO composite delivered 500 mA h g^{-1} after 400 cycles at 1 A g^{-1} due to the combined effects of the conductive rGO network and the wide interlayer spacing.[189] Similar to the strategies used for SnS, many examples of SnS_2/G composites have been reported. Other carbon materials have also been employed to buffer the volume changes of SnS_2 and improve its electrochemical performance,[190] e.g., carbon nanospheres, CNTs, hollow carbon nanospheres, CNFs, and others. Some SnS_2-based heterostructures (SnS_2/MXene, SnS_2/Sb_2S_3, SnS_2/CoS_2, SnS_2/Mn_2SnS_4) have been constructed to improve the electrochemical performance of SnS_2 through speeding up the charge-transfer kinetics.[182]

2.4.4.9 Sb_2S_3 anode

Sb_2S_3 consists of many layer units[191] and is regarded as a potential anode for SIBs due to its high theoretical capacity of 946 mA h g^{-1}.[192] Unfortunately, Sb_2S_3 suffers from

unavoidable volume expansion and particle aggregation, which lead to poor cycling performance.[193]

To address the above problems, Yan's group utilized an ionic liquid-assisted method to synthesize Sb_2S_3/rGO composite, in which Sb_2S_3 nanorods were wrapped by rGO sheets. This hybrid could delivered 400 mA h g^{-1} after 100 cycles at 50 mA g^{-1} because the graphene prevented particle aggregation and buffered the volume expansion.[194] Ji's group synthesized Sb_2S_3@C nanorods, which offered capacity of 699.1 mA h g^{-1} after 100 cycles at 100 mA g^{-1}.[195]

Apart from 1D morphology, some 3D Sb_2S_3 materials have been reported. Zhang's group prepared flower-like Sb_2S_3 by the polyol reflux method, which delivered 835.3 mA h g^{-1} over 50 cycles at 50 mA g^{-1}.[196] Liu's group reported Sb_2S_3 hollow microspheres with capacity of 384 mA h g^{-1} over 50 cycles at 200 mA g^{-1}.[197] Recently, Qiao's group prepared a multi-shell Sb_2S_3 anode by using zeolitic imidazolate framework-8 (ZIF-8) as precursor, as shown in **Figure 2.26**.[198] The multi-shell Sb_2S_3 showed capacity of ~500 mA h g^{-1} after 50 cycles at 1 A g^{-1} due to its hierarchical structure.

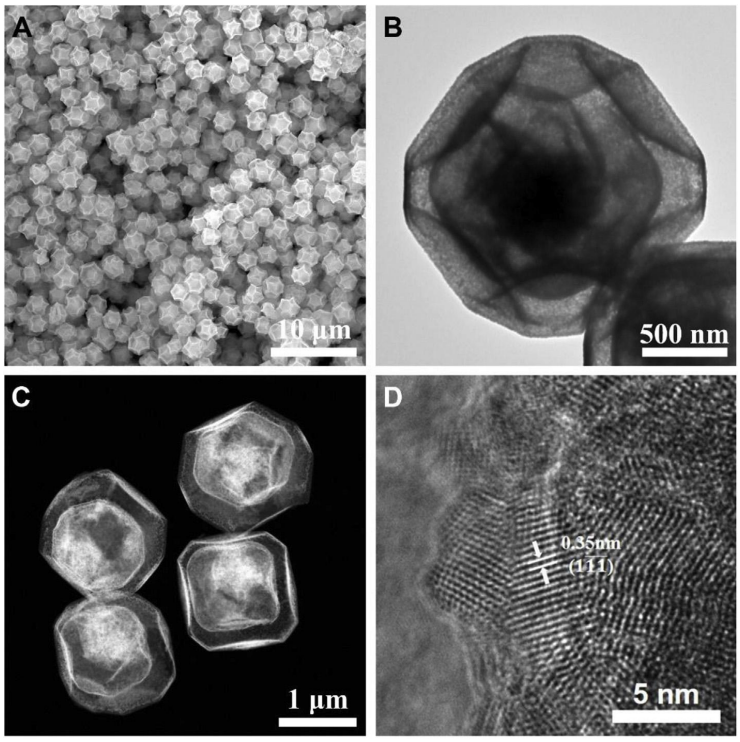

Figure 2.26 (a) SEM image; (b) TEM image; (c) scanning TEM (STEM) image; (d) high resolution TEM (HRTEM) image of multi-shell Sb_2S_3.[198]

Some Sb_2S_3-based heterostructures were claimed to improve Na storage.[199] Yin's group reported the synthesis of ZnS-Sb_2S_3@C polyhedra from ZIF-8 precursor, which could sustain a reversible capacity of 661.9 mA h g^{-1} after 50 cycles at 100 mA g^{-1}.[200] Wang's group designed SnS_2/Sb_2S_3 heterostructures with rGO that showed capacity of 567 mA h g^{-1} at 4 A g^{-1}, which was attributed to the improved Na^+ diffusion kinetics and electrical conductivity offered by the structure.[201] Zhao's group synthesized Sb_2S_3 nanorods/MoS_2 nanosheets to form core–shell heterostructures by a two-step hydrothermal method, which delivered ~560 mA h g^{-1} over 100 cycles at 100 mA g^{-1}.[202]

2.4.4.10 Bi_2S_3 anode

Bismuth sulfide (Bi_2S_3) consists of anisotropic layers interlinked with Bi_4S_6 units.[203] Bi_2S_3 features a two-step Na storage pathway, namely, conversion/alloying processes, with a theoretical capacity of 625 mA h g^{-1}.[204] Due to its high density (7.39 g cm^{-3}), Bi_2S_3 can achieve an extremely high volumetric capacity. Pristine Bi_2S_3 always suffers from bad cycling and rate performances, however, due to its irreversible phase conversion, large volume changes, and limited conductivity.[205, 206]

Sun's group prepared Bi_2S_3 nanorods/N-doped graphene aerogel (**Figure 2.27**) as a flexible anode for SIBs.[207] The aerogel showed ~ 650 mA h g^{-1} at 62.5 mA g^{-1}, which was ascribed to the ability of the graphene matrix to alleviate the volume changes and enhance conductivity. Li and co-workers reported a bio-inspired Bi_2S_3-PPy yolk-shell composite,[208] where PPy is polypyrrole, which exhibited ~600 mA h g^{-1} at 0.2 C due to its unique structure.

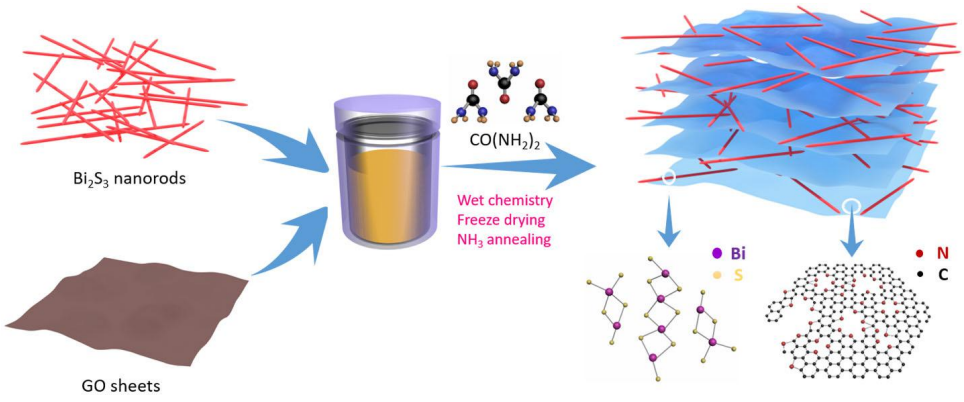

Figure 2.27 Synthesis of Bi_2S_3/rGO composite.[207]

2.4.5 Metal selenides

Metal selenides can be considered as promising anode materials since they have a wider crystal lattice and higher electrical conductivity than their oxide and sulfide counterparts. Moreover, they also have high bulk density, as well as excellent performance in terms of good reversibility and rate performance due to the low volume effect. Some selenides are discussed in the following part.

2.4.5.1 $MoSe_2$ anode

$MoSe_2$ stands out from various candidates as an attractive anode for SIBs, mainly due to its large interlayer spacing, small band gap, and high theoretical capacity (~422 mA h g^{-1}).[209] Morales et al. investigated the structural changes in $MoSe_2$ during the sodiation process.[210] $MoSe_2$ anode has relatively low electronic conductivity, however, and often suffers from large volume expansion, which limits its further application in SIBs. In order to address these issues, several useful strategies have been developed.[211]

Morphology control plays a crucial role in adjusting the electrochemical performance of $MoSe_2$. Kang's group designed yolk-shell $MoSe_2$ microspheres prepared by the selenization process, which exhibited a capacity of 433 mA h g^{-1} after 50 cycles at 0.2 A g^{-1}, which was attributed to the structure, which could buffer the large volume changes during cycling.[212] Jiang's group reported $MoSe_2$ nanospheres with a capacity of 416 mA h g^{-1} after 200 cycles at 0.1 C.[213]

Hybridization with carbon could not only provide $MoSe_2$ with high conductivity, but also provided room to buffer the volume changes during the sodiation/desodiation processes. Zhang's group reported a hierarchical $MoSe_2$/rGO composite with a reversible capacity of 430 mA h g^{-1} after 200 cycles at 0.5 A g^{-1}, which is attributed to the synergistic effects between the $MoSe_2$ nanosheets and the rGO.[214] Xie et al. reported that the porous $MoSe_2$/rGO composite displayed 445 mA h g^{-1} over 350 cycles at 200 mA g^{-1}.[215] To further improve the conductivity of the entire electrode, Niu *et al.* prepared a $MoSe_2$/N,P-co-doped carbon nanosheets composite,[216] which could retain a capacity of 378 mA h g^{-1} over 1000 cycles at 0.5 A g^{-1}. Zheng's group anchored $MoSe_2$ nanosheets on N, P-doped graphene to form $MoSe_2$/N, P-G composite, which exhibited a capacity of ~200 mA h g^{-1} at 10 A g^{-1} due to the widened interlayer distance for facilitating Na^+ diffusion.[217] The $MoSe_2$ undergoes the electrochemical process shown in **Figure 2.28**.

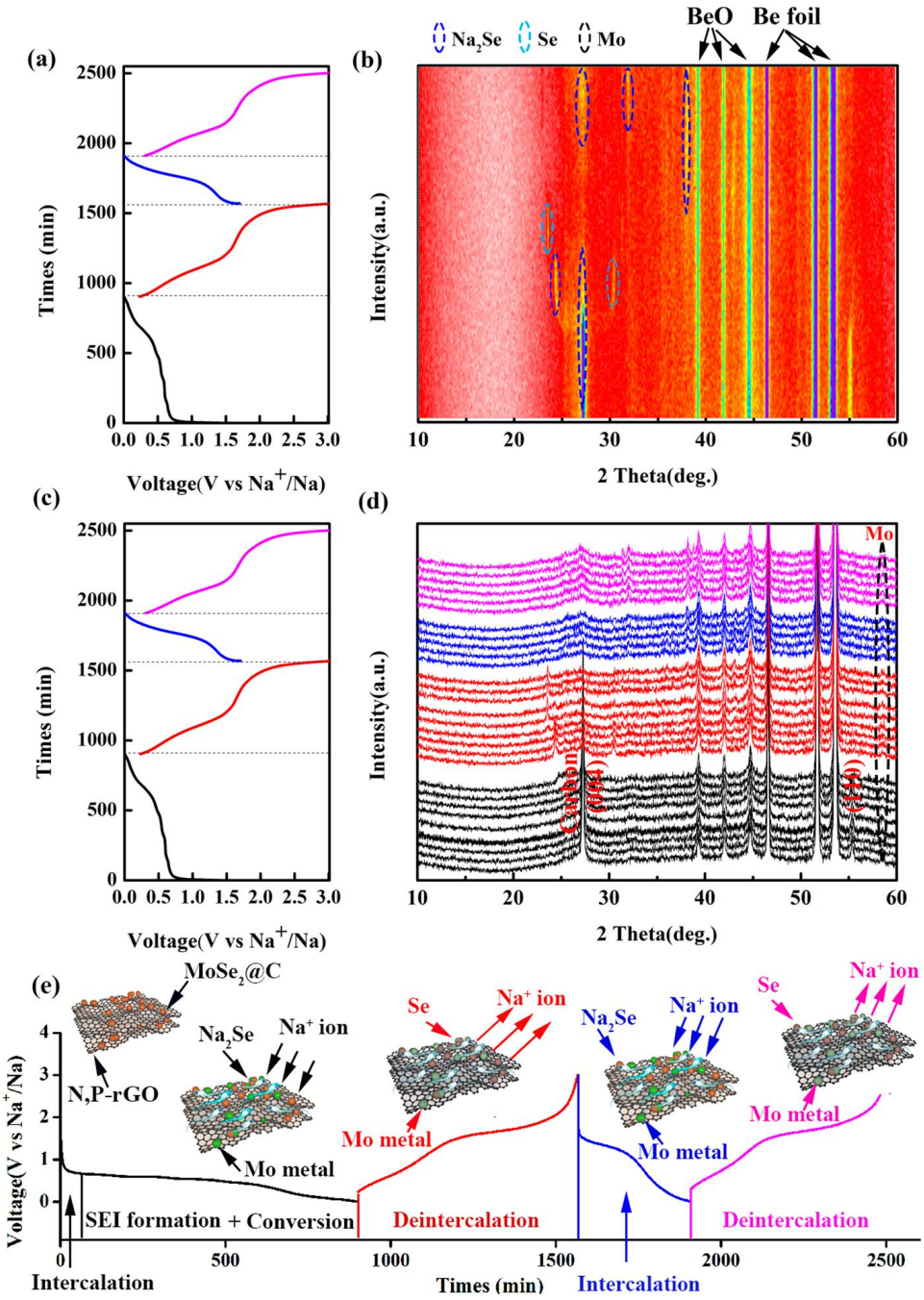

Figure 2.28 (a and c) Charge–discharge profiles; (b and d) *In situ* XRD patterns at different charge-discharge states of $MoSe_2$@C/N,P-rGO; (e) Schematic illustration of the proposed energy storage mechanism of $MoSe_2$@C/rGO at different stages.[217]

Liu *et al.* synthesized $MoSe_2$@hollow carbon nanospheres through a templating method, in which few-layer $MoSe_2$ nanosheets with expanded (002) planes (from 0.64 nm to 1.02 nm) were confined in the nanospheres.[218] The hybrids exhibited ~501 mA

h g^{-1} after 1000 cycles at 1 A g^{-1}. Another constraint on $MoSe_2$ anode for SIBs that can not be ignored is the "shuttle effect" of the intermediate reaction products, the polyselenides, which can diffuse to the electrolyte, causing loss of active materials and serious deterioration. To this end, Xie *et al.* proposed that wrinkled $MoSe_2$ nanosheets sandwiched by a vertical graphene core and an N-doped carbon shell effectively suppressed the "shuttle effect",[219] so that the composite exhibited a capacity of 298 mA h g^{-1} over 1000 cycles at 2.0 A g^{-1}.

2.4.5.2 WSe_2 anode

WSe_2 has a layered Se-W-Se sandwich structure with large interlayer spacing (0.65 nm), which makes it a potential anode for SIBs.[220] Few studies have investigated the ability of WSe_2 to store sodium ions, however. Yang et al. investigated WSe_2 nanoplates and found that they exhibited superior cycling performance and high rate capability.[221] Based on the *exsitu* XRD and Raman spectroscopy results, Na storage involves the alloying reaction and conversion reaction for WSe_2.

2.4.5.3 $TiSe_2$ and $NbSe_2$ anodes

Layered $TiSe_2$, with a large interlayer spacing of 0.601 nm, is expected to promote a reversible multi-step insertion/extraction processes for Na^+ in $TiSe_2$.[222] Zhang *et al.* explored the exfoliation of $TiSe_2$ *via* an ultrasonication- or grinding-assisted method. The exfoliated $TiSe_2$ showed a specific capacity of 147 mA h g^{-1} at 0.1 A g^{-1} for Na storage.[223] $NbSe_2$ is formed via interactions between Se-Nb-Se and Se-Se, which is

convenient for the reversible intercalation of ions. Dai's group found that $NbSe_2$ had a diffusion barrier of 0.086 eV for Na^+ and a theoretical specific capacity of 312 mA h g^{-1} using first-principles calculations.[224] Kim's group reported $NbSe_2$ synthesized by the gas-phase solid state method, which exhibited a reversible capacity of 142.5 mA h g^{-1} at 200 mA g^{-1} after 100 cycles.[225]

2.4.5.4 $FeSe_2$ anode

$FeSe_2$ has attracted attention for Na storage due to its environmental friendliness, low cost, and high conductivity.[226] Chen's group was the first to report $FeSe_2$ microspheres assembled from nanooctahedra as anode for SIBs,[227] which displayed a capacity of 447 mA h g^{-1} at 0.1 A g^{-1}. Zhao et al. synthesized ultra-small $FeSe_2$ nanoparticles that delivered a capacity of ~500 mA h g^{-1} in ether-based electrolyte.[228] Fan et al. reported core-shell $FeSe_2$@C hollow nanocubes **(Figure 2.29)**, which exhibited a capacity of 212 mA h g^{-1} after 3000 cycles at 10 A g^{-1} and attributed this performance to its structural advantages and high conductivity.[229] Ge et al. further studied $FeSe_2$ rods wrapped in N-doped C with a reversible capacity of 308 mA h g^{-1} after 10000 cycles at 10.0 A g^{-1}.[230] Most recently, An et al. synthesized a burr-globule-like $FeSe_2$/graphene hybrid by the hydrothermal method, which delivered a reversible capacity of 496.3 mA h g^{-1} after 400 cycles at 2.5 A g^{-1} due to the high pseudocapacitive contribution induced by its special structure.[231]

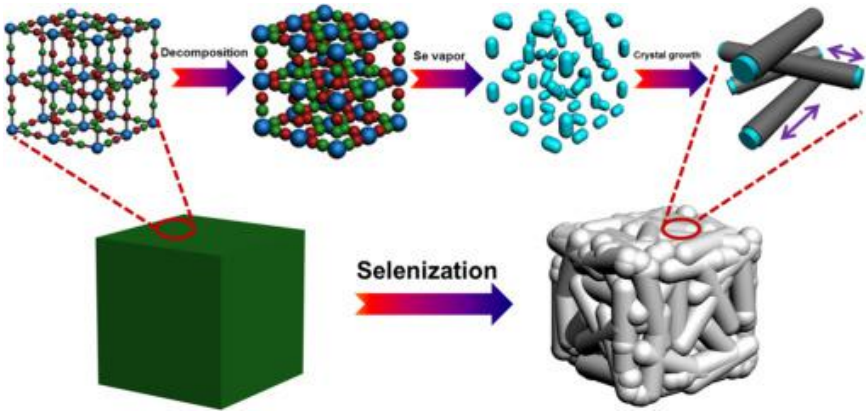

Figure 2.29 Synthesis process for $FeSe_2$ hollow nanocubes.[229]

2.4.5.5 CoSe and $CoSe_2$ anode

Cobalt selenides have been well studied as anodes for SIBs due to their versatility and high intrinsic electrical conductivity.[232] Zhang *et al.* synthesized yolk-shell CoSe@C dodecahedra, which could sustain a reversible capacity of 531.6 mA h g^{-1} at 0.5 A g^{-1} after 50 cycles.[233] Jiang's group confined ultrafine CoSe nanoparticles in N-doped carbon to form a composite with capacity of ~436 mA h g^{-1} at 0.5 A g^{-1} after 150 cycles. This superior performance is attributed to the combined effects of ultrafine CoSe and N-doped carbon nanosheets.[234]

$CoSe_2$ has been explored as a promising anode for SIBs, with the overall reaction of $CoSe_2 + 4Na^+ + 4e^- \leftrightarrow Co + 2Na_2Se$ by Chen's group.[235] The urchin-like $CoSe_2$ synthesized by the hydrothermal method delivered a high reversible capacity of 410 mA h g^{-1} after 1800 cycles at 1 A g^{-1}, which was attributed to the influence of its stable ether-based electrolyte and the pseudocapacitive contribution. To further improve the cycling stability of $CoSe_2$ anodes, Cui et al. synthesized $CoSe_2$@N-C

nanofibers with a reversible capacity of 371.8 mA h g^{-1} after 500 cycles at 0.2 A g^{-1}.[236] Moreover, doping and morphology control are also key strategies to improve the electrochemical performance of $CoSe_2$ electrodes. Lou's group reported Cu-doped $CoSe_2$ microboxes assembled from nanosheets with a reversible capacity of 492 mA h g^{-1}, due to their unique porous structure and Cu-doping.[237] Wang's group synthesized core–shell ZnSe-N-doped C@$CoSe_2$-N-doped C from the ZIF-8@ZIF-67 precursor, which exhibited a reversible capacity of 308.5 mA g^{-1} after 150 cycles at 0.1 A g^{-1}. This performance was attributed to the enhanced diffusion rates due to the interfacial effect.[238]

2.4.5.6 $NiSe_2$ anode

$NiSe_2$ possesses a high theoretical capacity of 495 mA h g^{-1}, which is based on the conversion reaction.[239] The first-ever study of $NiSe_2$ as anode material for SIBs was conducted by Kang's group.[240] Their porous $NiSe_2$/rGO nanofibers synthesized by an electrospinning/selenization process could deliver a reversible capacity of 486 mA h g^{-1} after 100 cycles at 200 mA g^{-1}. In order to improve the cycling performance, Zhu *et al.* prepared $NiSe_2$ octahedra by the hydrothermal method, and they showed long-term cycling stability (313 mA h g^{-1} after 4000 cycles at 5 A g^{-1}) and superior rate capability (175 mA h g^{-1} at 20 A g^{-1}),[241] which benefited from the exposed facets and the pseudocapacitive behaviour of $NiSe_2$. The Song group developed a layered Ni-hexamine framework as the precursor to prepare a 2D $NiSe_2$/N-rich carbon composite,[242] which exhibited a high reversible capacity (410 mA h g^{-1} at 1 A g^{-1}) and

excellent rate capability (255 mA h g^{-1} at 10 A g^{-1}) due to the synergistic effects between the N-rich carbon and the $NiSe_2$.

2.4.5.7 SnSe and $SnSe_2$ anodes

Layered SnSe and $SnSe_2$ undergo the conversion and alloying reaction mechanism, and they demonstrated high theoretical capacity (426 mA h g^{-1} for $SnSe_2$). Yang *et al.* reported a facile ball-milling method to prepare SnSe/rGO composite,[243] which exhibited an enhanced reversible capacity of 590 mA h g^{-1} after cycling at 0.05 A g^{-1}. Yuan *et al.* first developed a surfactant-free method for the phase-controlled synthesis of SnSe nanosheets,[244] which exhibited a reversible capacity of 738 mA h g^{-1} and superior rate capability even at 40 A g^{-1}. Zhang *et al.* adopted a hydrothermal method to prepare $SnSe_2$/rGO composites with a reversible capacity of 515 mA h g^{-1} after 100 cycles.[245] The excellent performance of this $SnSe_2$/rGO composite is attributed to the combination of the layered structure of $SnSe_2$ and the electrical conductivity of rGO. Ren *et al.* reported a cation-exchange strategy to synthesize SnSe nanoplates vertically grown on nitrogen-doped carbon (SnSe/NC, as shown in **Figure 2.30**),[246] which exhibited the large capacity of 723 mA h g^{-1} at 25 mA g^{-1}. This excellent capacity is attributed to the pseudocapacitive behaviour of SnSe/NC due to the fast electron/ion transfer facilitated by the strong electronic coupling of Sn-C bonding.

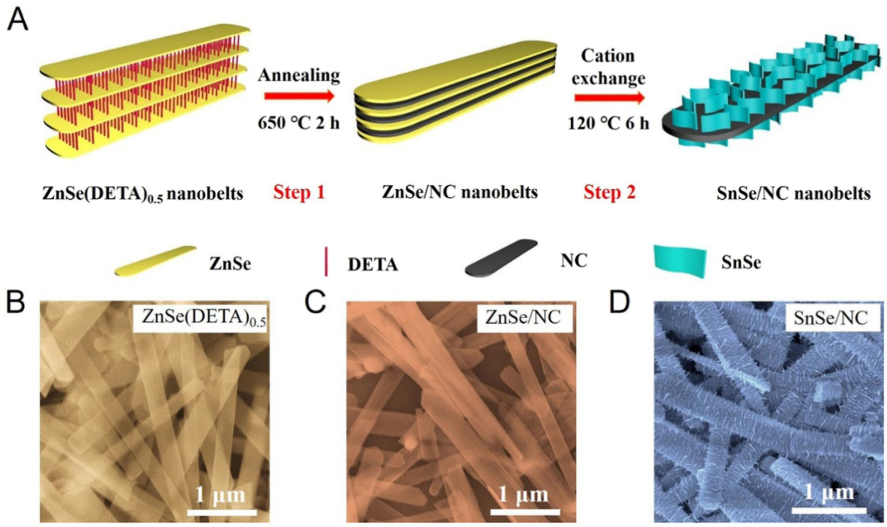

Figure 2.30 Synthesis route for SnSe/NC.[246]

2.4.5.8 Sb_2Se_3 and Bi_2Se_3 anodes

Sb_2Se_3 undergoes the conversion and alloying reactions in its sodiation/desodiation processes, with a theoretical capacity of 670 mA h g^{-1}. [247] Mai's group fabricated a free-standing Sb_2Se_3 membrane via the hydrothermal method combined with a subsequent vacuum filtration treatment.[248] The as-fabricated membrane delivered a reversible capacity of 289 mA h g^{-1} after 50 cycles at 100 mA g^{-1}. To improve the performance, Ou *et al.* reported the solvothermal synthesis of hierarchical Sb_2Se_3/rGO hybrids,[249] which exhibited a high reversible specific capacity of 682 mA h g^{-1} at 0.1 A g^{-1}, good reversible capacity of 386 mA h g^{-1} at 2.0 A g^{-1}, and excellent stability for 500 cycles. Fang *et al.* developed a template-engaged ion-exchange method for the synthesis of PPy-coated Sb_2Se_3 microclips,[250] which exhibited a high specific capacity of 630 mA h g^{-1} and excellent rate capability (486 mA h g^{-1} at 2 A g^{-1}), which were due to their unique structure and composition.

Bi_2Se_3 has the similar sodiation/desodiation process to Sb_2Se_3. Xie *et al*. prepared Bi_2Se_3/C composites via a higher-energy ball milling (HEBM) approach. Owing to its high intrinsic conductivity and the positive effects of carbon, Bi_2Se_3/C achieved a high initial reversible capacity of 527 mA h g^{-1} at 0.1 A g^{-1}.[251] To further improve the Na storage performance of Bi_2Se_3, Zhou's group synthesized the Bi_2Se_3/G composite with a two-step process, as shown in **Figure 2.31**, which delivered a high reversible capacity of 346 mA h g^{-1}.[252] In summary, one of the most important methods to improve the performance of Sb_2Se_3 and Bi_2Se_3 is by enhancing their electric conductivity through hybridization with various kinds of carbon.

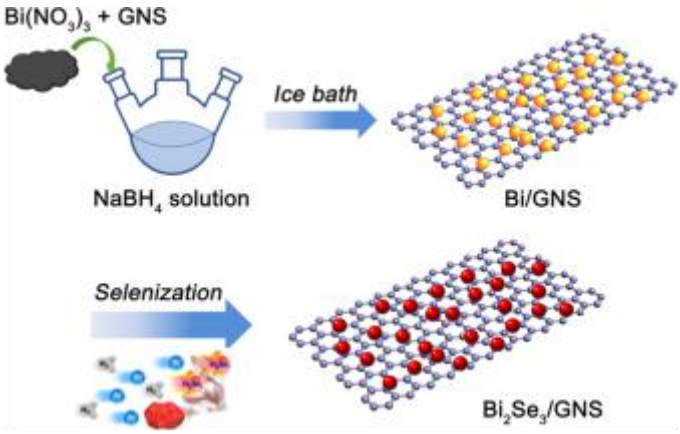

Figure 2.31 Two-step synthesis of Bi_2Se_3/G.[252]

2.4.6 Metal phosphides

Metal phosphides have just been considered as anode materials for SIBs. A pulverization problem exists, however, just as in the above materials, which leads to

capacity fading. This section will provide an overview of the recent results on metal phosphide anodes for SIBs.

2.4.6.1 Sn_4P_3

Sn_4P_3 has attracted interest due to its theoretical volumetric capacity (6650 mA h cm^{-3}). Lee's group was the first to report that Sn_4P_3 could deliver a reversible capacity of 718 mA h g^{-1} after 100 cycles, and concluded that the amorphous phosphorus matrix could effectively confined the Sn particles to enable good performance.[253] Yu's group found that their yolk-shell Sn_4P_3@C nanospheres synthesized by the template method could show a reversible capacity of 360 mA h g^{-1} after 400 cycles at 1.5 C, which was attributed to the ability of the void space in the yolk-shell structure to accommodate the expansion of Sn_4P_3 during sodiation.[254] Yin's group[255] synthesized a Sn_4P_3/graphene composite by a solution-based phosphorization reaction. The as-synthesized Sn_4P_3/graphene composite could present a reversible capacity of 656 mA h g^{-1} after 100 cycles at 100 mA g^{-1}, owing to its porous structure and the synergistic effects between its components. Li's group introduced TiC into Sn_4P_3 to achieve enhanced electrochemical performance.[256] Moreover, Choi's group realized improved performance of Sn_4P_3 anode through using fluoroethylene carbonate (FEC) and tris(trimethylsilyl) phosphite (TMSP) in the electrolyte.[257]

2.4.6.2 MP (M = Fe, Co)

FeP is easily prepared and low-cost, so it has been studied as an anode for SIBs. Chou's group found that FeP synthesized by the ball-milling method could deliver a reversible capacity of 764.7 mA h g^{-1}, which was attributed to the buffering provided by the Fe matrix to alleviate the volume expansion.[258] To improve the performance of FeP, Guo's group reported that FeP nanorod arrays on carbon cloth that were synthesized by hydrothermal/transformation methods could deliver a reversible capacity of 829 mA h g^{-1} after 100 cycles at 0.1 A g^{-1}, which was attributed to the short Na^+ diffusion pathways during the sodiation/desodiation processes.[259]

Yin's group designed core-shell structured FeP@CoP phosphide microcubes assembled from graphene by phosphorizing Prussian blue.[260] In this structure, the conductive graphene network could enhance the charge transfer kinetics, and thus, the optimized sample could maintain a reversible capacity of 456.2 mA h g^{-1} after 200 cycles at 100 mA g^{-1}, which was attributed to the core-shell structure, which could provide enough room for volume changes as well as short Na^+ diffusion paths. Kang's designed PPy encapsulated CoP nanowires grown on carbon paper (CP) to form core-shell CoP@PPy/CP.[261] The optimized structure played a role in enhancing the charge transfer and accommodating the volume change, so that the sample could show an areal capacity of 0.443 mA h cm^{-2} after 1000 cycles at 1.5 mA cm^{-2}. Research on sodium storage in CoP is just beginning. More attention should be paid in future.

2.4.6.3 CuP_2 anode

CuP_2, similar to FeP, has a potential advantage as an anode due to the presence of metallic Cu nanoparticles after the sodiation of CuP_2, which could enhance the electrochemical alloying of P with Na^+ due to its high conductivity. Li's group was the first to study CuP_2 as a potential anode for SIBs, which could exhibit a reversible capacity of ~430 mA h g^{-1} after 30 cycles at 150 mA g^{-1}.[262] Yu's group designed CuP_2 nanoparticles encapsulated by cross-linking hollow carbon sheets, which delivered a reversible capacity of ~410 mA h g^{-1} after 200 cycles at 80 mA g^{-1}.[263] The cross-linked hybrid structure was obtained through two steps involving the polymerization of dopamine hydrochloride and the carbonization of the composite, as shown in **Figure 2.32**. This hybrid structure endowed CuP_2 with good electrochemical sodium storage performance. Recently, Wu's group encapsulated CuP_2 nanoparticles int graphene networks, which could deliver a reversible capacity of 804 mA h g^{-1} at 100 mA g^{-1}.[264] In summary, the hybrids with carbon will be promising as CuP_2-based anodes.

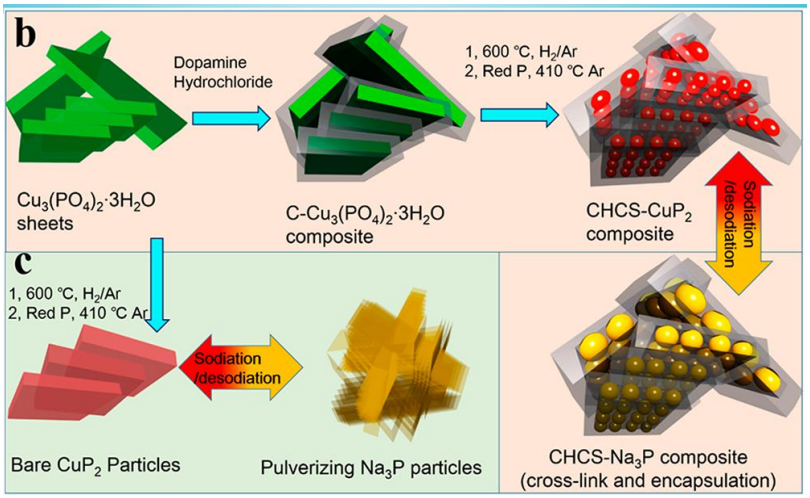

Figure 2.32 (a and b) Synthesis and reversible reactions with Na^+ ions of the composite and bare CuP_2.[263]

CHAPTER 3 EXPERIMENTAL PROCEDURE

In this doctoral work, I mainly synthesized carbon-based nanofibers by the electrospinning method. Moreover, hydrothermal synthesis was also used to obtain the WO_3 nanosheets and Fe_2O_3 nanoparticles, which were further electrospun into polymers for the final products, i.e. WS_2@N/S-C and Fe_7S_8@N/S-C. To determine the structures and components of the obtained composites, these products were investigated by many characterization techniques, such as SEM, TEM, XRD, BET, XPS, and others. Finally, these prepared composites were prepared into electrodes in batteries for electrochemical measurements. The whole experimental process is shown in Figure 3.1.

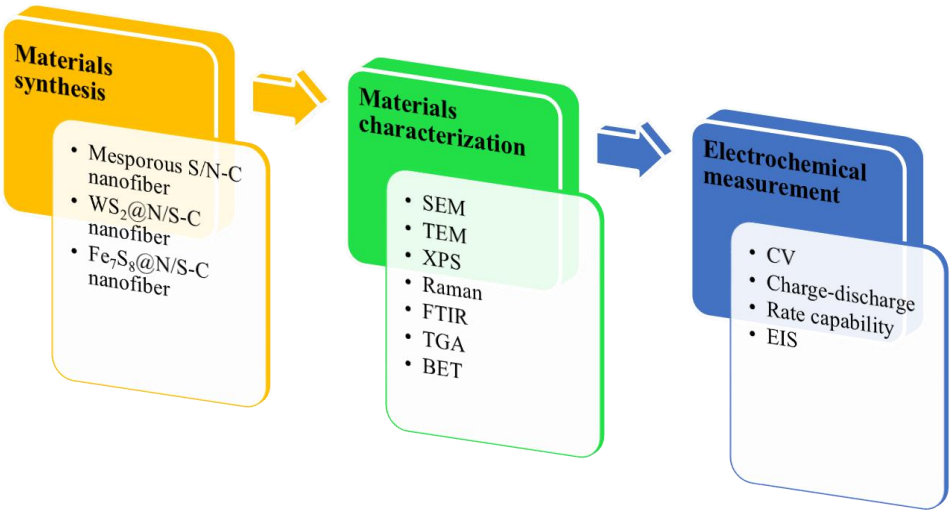

Figure 3.1 Outline of the experimental procedures and characterization techniques used in this thesis.

3.1 Chemicals and Materials

Table 3.1 lists the main chemicals used in this thesis, with each entry including the chemical, formula, purity, and suppliers.

Table 3.1 Chemicals employed in this thesis

Chemicals	**Formula**	**Purity (%)**	**Supplier**
Polyacrylonitrile	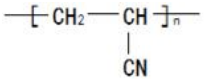	MW 150,000	Sigma Aldrich, USA.
Polymethylmethacrylate	$[C_5H_8O_2]_n$	MW 35,000	Shanghai Aladdin Reagent Co., Ltd.
Acetylene black	C	Battery grade	Shenzhen Poxon Machinery Technology Co., Ltd.
CR2025 type coin cells	N/A	N/A	China
N, N-dimethylformamide	C_3H_7NO	99.5	Sinopharm Chemical Reagent Co., Ltd.
Carboxymethyl cellulose	CMC	Battery grade	Shenzhen Poxon Machinery Technology Co., Ltd.

Sulfur	S	99.5%	Tianjin Kemiou Chemical Reagent Co., Ltd.
Ethanol	C_2H_6O	99.5	Sinopharm Chemical Reagent Co., Ltd.
Copper foil	Cu	Battery grade	Shenzhen Poxon Machinery Technology Co., Ltd.
Sodium tungstate dihydrate	$Na_2WO_4 \cdot 2H_2O$	99.99% (metals basis)	Shanghai Aladdin Reagent Co., Ltd.
Sodium metal	Na	99.7%	Shanghai Aladdin Reagent Co., Ltd.
Tetrafluoroboric acid	HBF_4	40 w%	Energy Chemical Co., Ltd.
Iron chloride, ferric chloride	$FeCl_3 \cdot 6H_2O$	Chemically Pure	Sinopharm Chemical Reagent Co., Ltd.
Pure ethanol	C_2H_5OH	Analytically pure	Tianjin ZhiYuan Reagent Co., Ltd.
Sodium perchlorate	$NaClO_4$	Battery grade	Suzhou Qianmin Chemical Reagent Co., Ltd.

Ethylene carbonate	$C_3H_4O_3$	Battery grade	Suzhou Qianmin Chemical Reagent Co., Ltd.
Diethyl carbonate	$C_5H_{10}O_3$	Battery grade	Suzhou Qianmin Chemical Reagent Co., Ltd.
Fluoroethylene carbonate	$C_3H_3FO_3$	Battery grade	Suzhou Qianmin Chemical Reagent Co., Ltd.

3.2 Materials Preparation

The anode materials in this doctoral work were synthesized by different methods, including the hydrothermal method and electrospinning method. These experimental methods and procedures are introduced in detail in this part.

3.2.1 Electrospinning method

The electrospinning method is a method to prepare nanofiber materials by applying a high voltage electrostatic field. As shown in Figure 3.2 a, the electrospinning device is composed of the collector, the syringe and the high voltage power source. The high voltage power is linked to the syringe and the collector, which is usually set as 10 to 30 kV; the distance between the collector and the syringe is generally set as 15-30 cm. For preparing the polymer solution, the material is first dissolved in a specific solvent, and then the resulting solution is added to a syringe. Due to the high voltage electrostatic field, the solution in the syringe will gradually be ejected and located at

the collector. The electrospinning process is affected by many factors, such as the precursor material, the shape of the collector, the applied high voltage, the composition and concentration of the polymer solution, the spinning distance, etc., which will all affect the diameter, morphology and structure of the final product. Therefore, electrospinning is one of the effective methods for preparing nanofiber materials because of its low cost, simple equipment and controllable morphology of the fibers.

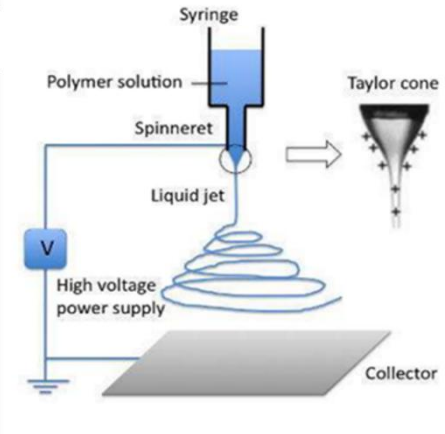

Figure 3.2 Schematic diagram of the electrospinning device.

To obtain the carbon-based composites or oxides, the obtained polymer nanofibers should be further annealed in non-oxidizing atmospheres or air. In this thesis work, we prepared the S/N-C nanofibers, WS_2@S/N-C nanofibers, and Fe_7S_8@S/N-C nanofibers by the electrospinning method combined with other techniques.

3.2.2 Hydrothermal method

Hydrothermal synthesis is a low-cost wet-chemical process to synthesize crystal materials and nanomaterials in a sealed and isolated solution-based system at high temperature (100-1000 ^{o}C) and high pressure (1 MPa-1 GPa). The reaction system is a stainless-steel autoclave with stainless-steel cover and polytetrafluoroethylene (PTFE) internal cups, as shown in Figure 3.3. Usually, 2/3 of the volume of the PTFE cup is the precursor volume limit to ensure safety. The hydrothermal method exhibits obvious advantages compared with conventional wet-chemical methods in preparing crystalline materials and nanomaterials. Because the compositions, morphologies, and crystal structures of the prepared materials can be easily adjusted through changing the reaction conditions, such as the condensation of the precursors, kinds of solvents, the reaction temperature, reaction time, et al. Therefore, synthesizing novel phases, new complexes, and materials with different morphologies can be obtained by using the hydrothermal method.

Figure 3.3 Hydrothermal autoclave (left) with a cross-sectional view (right).

In this thesis work, the WO_3 nanosheets and Fe_2O_3 nanoparticles were synthesized by hydrothermal methods.

3.3 Characterization Techniques

3.3.1 X-ray diffraction

X-ray diffraction (XRD) is a phase-identification technique to characterize and identify the crystalline structure, the crystallite size (grain size), and the preferred orientation of crystalline materials. The technique is based on the constructive interference of monochromatic X-rays in the crystalline material. Figure 3.4 illustrates the principle of XRD. When X-rays strike crystals, the crystalline substances act as three-dimensional diffraction gratings. The X-ray will be scatted by each set of lattice planes at a unique angle, which is called elastic scattering. The patterns of the scattered X-ray waves have a characteristic relationship with the given crystal materials, which can be determined by Bragg's law:

$$2d\sin\theta = n\lambda,$$

where d is the distance between lattice planes, θ is the angle of incidence with the lattice plane, n is any integer, and λ is the X-ray wavelength of the incident beam. Since, each crystal materials has their own unique lattice planes, there will be peaks at specific angles. Therefore, the phases and crystal structures can be identified through these unique X-ray peaks at different angles.

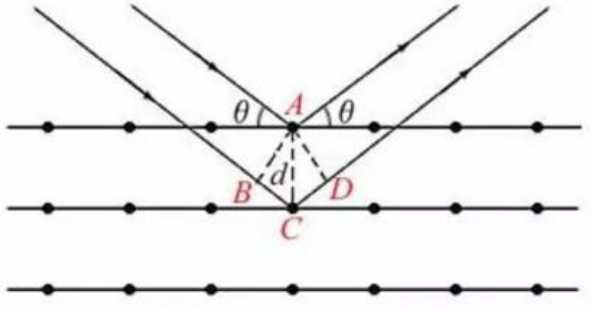

Figure 3.4 Fundamental principles of XRD.

In this thesis work, all the XRD measurements were performed on a Rigaku D/Max-2500 with Cu Kα radiation (λ = 1.5406 Å). Moreover, the working voltage and current were set as 40 kV and 25 mA, respectively.

3.3.2 Raman spectroscopy

When laser light from a monochromatic light source is employed to irradiate the sample, elastic scattering (Rayleigh scattering) and inelastic scattering (Stokes and anti-Stokes Raman scattering) will occur. The scattered light of the elastic scattering has the same wavelength with the excitation light, while the scattered light of the inelastic scattering has a shorter or longer wavelength compared with the excitation light. This energy shift is collectively referred as a Raman effect, which is the result of the interaction of photons with the molecular vibrations, phonons, or other excitations of the sample to provide characteristic shifts in laser energy. The energy shift is detected and recorded in the form of frequency or wavelength, and the spectrum contains chemical and structural information on the sample materials. The Raman spectra of the samples in this thesis work were obtained on a DXR microscope

(Thermo Fischer DXR) with a 532 nm laser as the excitation resource. *In-situ* Raman spectroscopy is a kind of Raman spectroscopy, but it is more sensitive than the Raman spectroscopy, which can monitor the structural changes of electrode materials during cycling process to speculate the reaction mechanism of redox process.

3.3.3 Fourier transform infrared spectroscopy

Fourier transform infrared spectroscopy (FTIR) is an adsorption spectrum showing molecular vibrations, which can be used to identify the molecular functional groups properties of organic materials. The absorption, emission, photoconductivity, or Raman scattering in the infrared spectrum of a material can be collected. The chemical bonds in the molecules of the sample material can be detected from the spectral pattern of molecular absorption and transmission. In this thesis work, the FTIR spectra in this thesis work were recorded on a Nicolet-460. For measurement, the sample materials were mixed with potassium bromide (KBr) powder, which acts as the background, and pressed in a die with a barrel.

3.3.4 X-ray photoelectron spectroscopy

X-ray photoelectron spectroscopy (XPS) is a surface-sensitive technique to test the elemental compositions, chemical states and electronic states of the surface of materials. When the sample is irradiated with X-rays, the inner electrons or valence electrons of the atom or molecule will be stimulated and escaped from the surface of the samples. The electron excited by a photon is called a photoelectron. Measuring the

energy of photoelectrons can obtain the information about the sample. XPS usually tests: (1) What elements and the quantity of those elements exist within sample surface. (2) Solid surface analysis: including the chemical composition or elemental composition of the surface, the atomic valence state, the surface energy state distribution, the electron cloud distribution of the surface electrons and the energy level structure. (3) Structure of the samples: the chemical shift of the internal electron binding energy can be accurately measured to provide information about chemical bonds and charge distribution. The XPS measurement in this thesis work was performed on an Escalab 250Xi.

3.3.5 Thermogravimetric analysis

Thermogravimetric analysis (TGA) is a thermal analysis method to study the thermal stability and composition of materials according to the weight loss or gain with increasing temperature. TGA depends on a function of temperature or time. The precise weight changes can be caused by decomposition, oxidation, or loss of volatiles (such as moisture). Through these changes, the composites of the measured sample can be calculated. The TGA performance in this thesis work was evaluated on a SDTQ600.

3.3.6 BET measurement

Brunauer-Emmett-Teller (BET) analysis is used for evaluating the specific surface area and pore size distribution of materials, which is based on a theory that deals with

the physical adsorption of gas molecules on a solid surface. During the BET test, the sample was put into a system filled with N_2 gas, and the surface of the material is physically adsorbed at a liquid nitrogen temperature. When the physical adsorption is in equilibrium, the specific surface area of the sample can be calculated by measuring the adsorption pressure at the equilibrium and the flow rate of the adsorbed gas to determine the amount of monolayer adsorption of the material. The Brunauer-Emmett-Teller (BET) surface areas of samples in this thesis work were measured on a Tristar 3020.

3.3.7 Scanning electron microscopy

Scanning electron microscopy (SEM) is a type of electron microscope to observe the surface morphology of the sample. When using a very narrow electron beam to scan the sample, various signals are generated by the interaction of the electron beam and the sample, including secondary electrons (SE), back-scattered electrons (BSE), characteristic X-rays, specimen currents under illumination, and transmitted electrons. We can collect these signals (mainly secondary electron signal) to get some information on the morphology, composition and other properties of the sample surface, such as electrical conductivity. The high-resolution images of a sample surface can be obtained to observe details under 1 nm in size.

Usually, SEM is equipped with some other detectors, such as energy-dispersive X-ray spectroscopy (EDS, EDX, or XEDS). EDS is an analytical technique to detect the

elemental analysis or chemical characteristics of a sample. Its characterization capabilities rely on an interaction between some source of X-ray excitation and the sample, because each element has a unique atomic structure, allowing a unique set of peaks on its X-ray spectrum. In this doctoral work, the SEM images were collected on a Helios Nanolab G3UC.

3.3.8 Transmission electron microscopy

Transmission electron microscopy (TEM) is a microscopy technique to obtain images and other information when an accelerated and concentrated electron beam passes through a very thin sample. The electron reacts with atoms in the sample to change direction, resulting in solid angle scattering. The size of the scattering angle is related to the density and thickness of the sample, so that images of different brightness and darkness can be formed. Due to the short wavelength of the electron, the resolution of the TEM is much higher than that of the optical microscope, which can reach 0.1 to 0.2 nm and the magnification is tens of thousands to millions of times. Therefore, the fine structure of the sample can be observed using TEM, and even a structure of only one column of atoms can be observed, which is tens thousands of times smaller than the smallest atomic structure observed by an optical microscope. In this doctoral work, the TEM observations were carried out on a JEOL 2011 TEM (200 keV).

3.4 Electrode Preparation and Coin-cell Assembly

The cells were assembled as Figure 3.5, with their main components of anode, separator, cathode, and electrolyte. The electrodes usually consist of the electrode material (active material), a conductive additive, and a binder in a certain ratio. These are mixed in a solvent (water or organic solvents) to form a slurry. The slurry is further spread on metal foil (aluminium for the cathode and copper foil for the anode), and then dried at a high temperature in vacuum. In this thesis, the active materials were used for the anode, and acetylene black and carboxymethyl cellulose (CMC) were the conductive additive and binder. The weight ratio of active material to acetylene black to CMC was set to 8:1:1. The mass loading of the active material was ~1 mg cm^{-2}.

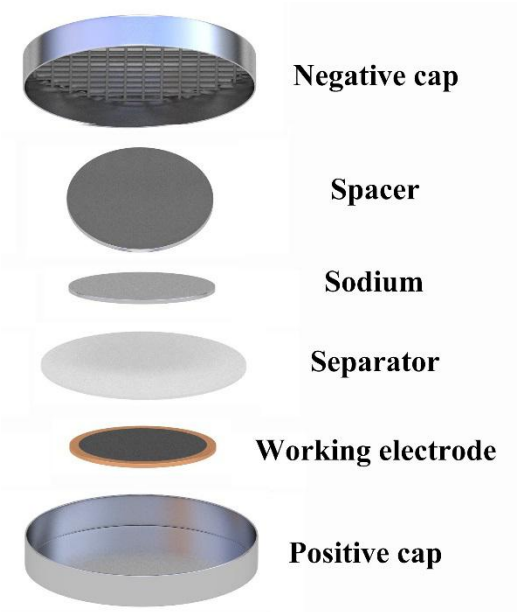

Figure 3.5 Stacking sequence of components of a coin cell.

In this thesis, the electrochemical performances of the active materials were evaluated using 2025 coin-type half cells. Before assembling the cells, the electrode needed to be cut into discs of 12 mm in diameter as the working electrode. The working electrode, Na metal as the counter electrode, and glass fiber as the separator were assembled with the electrolyte in an Ar-filled glovebox. Here, the electrolyte was 1 M $NaClO_4$ dissolved in a mixture of ethylene carbonate (EC) and diethyl carbonate (DEC) (v/v = 1:1) with 5 wt% fluoroethylene carbonate (FEC) as additive.

3.5 Electrochemical Measurements

3.5.1 Cyclic voltammetry tests

Cyclic voltammetry (CV) is a useful electrochemical research method to study the nature, mechanism and kinetic parameters of electrode reactions. The method controls the electrode potential at different scan rates, and scans one or more times with a triangular waveform. Different reduction and oxidation reactions can alternately occur on the electrode within the potential range, and the current-potential curve is recorded. According to the shape of the curve, the degree of reaction reversibility of the electrode, the possibility of intermediate or formation of a new phase can be judged. CV curve is often used to measure electrode reaction parameters, determine reaction mechanism, and observe what and how reactions can occur within the entire potential sweep range. In this thesis work, the CV measurements were carried out on a CHI660E electrochemical workstation.

3.5.2 Galvanostatic charge-discharge

The galvanostatic charge and discharge profiles are used for characterizing the redox processes of rechargeable cells during various cycles. When the battery is discharged or charged, its working voltage always changes with the continuation of time. The curve drawn by the operating voltage and discharge/charge time or capacity is called the discharge/charge characteristic curve. The curve is flat, indicating that the operating voltage of the battery is stable. Measuring the discharge/charge curve of the battery is one of the basic methods for studying the electrochemical performance of the battery. According to the discharge/charge curve, it can be judged whether the battery performance is stable, the maximum current allowed by the battery during stable operation, and the information for the potential *vs.* capacity or potential and current *vs.* time plots. In this thesis work, the galvanostatic charge/discharge tests were carried out on a battery test system (Land CT2001A).

3.5.3 Electrochemical impedance spectroscopy

Electrochemical impedance spectroscopy (EIS) is to measure the inner resistance of cells to study the dynamics and mechanism of electrode material. Normally, the EIS spectrum consists of a semicircle at high-frequency and a linear tail at low-frequency. The semicircle is attributed to the charge transfer resistance, reflecting the kinetic processes and the double-layer capacitance. The linear tail is related to the diffusion of alkali ions in the electrode materials. Moreover, EIS can measure the alkali ion

diffusion and apparent energy activation of the electrode. In this thesis, EIS data were collected on a CHI660E electrochemical workstation.

3.6 Calculation Methods

Density functional theory (DFT) is a quantum mechanical method for studying the electronic structure of multi-electron system. DFT was performed using the Vienna Ab-initio Simulation Package (VASP) based on the frozen-core projector augmented wave (PAW) method. The exchange correlation functional is based on the generalized gradient approximation (GGA) with the Perdew-Burke-Ernzerhof (PBE) functionals. The plane wave basis had the cut-off energy of 520 eV. The convergence criteria were set to 10^{-5} eV and 0.02 eV $Å^{-1}$ for the energy change and atomic force, respectively. The DFT-D3 method is invoked by setting the van der Waals correction (IVDW) with the value of 11. The surface structure was set with a 15 Å vacuum layer to avoid interaction between adjacent images.

CHAPTER 4 S/N-DOPED HIGH-CAPACITY MESOPOROUS CARBON ANODE FOR NA-ION BATTERIES

4.1 Introduction

Na-ion batteries (SIBs), as one of the most promising alternatives to commercial Li-ion batteries (LIBs), have attracted great attention for grid-scale energy storage systems because of the abundance and low-cost of sodium (Na) and its similar physical and electrochemical properties to lithium.[265-270] The larger radius of the Na^+ ion than that of Li^+ ion, however, reduces the mobility of Na^+ in various electrodes and at the electrode/electrolyte interface, which limits the rate performance and cycling life of SIBs. Therefore, it is still highly desirable to explore new anode materials for SIBs. Heteroatom doped carbonaceous materials,[271-277] alloys,[278-282] metal oxides/sulfides,[283-286] and their composites[287-289] have been investigated as anode materials for SIBs. Nevertheless, the large volume expansion of alloys and metal oxides/sulfides during sodiation and the correspondingly low capacity of titanates severely restrict their actual applications. As a result, low-cost carbon-based materials with various structures are the most promising anode materials for SIBs.[290]

It is well known that the intercalation of Na^+ into graphite depends on electrolyte solvents. Diglyme-based electrolytes with narrow wide electrochemical window demonstrated that the co-intercalation phenomena of ternary graphite intercalation compounds could enable the sodium storage within the graphite.[291-294] However, graphite cannot accept Na^+ ions in traditional carbonate electrolytes with wide

electrochemical window because of the inadequate interlayer spacing for Na^+ intercalation.[283] Although the capacity of graphite has been improved in carbonate electrolytes by optimizing its structure,[295-297] it still has a low initial Coulombic efficiency and a limited cycling performance. Therefore, to overcome these drawbacks, heteroatom (such as N, S, B, P) doped into carbon has been reported to be an effective method to change the physical and chemical properties of carbon materials by introducing more defect sites and increasing the surface area.[272, 298-301] Carbon materials usually have a capacitive charge storage mechanism that works by absorbing Na^+ ions into the voids or on the defect sites of carbon materials,[302] which can offer long cycling performance and superior rate capability because of the fast Na^+ transport on the carbon/electrolyte interface.

In this work, porous carbon nanofibers doped with high populations of N and S atoms (S/N-C) were prepared. The nitrogen and sulfur in the S/N-C nanofibers not only enhances the electronic conductivity,[303-306] but also provides more active sites to increase the capacitive storage. Moreover, numerous meso/micropores and channels in the S/N-C nanofibers were obtained by decomposing polymethylmethacrylate (PMMA) in the precursor at high temperature, which increases the contact area with the electrolyte to facilitate the adsorption of Na^+ ions and shortens the Na^+ diffusion path. The S/N-C nanofibers displayed a high reversible capacity of 552.5 mA h g^{-1} at a current density of 0.1 A g^{-1}, excellent cycling stability (335.8 mA h g^{-1} after 800 cycles at 5 A g^{-1} with a capacity retention of 94.5 %, calculated based on the 2nd capacity), and superior rate capability (333.4 mA h g^{-1} at 5 A g^{-1}).

4.2 Experimental Section

Synthesis of porous S/N-C nanofibers: The porous S/N-C nanofibers were synthesized by an electrospinning method,[307, 308] followed by a sulfidation treatment. 0.327 g polyacrylonitrile (PAN) and 0.327 g PMMA were separately dissolved in 3 ml N, N-dimethylformamide (DMF) at 60 °C with vigorous stirring for 1 h. Then, the two transparent solutions were mixed and stirred vigorously at 60 °C for another 4 h to obtain a homogeneous solution. The obtained mixture was ejected into a 10 ml syringe with a single-nozzle (diameter: 0.6 mm). The applied voltage and the feeding rate for electrospinning were 16 kV and 0.3 ml h^{-1}, respectively. The distance between the nozzle and collector is set to be 20 cm. The nanofibers were collected from the collector plate after electrospinning and stabilized at 60 °C for 12 h in a vacuum oven. The obtained nanofibers were stabilized at 230 °C for 2 h in air, and further carbonized with sulfur in a vacuum-tight tube by annealing the mixed nanofiber/sulfur (1:5 by weight) in a quartz boat at 500 °C for 3 h. The sample was annealed in Ar atmosphere at 230 ºC for 2 h to remove the residual sulfur and obtain the final S/N-C nanofibers. Here, the sulfur doping in the vacuum-tight tube could guarantee the high doping amount of sulfur into carbon nanofibers. Nitrogen-doped carbon (N-C) nanofibers were prepared by stabilization at 230 °C in air, followed by carbonizing the nanofibers at 500 °C for 3 h in vacuum.

Material characterization: Powder X-ray diffraction (PXRD) was used to characterize the sample structure. The surface structure and chemical states of samples were measured by X-ray photoelectron spectroscopy (XPS), Fourier

transform infrared (FT-IR) spectroscopy and Raman spectrum. The morphology was characterized by scanning electron microscopy (SEM) and transmission electron microscopy (TEM) equipped with an energy-dispersive X-ray analyser (EDX) that can be used to determine the element distribution. Elemental content analysis was conducted by CHNS/O elemental analyser. The surface area was determined via the Brunauer-Emmett-Teller (BET) technique.

Electrochemical measurements: CR2025 half-cells were assembled in an Ar-filled glove box for electrochemical measurements of the N-C and S/N-C samples. The electrodes were prepared by mixing the active materials, acetylene black, and carboxymethyl cellulose (CMC) in a weight ratio of 8:1:1 with a mixed solvent of ethanol and distilled water (3:2 by volume) to form a slurry. The resultant slurry was coated on Cu foil, dried in a vacuum oven at 60 °C overnight, and then cut into discs with a diameter of 12 mm. The mass loading of the active material is about 1 mg cm^{-2}. Sodium metal and glass fibers were used for the counter electrode and separator, respectively. 1 M $NaClO_4$ in ethylene carbonate (EC) and diethyl carbonate (DEC) (1:1 by volume), along with 5% fluoroethylene carbonate (FEC), was the electrolyte. The cells were cycled between 0 and 3 V at room temperature.

Calculation details: The density functional theory (DFT) calculations were performed with the Vienna Ab-initio Simulation Package (VASP).[309, 310] The interactions between core and valence electrons were described using the frozen-core projector-augmented wave (PAW) method.[311-313] The exchange-correlation function was calculated by the Perdew-Burke-Ernzerhof generalized gradient approximation

(PBE-GGA) method. The plane wave basis was used with the energy cut-off set to 350 eV. The convergence criteria of 10^{-5} eV and 0.02 eV $Å^{-1}$ were adopted for the total energy calculation. The so-called climbing image nudged elastic band method (cNEB) was employed to study the diffusion properties of Na^+. The adsorption energy (E_{ad}) of a Na ion on the surface of S/N co-doped carbon was calculated according to following equation:

$$E_{ad} = E_{(S/N\text{-}C\ +Na)} - E_{(S/N\text{-}C)} + E_{Na}$$

Where $E_{(S/N\text{-}C\ +Na)}$, $E_{(S/N\text{-}C)}$, and E_{Na}, are the total energies of one Na^+ adsorbed at the surface of S/N-C, the clean surface of S/N-C, and one Na atom in the same slab, respectively.

4.3 Results and Discussion

4.3.1 Structure and morphology

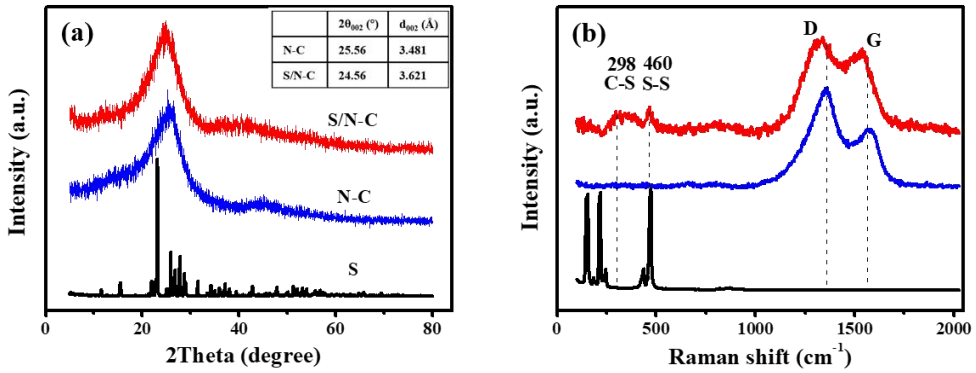

Figure 4.1 (a) XRD patterns and (b) Raman spectra of sulfur, N-C and S/N-C samples.

The two broad peaks in the X-ray diffraction (XRD) patterns (**Figure 4.1 a**) correspond to the (002) and (100) diffractions of carbon materials, indicating the

amorphous nature of the N-C and S/N-C samples. No peaks related to sulfur S_8 were observed in the S/N-C sample. The larger interlayer distance (3.621 Å) of the S/N-C sample than that of carbon (3.481 Å) facilitates the insertion/extraction of Na^+ ions and results in improved electrochemical performance.[301, 314] **Figure 4.1 b** shows the Raman spectra of commercial sulfur, N-C and S/N-C nanofibers. The sulfur shows three typical peaks below 500 cm^{-1}, which correspond to the vibration of S_8. The N-C sample only exhibits two major peaks at 1350 and 1580 cm^{-1}, corresponding to the disorder induced D band and the graphitic G band, respectively. Two additional peaks at 298 and 460 cm^{-1} in the S/N-C sample are related to the C-S and S-S stretching, indicating the disordered distribution of C and S atoms. Moreover, there are no typical peaks of S_8 in the S/N-C Raman spectrum, which agrees well with the XRD results.

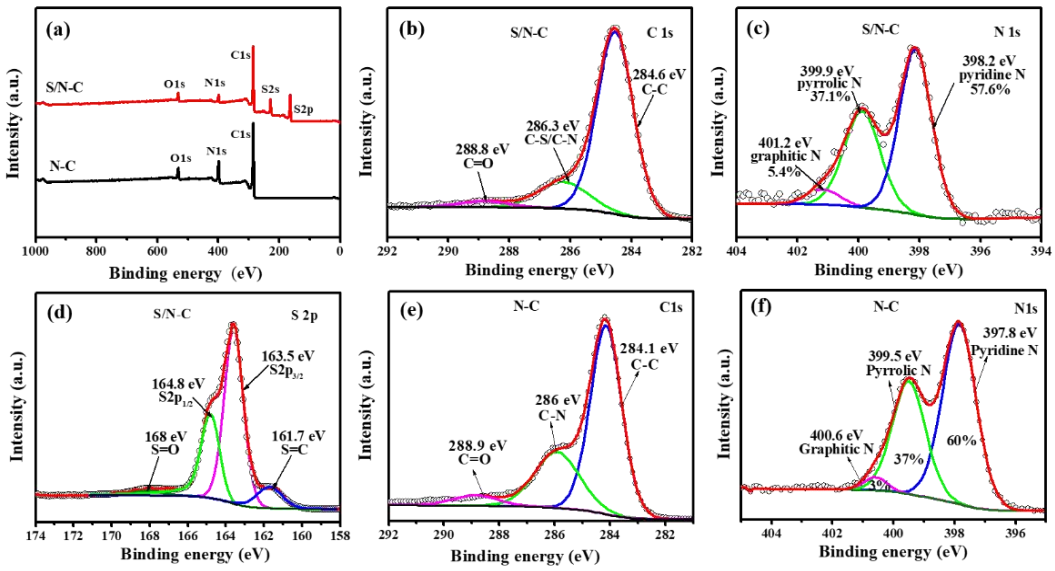

Figure 4.2 (a) XPS spectra of N-C and S/N-C samples; high-resolution XPS spectra of (b) C 1s, (c) N 1s, and (d) S 2p for the S/N-C sample; high-resolution XPS spectra of (e) C 1s, and (f) N 1s for the N-C sample.

XPS measurements were carried out on the S/N-C and N-C samples to investigate their composition and surface chemical structure (**Figure 4.2**). There are two peaks at

165 and 229 eV in the XPS spectrum of the S/N-C sample (**Figure 4.2 a**), which are assigned to S 2p and S 2s, respectively. The three peaks at 284.6, 286.3, and 288.8 eV for C 1s in the S/N-C sample (**Figure 4.2 b**) are attributed to C-C, C-S/C-N, and C=O groups, respectively, verifying the existence of S- and N- containing functional groups.[315] The content of N in N-C nanofibers is confirmed to be 17.36% by element analysis. However, the content of N in S/N-C nanofibers is decreased to 12.59% when high sulfur content (27.95%) exists in S/N-C nanofibers. The C 1s spectrum of the N-C sample (**Figure 4.2 e**) shows a similar result to that of the S/N-C sample. The high-resolution XPS spectrum of N 1s in the S/N-C sample (**Figure 4.2 c**) is fitted into three peaks located at 398.2, 399.9, and 401.2 eV, which are assigned to pyridinic N, pyrrolic N, and graphitic N doped into the S/N-C sample, respectively.[316] The doped nitrogen could improve the electronic conductivity of the carbon nanofibers by imposing an electron donor effect. Compared with the N 1s spectrum of the N-C sample (**Figure 4.2 f**), the content of graphitic N in S/N-C sample was increased from 3 to 5.4%, while the content of pyridinic N decreased from 60 to 57.6%. The introduction of sulfur could promote the transformation of pyridinic N to graphitic N. The S 2p spectrum of the S/N-C sample in **Figure 4.2 d** can be deconvoluted into four peaks, *i.e.*, C=S at 161.7 eV, S $2p_{3/2}$ at 163.5 eV, S $2p_{1/2}$ at 164.8 eV, and S=O at 168 eV.[317, 318] The existence of C=S bonds confirms the successful doping of S into carbon.

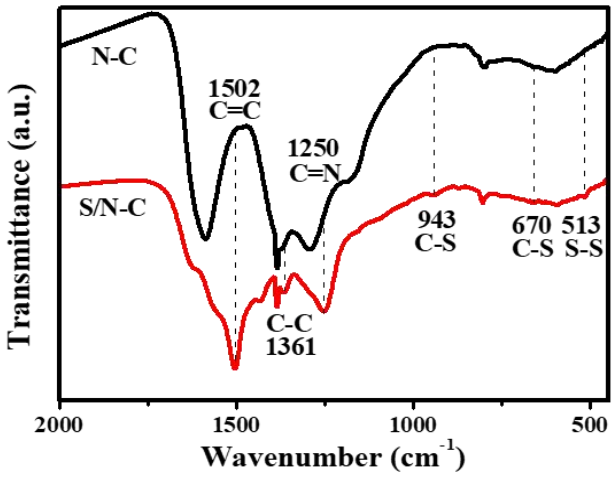

Figure 4.3 FT-IR spectra of the N-C and S/N-C samples.

Further structural information on the N-C and S/N-C samples was provided by FT-IR spectroscopy, as shown in **Figure 4.3**. Compared with the N-C sample, the S/N-C sample exhibited three relatively weak peaks at 513, 670, and 939 cm^{-1}. The peaks at 513 and 670 cm^{-1} correspond to S-S stretching and the C-S stretching, respectively. The peak at 939 cm^{-1} corresponds to the breathing of a ring with a C-S bond. Thus, these peaks verify the formation of C-S and S-S bonds after the sulfurization reaction, which is consistent with the reported Raman results.[319]

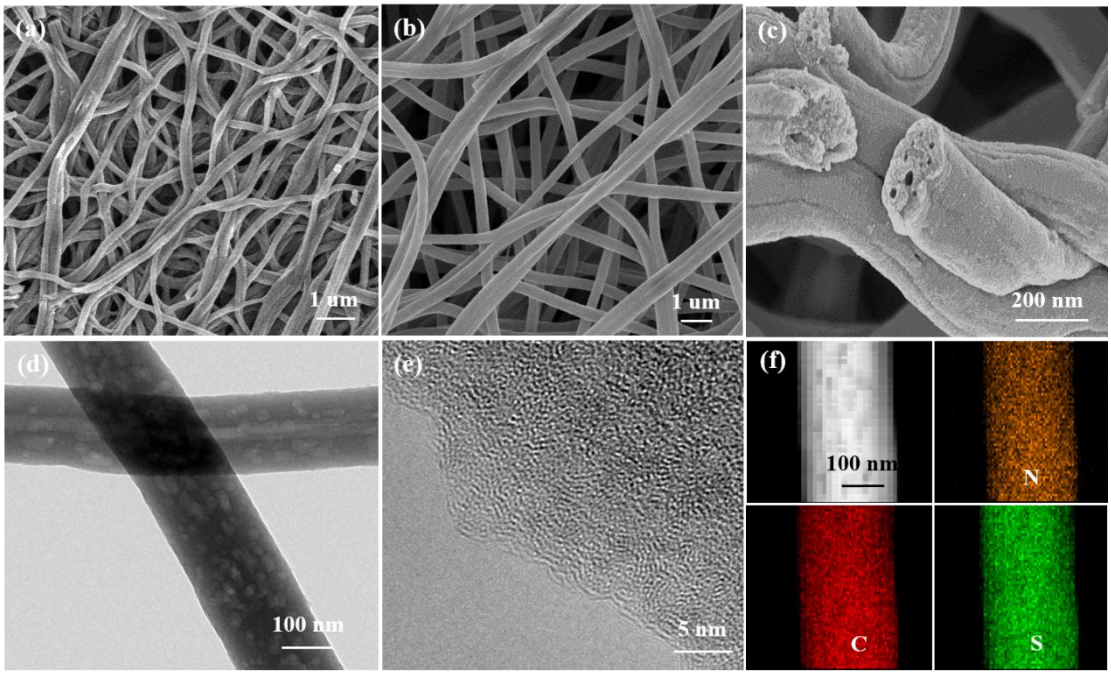

Figure 4.4 (a and b) SEM images of S/N-C nanofibers and N-C nanofibers; (c) high-magnification SEM image of S/N-C nanofibers; (d) low-magnification and (e) high- magnification TEM images of S/N-C nanofibers; (f) element mapping of the part of a S/N-C nanofiber.

The morphology of the S/N-C and N-C samples was characterized by SEM and TEM (**Figure 4.4**). The S/N-C nanofibers (**Figure 4.4 a**) have a diameter of ~ 200 nm and a rough surface due to the sulfidation treatment; the reaction of sulfur with carbon results in more defects and a higher surface area. The N-C nanofibers, however, show a relatively smooth surface (**Figure 4.4 b**). Some meso-/micro-pores inside the individual nanofibers (**Figure 4.4 c**) are ascribed to the decomposition of PMMA at high temperature. In contrast, the PAN is fully transformed to carbon, resulting in a continuous fiber morphology.[320] These results indicate that the PMMA mainly stayed inside the fibers during electrospinning process while the PAN as the framework was continuously distributed throughout the whole nanofiber. Some isolated hollow cores existed along with the whole nanofibers (**Figure 4.4 d**), which could sufficiently

shorten the diffusion paths of Na^+ ions and facilitate electrolyte permeation into the entire structure. The high-magnification TEM image (**Figure 4.4 e**) confirms the amorphous structure of the S/N-C nanofibers, and the energy dispersive spectroscopy (EDS) elemental mapping (**Figure 4.4 f**) indicates a homogeneous distribution of C, N, and S elements in the S/N-C nanofibers. Moreover, the surface areas of the N-C and S/N-C nanofibers were analyzed by nitrogen adsorption/desorption isotherms (**Figure 4.5**): the S/N-C nanofibers (16.1 $m^2 g^{-1}$) exhibit a higher specific surface area than the N-C nanofibers (7.8 $m^2 g^{-1}$).

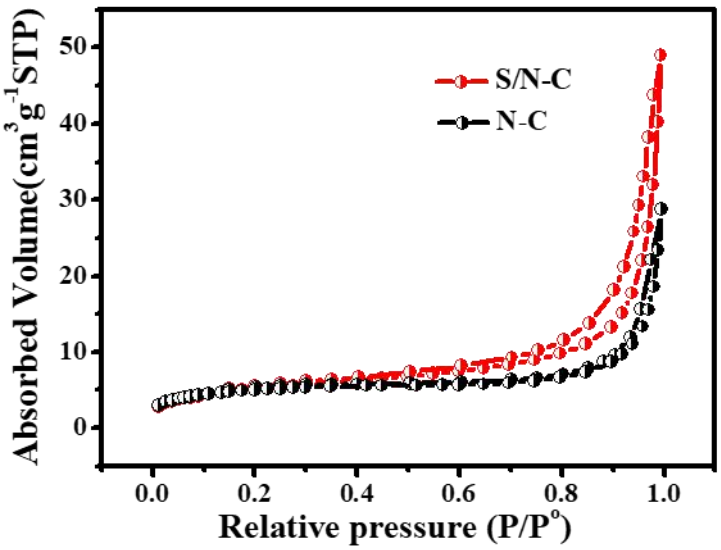

Figure 4.5 Nitrogen adsorption/desorption isotherms of N-C and S/N-C nanofibers.

4.3.2 Electrochemical characterization

Figure 4.6 shows the first three cyclic voltammetry (CV) curves of the N-C and S/N-C electrodes at 0.1 mV s^{-1}. A large and broad cathodic peak for the N-C electrode that appeared below 0.5 V (**Figure 4.6 a**), which is related to solid-electrolyte interphase (SEI) formation, disappeared after the 1st cycle; the weak cathodic peak at

1.9 V is attributed to the reaction between metallic Na and the functional groups on the carbon surface.[299] The redox peaks at 0 and 0.1 V correspond to the reversible insertion/extraction of Na^+ ions into/out of the porous carbon nanofibers. The hysteresis can be ascribed to the defect structure of the carbon materials, as reported for LIBs.[321] The CV curves of S/N-C electrode (**Figure 4.6 b**) show two more redox couples at 1.8/2.2 V and 1.2/1.85 V, which can be attributed to the stepped redox reactions between Na^+ and S in S/N-C electrode.[322] These results indicate that the bonded S is electrochemically active and can react with Na to improve the capacity of carbon.

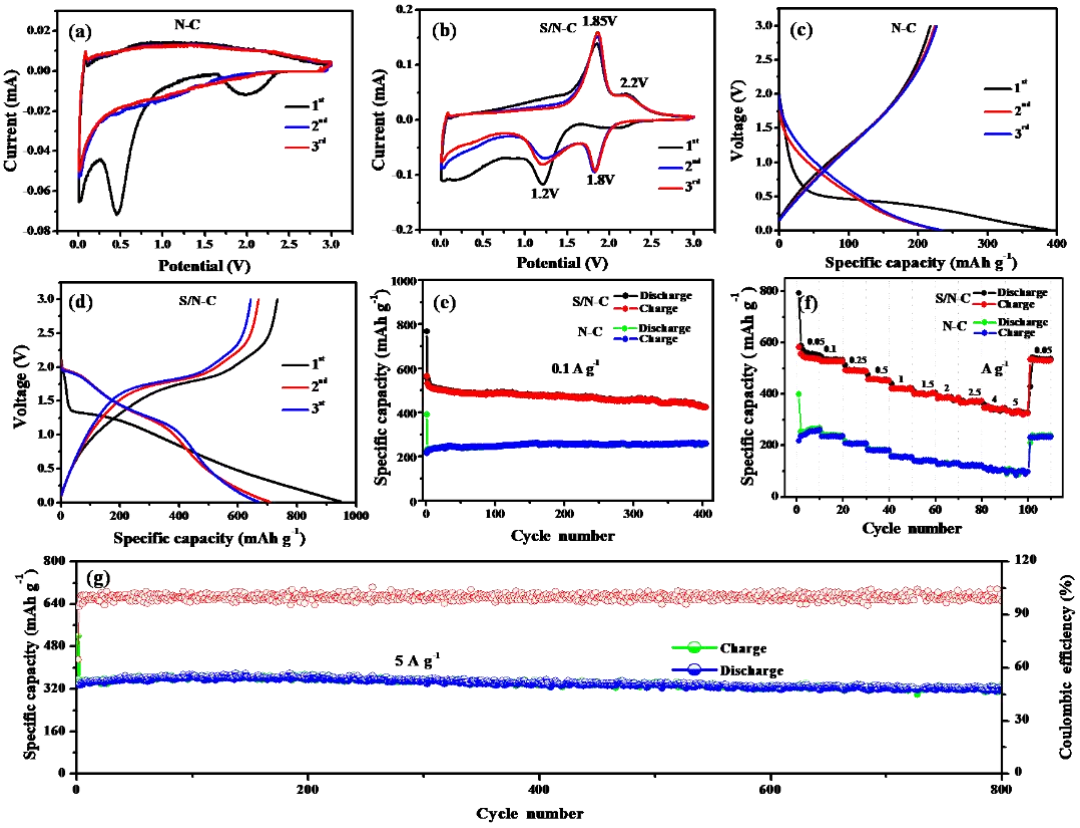

Figure 4.6 Electrochemical performance of N-C and S/N-C electrodes. (a-b) The first three CV curves at 0.1 mV s^{-1}; (c-d) The charge-discharge profiles at 0.1 A g^{-1}; (e) Cycling performance at 0.1 A g^{-1}; (f) Rate capability at various current densities; (g) Long cycling performance of S/N-C at 5 A g^{-1}.

The charge-discharge profiles for the first 3 cycles of N-C and S/N-C electrodes are shown in **Figure 4.6 c** and **d**. The N-C electrode delivered an initial discharge capacity of 390.9 mA h g^{-1} at 0.1 A g^{-1} with an initial Coulombic efficiency of 55.6%. The low Coulombic efficiency is ascribed to the irreversible reaction between Na and the functional groups in the N-C electrode, as well as the formation of SEI layer. Nevertheless, the initial discharge capacity of S/N-C electrode (766.8 mA h g^{-1}) is almost twice as high as that of N-C electrode. In addition, the initial Coulombic efficiency of the S/N-C electrode (73.4 %) is much higher than that of N-C electrode because of the reduced amount of C=O bonds in S/N-C electrode, which consume Na^+ during SEI formation.[323, 324] The discharge profile of S/N-C electrode includes two slopes. The capacity at voltages above 1 V is due to the stepped reduction of the bonded S, which is consistent with the CV results. The high specific capacity and Coulombic efficiency of the S/N-C electrode indicates that the sulfur doping could effectively increase the density of active sites and enlarge the interlayer spacing d_{002} to facilitate the adsorption and transportation of Na^+ in the carbon.

Figure 4.6 e shows the cycling performance of the S/N-C and N-C electrodes at a current density of 0.1 A g^{-1}. The S/N-C electrode delivered an initial discharge capacity of 766.8 mA h g^{-1} and a reversible capacity of 426.3 mA h g^{-1} after 400 cycles, while N-C electrode is only 253.7 mA h g^{-1} after 400 cycles. The excellent cycling performance of the S/N-C nanofibers can be attributed to the presence of more active sites induced by S doping and the synergistic effects of N and S co-doping. **Figure 4.6 f** shows the rate capabilities of the electrodes at various current

densities; the S/N-C electrode exhibits much higher capacity than the N-C electrode and shows stable cycling performance at different current densities. The S/N-C electrode exhibited surprisingly high capacity of 372.8, 357.8, and 333.4 mA h g^{-1} at a high current density of 2.5, 4, and 5 A g^{-1}, respectively. **Figure 4.6 g** shows the long cycling performance of the S/N-C electrode at 5 A g^{-1}; it has a discharge capacity of 335.8 mA h g^{-1} after 800 cycles. The sulfur doping could enlarge the interlayer spacing (3.62 Å) of the carbon materials, thus improving the insertion/extraction of Na^+ ions.

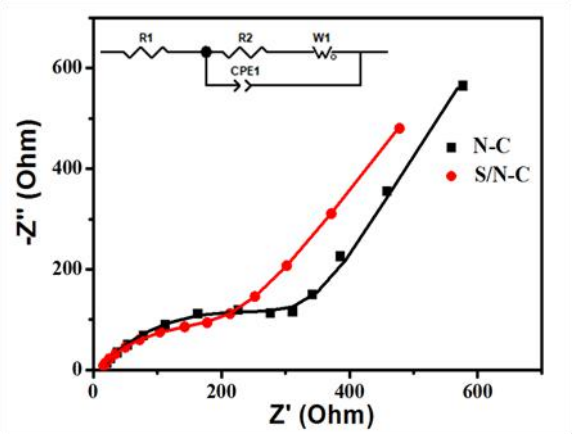

Figure 4.7 Nyquist plots of EIS data for N-C and S/N-C nanofiber electrodes. The inset is the equivalent circuit diagram.

Moreover, electrochemical impedance spectroscopy (EIS) measurements were conducted to characterize the internal resistance and charge-transfer process (**Figure 4.7**). The much lower charge-transfer resistance (R_{ct}) of the S/N-C electrode than that of the N-C electrode would give it better rate capability. Moreover, the interconnected pores derived from the deposition of PMMA during thermal treatment of the nanofibers could facilitate the transportation of Na^+ ions.

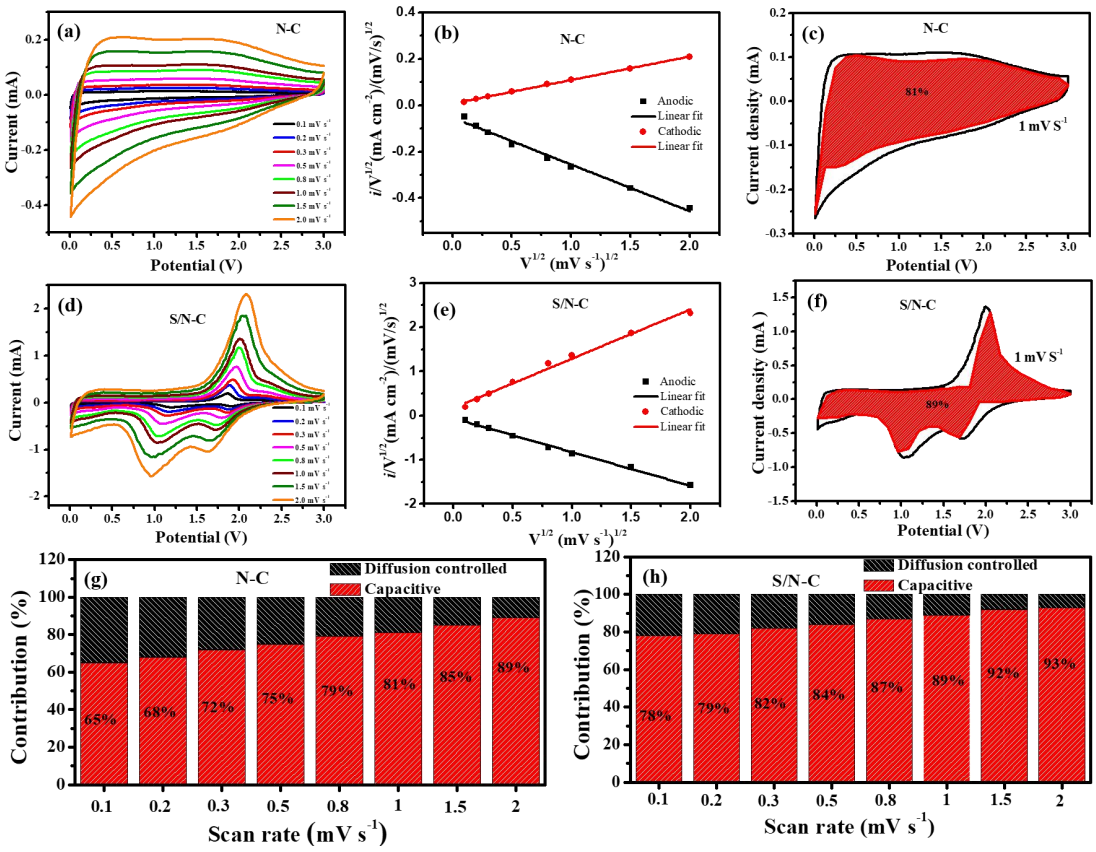

Figure 4.8 CV curves of (a) N-C and (d) S/N-C electrodes at different scan rates; linear fitting of peak current dependence (normalized by $v^{1/2}$) on the square root of the scan rate ($v^{1/2}$) for the (b) N-C and (e) S/N-C electrodes; capacitive and diffusive contributions to the current density of (c) N-C and (f) S/N-C electrodes at 1.0 mV s^{-1}; percentage of the capacitive contribution to the current density of the (g) N-C and (h) S/N-C electrodes at different scan rates.

To further understand the good electrochemical performance of S/N-C nanofibers, the energy storage mode was studied based on CV profiles. **Figure 4.8 a** and **d** displays the CV curves of N-C and S/N-C electrodes at various scan rates, which all show similar shapes even at the high scan rate of 2 mV s^{-1}. According to a report from Dunn's group,[325] the measured current (i, mA) is related to the scan rate (v, mV s^{-1}) as follows:

$$i(V) = k_1 v + k_2 v^{1/2} \quad (1)$$

The whole current response $i(V)$ at an applied voltage consists two parts: one is the surface-controlled contribution (capacitive, $k_1 v$), and the other is the diffusion-controlled contribution ($k_2 v^{1/2}$). By solving for the values of k_1 and k_2, we can separate the current into the capacitive contribution and the diffusion-controlled contribution. The $i(V)/v^{1/2}$ - $v^{1/2}$ plots at a specific voltage during discharge and charge processes at various scan rates were calculated, as shown in **Figure 4.8 b** and **e**. The values of k_1 (the slope) and k_2 (the intercept) could be obtained after linear fitting, thus obtaining the contributions of surface and diffusion-controlled current. **Figure 4.8 c** shows the CV profile of the N-C electrode at 1 mV s^{-1} with its capacitive contribution (red region) of 81%, which is much lower than (89%) for the S/N-C electrode (**Figure 4.8 f**) because of the pseudocapacitive interaction between the Na^+ and the O-, N- and S-containing functional groups. This is because the C=O groups could reversibly react with Na to form sodium enolate groups (C-O-Na) in surface-induced way.[276] Qian and co-workers investigated the nitrogen and sulfur doping which contributed to the capacitive charge storage.[277] In addition, the porous S/N-C nanofibers are easily wet by the electrolyte to improve the capacitive contribution. **Figure 4.8 g** and **h** present the calculated capacitive contributions for N-C and S/N-C electrodes at various scan rates. The proportion of capacitive contribution gradually increases with the increasing scan rate and finally reaches a maximum value of 93% at the scan rate of 2 mV s^{-1}, implying that the capacitive contribution occupies a high percentage of the total capacity at high scan rates.

4.3.3 Theoretical calculations

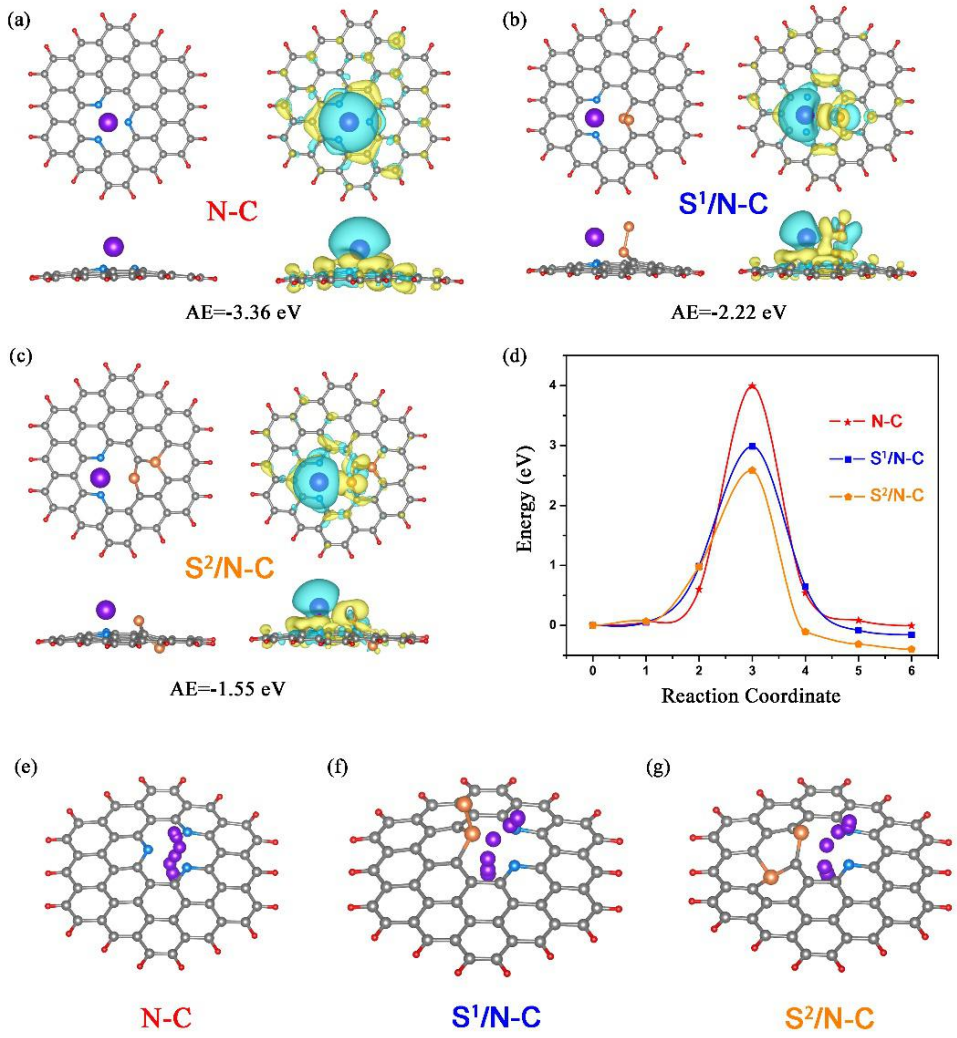

Figure 4.9 Optimized structure and charge density difference of (a) N-C, (b) S^1/N-C, and (c) S^2/N-C; (d) Na^+ diffusion energy and the related migration path for (e) N-C, (f) S^1/N-C, and (g) S^2/N-C. Grey, red, orange, blue, and purple spheres represent C, H, S, N, and Na atoms, respectively.

Density functional theory (DFT) calculations were carried out to reveal the mechanism behind outstanding sodium storage and diffusion performance of S/N-C. To elucidate the synergistic effects of S and N co–doping, all the reasonable molecular models were optimized, and the related charge density differences are

shown in **Figure 4.9**. In N-C nanofibers, the N atoms have much stronger adsorption to Na^+ than S^1/N-C (-2.21 eV for S-S structure) and S^2/N-C (-1.55 eV for S-C-S structure) for the S/N-C nanofibers; the stronger binding energy will increase the activation energy for Na^+ transport on the N-C nanofibers. The N-C sample with an ultrahigh diffusion barrier of 3.99 eV has low Na ion migration (**Figure 4.9 d and e**), which increases the charge transfer resistance and decreases the rate performance. The S^1/N-C and S^2/N-C of S/N-C nanofibers have a much smaller diffusion barrier (by 1 eV) than that of the N-C nanofibers (S^1/N-C: 3 V in **Figure 4.9 d-f** and S^2/N-C: 1.41 eV in **Figure 4.9 d-g**. Therefore, S and N co-doping reduces the adsorption of Na^+ and improves the storage/diffusion capability of Na^+ in S/N-C nanofibers.

4.3.4 *In situ* Raman analysis

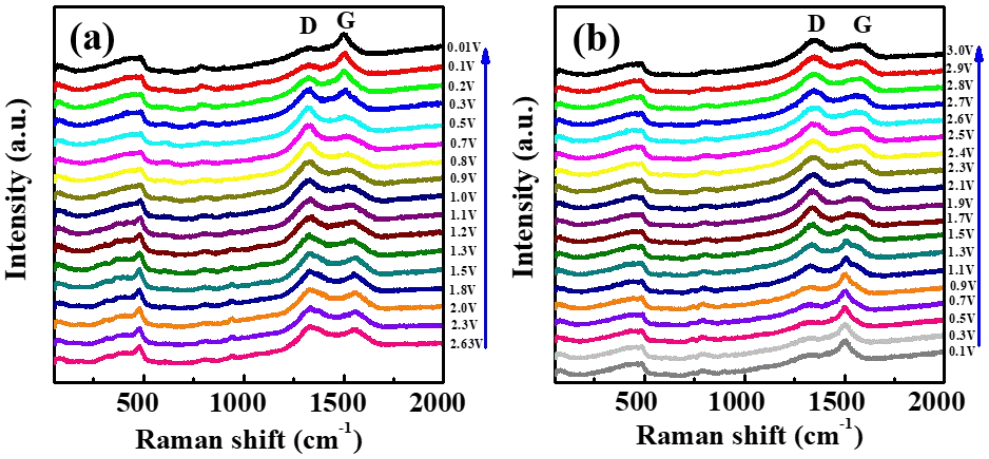

Figure 4.10 (a-b) *In situ* Raman spectra of S/N-C electrode in the first cycle with a scan rate of 1.0 mV s^{-1} in discharge and charge processes.

To monitor the structural evolution of S/N-C nanofibers during discharge/charge in SIBs, *in situ* Raman spectroscopy was conducted at 1.0 mV s^{-1}, as shown in **Figure 4.10**. The intensities and positions of the D and G-band (~ 1330 and 1600 cm^{-1}) of

carbonaceous materials are affected by the intercalation or adsorption of Na^+ ions during the cycling process.[326] During the discharge process (**Figure 4.10 a**), the intensity of the D-band decreases, which can be ascribed to the introduction of Na^+, which occupies the defect or edge sites. Moreover, the G-band of the S/N-C sample exhibits an obvious red-shift during the discharge process, which is related to the charge transfer effects caused by the adsorption and intercalation of Na^+ ions and the formation of the SEI layer.[327] When then charged to 3.0 V, the intensity of the D-band could recover its intensity before discharge (**Figure 4.10 b**), indicating the reversible desorption of Na^+ from the defect or edge sites. The G-band could undergo a blue-shift, in contrast to the discharge process. These phenomena both demonstrate that the S/N-C sample features a highly reversible charging/discharging process.

4.4 Conclusion

S and N co-doping in carbon nanofibers introduces more active sites for Na^+ storage and increases the interaction between mesoporous carbon and liquid electrolytes. The presence of S also reduces the strong adsorption energy of Na^+ on the carbon surface, which frees up the Na^+ transport across the carbon/electrolyte interface and increases the cycling performance of S/N-C at high current densities. A Na-ion battery with the porous S/N-C nanofibers showed a high initial discharge and charge capacity of 766.8 and 563.4 mA h g^{-1} at 0.1 A g^{-1} with an improved initial Coulombic efficiency of 73.5%, excellent rate capability (333.4 mA h g^{-1} at 5 A g^{-1}), and superior cycling stability (335.8 mA h g^{-1} at 5 A g^{-1} after 800 cycles). The sodium storage mechanism

analysis indicates that the capacitive contribution dominates the whole capacity because of the mesoporous defect–rich structure of the S/N-C electrode.

CHAPTER 5 LOTUS RHIZOME-LIKE S/N-C FOR STRENGTHENING WS_2 WITH SUPERIOR SODIUM STORAGE

5.1 Introduction

Sodium-ion batteries (SIBs) have promisingly replaced for lithium-ion batteries (LIBs) as power sources for smart grids and low-speed electric vehicles, owing to the low cost and abundance of sodium (Na) resources and their high safety due to the high potential of Na (-2.714 V).[328-330] Nevertheless, the radius of Na ions (1.06 Å) is larger than that of lithium (Li) ions (0.76 Å), leading to sluggish diffusion kinetics for Na^+, making it difficult to find appropriate anode materials with larger interlayer spacing and good reversible Na^+ storage for SIBs. [331, 332] So far, a large number of anode materials have been explored for SIBs, including carbonaceous materials,[333-335] alloying reaction metals and alloys (Sn, Sb, Bi, and their alloys),[336-339] metal oxides[340-342] and chalcognides,[343-345] and others. Among them, carbonaceous materials usually exhibit excellent cycling performance, although they possess relatively low capacity.[346-348] The alloyed metal materials always show high theoretical capacity, but the large volume change problem during the alloying/de-alloying process leads to poor rate capability.[349] In addition, the large volume expansion for Na^+ storage due to the formation of Na_2O and Na_2S (or Na_2Se)[350-353] will shorten the cycling life of these anode compounds. Therefore, it is essential to find effective strategies to obtain

excellent anode materials with well-balanced performance in terms of high capacity, excellent rate capability, and long-term cycling stability.

Two-dimensional (2D) transition-metal dichalcogenides (TMDCs) have obtained great interest as anode materials for SIBs due to their unique layered structure.[354, 355] As one example of typical TMDCs, tungsten disulfide (WS_2) exhibits larger layer spacing with weak Van Der Waals interaction and higher electronic conductivity than the traditional MoS_2.[356] Benefiting from its structural characteristics and conductive nature, the WS_2 anode material exhibits high rate capability for SIBs,[357-360] although the long-term cycling performance of WS_2 as anode for SIBs is not satisfactory for practical application.[361] Actually, this is a common issue for metal sulfides as electrode materials for LIBs and SIBs because the cycling life is strongly influenced by certain factors,[361-363] *i.e.*, the large volume changes during electrochemical processes, the Li^+/Na^+ diffusion kinetics, and the obvious dissolution of the polysulfide intermediates. Thus, it is desirable to look for effective means to solve the problem of WS_2 as anode material to obtain stable long-term cycling and high rate capability.

Carbon scaffolds have been employed to effectively host metal sulfides as electrode materials,[364-366] *i.e.*, one-dimensional (1D) carbon nanofibers, graphene, or mesoporous carbon. Among them, the carbon nanofibers have been demonstrated to be a good substrate for hosting metal sulfides as anode materials.[367-371] First, their highly conductive nature, along with the large longitudinal aspect ratio of carbon nanofibers could facilitate electron transfer among the metal sulfide particles and

improve the Na^+ diffusion kinetics at the same time, resulting in high rate capability for electrodes. Second, carbon nanofibers can alleviate the mechanical stress during the electrochemical process and prevent the pulverization of the embedded metal sulfide materials, which can yield electrodes with stable long cycling performance. Last but not least, heteroatom doping is favourable to improve the capacity of carbon nanofibers, which can be easily prepared by electrospinning. Based on the above analysis, it would be a promising method to achieve enhanced sodium storage performance with large capacity, excellent rate capability, and cycling stability by embedding WS_2 nanosheets in heteroatom doped carbon nanofibers.

Herein, we have designed a novel method to prepare lotus rhizome-like WS_2@S/N-co-doped carbon nanofibers (denoted as WS_2@S/N-C) to realize the above targets. The synthetic procedures are shown in **Figure 5.1**. The WO_3 nanosheets are first synthesized via the hydrothermal method, and then embedded into polymer nanofibers via electrospinning. Subsequently, WS_2@S/N-C nanofibers are obtained through carbonizing the WO_3/poly-acrylonitrile/polymethyl methacrylate (PAN/PMMA) nanofibers with sulfur. The designed WS_2@S/N-C nano-architecture offers various advantages: i) the embedding of WS_2 nanosheets in carbon nanofibers could enhance the overall electrode conductivity, offering high reversible capacity; ii) the formation of lotus rhizome-like carbon nanofibers could facilitate electron transfer and prevent the pulverization of the electrode structure, resulting in a stable long-term cycling life span. The WS_2@S/N-C electrode presents a high rate capacity of 108 mA h g^{-1} at 30 A g^{-1}, a good reversible capacity of 321 mA h g^{-1} at 100 mA g^{-1} (*vs.* 25 mA

h g^{-1} for WS_2) after 100 cycles, and a stable capacity of 175 mA h g^{-1} at 5 A g^{-1} after 1000 cycles. In addition, both the kinetics calculations and the theoretical analysis demonstrate that S/N-C nanofibers could improve the rate capability of WS_2 materials.

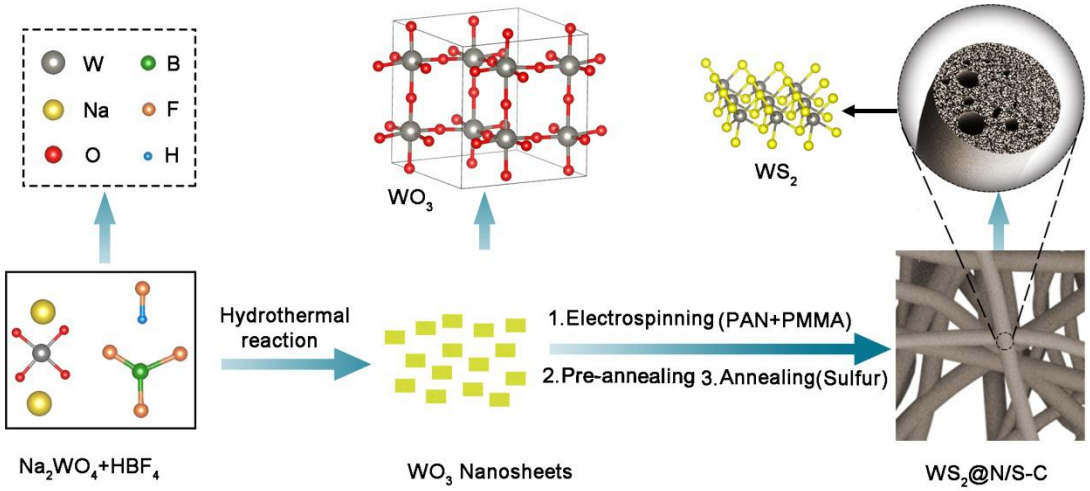

Figure 5.1 Schematic illustration of the synthetic route to prepare the porous WS_2@S/N-C nanofibers.

5.2 Experimental Section

Synthesis of WO_3 nanosheets: WO_3 nanosheets were synthesized according to the literature with minor modification.[372] Typically, 1.0 g $Na_2WO_4 \cdot 2H_2O$ was first dissolved in 40 mL water, and then 3.0 mL HBF_4 solution (40% by weight) was dropped into the solution. After that, the mixture was maintained under hydrothermal conditions at 100 °C for 10 h. Finally, the resulting product was collected with distilled water and absolute ethanol to obtain the pure WO_3.

Synthesis of WS_2@S/N-C nanofibers: The WS_2@S/N-C nanofibers were produced through the electrospinning method. In a typical synthesis, 0.24 g PMMA and 0.36 g

PAN were firstly dissolved in 5 mL dimethylformamide (DMF) solution under vigorous stirring at 60 °C for 4 h. Then, 0.3g as-synthesized WO_3 were added in the above solution to obtain a stable suspension for the electrospinning with an applied voltage of 13 kV and a feeding rate of 0.3 mL h^{-1}. Moreover, the distance between the stainless steel needle and the collector was set to be 15 cm. To stabilize the structure, the obtained fiber-like membrane was annealed at 230 °C for 2 h in air. The pretreated nanofibers were further carbonized with sulfur powder (mass ratio of 1:4) in flowing Ar. The nanofibers and sulfur were carbonized at 600 °C for 2 h to transform the WO_3 into WS_2 in carbon nanofibers.

For comparison, 0.3 g WO_3 and 1.2 g sulfur power were further carbonized by the same method to convert the WO_3 into WS_2. In addition, S/N-C nanofibers were synthesized according to the similar procedure without WO_3 precursor.

Material characterizations: The morphologies and structure of the as-synthesized samples were measured by field emission scanning electron microscopy (FE-SEM, Helios Nanolab G3UC) equipped with Energy Dispersive Spectrometer (EDS) and field emission transmission electron microscopy (TEM, FEI Titan G2 60–300). The crystal structure and phase composition were confirmed by X-ray powder diffraction (XRD, Rigaku D/Max-2500). Raman spectroscopy (DXR microscope, Thermo Fischer DXR) was carried out with 532 nm laser as excitation resource. Fourier transform infrared spectra were also collected (FT-IR, Nicolet-460). Thermogravimetric analysis (TGA, SDTQ600) was used to confirm the content of WS_2 in the composite. The chemical states of the samples were investigated by X-ray

photoelectron spectroscopy (XPS, Escalab 250Xi). Nitrogen adsorption and desorption isotherms (BET, Tristar 3020) was used to determine the Brunauer-Emmett-Teller (BET) surface area.

Electrochemical measurements: All the electrochemical tests were carried out using 2025 coin-type half cells. The working electrodes were prepared by mixing the active material powder, acetylene black, and carboxymethyl cellulose (CMC) in a weight ratio of 8:1:1 to form a slurry, which was then spread onto Cu foil, subsequently dried in a vacuum oven at 60 °C for 12 h, and then cut into 12 mm-diameter discs. The mass loading amount of the active material was about 0.7-0.8 mg cm^{-2}. Half cells were made up using Na metal as the counter electrode and glass fiber as the separator, which were assembled in an Ar-filled glove box. The electrolyte was 1 M $NaClO_4$ dissolved in a mixture of ethylene carbonate (EC) and diethyl carbonate (DEC) (1: 1 by volume ratio) with 5 wt% fluoroethylene carbonate (FEC) as addtive. The galvanostatic charge/discharge tests were performed on a battery test system (Land CT2001A), and the cyclic voltammetry (CV) was carried out on an electrochemical workstation (CHI660E), both in the voltage range of 0.01-3 V. All the electrochemical tests were conducted at room temperature.

Calculation details: To investigate the reasons for the enhanced sodium storage performance, density functional theory (DFT) calculations were used to investigate the adsorption behavior of Na on the pristine WS_2 and WS_2 with N/S-doped graphene (WS_2/NS@graphene) by using the Vienna Ab-initio Simulation Package (VASP).[373, 374] The exchange-correlation functional were determined by the generalized gradient

approximation (GGA) with the Perdew-Burke-Ernzerhof (PBE) form.[375] The frozen-core projector-augmented wave (PAW) method[376, 377] was used for interactions between the core electrons and the valence electrons. The convergence criterion was set at 10^{-5} eV, and atomic positions were allowed to move until the forces acting on each atom were less than 0.02 eV/Å for the total energy calculations, with a high energy cut-off of 520 eV. The Brillouin zone was integrated with $3 \times 3 \times 1$ Monkhorst-Pack k-point grids for geometry optimization. Moreover, the vacuum space of 20 Å was used in the z-direction could avoid any interaction between the adjacent repeating layers.

The adsorption energy (E_{ad}) of at Na atom sites in WS_2 and WS_2 with N, S doped graphene (WS_2/NSG) was calculated as follows:

$$E_{ad} = E_{\mathrm{WS2-Na,WS2/NSG-Na}} - E_{\mathrm{WS2,WS2/NSG}} - E_{Na}$$

Where $E_{\mathrm{WS2-Na,WS2/NSG-Na}}$ is the total energy for one Na atom in WS_2 and WS_2/NSG; $E_{\mathrm{WS2,WS2/NSG}}$ is the total energy for WS_2 and WS_2/NSG without the adsorption of Na; E_{Na} is for one Na atom in the same slab.

Herein, both the interaction between WS_2 or WS_2/NSG and Na ion indicates massive charge transfer, which can be visualized by three-dimensional charge difference mapping, and the definition is as follow:

$$\Delta\rho = \rho_{\mathrm{WS2-Na,WS2/NSG-Na}} - \rho_{\mathrm{WS2,WS2/NSG}} - \rho_{Na}$$

Where $\rho_{WS2-Na,WS2/NSG-Na}$ is the charge density of the composite or WS_2 with one Na atom adsorbed; $\rho_{WS2,WS2/NSG}$ is the charge density of the composite or WS_2 without Na; ρ_{Na} is the charge density of one Na atom in the same slab, respectively.

5.3 Results and Discussion

5.3.1 Structure and morphology

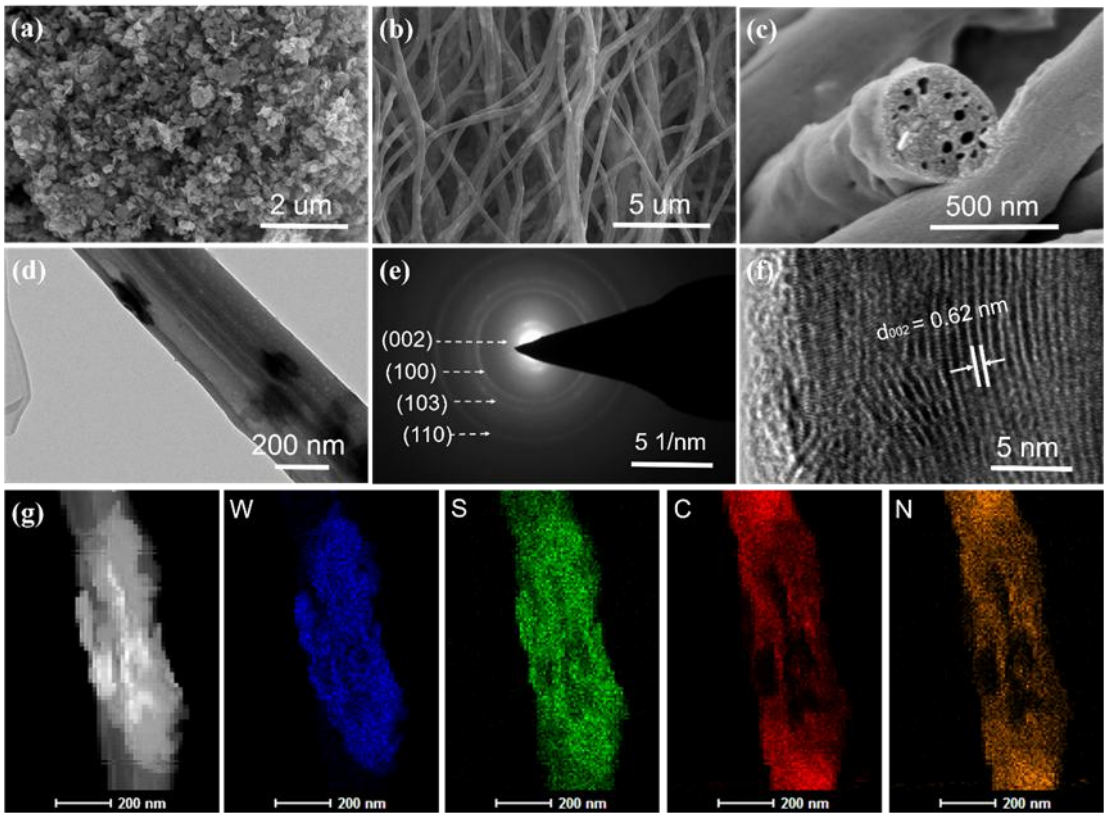

Figure 5.2 (a) Low-resolution SEM image of WO_3 nanosheets; (b) low-resolution and (c) high-resolution SEM images, (d) low-resolution TEM image, (e) electron diffraction pattern, (f) high-resolution TEM image, and (g) element mappings of WS_2@ S/N-C.

The structure and morphology of the samples were investigated by SEM and TEM. The SEM image in **Figure 5.2 a** exhibits the as-synthesized WO_3 nanosheets with a size about 40 nm, which could be electrospun into PAN/PMMA. WO_3 nanosheets

could further changed into WS_2@S/N-C nanofibers through a carbonization and sulfidation process. In **Figure 5.2 b**, WS_2@S/N-C nanofibers exhibit a length of several tens micrometers and a diameter of 400 nm. The WS_2@S/N-C nanofibers (**Figure 5.2 c)** show a porous lotus-rhizomes-like structure due to the decomposition of PMMA during the carbonization process. The embedding could prevent the aggregation of WS_2 nanosheets during the sulfidation process. In **Figure 5.2 d**, there are some dark parts in the single nanofiber owing to the presence of WS_2 nanosheets embedded in the carbon nanofibers. The selected area electron diffraction (SAED) pattern of WS_2 nanosheets in the WS_2@S/N-C nanofibers is shown in **Figure 5.2 e**. The diffraction rings from inside to outside are attributed to the (002), (100), (103), and (110) planes, respectively. The high resolution (HR)-TEM image of the vertically grown WS_2 nanosheets in **Figure 5.2 f** displays a 0.62 nm interlayer spacing, which can be attributed to the (002) planes of hexagonal WS_2, consistent with the XRD results for WS_2@S/N-C. This value is in accord with the theoretical interlayer spacing along the *c*-axis direction. The energy dispersive X-ray (EDX) element mapping images indicate that the W, S, C, and N elements are not uniformly distributed throughout the WS_2@S/N-C nanofiber (**Figure 5.2 g**), which is due to the distribution of the isolated nanosheets. Moreover, pure WS_2, was synthesized by the direct sulfidation of WO_3, which shows similar morphology with that of WO_3 (**Figure 5.3 a** and **b**) and has clear crystal fringles (Figure **5.3 c** and **d**).

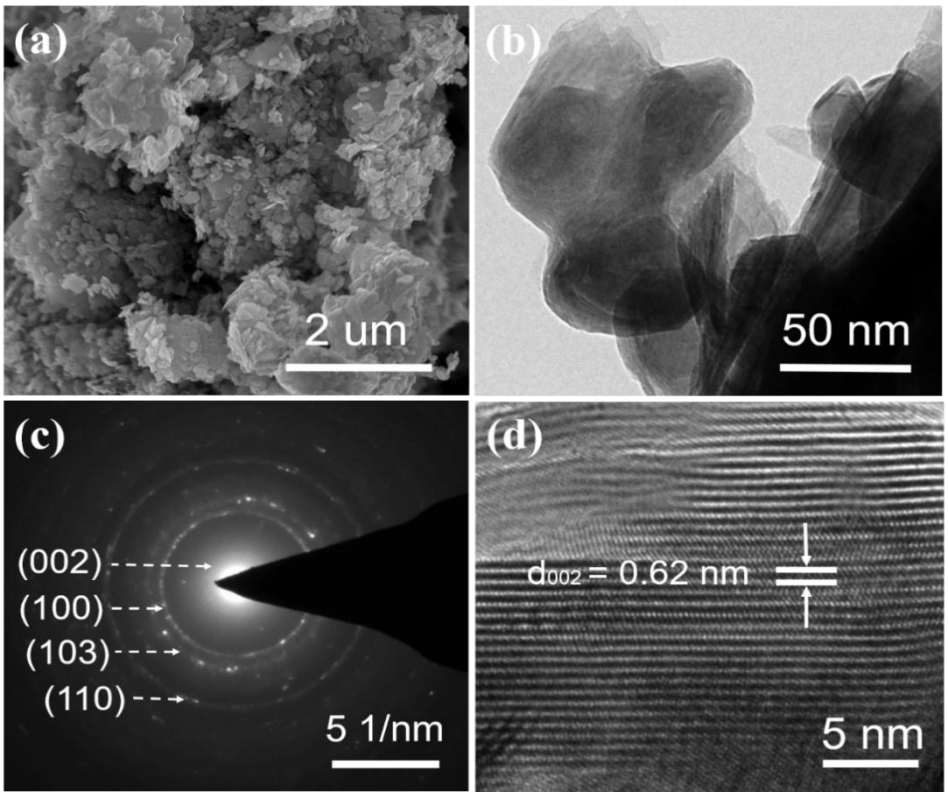

Figure 5.3 (a) The SEM and (b) TEM images of synthesized WS_2; (c) SAED images and (d) high-resolution TEM images of WS_2.

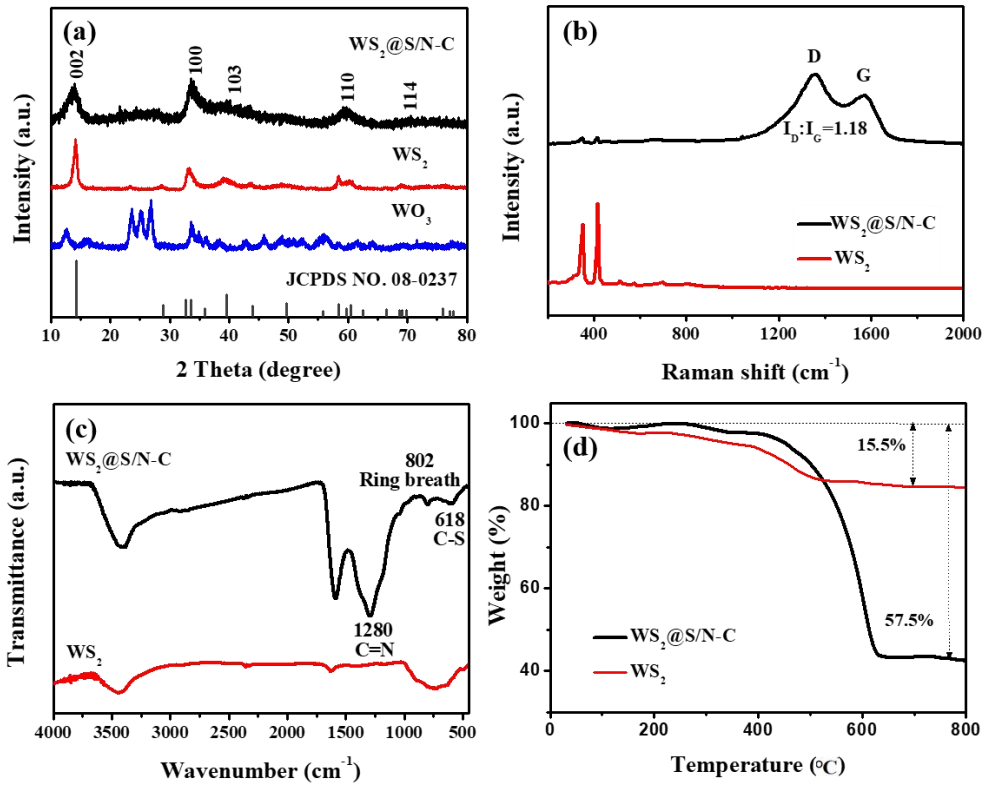

Figure 5.4 (a) XRD patterns of WO_3, WS_2, and WS_2@S/N-C; (b) Raman spectra, (c) FT-IR spectra, and (d) TGA curves of WS_2 and WS_2@S/N-C.

The components and crystalline phases of the materials were characterized by the XRD. **Figure 5.4 a** compares the XRD patterns of the WO_3, WS_2, and WS_2@S/N-C samples. The diffraction peaks of the pristine WO_3 can be well assigned to a monoclinic phase. The phase transition from monoclinic WO_3 to hexagonal WS_2 can be achieved by carbonization of WO_3 with sulfur. Strong peaks located at 14.3, 32.76, 39.5, 58.4, and 66.5° can be indexed to the (002), (100), (103), (110), and (114) planes of the hexagonal structure of WS_2 (JCPDS no. 08-0237), respectively. Moreover, the obviously weaker intensity of WS_2@S/N-C compared to the WS_2 implies that the sample was successfully wrapped by carbon nanofibers, which may accomodate the volume changes and prevent the pulverization of the electrode structure over a long-term cycling lifespan. Further structural information of the

WS_2@S/N-C and WS_2 was acquired by Raman spectroscopy and FTIR analysis. The peaks of the WS_2 and WS_2@S/N-C samples in the Raman spectra (**Figure 5.4 b**) located at 351 and 416 cm^{-1} can be ascribed to the Raman active E_{2g} and A_{1g} vibration modes for WS_2.[360] Compared to the WS_2, there is weaker intensity for WS_2@S/N-C due to the wrapping with carbon nanofibers. The peaks around 1350 and 1560 cm^{-1} are attributed to the disorder-induced D band and the graphitic G band for the WS_2@S/N-C sample, respectively. In addition, the intensity ratio of the D-band to G-band (1.3, I_D:I_G) implies that more defects exist in WS_2@S/N-C, which is associated with the N, S-co-doping.[378] In the FTIR spectrum of WS_2@S/N-C (**Figure 5.4 c**), three new bands at 618, 802, and 1280 cm^{-1} can be respectively attributed to C-S stretching, ring breathing (main-chain hexahydric-ring), and C=N symmetric stretching modes.[379, 380] The observation of C-S bonds confirmed that the S was bonded with C, which can afford a superior reversible capacity.[381] The content of WS_2 in the WS_2@S/N-C sample was confirmed by TGA analysis (**Figure 5.4 d**). A weight loss of 14.5 % was observed for pure WS_2 due to the oxidation of WS_2 into WO_3. The weight loss (57.5 %) for the WS_2@S/N-C sample is associated with the combination of oxidation of WS_2 and combustion of S/N-C. The content of WS_2 in the WS_2@S/N-C sample was calculated to be 45.4 wt%. Moreover, based on the nitrogen adsorption and desorption isotherms, the Brunauer-Emmett-Teller (BET) surface areas of WS_2 and WS_2@S/N-C samples were found to be 17.74 and 23.4 m^2 g^{-1}, as shown in **Figure 5.5**.

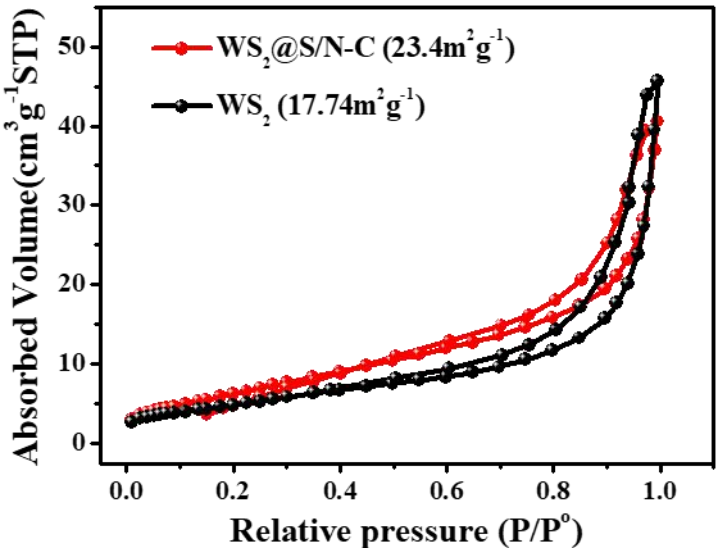

Figure 5.5 Nitrogen adsorption and desorption isotherms of WS_2@S/N-C nanofibers and pure WS_2.

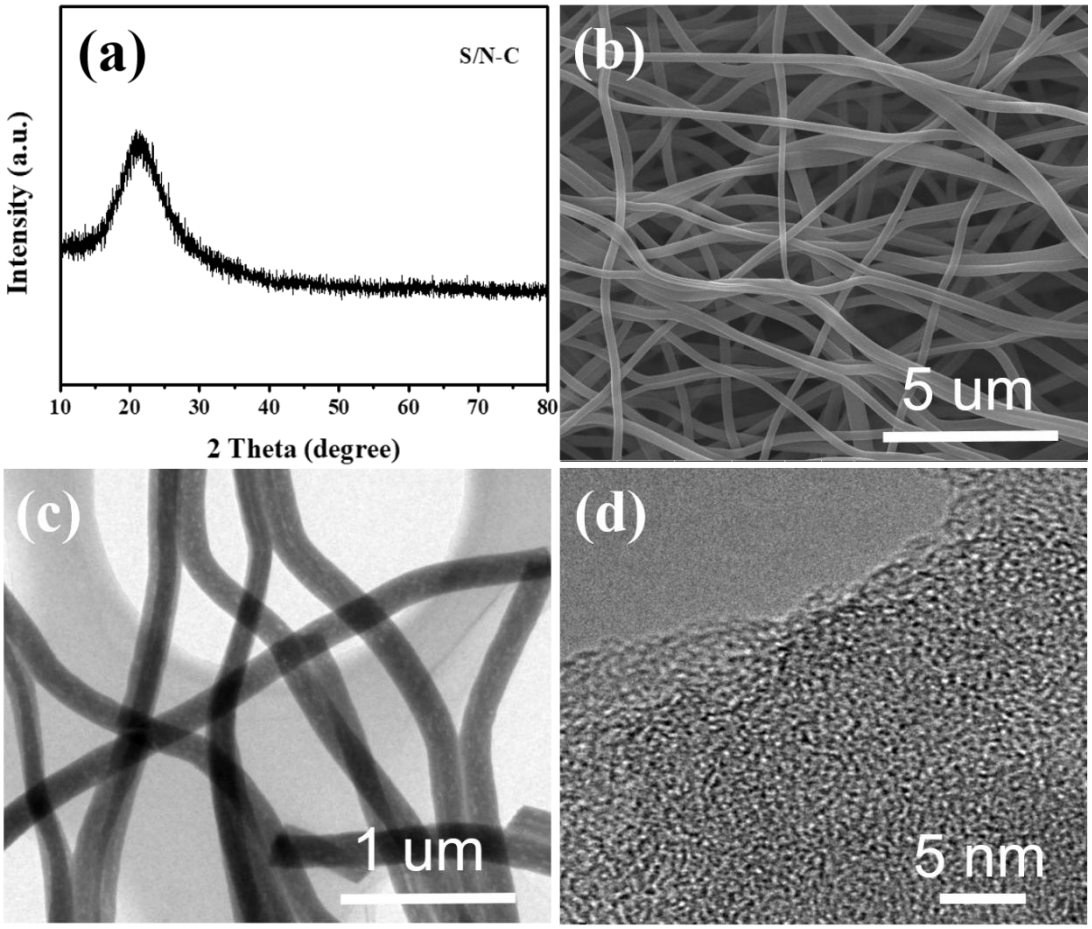

Figure 5.6 Characterizations of S/N-C nanofibers: (a) XRD pattern; (b) SEM image; (c) TEM image and (d) HR-TEM image.

Furthermore, S/N-C nanofibers were also characterized by XRD, SEM, TEM, HR-TEM, as shown in **Figure 5.6**. XRD pattern in **Figure 5.6 a** indicates S/N-C sample is typical carbon material, without other impurities. The SEM and TEM images (**Figure 5.6 b** and **c**) show porous nanofibers structure with a length about several tens of micrometers. The amorphous nature of S/N-C sample is confirmed by HR-TEM image, as shown in **Figure 5.6 d**. In addition, the content of sulfur doping in the carbon of WS_2@S/N-C and S/N-C samples is confirmed to be ~4.8 % and ~6 % by EDS (**Figure 5.7**), respectively.

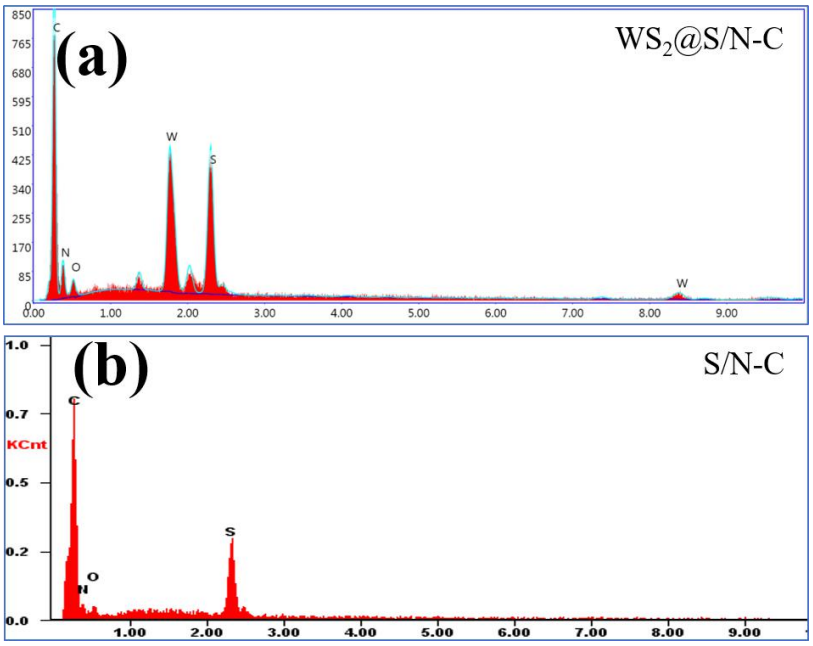

Figure 5.7 EDS spectra of (a) WS_2@S/N-C nanofibers and (b) S/N-C nanofibers.

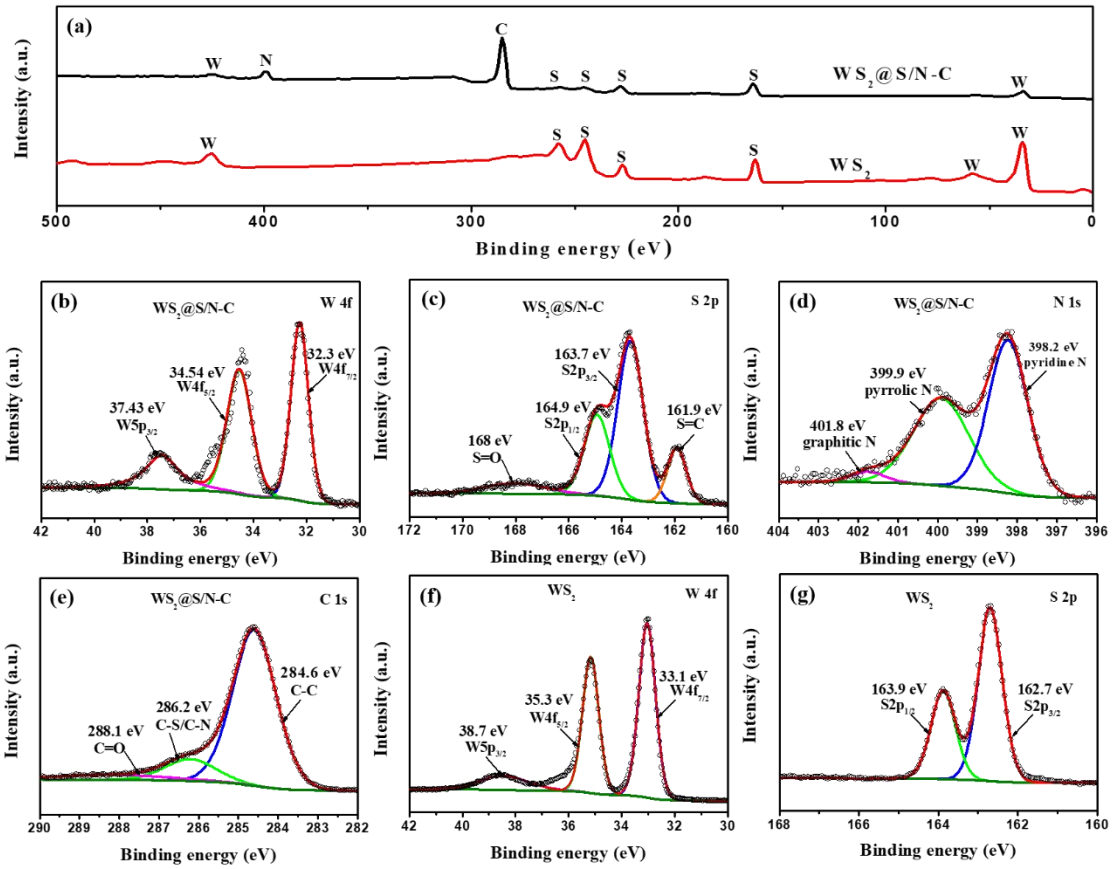

Figure 5.8 (a) XPS full survey spectra of WS_2@S/N-C nanofibers and pure WS_2; (b-e) High-resolution XPS spectra of WS_2@S/N-C: (a) W; (b) S; (c) N; (d) C; (f and g) High-resolution XPS spectra of W and S elements for pure WS_2.

The chemical status of the WS_2@S/N-C and WS_2 samples was characterized by XPS (**Figure 5.8 a)**. Compared to the spectrum of pure WS_2, the spectrum of WS_2@S/N-C reveals extra distinctive C and N peaks, which demonstrate successful doping, which is consistent with its FTIR spectrum. For WS_2@S/N-C, there are three strong peaks from W centered at 32.3, 34.54, and 37.43 eV, as shown in **Figure 5.8 b**, which exhibit a shift to lower energy than that for pure WS_2 (**Figure 5.8 f**). This might be associated with the interaction between WS_2 and C, N. There are two major peaks from S centered at 162.7 and 163.9 eV in pure WS_2 (**Figure 5.8 g**), slightly shifted to lower energy than the S peaks (163.7 and 164.9 eV) of WS_2@S/N-C (**Figure 5.8 c**).

Moreover, two shoulder peaks at 161.9 and 168.0 eV (**Figure 5.8 c)** are related to the S=C and S-O bonds in carbon nanofibers, indicating that S was successfully incorporated into the carbon matrix. Furthermore, there are three peaks located at 398.2, 399.9, and 401.8 eV in the N 1s spectrum of WS_2@S/N-C (**Figure 5.8 d**), indicating the existence of pyridinic, pyrrolic, and graphitic nitrogen in WS_2@S/N-C, respectively.[382] The pyrrolic and pyridinic nitrogen can give rise to surface defects in carbon structures that can offer channels to facilitate Na^+ diffusion.[332] In **Figure 5.8 e**, the C 1s spectrum can be fitted into three peaks for carbon atoms, including for C-C bonds (284.6 eV), C-S/C-N bonds (286.2 eV), and C=O bonds (288.1 eV). In consequence, it is clear that the nitrogen and sulfur dual-doping allows the Na^+ ions and electrons to achieve high transfer rates for good performance.[383]

5.3.2 Electrochemical performance

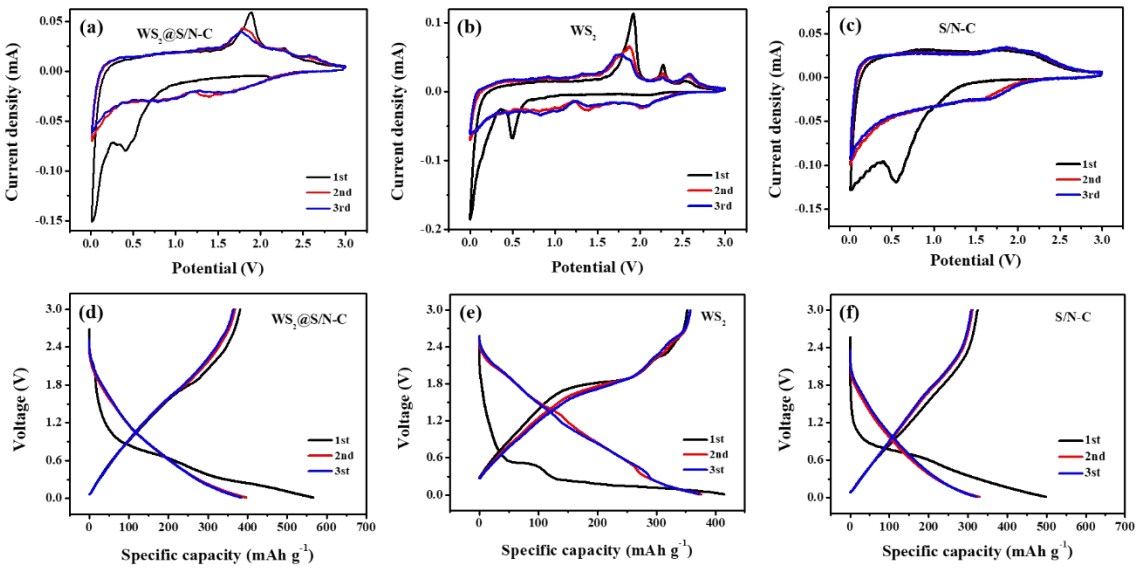

Figure 5.9 CV curves of (a) WS_2@S/N-C, (b) WS_2 and (c) S/N-C electrodes in the voltage range of 0.01-3 V at a scan rate of 0.1 mV s^{-1}; Charge-discharge profiles of (d) WS_2@S/N-C, (e) pure WS_2 and (f) S/N-C electrodes at a current density of 0.1 A g^{-1}.

The electrochemical properties of the WS_2@S/N-C, WS_2 and S/N-C electrodes were characterized by CV and galvanostatic charge-discharge cycling. **Figure 5.9 a-c** display the CV profiles of the WS_2@S/N-C nanofibers, pure WS_2 and S/N-C nanofibers for the initial 3 cycles at a scan rate of 0.1 mV s^{-1}, respectively. For the WS_2@S/N-C electrode, the reduction peak centered at 0.5 V in the first cycle is attributed to the conversion reaction (Na_xWS_2 + (4-x) Na^+ + (4-x) e^- → W + 2 Na_2S) and the formation of an irreversible solid electrolyte interphase (SEI) film. In the following cycles, the reduction peak at ~ 0.5 V disappears while new reduction peaks appear in the potential range from 1.2 to 1.5 V, indicating the presence of reversible conversion mechanism (4 Na^+ + WS_2 + 4 e^- → W + 2 Na_2S). In the anodic scans, three peaks located at 1.8, 2.2, and 2.5 V are corresponded to the oxidation of W to WS_2 during the desodiation process.[360] Compared with the WS_2@S/N-C electrode, similar reduction and oxidation peaks were also observed for pure WS_2. For the S/N-C electrode, a reduction peak centered at ~ 0.5 V in the first cycle is associated with the formation of an irreversible solid electrolyte interphase (SEI) film. The reduction and oxidation peaks of the WS_2@S/N-C and S/N-C electrodes show a much more stable profile and tend to overlap each other in the following two cycles, indicating faster Na^+ ion insertion/extraction kinetics and higher reversibility of the electrode reactions for WS_2@S/N-C and S/N-C electrodes. This confirmed the S/N-C nanofibers could stabilize the WS_2 during the electrochemical process. The charge/discharge curves of the WS_2@S/N-C nanofibers, pure WS_2 and S/N-C nanofibers in **Figure 5.9 d-f** were collected at 0.1 Ag^{-1}. The WS_2@S/N-C nanofibers

delivered a discharge and charge capacity of 566 and 381 mA h g^{-1}, while pure WS_2 and S/N-C nanofibers exhibited the capacity of (416 and 352 mA h g^{-1}) and (465.8 and 356.9 mA h g^{-1}), respectively. Moreover, the coincidence of subsequent discharge/charge curves for pure WS_2@S/N-C indicates a reversible and stable electrochemical performance.

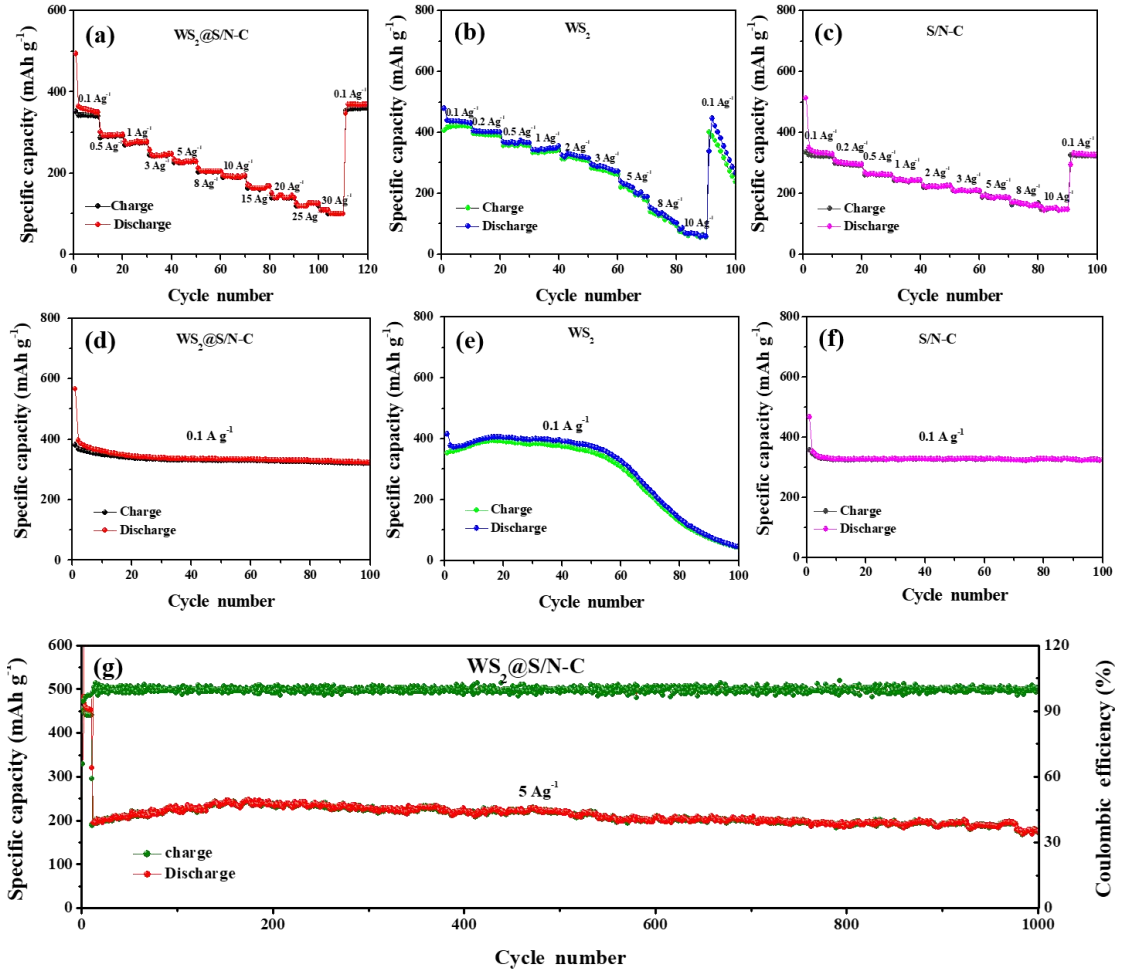

Figure 5.10 Rate capability of the (a) WS_2@S/N-C, (b) WS_2 and (c) S/N-C electrodes at various current densities; Cycling performance of the (d) WS_2@S/N-C, (e) WS_2 and (f) S/N-C electrodes at a current density of 0.1 A g^{-1}; (g) Long-term cycling performance and Coulombic efficiency of WS_2@S/N-C electrode at a current density of 5 A g^{-1}.

Figure 5.10 a shows the capacity of the WS_2@S/N-C electrode at various current densities from 0.1 to 30 A g^{-1}. The electrode delivers a reversible capacity of 371, 291,

275, 246, 230, 204, 192, 167, 145, and 125 mA h g^{-1} at the current density of 0.1, 0.5, 1, 3, 5, 8, 10, 15, 20, and 25 A g^{-1}, respectively. Even at a very high current density of 30 A g^{-1}, it still delivers a capacity of 108 mA h g^{-1} and when the current density returns to 0.1 A g^{-1}, it keeps a reversible capacity of 360 mA h g^{-1}. The pure WS_2 electrode and S/N-C electrodes (**Figure 5.10 b** and **c**), however, exhibit much poorer rate performance. The reversible capacity for the pure WS_2 electrode rapidly declines to 237 mA h g^{-1} when the current density returns to 0.1 A g^{-1}. The S/N-C electrode could keep a reversible capacity of 322.2 mA h g^{-1}, which is obviously lower than that of WS_2@S/N-C electrode. The excellent rate performance of WS_2@S/N-C can be attributed to its structure. The lotus rhizome-like carbon nanofibers could offer short paths to facilitate electron transfer, prevent pulverization of the electrode structure, and offer convenient Na^+ transport. Moreover, the discharge capacity of WS_2@S/N-C reached 319 mAh g^{-1} at 0.1 A g^{-1} after 100 cycles (**Figure 5.10 d**), showing good cycling stability. In comparison, the pure WS_2 only possessed 43 mA h g^{-1} after 100 cycles (**Figure 5.10 e**). The S/N-C can sustain 315 mA h g^{-1} after 100 cycles with good stability (**Figure 5.10 f**). This demonstrates that S/N-C nanofibers facilitated the stability of WS_2. Moreover, the WS_2@S/N-C even exhibited a capacity of 174 mA h·g^{-1} at a current of 5 A g^{-1} over 1000 cycles, with a capacity retention of 89 %, demonstrating excellent ultra-long cycling stability (**Figure 5.10 g**).

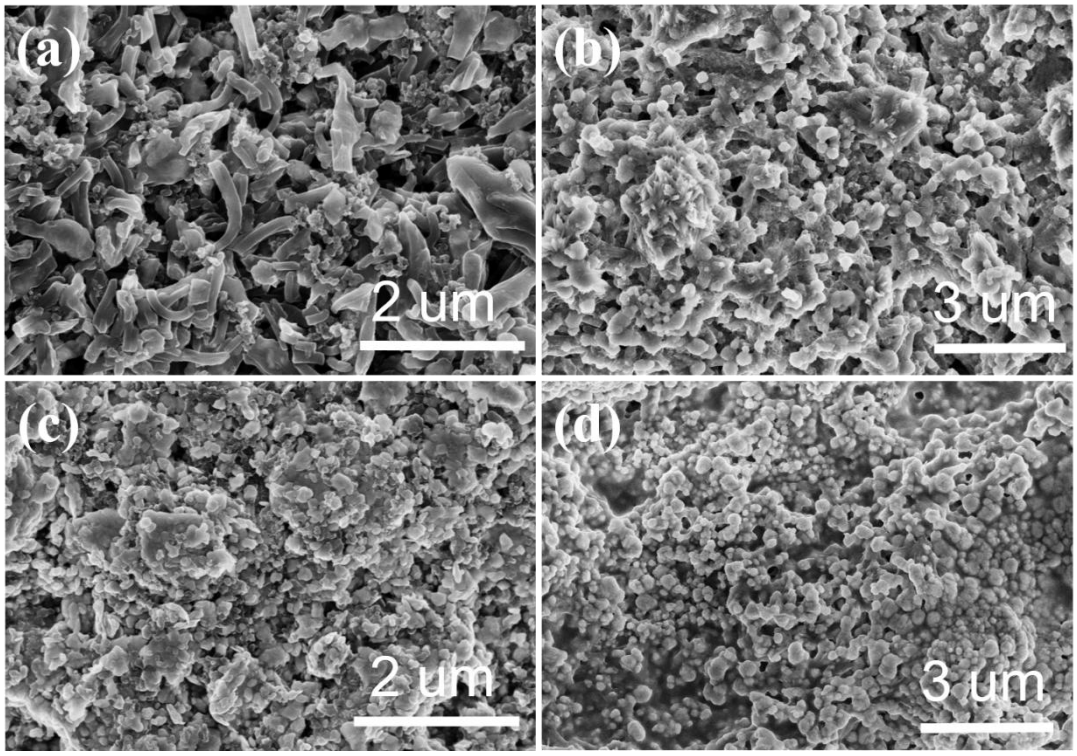

Figure 5.11 Low-resolution SEM images of WS_2@S/N-C electrode: (a) fresh electrode and (b) cycled electrode after 100 cycles; low-resolution SEM images of WS_2 electrode: (c) fresh electrode and (d) cycled electrode after 100 cycles.

To further explain the difference in cycling stability between the two kinds of electrodes, the morphologies of fresh and cycled WS_2@S/N-C and pure WS_2 electrodes were characterized by SEM, as shown in **Figure 5.11**. Obviously, compared with fresh WS_2@S/N-C electrode, the surface of cycled electrode after 100 cycles became rough due to the formation of solid electrolyte interphase (SEI). Although some small particles emerged, the rod-like morphology was partially maintained. On the contrary, the morphology of the cycled WS_2 electrode changed significantly and no nanosheets could be observed. Based on above results, it was revealed that the different structural stabilities led to the different cycling stabilities. Moreover, electrochemical impedance spectroscopy (EIS) was also carried out to study the reaction kinetics of WS_2@S/N-C and pure WS_2 electrode after 1st cycle at

0.1 A g^{-1}. In **Figure 5.12**, the WS_2@S/N-C electrode exhibits a much lower charge transfer resistance (R_{ct}, 298 Ω) than the pure WS_2 electrode (2129 Ω), based on the equivalent circuit simulation, which implies faster charge transfer at the electrode/electrolyte interface.

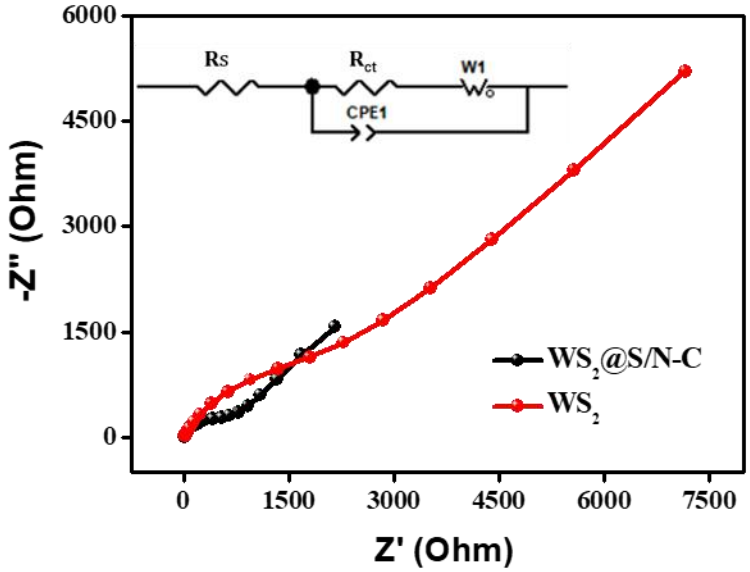

Figure 5.12 EIS spectra of WS_2@S/N-C and pure WS_2 after 1st cycle at 0.1 A g^{-1}. The inset is the equivalent circuit.

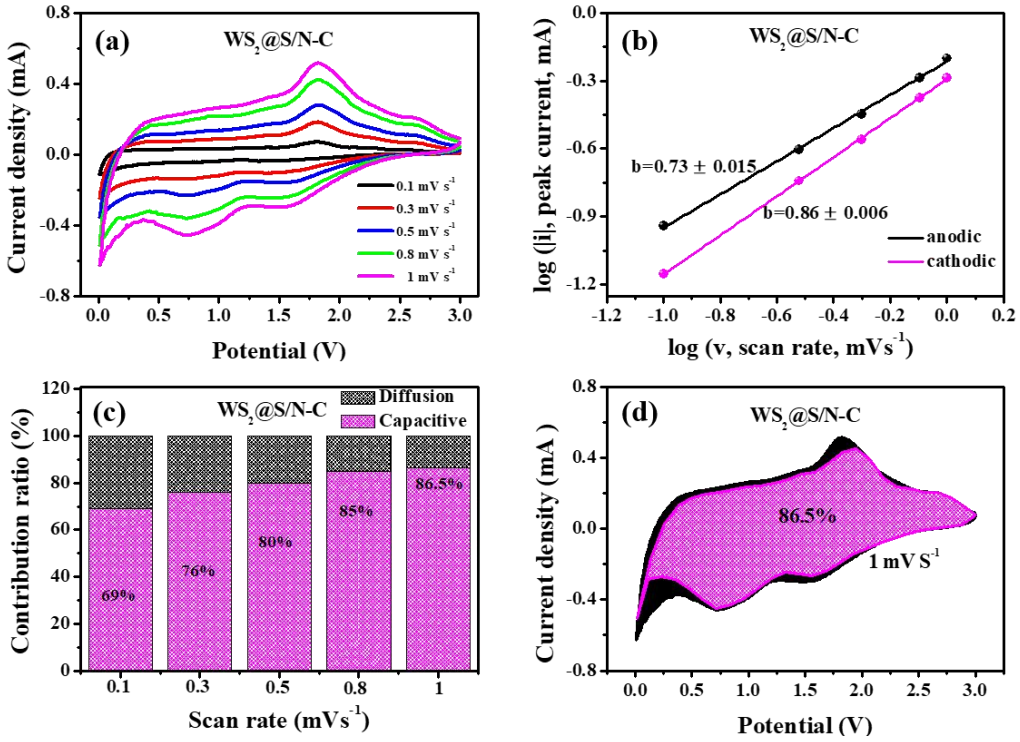

Figure 5.13 (a) CV curves of WS_2@S/N-C electrodes at different scan rates; (b) log i *vs.* log v plots of WS_2@S/N-C electrodes; (c) Ratio of diffusion and capacitive contributions to the capacity at various scan rates for WS_2@S/N-C electrodes; (d) Capacitive charge storage contribution (pink region) for WS_2@S/N-C electrode at 1.0 mV s^{-1}.

To further evaluate the electrochemical performance of WS_2@S/N-C anode, CV measurements at a series of scan rates from 0.1 mV s^{-1} to 1 mV s^{-1} were carried out. As shown in **Figure 5.13 a**, with the scan rates increasing, all the CV curves retained similar shapes with only a small deviation of the redox peaks, suggesting high rate capability and small potential polarization. As it is well known, the electrochemical capacity is contributed by two mechanisms, the faradaic charge transfer process (ion diffusion) and the non-faradaic contribution (pseudocapacitance).[384] The relationship between peak current and scan rate can indicate the contribution of each part, as follows:[385]

$$i = av^b \quad (1)$$

and

$$log\ i = b\ log\ v + log\ a\ (2)$$

where i represents the peak current, v is the scan rate, and a and b are adjustment parameters, respectively. The b value reveals the different types of charge storage. The values of 0.5 and 1 represent the faradaic charge transfer process and the non-faradaic contribution, respectively. In **Figure 5.13 b**, the b values of WS_2@S/N-C anode were calculated to be 0.73 ± 0.015 for the anodic peaks and 0.86 ± 0.006 for the cathodic peaks, suggesting that the sodium storage reaction of WS_2@S/N-C anode was determined by both pseudocapacitive behavior and ion diffusion control. The percent contributions of the two parts at a serious of scan rates can be calculated from the following equation:

$$i = k_1 v + k_2 v^{1/2}\ (3)$$

where $k_1 v$ represents the pseudocapacitive part and $k_2 v^{1/2}$ represents the ion diffusion part. From **Figure 5.13 c**, the pseudocapacitive contribution increased from 69% to 86.5% as the scan rate increased from 0.1 mV s^{-1} to 1 mV s^{-1}. The detailed pseudocapacitive fraction at 1 mV s^{-1} is also illustrated in **Figure 5.13 d**. These results mean that the pseudocapacitive contribution plays the major role in the overall capacity of the WS_2@S/N-C anode.

5.3.3 Theoretical calculations

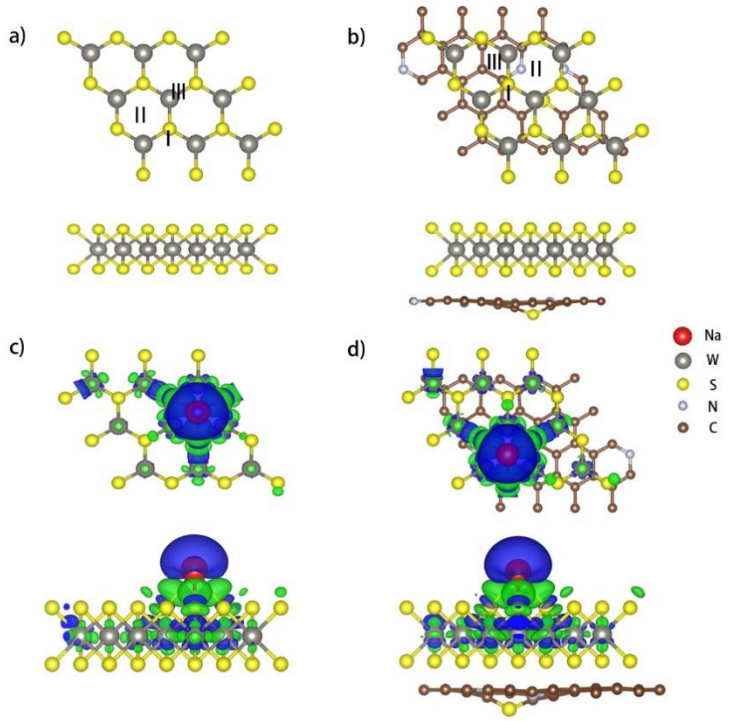

Figure 5.14 Adsorption sites for of I, II and III Na on (a) pure WS_2 and (b) the WS_2 in WS_2@S/N-C; Differences of charge density (charge accumulation: green, charge depletion: blue) with an isosurface level of 0.001 e/Å3 for Na on (c) pure WS_2 and (d) the WS_2 in WS_2@S/N-C in the most stable adsorption configuration.

To obtain theoretical support for the results, we studied the Na^+ adsorption behavior on both pristine WS_2 surface and WS_2@S/N-C surface by DFT calculations. According to the previous theoretical calculations, the S/N co-doped graphene model can be as the S/N co-doped carbon nanofiber to analyse the adsorption behavior for the Li^+, Na^+ and K^+.[332, 386-390] Thus, we designed the heterostructure of WS_2 and S/N co-doped graphene to investigate the synergistic effects for Na adsorption. As shown in **Figure 5.14 a** and **b**, both the pristine WS_2 and WS_2@S/N-C have three adsorption sites of S-top (I), hollow (II) and W-top (III), respectively. And the adsorption energies of Na atom adsorption on pristine WS_2 and WS_2@S/N-C were calculated and

illustrated in **Tables 5.1** and **5.2**. For the S-top site, the adsorption energy of the Na in WS_2@S/N-C was -0.897 eV that was lower than that in pristine WS_2 (-0.494 eV). After the Na adsorption on the hollow site of pristine WS_2 and WS_2@S/N-C, the adsorption energies are of -0.744 eV and -1.168 eV, respectively. Clearly, the W-top site on WS_2@S/N-C has the smaller adsorption energy of -1.208 eV than that of pristine WS_2 (-0.759 eV). The smaller adsorption energies of Na adsorption on WS_2@S/N-C than that of pristine WS_2, indicating that WS_2@S/N-C is helpful for Na storage. Moreover, we calculated the three-dimensional charge density difference to understand the mechanism of charge transfer on W-top site of pristine WS_2 or WS_2@S/N-C with a Na atom. As shown in **Figure 5.14 c**, the charge accumulation is found on the W atoms, and the charge depletion appears on the Na ion at the same time. The results demonstrate that the charge has accumulated much more massively on the WS_2@S/N-C (**Figure 5.14 d**) than on the pristine WS_2 (**Figure 5.14 c**), which can be verified by the Bader charges. According to Bader charge analysis, 0.79 e of the Na atom is transferred onto the WS_2@S/N-C (**Table 5.2**), while only 0.76 e of the Na atom for the pristine WS_2 (**Table 5.1**). This shows that S/N-C could trap more Na atoms due to increasing the adsorption energy of the Na atom.

Table 5.1 The adsorption behaviour of Na on pristine WS_2.

Adsorption sites / WS_2	I(S-top)	II(Hollow)	III (W-top)
E_{ad} (eV)	-0.494	-0.744	-0.759
Q_{Na} (|e|)	0.56	0.74	0.76

Table 5.2 The adsorption behaviour of Na on WS_2@S/N-C**.**

Adsorption sites / WS_2@S/N-C	I(S-top)	II(Hollow)	III (W-top)
E_{ad} (eV)	-0.897	-1.168	-1.208
Q_{Na} (|e|)	0.65	0.79	0.79

5.4 Conclusion

In conclusion, we have successfully realized the incorporation of WS_2 nanosheets into carbon nanofibers via an electrospinning/sulfidation process. Compared to pure WS_2, the WS_2@S/N-C nanofibers exhibit a higher rate capacity of 108 mA h g^{-1} at 30 A g^{-1} and a stable capacity of 174 mA h g^{-1} at 5 A g^{-1} after 1000 cycles. The theoretical studies demonstrate that S/N-C nanofibers effectively facilitate the storage of Na on

WS_2. Moreover, analysis of the sodium storage mechanism has demonstrated that the capacitive contribution plays the dominant role in the whole capacity contribution owing to the S/N-heteroatom doping and the existence of the mesoporous defect-rich structure in the S/N-C matrix.

CHAPTER 6 S/N-DOPED CARBON NANOFIBERS AFFORDING FE_7S_8 PARTICLES WITH SUPERIOR SODIUM STORAGE

6.1 Introduction

In recent years, battery technologies have drawn great attention as power sources for transferring the electric energy derived from sustainable energy to electric grids including: lithium-ion batteries (LIBs),[391, 392] low cost sodium-ion batteries (SIBs),[393-396] aqueous flow batteries,[397, 398] zinc-ion batteries[399, 400] or other aqueous batteries.[401, 402] Among them, SIBs have cost-effective characteristics in comparison with LIBs due to the high abundance in earth and low cost of sodium resources. Moreover, compared with other batteries, SIBs have obvious advantage of high energy density since they have the high-output-voltage electrolytes and high-capacity electrode materials.[403, 404] Therefore, low-cost SIBs are demonstrated to exhibit superior advantages as potential power sources.

In the construction, SIBs have the similarity with LIBs, and share the similar working mechanism with LIBs,[405] which offer SIBs with feasible manufacturing process. For electrode materials of SIBs, the design of cathode materials and anode materials can get some ideas from LIBs.[406] However, the commercial graphite could hardly work well in SIBs with traditional carbonate-based electrolytes because the interlayer distance of the graphite is unsuitable to host sodium in carbonate-based electrolytes.[407-410] Thus, other low-cost anode materials are highly needed so far.

Iron-based compounds, i.e., oxides and chalcogenides, are considered to be cost-effective, high-performance anode materials for SIBs.[411, 412] Iron chalcogenides have higher conductivity than iron oxides due to their structural characteristics, which makes them more suitable to be anode materials for SIBs. Moreover, low cost and rich natural resources of iron and sulfur elements have driven us to explore iron sulfides as potential anode materials.[413, 414] Especially, the rich chemical stoichiometries (e.g., FeS,[415-418] Fe_7S_8,[419-424] Fe_3S_4[425, 426] and FeS_2[427]) and high capacity of iron sulfides offer them interesting electrochemical properties. Nevertheless, iron sulfides usually suffer poor electrochemical performance due to the intrinsic sluggish kinetics and severe volume change during sodiation process. To solve these issues, one of effective methods is to design carbon/iron sulfide composites to improve the electrochemical performance. So far, a variety of carbon materials are used, i.e., graphene, carbon nanotubes, biomass-derived carbon, *etc*.

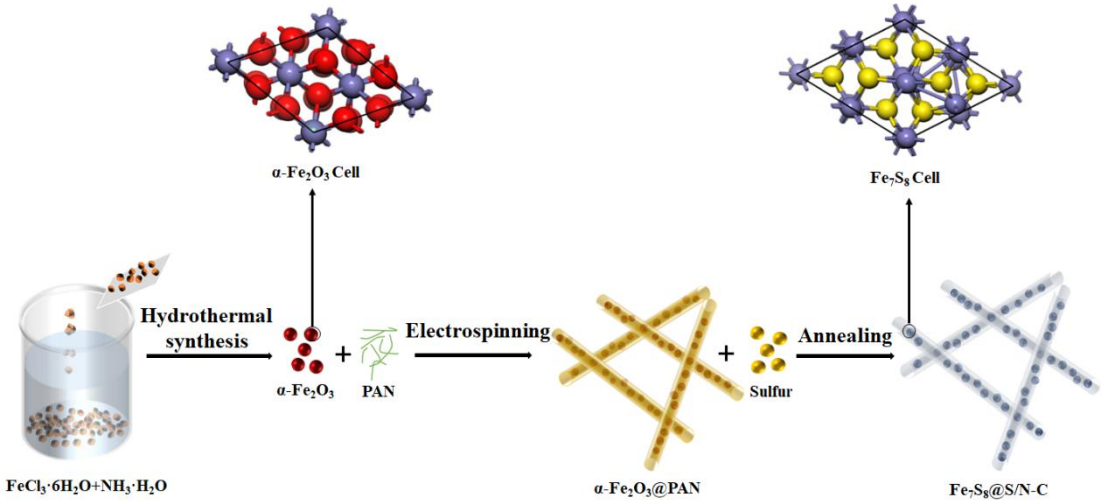

Figure 6.1 Illustrative synthesis scheme of Fe_7S_8@S/N-C nanofibers.

Electrospun carbon nanofibers are found to be the excellent matrix for active materials for SIBs, because they not only can provide short electron/ion paths, but also be easily modified to change their properties.[428, 429] Especially, doping, i.e., nitrogen-doping, and sulfur-doping, can improve the electrochemical performance of carbon nanofibers.[332] Under this background, we designed the Fe_7S_8 dedicated sulfur, nitrogen-co-doped carbon nanofibers (Fe_7S_8@S/N-C) through one-step synthesis process, as shown in **Figure 6.1**. The α-Fe_2O_3 nanoparticles were synthesized by hydrothermal method, then added into PAN for electrospinning. The Fe_7S_8@S/N-C were obtained through high temperature annealing with sulfur. Owing to unique structural characteristics, the Fe_7S_8@S/N-C electrode exhibited stable cycling performance with 347 mA h g^{-1} after 150 cycles at 1 A g^{-1} and superior rate capability with 220 mA h g^{-1} at 5.0 A g^{-1}.

6.2 Experimental Section

Synthesis of Fe_7S_8@S/N-C: α-Fe_2O_3 nanoparticles were prepared through a simple hydrothermal method according to the literature with little modification.[430] In a typical synthesis, 0.54 g $FeCl_3 \cdot 6\ H_2O$ was firstly dissolved into 20 mL deionized water. Then, 10 mL aqueous ammonia was added to the above solution drop by drop. After that, this mixture was transferred into an autoclave of 50 mL and maintained at 180 °C for 12 h. The resulting product was collected by centrifugation and washed with DI water and ethanol several times.

The Fe_7S_8@S/N-C composites were synthesized through the electrospinning/sulfidation processes. Typically, 0.5 g as-prepared α-Fe_2O_3 nanoparticles and 1 g polyacrylonitrile (PAN) were added into 10 mL N,N-dimethylformamide (DMF) and stirred at 60 °C overnight to form a stable suspension. Then, the obtained suspension was transferred into a syringe. A stainless-steel plate was placed to collect the nanofibers with a distance of 15 cm away from the syringe. The flow rate was ~ 0.4 mL h^{-1} and the voltage applied was 15 kV. The collected nanofibers were pre-oxidized at 230 °C for 2 h in air. Finally, 0.5 g pre-treated nanofibers were carbonized with 0.5 g sulfur at 600 °C for 2 h in argon atmosphere to obtain Fe_7S_8@S/N-C. For comparison, 0.5 g α-Fe_2O_3 nanoparticles and 0.5 g sulfur power were heated under the same condition to transfer α-Fe_2O_3 to Fe_7S_8. The pure S/N-C nanofibers were synthesized by the same method without using α-Fe_2O_3 precursor.

Materials characterization: The morphology information of the samples were characterized by the scanning electron microscope (SEM, Hitachi S4800) with Energy Dispersive Spectrometer (EDS) and field-emission transmission electron microscope (TEM, Tecnai G2 20). The X-ray diffractions (XRD, Rigaku D/max-2500 X-ray diffractometer, Cu Kα, λ = 0.154056 nm) were carried out with a scan rate of 8° min^{-1}. The thermogravimetric analysis (TGA) was done in air using the STD Q600 thermogravimetric analyser. The Brunauer-Emmett-Teller surface area (BET) and pore size distribution were obtained by a Nova 2000e volumetric adsorption analyser. Raman spectra was carried out using a HORIBA LabRAM HR Evolution Raman

spectrometer. The X-ray photoelectron spectroscopies (XPS) was characterized to evaluate the elemental composition of the samples on a Thermo scientific K_{α} spectrometer.

Electrochemical measurements: In the typical electrochemical evaluations, the working electrodes were composed of 80 wt% active materials with 10 wt% acetylene black, and 10 wt% carboxymethyl cellulose (CMC) as the conductive agent and binder, respectively. The specific capacity was calculated based on the entire mass of the electrode. A sodium foil was used as the counter electrode. The used electrolyte was 1 M $NaClO_4$ in the propylene carbonate and ethylene carbonate (PC-EC, 1:1, v:v), and glass fiber (Whatman, Grade GF/A) was applied as the separator. The CR2025-type coin cells were assembled in the Ar-filled glove box. Galvanostatic charge-discharge test were measured at room temperature between the voltage range of 0.01 - 2.5 V.

6.3 Results and Discussion

6.3.1 Structure and morphology

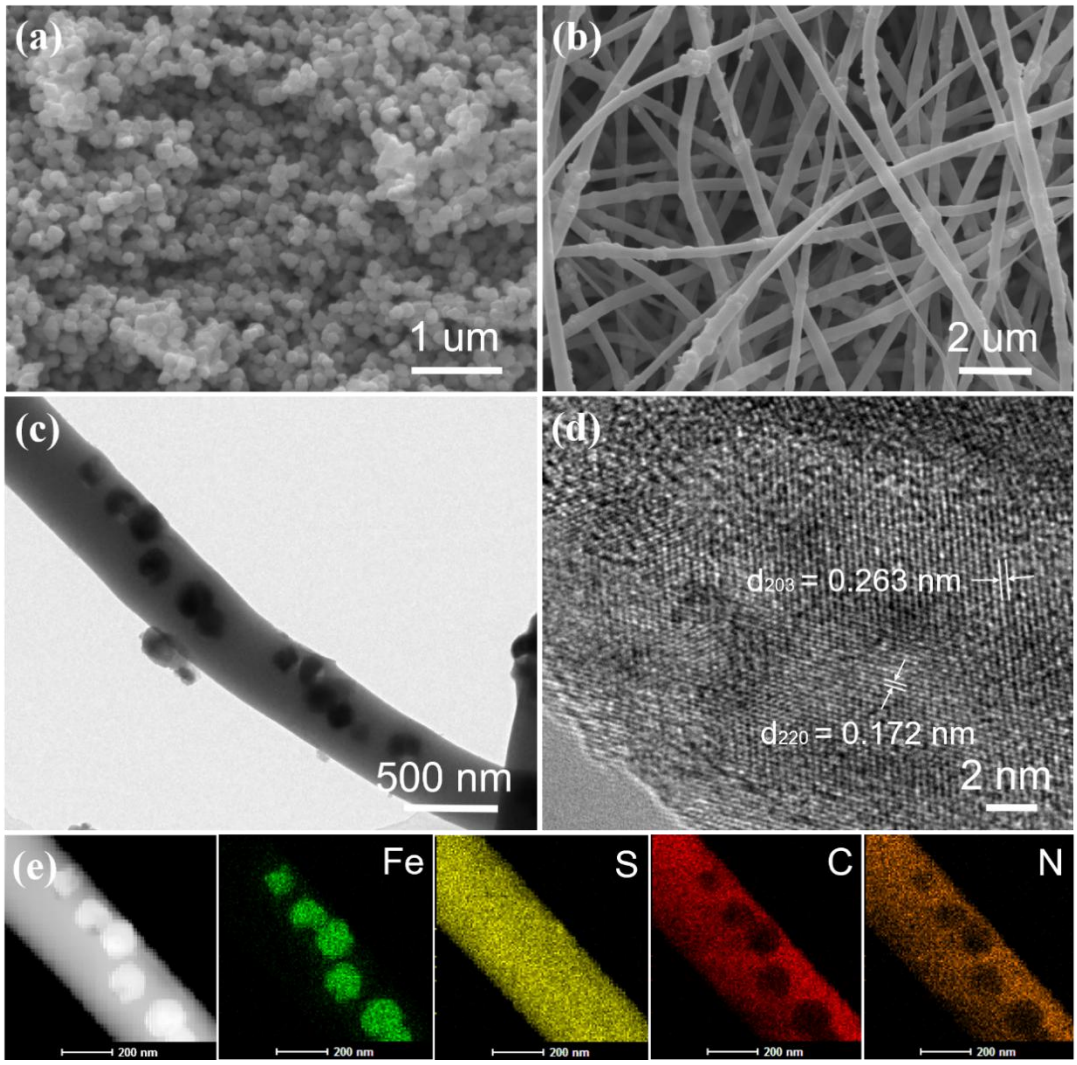

Figure 6.2 (a) SEM image of α-Fe_2O_3 nanoparticles; (b) SEM image of Fe_7S_8@S/N-C nanofibers; (c) Low-resolution and (d) high-resolution TEM images of a Fe_7S_8@S/N-C nanofiber; (e) Element mapping of a Fe_7S_8@S/N-C nanofiber.

The morphologies and structures of as-prepared α-Fe_2O_3, Fe_7S_8, Fe_7S_8@S/N-C and S/N-C samples were characterized by SEM and TEM techniques, respectively, as shown in **Figure 6.2** and **6.3**. **Figure 6.2 a** shows that the diameters of α-Fe_2O_3 particles distributes in the range of 100-200 nm. The prepared α-Fe_2O_3 precursor could be electrospun into PAN polymer fibers, and further transformed into Fe_7S_8@S/N-C composite through the carbonization and sulfidation process. Fe_7S_8@S/N-C shows the fiber-like structure, and there are no particles on the surface,

as shown in **Figure 6.2 b**. TEM image further confirmed that Fe_7S_8 particles were embedded into carbon nanofibers (**Figure 6.2 c**), which had a diameter of 200-400 nm. The HR-TEM image of Fe_7S_8@S/N-C in **Figure 6.2 d** indicates that two lattice fringes with 0.263 nm and 0.172 nm can be observed, which are assigned to the (203) and (220) planes, respectively. The energy dispersive X-ray (EDX) element mapping images indicate that the S, C, and N elements are uniformly distributed throughout the Fe_7S_8@S/N-C nanofiber (**Figure 6.2 e**), while Fe element is isolated distributed due to the distribution of isolated Fe_7S_8 nanoparticles in the nanofibers. After the sulfidation of α-Fe_2O_3 particles, the obtained Fe_7S_8 nanoparticles (Figure **6.3 a** and **b**) exhibited irregular morphology and had a diameter of 100-400 nm. To carry out control experiment, S/N-C nanofibers were also obtained, and characterized by SEM and HR-TEM images (**Figure 6.3 c** and **d**), which indicated an amorphous structure of the S/N-C nanofibers.

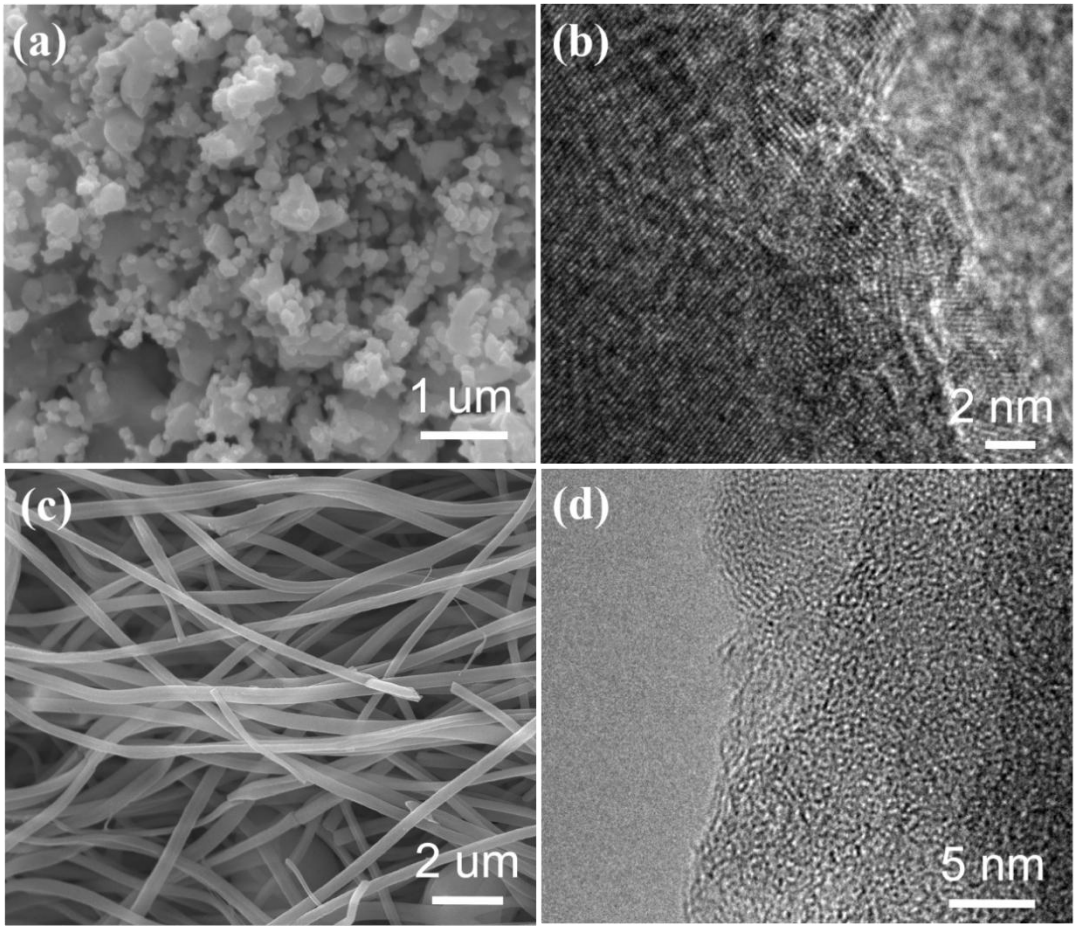

Figure 6.3 (a) SEM image and (b) HR-TEM image of Fe_7S_8; (c) SEM image and (d) HR-TEM image of S/N-C.

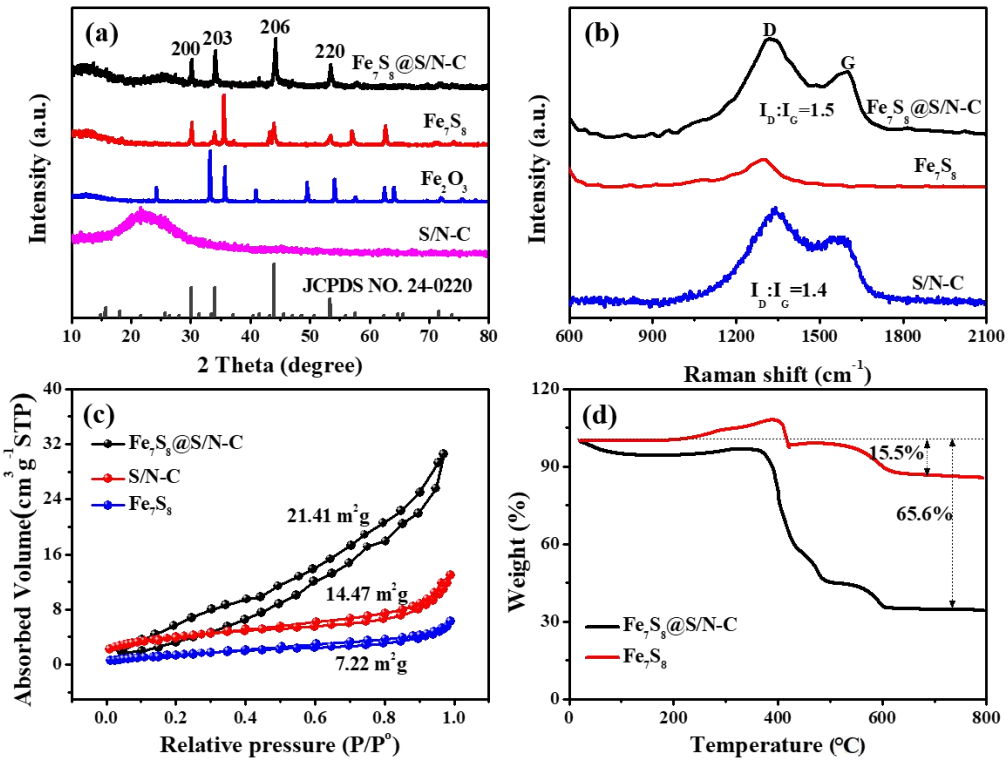

Figure 6.4 (a) XRD patterns of as-prepared α-Fe_2O_3, Fe_7S_8, S/N-C and Fe_7S_8@S/N-C samples; (b) Raman spectra, (c) N_2 adsorption-desorption isotherms and (d) TGA data of as-prepared Fe_7S_8, Fe_7S_8@S/N-C and S/N-C samples.

XRD measurement was carried out to characterize the crystal phase of the as-prepared α-Fe_2O_3, Fe_7S_8, Fe_7S_8@S/N-C and S/N-C samples, as shown in **Figure 6.4 a**. The XRD patterns of Fe_7S_8, Fe_7S_8@S/N-C in **Figure 6.4 a** show four obvious peaks located at 30.0°, 33.9°, 44.0°, and 53.3°, respectively, which can be well indexed to pyrrhotite Fe_7S_8 (JCPDS No. 24-0220). This indicates that α-Fe_2O_3 was completely transformed into Fe_7S_8. Moreover, the sharp diffraction patterns of both Fe_7S_8 and Fe_7S_8@S/N-C with no other impurity peaks suggest the good crystallinity and high purity. The XRD pattern of S/N-C in **Figure 6.4 a** is ascribed to the typical carbon. As displayed in Raman spectra (**Figure 6.4 b**), Fe_7S_8@S/N-C and S/N-C samples show D peak (1320 cm^{-1}) and G peak (1590 cm^{-1}). The intensity ratio of the D peak to

G peak for Fe_7S_8@S/N-C (I_D : I_G, 1.5) and S/N-C samples (I_D : I_G, 1.4) indicates that there are more defect sites in Fe_7S_8@S/N-C, which might be caused by more N and S doping.[431] The Raman spectrum of pure Fe_7S_8 only shows some small peaks located around 1320 cm^{-1}, which are attributed to the small defect sites in Fe_7S_8.[432] **Figure 6.4 c** shows the N_2 adsorption-desorption isotherms of Fe_7S_8@S/N-C, S/N-C and Fe_7S_8 samples, and the Brunauer-Emmett-Teller (BET) specific surfaces of Fe_7S_8@S/N-C, S/N-C and Fe_7S_8 samples are 21.41, 14.47 and 7.22 g m^{-2}, respectively. The thermogravimetric analysis (TGA) was carried out in air atmosphere, as shown in **Figure 6.4 d**. For Fe_7S_8, there is an obvious mass increasing below 400 °C because the oxidation of Fe^{2+} to Fe^{3+}. In the range of 400 - 600 °C, most S was oxidized to SO_3 or SO_2, causing the weight loss of 14.4 %. Fe_7S_8@S/N-C composite suffered from a larger weight loss than Fe_7S_8. It can be calculated that the content of Fe_7S_8 in the composite is ~ 46.1%. Moreover, the content of sulfur doping in the carbon of Fe_7S_8@S/N-C and S/N-C samples is confirmed to be ~ 5.5 % and ~ 4.25% by EDS, respectively.

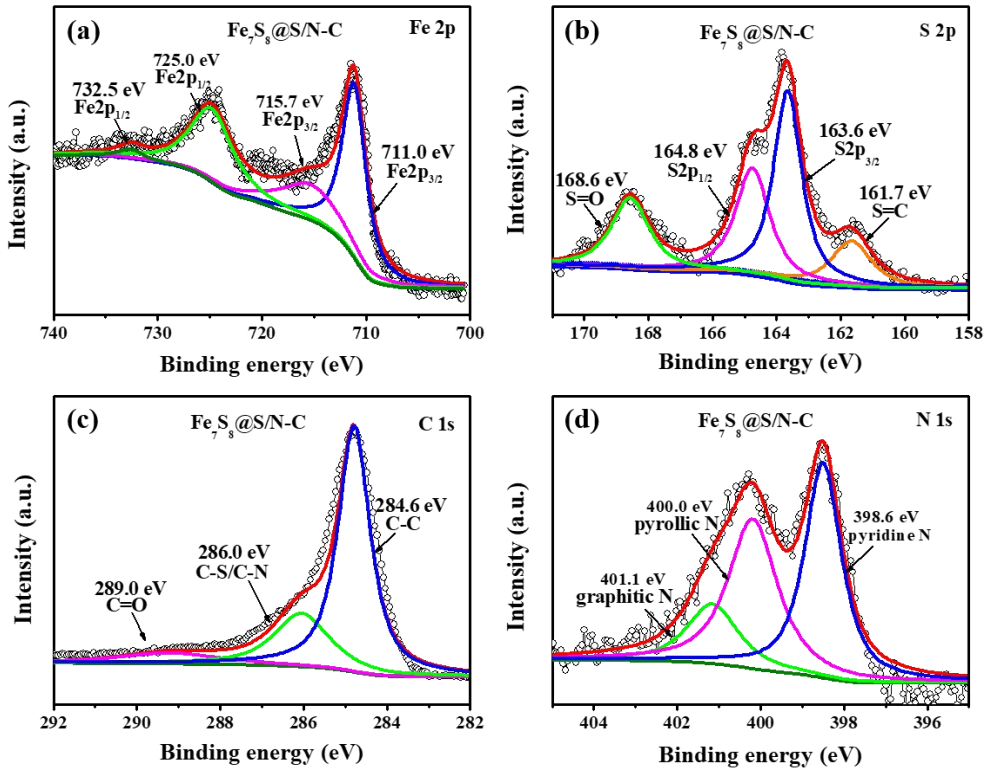

Figure 6.5 High-resolution XPS spectra of Fe_7S_8@S/N-C: (a) Fe 2p; (b) S 2p; (c) C 1s; (d) N 1s.

In order to understand the chemical status of Fe_7S_8@S/N-C, XPS measurement was conducted, as shown in **Figure 6.5**. The Fe 2p spectrum in **Figure 6.5 a** shows that two valences of Fe existed in the sample. The peaks of Fe $2p_{3/2}$ at 711 eV and 715.7 eV (satellite peak) indicate the existence of Fe^{2+} while the Fe $2p_{1/2}$ peaks at 725 eV and 732.5 eV (satellite peak) can be assigned to Fe^{3+}.[433] In the S 2p spectrum (**Figure 6.5 b**), the peaks at 163.6 eV and 164.8 eV can be attributed to the Fe-S bonding. The small peak at 161.7 eV suggests that some C-S bonds formed during sulfidation process. Besides, another peak located at 168.6 eV can be indexed to the S-O bond caused by the adsorbed oxygen on the active surface of Fe_7S_8 particles in the sample.[434] In C 1s spectrum (**Figure 6.5 c**), the peaks at 289.0, 286.0 and 284.6 eV are attributed to C=O, C-N/C-S and C-C bonds, respectively. In addition, N 1s spectrum

in **Figure 6.5 d** reveals that there are pyridine, pyrrolic and graphitic N.[435] In this work, N-, S- dual doping can bring following advantages for Fe_7S_8@S/N-C: First, the N and S atoms can enhance the electronic conductivity of carbon nanofibers; Second, the defect sites brought by N and S could offer much more absorption sites for Na ions to improve its capacitive capability. Third, the disorder honeycomb carbon caused by N, S-doping offers channels for the diffusion of Na^+, which brings a high rate performance.

6.3.2 Electrochemical characterization

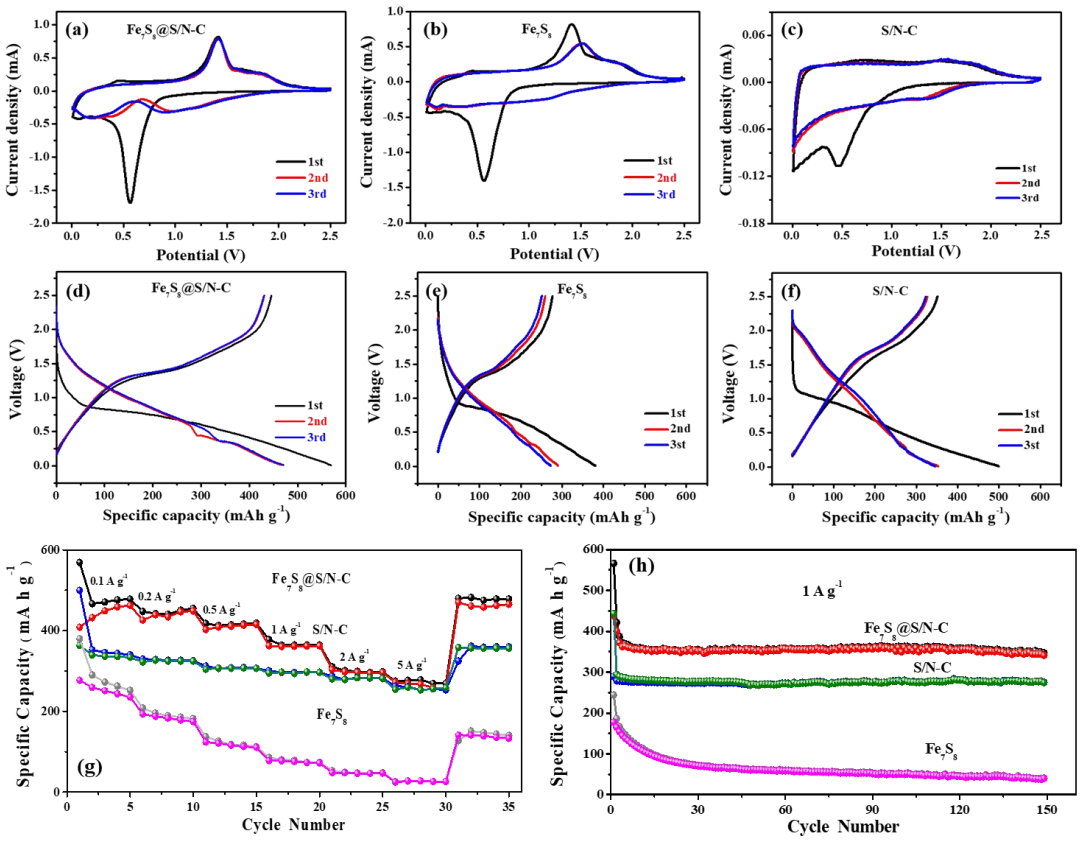

Figure 6.6 CV curves of (a) Fe_7S_8@S/N-C, (b) Fe_7S_8 and (c) S/N-C electrodes at 0.2 mV s^{-1}. The charge-discharge profiles of (d) Fe_7S_8@S/N-C, (e) Fe_7S_8 and (f) S/N-C electrodes at 0.1 A g^{-1}. (g) Rate capability of Fe_7S_8@S/N-C, Fe_7S_8 and S/N-C

electrodes at various current densities. (h) Cycling performance of Fe_7S_8@S/N-C, Fe_7S_8 and S/N-C electrodes at 1 A g^{-1}.

The Na storage performance of the Fe_7S_8@S/N-C, Fe_7S_8 and S/N-C electrodes was first evaluated by CV. **Figure 6.6 a** exhibits the initial three CV scans of Fe_7S_8@S/N-C electrode. During the first scan process, there exists a sharp cathodic peak at ~ 0.6 V, presenting the intercalation reaction (***Eqn.* 1**) and the formation of electrolyte interphase (SEI) film. In the low potential range, the small cathodic peak is ascribed to the conversion reaction to form Fe and Na_2S (***Eqn.* 2**).[424] In the first anodic scan, the sharp peak at 1.4 V and broad peak at about 1.6-2.0 V indicate the counter reaction of conversion reaction (***Eqn.* 3**) and the deintercalation reaction (***Eqn.* 4**), respectively.[421] According to previous work, only part of Na ions can be deintercalated out of the Fe_7S_8-based electrode, leading to the irreversible capacity in the initial cycle.

Sodiation: $Fe_7S_8 + 8\ Na^+ + 8e^- \rightarrow 4\ Na_2FeS_2 + 3\ Fe$ (1)

$Na_2FeS_2 + 2\ Na^+ + 2\ e^- \rightarrow 2\ Na_2S + Fe$ (2)

Desodiation: $2\ Na_2S + Fe \rightarrow Na_2FeS_2 + 2\ Na^+ + 2\ e^-$ (3)

$Na_2FeS_2 \rightarrow Na_{2-x}FeS_2 + x\ Na^+ + x\ e^-$ (4)

In the subsequent cathodic scans, the sharp peak at 0.6 V became broader and shifted to 0.95 V because of the formation of SEI film. Besides, the CV profiles of the 2nd and 3rd cycles did not change obviously, demonstrating a good structural stability. For Fe_7S_8 electrode, as shown in **Figure 6.6 b**, it suffered a worse reversibility. During the second and third cycles, the intercalation reaction of Na^+ ion could hardly take place. This proves the N-doped carbon nanofibers can protect the Fe_7S_8 from

structure collapse, thus improving its cycling stability. In **Figure 6.6 c**, the reduction peak around at ~ 0.5 V in the first cycle is ascribed to the formation of an irreversible solid electrolyte interphase (SEI) film. In the following cycles, the curves are well overlapped, demonstrating good reversibility.

The charge-discharge profiles of the first three cycles for the Fe_7S_8@S/N-C, Fe_7S_8 and S/N-C electrodes are in good accordance with the CV curves. As displayed in **Figure 6.6 d**, during the first discharge process, a remarkable plateau located at 0.6-0.9 V was attributed to the irreversible intercalation reaction and formation of SEI film. In the subsequent cycles, two plateaus can be observed, caused by the reversible intercalation and conversion reactions. In contrast, for Fe_7S_8 and S/N-C electrodes (**Figure 6.6 e** and **f**), there was no remarkable plateau on the discharge profiles during the 2nd and 3rd cycles. Moreover, the coincidence of subsequent discharge/charge curves for Fe_7S_8@S/N-C and S/N-C electrodes indicates that S/N-C could afford Fe_7S_8 with a reversible and stable Na storage performance.

Benefited from the defect-decorated carbon nanofibers as conductive matrix with high ion diffusion rate, the Fe_7S_8@S/N-C electrode showed the best rate capability among three electrodes, as shown in **Figure 6.6 g**. With the current density increasing, the Fe_7S_8@S/N-C electrode delivered capacities of 470, 445, 415, 365, 280 and 220 mA h g^{-1}, at 0.1, 0.2, 0.5, 1, 2, 5 A g^{-1}, respectively. When the current density was adjusted back to 0.1 A g^{-1}, a capacity of 475 mA h g^{-1} could still be obtained. The Fe_7S_8 electrode only showed the limited capacities of 272, 208, 137, 86, 53 and 26 mA h g^{-1}, at the current densities of 0.1, 0.2, 0.5, 1, 2, 5 A g^{-1}, respectively. Besides, when

current density was back to 0.1 A g^{-1}, Fe_7S_8 electrode only offered a capacity of 147 mA h g^{-1}. This suggests that S/N-C nanofibers could improve the performance of Fe_7S_8 in the stability and conductivity. Moreover, although S/N-C also exhibited good stability and rate capability, it sustained relatively lower capacities than Fe_7S_8@S/N-C at all current densities. As shown in **Figure 6.6 h**, Fe_7S_8@S/N-C still showed a high capacity of 347 mA h g^{-1} after 150 cycles at 1 A g^{-1}, with the retention rate of about 94% (compared with the 2nd cycle). However, the Fe_7S_8 and S/N-C displayed a capacity of 41 and 274 mA h g^{-1} at the same current density after 150 cycles, respectively. This is because the void space in carbon nanofibers can alleviate the volume change of Fe_7S_8 particles during sodiation/desodiation and the carbon nanofibers can prevent the loss of active materials. Table 6.1 lists the contrasting cycling performance of Fe_7S_8 anode for SIBs.

Table 6.1 Comparisons of electrochemical performances of this work with the reported Fe_7S_8 for Sodium ion batteries.

Materials	1st discharge capacity (mA h g^{-1})	Cycle number	Capacity after the reported cycles (mA h g^{-1})	Refs.
Fe_7S_8@S/N-C nanofibers	~ 480 (1 A g^{-1})	150	347 (1 A g^{-1})	**This work**
ultrafine Fe_7S_8@C nanocrystals	629 (180 mA g^{-1})	1000	447 (180 mA g^{-1})	436
Fe_7S_8/N-graphene	758.7 (0.4 A g^{-1})	500	393.1 (0.4 A g^{-1})	437
Fe_7S_8@C	620 (0.1 A g^{-1})	100	375 (0.1 A g^{-1})	438
Fe_7S_8@NC-PS	750 (2 A g^{-1})	150	600 (2 A g^{-1})	439

Fe_7S_8@C	~ 610 (1 A g^{-1})	1000	606.7 (1 A g^{-1})	440
Fe_7S_8@C	~ 680 (0.5 A g^{-1})	500	370 (0.5 A g^{-1})	441
Fe_7S_8/C	600 (0.1 A g^{-1})	100	497 (0.1 A g^{-1})	442
Fe_7S_8@C-G	400 (0.5 A g^{-1})	150	449 (0.5 A g^{-1})	443
MOFs derived Fe_7S_8/C composites	800 (0.1 A g^{-1})	100	500 (0.1 A g^{-1})	444
Yolk-shell Fe_7S_8@C nanoboxes	~ 820 (0.1 A g^{-1})	200	491.6 (0.1 A g^{-1})	445
Spindle-like Fe_7S_8/N-doped carbon nanohybrids	~ 400 (0.5 A g^{-1})	500	406.7 (0.5 A g^{-1})	446

The EIS profiles of the Fe_7S_8@S/N-C and Fe_7S_8 electrodes are shown in **Figure 6.7**. Before and after galvanostatic tests, the charge transfer resistances of Fe_7S_8@S/N-C were both smaller than those of Fe_7S_8, indicating the higher electronic conductivity of Fe_7S_8@S/N-C.

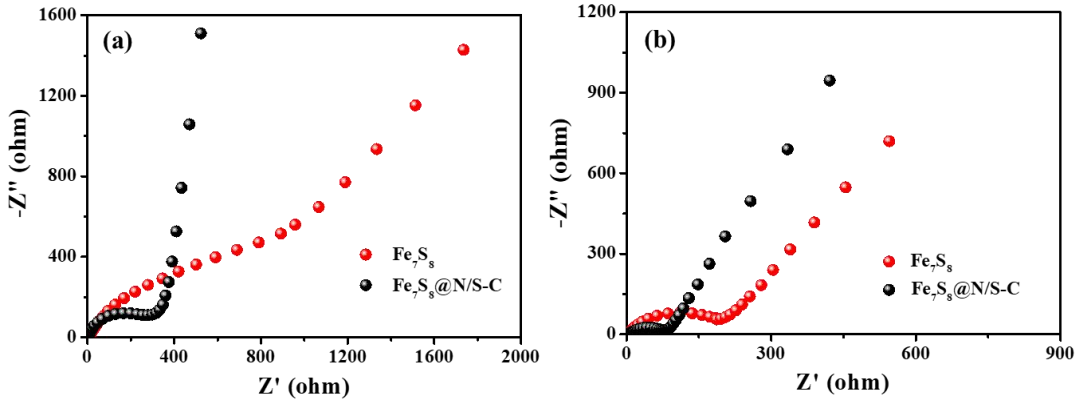

Figure 6.7 Nyquist plots of the Fe_7S_8 and Fe_7S_8@S/N-C electrodes (a) before and (b) after 10 cycles.

To explore the sodium storage kinetics of Fe_7S_8@S/N-C electrode, CV measurements were carried out at various scan rates from 0.2 to 5 mV s^{-1}. As displayed in **Figure 6.8**

a, both the anodic and cathodic peaks became broader with the scan rate increasing. The curves at low and high scan rates show the similar shapes, indicating a small polarization voltage. As well known, the electrochemical energy storage contribution of metal sulfides is generally consisted of two parts: diffusion-controlled process and capacitance-controlled behaviour. The relationship between the peak current (i) and sweep rate (v) obeys the law as follows:[447]

$$i = av^b \qquad (5)$$

where a and b are adjustable parameters. When the b-value is close to 0.5, indicating the diffusion-controlled process. It reveals the capacitance-controlled behaviour as the value is equal to 1. The b-value can be calculated by fitting the log(v) to log(i). Surprisingly, depending on the calculation result, the b-values are 0.88 and 0.68 for anodic and cathodic peaks, respectively, as shown in **Figure 6.8 b**.

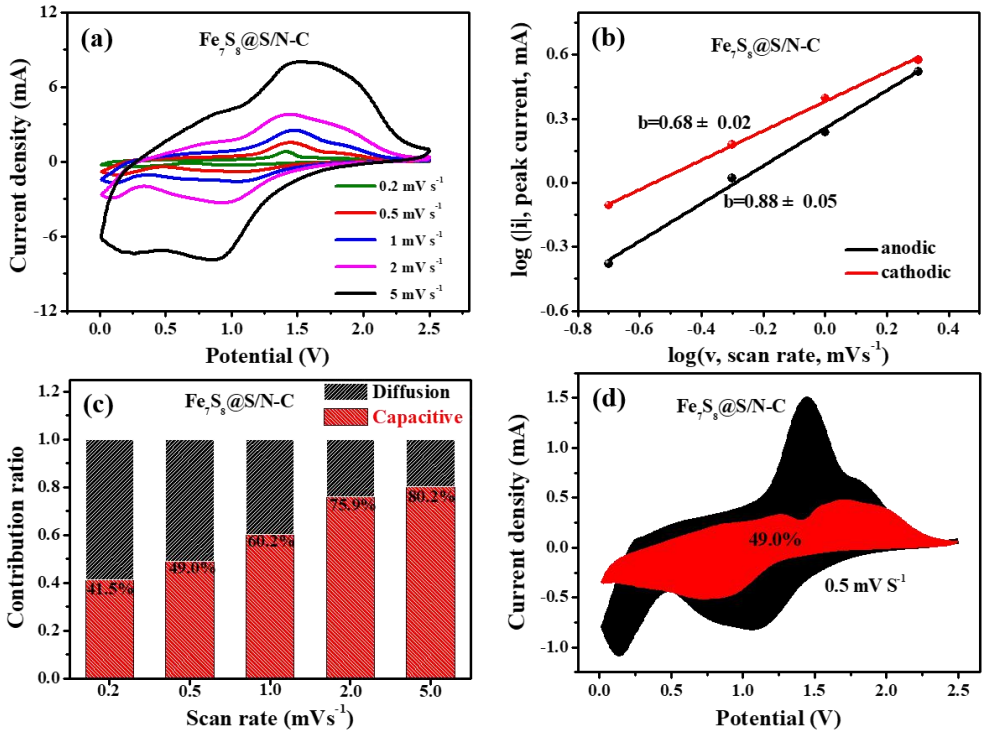

Figure 6.8 (a) CV curves at various sweep rates from 0.2 to 5 mV s^{-1}, (b) relationship between the peak currents and scan rates in logarithmic format, (c) capacitive contribution at a scan rate of 0.5 mV s^{-1} and (d) contribution ratio of the capacitive and diffusion-controlled capacity of Fe_7S_8@S/N-C electrode.

The total capacitive contribution to the total capacity can be calculated by the following equations:[448]

$$i = k_1 v + k_2 v^{1/2} \qquad (6)$$

where $k_1 v$ reveals the capacitive contribution and $k_2 v$ represents the diffusion-controlled contribution. As shown in **Figure 6.8 c**, 49.0 % of the total capacity at the scan rate of 0.5 mV s^{-1} come from capacitive controlled processes for Fe_7S_8@S/N-C electrode. From **Figure 6.8 d**, the contribution ratio of capacitance-controlled process gradually increased with the increase of the scan rates and finally a maximum value of 80.2 % achieved at 5 mV s^{-1}. For pure Fe_7S_8 electrode, based on the calculation of CV curves (**Figure 6.9 a**), a higher ratio of

capacitive contribution in **Figure 6.9 b** reached. Based on above results, it indicates that the fast charge-discharge process not only occurs on the defect-site of S, N-doped carbon nanofibers, but also takes place on the surface of Fe_7S_8.

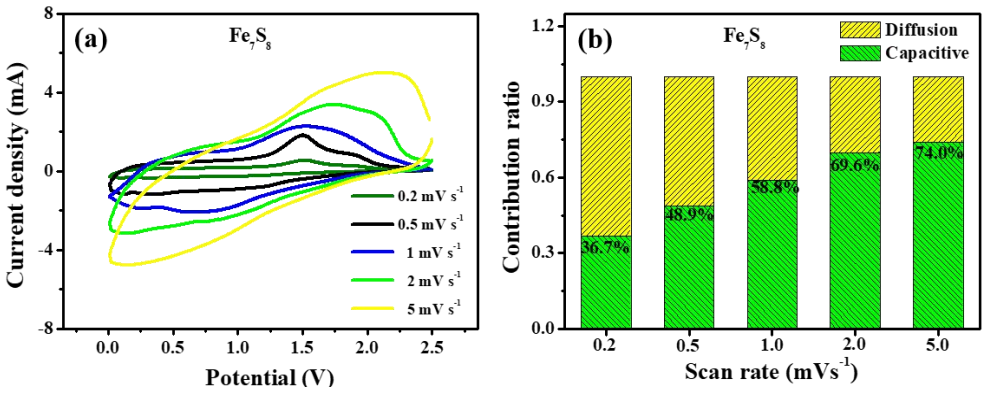

Figure 6.9 (a) CV curves at various sweep rates from 0.2 to 5 mV s^{-1} and (b) contribution ratio of the capacitive and diffusion-controlled capacity of Fe_7S_8@S/N-C electrode.

6.4 Conclusion

In conclusion, we have successfully synthesized the Fe_7S_8@S/N-C nanofibers by electrospinning/sulfidation methods using α-Fe_2O_3 nanoparticles as the precursor. The Fe_7S_8@S/N-C demonstrated superior rate capability and stable cycling performance, which can be ascribed to S/N-C nanofibers because they can facilitate the stability of Fe_7S_8 during charge/discharge processes. This work will give useful guidance to design other metal sulfide anodes with the adjustment of structure and compositions.

CHAPTER 7 CONCLUSIONS AND OUTLOOK

7.1 General Conclusion

This thesis work is focused on preparing nanofiber-like functional carbon-based anode materials for SIBs, including nitrogen/sulfur co-doped carbon nanofibers (N/S-C), WS_2 coated nitrogen/sulfur co-doped carbon nanofibers (WS_2@N/S-C), and Fe_7S_8 embedded nitrogen/sulfur co-doped carbon nanofibers (Fe_7S_8@N/S-C). The preparation, structures, compositions and electrochemical performance of these materials were thoroughly studied. These materials exhibited excellent electrochemical performance in long-term cyclability and rate capability, which can be attributed to the synergistic effect of N, S-co-doping, the high conductivity of carbon nanofibers and metal sulfides embedded into the carbon nanofibers. These results were summarized as follows.

The cycling life of Na-ion batteries is limited by the volumetric changes of sodium anodes during the sodiation/desodiation processes. To solve the problem, we have used the electrospinning method to successfully fabricate mesoporous S/N-C nanofibers, which show a high capacity and high-rate capability as an anode material for Na-ion battery. The S/N-C nanofibers delivered a high reversible capacity of 552.5 and 355.3 mA h g^{-1} at 0.1 and 5 A g^{-1}, respectively due to the high S-doping (27.95%) in the carbon nanofibers. The introduction of N and S in S/N-C nanofibers increases the active sites for Na^+ storage and reduces the energy required for Na^+ transfer, as

confirmed by *in situ* Raman spectroscopy and DFT calculations. Moreover, the mesoporous S/N nanofibers are wetted by liquid electrolyte, which facilitates the Na^+ transport and increases the rate performance, thus making them a suitable anode material for SIBs and other electrochemical energy storage devices.

WS_2 nanosheets embedded lotus rhizome-like heteroatoms doped carbon nanofibers (WS_2@S/N-C) with abundant hierarchical tubes inside were designed. The prepared WS_2@S/N-C nanofibers exhibit a high discharge capacity of 381 mA h g^{-1} at 100 mA g^{-1}, an excellent rate capacity of 108 mA h g^{-1} at 30 A g^{-1}, and a stable capacity of 175 mA h g^{-1} at 5 A g^{-1} after 1000 cycles. The excellent performance of WS_2@S/N-C is attributed to the synergistic effect of WS_2 nanosheets with larger interlayer distance and stable lotus rhizome-like S/N-C nanofiber frameworks to alleviate the mechanical stress. Moreover, the WS_2@S/N-C electrode shows obvious pseudocapacitance effect at 1 mV s^{-1} with a capacitive contribution of 86.5%. In addition, the DFT calculations further indicate that WS_2@S/N-C electrode is more favorable for Na storage. This novel synthetic strategy is a promising method, which can be applied to synthesize other electrode materials for energy storage devices in the future.

Iron sulfides have attained interest as electrode candidates for sodium-ion batteries (SIBs) owing to the rich chemical stoichiometries and high capacity. However, they usually exhibit poor cycling performance that is attributed to the large volume change during electrochemical sodiation process. We synthesized the Fe_7S_8@sulfur, nitrogen-doped carbon (S/N-C) nanofibers through electrospinning/sulfurization

processes with Fe_2O_3 particles as the precursor. The as-designed Fe_7S_8@S/N-C nanofibers presented a discharge capacity of 347 mA h g^{-1} after 150 cycles at 1 A g^{-1} and a high rate capacity of 220 mA h g^{-1} at 5 A g^{-1} in virtue of unique structural characteristics. The as-designed one-dimensional composites are promising anode materials for SIBs in the future.

7.2 Outlook

Although some advances have been achieved to develop high-performance anode materials for SIBs, it remains great challenge in meeting the practical applications of SIBs. The low initial Columbic efficiency, cycling performance and complicated preparing process of anode materials still hinder the development in SIBs. Therefore, developing Na storage anode materials with good electrochemical performance is in high demand. The research strategy to fabricate high-performance anodes in this thesis could be meaningful and give some insights into exploring new anode materials for SIBs to other researchers.

However, to meet the demands for practical applications, some future research directions should be carried out as follows:

7.2.1 Large-scale preparation of nanofibers

Our present electrospinning technology offers us with uniform nanofibers, which can be controlled from the porosity to components. This will provide us a good platform

to study the influence of active components on the Na storage performance as model samples. However, its preparation efficiency is low, which limits the potential application in large-scale battery industry. Therefore, it is necessary to develop advanced electrospinning technologies to prepare functional nanofibers in a large scale with high efficiency. Some strategies are proposed, such as using more nozzles in each time, speeding up the feeding rate while keeping the formation of nanofibers.

7.2.2 Pre-sodiation of the as-obtained nanofibers

Although the materials in our thesis work demonstrated excellent electrochemical performance in cycling stability and rate capability, there is still serious problem of low initial Coulombic efficiency for the anode materials, which hindered their practical application. One of the most possible reasons is the irreversible reaction in the first charge/discharge process. Thus, to improve the initial Coulombic efficiency, it is proven to be effective to pre-sodiate the as-obtained nanofibers by electrochemical methods.

7.2.3 Detailed Na storage mechanism study

Although many high-performance anode materials have been explored for SIBs, the detailed Na storage mechanisms are still unclear, which will hinder their further development. Although some techniques have been used, such as *in-situ* Raman spectrum, *in-situ* XRD and DFT calculations, some precise *in-situ* techniques are still needed to study the Na storage mechanism of some materials, such as *in-situ* TEM,

in-situ synchrotron radiation, molecular dynamics and others. With the help of these techniques, detailed Na storage mechanism will be clearer, which can give some suggestions of designing novel anode materials for SIBs.

7.2.4 Optimizing electrolyte formulations

Electrolytes play crucial roles in determining the performance of the anode materials for SIBs, especially carbon materials. As we know, the electrolyte is composed of organic solvents, electrolyte salts, and functional additives. Thus, how to adjust the components of the electrolyte to match the anode material is important but complicated. Moreover, the optimized performance of anode materials can be obtained through optimizing the electrolyte formulations.

REFERENCES

1. N. Yabuuchi, K. Kubota, M. Dahbi and S. Komaba, *Chemical Reviews*, 2014, **114**, 11636-11682.
2. B. L. Ellis and L. F. Nazar, *Current Opinion in Solid State and Materials Science*, 2012, **16**, 168-177.
3. X. Xiang, K. Zhang and J. Chen, *Cheminform*, 2015, **46**, 5343-5364.
4. H. Pan, Y. S. Hu and L. Chen, *Energy & Environmental Science*, 2013, **6**, 2338-2360.
5. A. Ponrouch, D. Monti, A. Boschin, B. Steen, P. Johansson and M. Palacin, *Journal of Materials Chemistry A*, 2015, **3**, 22-42.
6. A. Ponrouch, R. Dedryvere, D. Monti, A. Demet, J. Atebamba, L. Croguennec, C. Masquelier, P. Johansson and M. R. Palacin, *Energy & Environmental Science*, 2013, **6**, 2361-2369.
7. K. Hayashi, K. Shima and F. Sugiyama, *Journal of The Electrochemical Society*, 2013, **160**, A1467-A1472.
8. S. W. Kim, D. H. Seo, X. Ma, G. Ceder and K. Kang, *Advanced Energy Materials*, 2012, **2**, 710-721.
9. M. D. Slater, D. Kim, E. Lee and C. S. Johnson, *Advanced Functional Materials*, 2013, **23**, 947-958.
10. P. K. Nayak, L. Yang, W. Brehm and P. Adelhelm, *Angewandte Chemie International Edition*, 2017, **57**, 102-120.
11. M. S. Whittingham, *Science*, 1976, **192**, 1126-1127.
12. M. S. Whittingham, *Progress in Solid State Chemistry*, 1978, **12**, 41-99.
13. P. F. Wang, Y. You, Y. X. Yin and Y. G. Guo, *Advanced Energy Materials*, 2017, **8**, 1701912.
14. J. Qian, W. Chen, Y. Cao, Z. Ma, Y. Huang, X. Ai and H. Yang, *Advanced Energy Materials*, 2018, **8**, 1702619.
15. P. Barpanda, L. Lander, S.-I. Nishimura and A. Yamada, *Advanced Energy Materials*, 2018, **8**, 1703055.
16. Y. Huang, L. Zhao, L. Li, M. Xie, F. Wu and R. Chen, *Advanced Materials*, 2019, **31**, e1808393.
17. Y. Sun, P. Shi, H. Xiang, X. Liang and Y. Yu, *Small*, 2019, **15**, e1805479.
18. Y.-X. Wang, S.-L. Chou, H.-K. Liu and S.-X. Dou, *Carbon*, 2013, **57**, 202-208.
19. Y. Matsuo and K. Ueda, *Journal of Power Sources*, 2014, **263**, 158-162.
20. Y. Wen, K. He, Y. Zhu, F. Han, Y. Xu, I. Matsuda, Y. Ishii, J. Cumings and C. Wang, *Nature Communications*, 2014, **5**, 4033.
21. B. Jache and P. Adelhelm, *Angewandte Chemie International Edition*, 2014, **53**, 10169-10173.
22. H. Kim, J. Hong, Y. U. Park, J. Kim, I. Hwang and K. Kang, *Advanced Functional Materials*, 2015, **25**, 534-541.

23. Z. Zhu, F. Cheng, Z. Hu, Z. Niu and J. Chen, *Journal of Power Sources*, 2015, **293**, 626-634.
24. M. Cabello, X. Bai, T. Chyrka, G. F. Ortiz, P. Lavela, R. Alcántara and J. L. Tirado, *Journal of The Electrochemical Society*, 2017, **164**, A3804-A3813.
25. M. Goktas, C. Bolli, E. J. Berg, P. Novák, K. Pollok, F. Langenhorst, M. V. Roeder, O. Lenchuk, D. Mollenhauer and P. Adelhelm, *Advanced Energy Materials*, 2018, **8**, 1702724.
26. K. Gotoh, H. Maruyama, T. Miyatou, M. Mizuno, K. Urita and H. Ishida, *The Journal of Physical Chemistry C*, 2016, **120**, 28152-28156.
27. I. Hasa, X. Dou, D. Buchholz, Y. Shao-Horn, J. Hassoun, S. Passerini and B. Scrosati, *Journal of Power Sources*, 2016, **310**, 26-31.
28. Z.-L. Xu, G. Yoon, K.-Y. Park, H. Park, O. Tamwattana, S. J. Kim, W. M. Seong and K. Kang, *Nature Communications*, 2019, **10**, 2598.
29. B. Xiao, T. Rojo and X. Li, *ChemSusChem*, 2019, **12**, 133-144.
30. E. Irisarri, A. Ponrouch and M. Palacin, *Journal of The Electrochemical Society*, 2015, **162**, A2476-A2482.
31. Z. Yuan, L. Si and X. Zhu, *Journal of Materials Chemistry A*, 2015, **3**, 23403-23411.
32. X. Dou, I. Hasa, D. Saurel, C. Vaalma, L. Wu, D. Buchholz, D. Bresser, S. Komaba and S. Passerini, *Materials Today*, 2019, **23**, 87-104.
33. M. Dahbi, T. Nakano, N. Yabuuchi, T. Ishikawa, K. Kubota, M. Fukunishi, S. Shibahara, J.-Y. Son, Y.-T. Cui and H. Oji, *Electrochemistry Communications*, 2014, **44**, 66-69.
34. K. Takada, Y. Yamada, E. Watanabe, J. Wang, K. Sodeyama, Y. Tateyama, K. Hirata, T. Kawase and A. Yamada, *ACS Applied Materials & Interfaces*, 2017, **9**, 33802-33809.
35. L. Fan, Q. Liu, S. Chen, Z. Xu and B. Lu, *Advanced Energy Materials*, 2017, **7**, 1602778.
36. R. Alcántara, J. J. Mateos and J. Tirado, *Journal of The Electrochemical Society*, 2002, **149**, A201-A205.
37. B. Cao, H. Liu, B. Xu, Y. Lei, X. Chen and H. Song, *Journal of Materials Chemistry A*, 2016, **4**, 6472-6478.
38. X. Gao, Y. An, W. Zhang, M. Yu, L. Ci and J. Feng, *Materials Technology*, 2018, **33**, 810-814.
39. Z. Li, J. Ding and D. Mitlin, *Accounts of Chemical Research*, 2015, **48**, 1657-1665.
40. H. Ying and W. Q. Han, *Advanced Science*, 2017, **4**, 1700298.
41. Y. Xu, Y. Zhu, Y. Liu and C. Wang, *Advanced Energy Materials*, 2013, **3**, 128-133.
42. Y. Liu, N. Zhang, L. Jiao and J. Chen, *Advanced Materials*, 2015, **27**, 6702-6707.
43. X. Xie, K. Kretschmer, J. Zhang, B. Sun, D. Su and G. Wang, *Nano Energy*, 2015, **13**, 208-217.
44. W. Chen and D. Deng, *Carbon*, 2015, **87**, 70-77.

45. H. Li, L. Yang, J. Liu, S. Li, L. Fang, Y. Lu, H. Yang, S. Liu and M. Lei, *Journal of Power Sources*, 2016, **324**, 780-787.
46. Y. Jeon, X. Han, K. Fu, J. Dai, J. H. Kim, L. Hu, T. Song and U. Paik, *Journal of Materials Chemistry A*, 2016, **4**, 18306-18313.
47. Y.-M. Lin, P. R. Abel, A. Gupta, J. B. Goodenough, A. Heller and C. B. Mullins, *ACS Applied Materials & Interfaces*, 2013, **5**, 8273-8277.
48. M. L. Martine, G. Parzych, F. Thoss, L. Giebeler and J. Eckert, *Solid State Ionics*, 2014, **268**, 261-264.
49. Y. Zhang, J. Xie, T. Zhu, G. Cao, X. Zhao and S. Zhang, *Journal of Power Sources*, 2014, **247**, 204-212.
50. H. Hou, M. Jing, Y. Yang, Y. Zhu, L. Fang, W. Song, C. Pan, X. Yang and X. Ji, *ACS Applied Materials & Interfaces*, 2014, **6**, 16189-16196.
51. S. Liu, J. Feng, X. Bian, J. Liu and H. Xu, *Energy & Environmental Science*, 2016, **9**, 1229-1236.
52. J. Gu, Z. Du, C. Zhang, J. Ma, B. Li and S. Yang, *Advanced Energy Materials*, 2017, **7**, 1700447.
53. L. Baggetto, K. J. Carroll, H.-Y. Hah, C. E. Johnson, D. R. Mullins, R. R. Unocic, J. A. Johnson, Y. S. Meng and G. M. Veith, *The Journal of Physical Chemistry C*, 2014, **118**, 7856-7864.
54. J. Liu, Z. Yang, J. Wang, L. Gu, J. Maier and Y. Yu, *Nano Energy*, 2015, **16**, 389-398.
55. L. Hu, X. Zhu, Y. Du, Y. Li, X. Zhou and J. Bao, *Chemistry of Materials*, 2015, **27**, 8138-8145.
56. H. Hou, M. Jing, Y. Yang, Y. Zhang, W. Song, X. Yang, J. Chen, Q. Chen and X. Ji, *Journal of Power Sources*, 2015, **284**, 227-235.
57. P. R. Abel, Y.-M. Lin, T. De Souza, C.-Y. Chou, A. Gupta, J. B. Goodenough, G. S. Hwang, A. Heller and C. B. Mullins, *The Journal of Physical Chemistry C*, 2013, **117**, 18885-18890.
58. L. Baggetto, J. K. Keum, J. F. Browning and G. M. Veith, *Electrochemistry Communications*, 2013, **34**, 41-44.
59. X. Wang, L. Fan, D. Gong, J. Zhu, Q. Zhang and B. Lu, *Advanced Functional Materials*, 2016, **26**, 1104-1111.
60. Q. Li, Z. Zhang, S. Dong, C. Li, X. Ge, Z. Li, J. Ma and L. Yin, *Particle & Particle Systems Characterization*, 2017, **34**, 1600115.
61. F. Yang, F. Yu, Z. Zhang, K. Zhang, Y. Lai and J. Li, *Chemistry-A European Journal*, 2016, **22**, 2333-2338.
62. J. Yang, M. Ma, C. Sun, Y. Zhang, W. Huang and X. Dong, *Journal of Materials Chemistry A*, 2015, **3**, 1258-1264.
63. S. Liu, J. Feng, X. Bian, J. Liu and H. Xu, *Journal of Materials Chemistry A*, 2016, **4**, 10098-10104.
64. S. Liu, Z. Luo, J. Guo, A. Pan, Z. Cai and S. Liang, *Electrochemistry Communications*, 2017, **81**, 10-13.
65. H. Yin, Q. Li, M. Cao, W. Zhang, H. Zhao, C. Li, K. Huo and M. Zhu, *Nano Research*, 2017, **10**, 2156-2167.

66. P. Xue, N. Wang, Z. Fang, Z. Lu, X. Xu, L. Wang, Y. Du, X. Ren, Z. Bai and S. Dou, *Nano Letters*, 2019, **19**, 1998-2004.
67. C. Wang, L. Wang, F. Li, F. Cheng and J. Chen, *Advanced Materials*, 2017, **29**, 1702212.
68. Y. Fu, Q. Wei, G. Zhang and S. Sun, *Advanced Energy Materials*, 2018, **8**, 1703058.
69. J. Qian, X. Wu, Y. Cao, X. Ai and H. Yang, *Angewandte Chemie International Edition*, 2013, **52**, 4633-4636.
70. Y. Kim, Y. Park, A. Choi, N. S. Choi, J. Kim, J. Lee, J. H. Ryu, S. M. Oh and K. T. Lee, *Advanced Materials*, 2013, **25**, 3045-3049.
71. J. Song, Z. Yu, M. L. Gordin, S. Hu, R. Yi, D. Tang, T. Walter, M. Regula, D. Choi and X. Li, *Nano Letters*, 2014, **14**, 6329-6335.
72. W. Li, S. Hu, X. Luo, Z. Li, X. Sun, M. Li, F. Liu and Y. Yu, *Advanced Materials*, 2017, **29**, 1605820.
73. Y. Zhu, Y. Wen, X. Fan, T. Gao, F. Han, C. Luo, S.-C. Liou and C. Wang, *ACS Nano*, 2015, **9**, 3254-3264.
74. G.-L. Xu, Z. Chen, G.-M. Zhong, Y. Liu, Y. Yang, T. Ma, Y. Ren, X. Zuo, X.-H. Wu and X. Zhang, *Nano Letters*, 2016, **16**, 3955-3965.
75. L. Wu, D. Bresser, D. Buchholz and S. Passerini, *Journal of The Electrochemical Society*, 2015, **162**, A3052-A3058.
76. H. A. Cha, H. M. Jeong and J. K. Kang, *Journal of Materials Chemistry A*, 2014, **2**, 5182-5186.
77. H. Xiong, M. D. Slater, M. Balasubramanian, C. S. Johnson and T. Rajh, *The Journal of Physical Chemistry Letters*, 2011, **2**, 2560-2565.
78. Z. Bi, M. P. Paranthaman, P. A. Menchhofer, R. R. Dehoff, C. A. Bridges, M. Chi, B. Guo, X.-G. Sun and S. Dai, *Journal of Power Sources*, 2013, **222**, 461-466.
79. P. Li, X. Guo, S. Wang, R. Zang, X. Li, Z. Man, P. Li, S. Liu, Y. Wu and G. Wang, *Journal of Materials Chemistry A*, 2019, **7**, 2553-2559.
80. B. Wang, F. Zhao, G. Du, S. Porter, Y. Liu, P. Zhang, Z. Cheng, H. K. Liu and Z. Huang, *ACS Applied Materials & Interfaces*, 2016, **8**, 16009-16015.
81. Y. Xu, M. Zhou, L. Wen, C. Wang, H. Zhao, Y. Mi, L. Liang, Q. Fu, M. Wu and Y. Lei, *Chemistry of Materials*, 2015, **27**, 4274-4280.
82. J. Chen, Y. Zhang, G. Zou, Z. Huang, S. Li, H. Liao, J. Wang, H. Hou and X. Ji, *Small*, 2016, **12**, 5554-5563.
83. H. Yang, R. Xu, Y. Gong, Y. Yao, L. Gu and Y. Yu, *Nano Energy*, 2018, **48**, 448-455.
84. H. Kim, E. Lim, C. Jo, G. Yoon, J. Hwang, S. Jeong, J. Lee and K. Kang, *Nano Energy*, 2015, **16**, 62-70.
85. E. Lim, C. Jo, M. S. Kim, M. H. Kim, J. Chun, H. Kim, J. Park, K. C. Roh, K. Kang and S. Yoon, *Advanced Functional Materials*, 2016, **26**, 3711-3719.
86. F. Liu, X. Cheng, R. Xu, Y. Wu, Y. Jiang and Y. Yu, *Advanced Functional Materials*, 2018, **28**, 1800394.
87. L. Wang, X. Bi and S. Yang, *Advanced Materials*, 2016, **28**, 7672-7679.

88. S. Hariharan, K. Saravanan, V. Ramar and P. Balaya, *Physical Chemistry Chemical Physics*, 2013, **15**, 2945-2953.
89. L. Xu, H. Sitinamaluwa, H. Li, J. Qiu, Y. Wang, C. Yan, H. Li, S. Yuan and S. Zhang, *Journal of Materials Chemistry A*, 2017, **5**, 2102-2109.
90. Y. Zhao, F. Wang, C. Wang, S. Wang, C. Wang, Z. Zhao, L. Duan, Y. Liu, Y. Wu and W. Li, *Nano Energy*, 2019, **56**, 426-433.
91. Z. Jian, B. Zhao, P. Liu, F. Li, M. Zheng, M. Chen, Y. Shi and H. Zhou, *Chemical Communications*, 2014, **50**, 1215-1217.
92. T. Li, A. Qin, L. Yang, J. Chen, Q. Wang, D. Zhang and H. Yang, *ACS Applied Materials & Interfaces*, 2017, **9**, 19900-19907.
93. T. Hou, X. Sun, D. Xie, M. Wang, A. Fan, Y. Chen, S. Cai, C. Zheng and W. Hu, *Chemistry-A European Journal*, 2018, **24**, 14786-14793.
94. X. Ding, X. Huang, J. Jin, H. Ming, L. Wang and J. Ming, *Electrochimica Acta*, 2018, **260**, 882-889.
95. Y. Fu, Q. Wei, X. Wang, G. Zhang, H. Shu, X. Yang, A. C. Tavares and S. Sun, *RSC Advances*, 2016, **6**, 16624-16633.
96. H. Liu, M. Jia, Q. Zhu, B. Cao, R. Chen, Y. Wang, F. Wu and B. Xu, *ACS Applied Materials & Interfaces*, 2016, **8**, 26878-26885.
97. D. Kong, C. Cheng, Y. Wang, Z. Huang, B. Liu, Y. Von Lim, Q. Ge and H. Y. Yang, *Journal of Materials Chemistry A*, 2017, **5**, 9122-9131.
98. B.-H. Hou, Y.-Y. Wang, J.-Z. Guo, Y. Zhang, Q.-L. Ning, Y. Yang, W.-H. Li, J.-P. Zhang, X.-L. Wang and X.-L. Wu, *ACS Applied Materials & Interfaces*, 2018, **10**, 3581-3589.
99. M. M. Rahman, A. M. Glushenkov, T. Ramireddy and Y. Chen, *Chemical Communications*, 2014, **50**, 5057-5060.
100. Y. Liu, Z. Cheng, H. Sun, H. Arandiyan, J. Li and M. Ahmad, *Journal of Power Sources*, 2015, **273**, 878-884.
101. M. Xu, Q. Xia, J. Yue, X. Zhu, Q. Guo, J. Zhu and H. Xia, *Advanced Functional Materials*, 2019, **29**, 1807377.
102. Y. Zhang, Y. V. Lim, S. Huang, M. E. Pam, Y. Wang, L. K. Ang, Y. Shi and H. Y. Yang, *Small*, 2018, **14**, 1800898.
103. B. Wang, G. Wang, X. Cheng and H. Wang, *Chemical Engineering Journal*, 2016, **306**, 1193-1202.
104. F. Zou, Y.-M. Chen, K. Liu, Z. Yu, W. Liang, S. M. Bhaway, M. Gao and Y. Zhu, *ACS Nano*, 2015, **10**, 377-386.
105. S. Yuan, X. l. Huang, D. l. Ma, H. g. Wang, F. z. Meng and X. b. Zhang, *Advanced materials*, 2014, **26**, 2273-2279.
106. C. Chen, Y. Dong, S. Li, Z. Jiang, Y. Wang, L. Jiao and H. Yuan, *Journal of Power Sources*, 2016, **320**, 20-27.
107. X. Wang, Y. Liu, Y. Wang and L. Jiao, *Small*, 2016, **12**, 4865-4872.
108. Y. Wang, D. Su, C. Wang and G. Wang, *Electrochemistry Communications*, 2013, **29**, 8-11.
109. Y.-X. Wang, Y.-G. Lim, M.-S. Park, S.-L. Chou, J. H. Kim, H.-K. Liu, S.-X. Dou and Y.-J. Kim, *Journal of Materials Chemistry A*, 2014, **2**, 529-534.

110. M. Dirican, Y. Lu, Y. Ge, O. Yildiz and X. Zhang, *ACS Applied Materials & Interfaces*, 2015, **7**, 18387-18396.
111. D. Ma, Y. Li, H. Mi, S. Luo, P. Zhang, Z. Lin, J. Li and H. Zhang, *Angewandte Chemie International Edition*, 2018, **57**, 8901-8905.
112. Z. Chen, D. Yin and M. Zhang, *Small*, 2018, **14**, 1703818.
113. M. Hu, Y. Jiang, W. Sun, H. Wang, C. Jin and M. Yan, *ACS Applied Materials & Interfaces*, 2014, **6**, 19449-19455.
114. X. Guo, X. Xie, S. Choi, Y. Zhao, H. Liu, C. Wang, S. Chang and G. Wang, *Journal of Materials Chemistry A*, 2017, **5**, 12445-12452.
115. C. Nithya, *ChemPlusChem*, 2015, **80**, 1000-1006.
116. H. Yin, M.-L. Cao, X.-X. Yu, H. Zhao, Y. Shen, C. Li and M.-Q. Zhu, *Materials Chemistry Frontiers*, 2017, **1**, 1615-1621.
117. W. Luo, F. Li, Q. Li, X. Wang, W. Yang, L. Zhou and L. Mai, *ACS Applied Materials & Interfaces*, 2018, **10**, 7201-7207.
118. J. Huang, Z. Xu, L. Cao, Q. Zhang, H. Ouyang and J. Li, *Energy Technology*, 2015, **3**, 1108-1114.
119. X. Xia, S. Deng, D. Xie, Y. Wang, S. Feng, J. Wu and J. Tu, *Journal of Materials Chemistry A*, 2018, **6**, 15546-15552.
120. S. Hariharan, K. Saravanan and P. Balaya, *Electrochemistry Communications*, 2013, **31**, 5-9.
121. M. Sreedhara, A. Santhosha, A. J. Bhattacharyya and C. Rao, *Journal of Materials Chemistry A*, 2016, **4**, 9466-9471.
122. K. Zhu, X. Wang, J. Liu, S. Li, H. Wang, L. Yang, S. Liu and T. Xie, *ACS Sustainable Chemistry & Engineering*, 2017, **5**, 8025-8034.
123. W. Kang, Y. Wang, D. Cao, Z. Kang and D. Sun, *Journal of Alloys and Compounds*, 2018, **743**, 410-418.
124. J. Park, J.-S. Kim, J.-W. Park, T.-H. Nam, K.-W. Kim, J.-H. Ahn, G. Wang and H.-J. Ahn, *Electrochimica Acta*, 2013, **92**, 427-432.
125. L. David, R. Bhandavat and G. Singh, *ACS Nano*, 2014, **8**, 1759-1770.
126. D. Sun, D. Ye, P. Liu, Y. Tang, J. Guo, L. Wang and H. Wang, *Advanced Energy Materials*, 2018, **8**, 1702383.
127. X. Geng, Y. Jiao, Y. Han, A. Mukhopadhyay, L. Yang and H. Zhu, *Advanced Functional Materials*, 2017, **27**, 1702998.
128. S. McDonnell, B. Brennan, A. Azcatl, N. Lu, H. Dong, C. Buie, J. Kim, C. L. Hinkle, M. J. Kim and R. M. Wallace, *ACS Nano*, 2013, **7**, 10354-10361.
129. W. Ren, W. Zhou, H. Zhang and C. Cheng, *ACS Applied Materials & Interfaces*, 2016, **9**, 487-495.
130. D. D. Xia, F. Gong, X. Pei, W. Wang, H. Li, W. Zeng, M. Wu and D. V. Papavassiliou, *Chemical Engineering Journal*, 2018, **348**, 908-928.
131. C. Zhu, P. Kopold, W. Li, P. A. van Aken, J. Maier and Y. Yu, *Journal of Materials Chemistry A*, 2015, **3**, 20487-20493.
132. Y. Wang, D. Kong, W. Shi, B. Liu, G. J. Sim, Q. Ge and H. Y. Yang, *Advanced Energy Materials*, 2016, **6**, 1601057.

133. Y. V. Lim, Y. Wang, D. Kong, L. Guo, J. I. Wong, L. Ang and H. Y. Yang, *Journal of Materials Chemistry A*, 2017, **5**, 10406-10415.
134. G. H. Newman and L. P. Klemann, *Journal of The Electrochemical Society*, 1980, **127**, 2097-2099.
135. B. Han, S. Chen, J. Zou, R. Shao, Z. Dou, C. Yang, X. Ma, J. Lu, K. Liu and D. Yu, *Nanoscale*, 2019, **11**, 7474-7480.
136. Y. Liu, H. Wang, L. Cheng, N. Han, F. Zhao, P. Li, C. Jin and Y. Li, *Nano Energy*, 2016, **20**, 168-175.
137. Z. Hu, Z. Tai, Q. Liu, S. W. Wang, H. Jin, S. Wang, W. Lai, M. Chen, L. Li and L. Chen, *Advanced Energy Materials*, 2019, **9**, 1803210.
138. C. G. Hawkins and L. Whittaker-Brooks, *Journal of Materials Chemistry A*, 2018, **6**, 21949-21960.
139. Q. Peng, Z. Wang, B. Sa, B. Wu and Z. Sun, *ACS Applied Materials & Interfaces*, 2016, **8**, 13449-13457.
140. Z. Xiao, Z. Yang, L. Zhang, H. Pan and R. Wang, *ACS Nano*, 2017, **11**, 8488-8498.
141. C. Lepienski, M. Meruvia, W. Veiga and F. Wypych, *Journal of Materials Research*, 2000, **15**, 2061-2064.
142. X. Ou, X. Xiong, F. Zheng, C. Yang, Z. Lin, R. Hu, C. Jin, Y. Chen and M. Liu, *Journal of Power Sources*, 2016, **325**, 410-416.
143. J. S. Cho, J.-S. Park and Y. C. Kang, *Nano Research*, 2017, **10**, 897-907.
144. Z.-G. Wu, J.-T. Li, Y.-J. Zhong, J. Liu, K. Wang, X.-D. Guo, L. Huang, B.-H. Zhong and S.-G. Sun, *Journal of Alloys and Compounds*, 2016, **688**, 790-797.
145. X. Wei, W. Li, J.-a. Shi, L. Gu and Y. Yu, *ACS Applied Materials & Interfaces*, 2015, **7**, 27804-27809.
146. D. Li, Y. Sun, S. Chen, J. Yao, Y. Zhang, Y. Xia and D. Yang, *ACS Applied Materials & Interfaces*, 2018, **10**, 17175-17182.
147. Q. Wang, W. Zhang, C. Guo, Y. Liu, C. Wang and Z. Guo, *Advanced Functional Materials*, 2017, **27**, 1703390.
148. M. J. Choi, J. Kim, J. K. Yoo, S. Yim, J. Jeon and Y. S. Jung, *Small*, 2018, **14**, 1702816.
149. A. Jin, M.-J. Kim, K.-S. Lee, S.-H. Yu and Y.-E. Sung, *Nano Research*, 2019, **12**, 695-700.
150. Q. Li, Q. Wei, W. Zuo, L. Huang, W. Luo, Q. An, V. O. Pelenovich, L. Mai and Q. Zhang, *Chemical Science*, 2017, **8**, 160-164.
151. Q.-T. Xu, J.-C. Li, H.-G. Xue and S.-P. Guo, *Journal of Power Sources*, 2018, **396**, 675-682.
152. M. Walter, T. Zünd and M. V. Kovalenko, *Nanoscale*, 2015, **7**, 9158-9163.
153. K. Zhang, M. Park, L. Zhou, G. H. Lee, J. Shin, Z. Hu, S. L. Chou, J. Chen and Y. M. Kang, *Angewandte Chemie International Edition*, 2016, **55**, 12822-12826.
154. W. Chen, S. Qi, M. Yu, X. Feng, S. Cui, J. Zhang and L. Mi, *Electrochimica Acta*, 2017, **230**, 1-9.

155. F. Wang, G. Li, X. Meng, Y. Li, Q. Gao, Y. Xu and W. Cui, *Inorganic Chemistry Frontiers*, 2018, **5**, 2462-2471.
156. S. Peng, X. Han, L. Li, Z. Zhu, F. Cheng, M. Srinivansan, S. Adams and S. Ramakrishna, *Small*, 2016, **12**, 1359-1368.
157. Y. Zhao, Q. Pang, Y. Meng, Y. Gao, C. Wang, B. Liu, Y. Wei, F. Du and G. Chen, *Chemistry-A European Journal*, 2017, **23**, 13150-13157.
158. J. Yu, X. Li, Y. Sun and X. Liu, *Ceramics International*, 2018, **44**, 17113-17117.
159. S. Chen, J. Zhao, Y. Pang and S. Ding, *Nanotechnology*, 2019, **30**, 425402.
160. Q. Zhou, L. Liu, Z. Huang, L. Yi, X. Wang and G. Cao, *Journal of Materials Chemistry A*, 2016, **4**, 5505-5516.
161. Y. Jiang, G. Zou, W. Hong, Y. Zhang, Y. Zhang, H. Shuai, W. Xu, H. Hou and X. Ji, *Nanoscale*, 2018, **10**, 18786-18794.
162. D. Liu, A. Hu, Y. Zhu, S. Zhou, Y. Duan, Q. Tang, W. Deng and X. Chen, *Ceramics International*, 2019, **45**, 3591-3599.
163. Y. N. Ko and Y. C. Kang, *Carbon*, 2015, **94**, 85-90.
164. M. Yin, X. Feng, D. Zhao, Y. Zhao, H. Li, W. Zhou, H. Liu, X. Bai, H. Wang and C. Feng, *ACS Sustainable Chemistry & Engineering*, 2019, **7**, 6122-6130.
165. H. Geng, J. Yang, Z. Dai, Y. Zhang, Y. Zheng, H. Yu, H. Wang, Z. Luo, Y. Guo and Y. Zhang, *Small*, 2017, **13**, 1603490.
166. Y. Fang, B. Y. Guan, D. Luan and X. W. Lou, *Angewandte Chemie International Edition*, 2019, **131**, 7821-7825.
167. Z. Shadike, M.-H. Cao, F. Ding, L. Sang and Z.-W. Fu, *Chemical Communications*, 2015, **51**, 10486-10489.
168. Y. Pan, X. Cheng, L. Gong, L. Shi, T. Zhou, Y. Deng and H. Zhang, *ACS Applied Materials & Interfaces*, 2018, **10**, 31441-31451.
169. H. Xia, K. Li, Y. Guo, J. Guo, Q. Xu and J. Zhang, *Journal of Materials Chemistry A*, 2018, **6**, 7148-7154.
170. J. Li, J. Li, D. Yan, S. Hou, X. Xu, T. Lu, Y. Yao, W. Mai and L. Pan, *Journal of Materials Chemistry A*, 2018, **6**, 6595-6605.
171. J. Tang, S. Ni, D. Chao, J. Liu, X. Yang and J. Zhao, *Electrochimica Acta*, 2018, **265**, 709-716.
172. Q. Chen, S. Sun, T. Zhai, M. Yang, X. Zhao and H. Xia, *Advanced Energy Materials*, 2018, **8**, 1800054.
173. C. Shang, S. Dong, S. Zhang, P. Hu, C. Zhang and G. Cui, *Electrochemistry Communications*, 2015, **50**, 24-27.
174. X. Xia, J. Xie, S. Zhang, B. Pan, G. Cao and X. Zhao, *Inorganic Chemistry Frontiers*, 2017, **4**, 131-138.
175. H. Fan, H. Yu, X. Wu, Y. Zhang, Z. Luo, H. Wang, Y. Guo, S. Madhavi and Q. Yan, *ACS Applied Materials & Interfaces*, 2016, **8**, 25261-25267.
176. Q. Pan, J. Xie, S. Liu, G. Cao, T. Zhu and X. Zhao, *RSC Advances*, 2013, **3**, 3899-3906.
177. Y. Zhang, C. Lv, X. Wang, S. Chen, D. Li, Z. Peng and D. Yang, *ACS Applied Materials & Interfaces*, 2018, **10**, 40531-40539.

178. G. Zhao, Y. Zhang, L. Yang, Y. Jiang, Y. Zhang, W. Hong, Y. Tian, H. Zhao, J. Hu and L. Zhou, *Advanced Functional Materials*, 2018, **28**, 1803690.
179. W. Zhao, S. Ci, X. Hu, J. Chen and Z. Wen, *Nanoscale*, 2019, **11**, 4688-4695.
180. Y. Lin, Z. Qiu, D. Li, S. Ullah, Y. Hai, H. Xin, W. Liao, B. Yang, H. Fan and J. Xu, *Energy Storage Materials*, 2018, **11**, 67-74.
181. J. Lu, S. Zhao, S. Fan, Q. Lv, J. Li and R. Lv, *Carbon*, 2019, **148**, 525-531.
182. Y. Wu, P. Nie, L. Wu, H. Dou and X. Zhang, *Chemical Engineering Journal*, 2018, **334**, 932-938.
183. H. Bian, Z. Li, X. Xiao, P. Schmuki, J. Lu and Y. Y. Li, *Advanced Functional Materials*, 2019, **29**, 1901000.
184. P. K. Dutta, U. K. Sen and S. Mitra, *RSC Advances*, 2014, **4**, 43155-43159.
185. T. Zhou, W. K. Pang, C. Zhang, J. Yang, Z. Chen, H. K. Liu and Z. Guo, *ACS Nano*, 2014, **8**, 8323-8333.
186. S.-W. Zhang, W. Lv, D. Qiu, T. Cao, J. Zhang, Q. Lin, X. Chen, Y.-B. He, F. Kang and Q.-H. Yang, *Journal of Materials Chemistry A*, 2019, **7**, 10761-10768.
187. Y. Zheng, T. Zhou, C. Zhang, J. Mao, H. Liu and Z. Guo, *Angewandte Chemie International Edition*, 2016, **55**, 3408-3413.
188. X. Xie, D. Su, S. Chen, J. Zhang, S. Dou and G. Wang, *Chemistry-An Asian Journal*, 2014, **9**, 1611-1617.
189. B. Qu, C. Ma, G. Ji, C. Xu, J. Xu, Y. S. Meng, T. Wang and J. Y. Lee, *Advanced Materials*, 2014, **26**, 3854-3859.
190. J. Wang, C. Luo, J. Mao, Y. Zhu, X. Fan, T. Gao, A. C. Mignerey and C. Wang, *ACS Applied Materials & Interfaces*, 2015, **7**, 11476-11481.
191. J. Pan, Z. Zuo, J. Deng, Q. Yao, Z. Wang and H. Zhou, *Surfaces and Interfaces*, 2018, **10**, 170-175.
192. J.-H. Choi, C.-W. Ha, H.-Y. Choi, H.-C. Shin, C.-M. Park, Y.-N. Jo and S.-M. Lee, *Electrochimica Acta*, 2016, **210**, 588-595.
193. Y. Denis, P. V. Prikhodchenko, C. W. Mason, S. K. Batabyal, J. Gun, S. Sladkevich, A. G. Medvedev and O. Lev, *Nature Communications*, 2013, **4**, 2922.
194. Z. Z. Pan, Y. Yan, N. Cui, J. C. Xie, Y. B. Zhang, W. S. Mu and C. Hao, *Advanced Materials Interfaces*, 2018, **5**, 1701481.
195. H. Hou, M. Jing, Z. Huang, Y. Yang, Y. Zhang, J. Chen, Z. Wu and X. Ji, *ACS Applied Materials & Interfaces*, 2015, **7**, 19362-19369.
196. Y. Zhu, P. Nie, L. Shen, S. Dong, Q. Sheng, H. Li, H. Luo and X. Zhang, *Nanoscale*, 2015, **7**, 3309-3315.
197. J. Xie, L. Liu, J. Xia, Y. Zhang, M. Li, Y. Ouyang, S. Nie and X. Wang, *Nano-micro letters*, 2018, **10**, 12.
198. F. Xie, L. Zhang, Q. Gu, D. Chao, M. Jaroniec and S.-Z. Qiao, *Nano Energy*, 2019, **60**, 591-599.
199. T. Zheng, G. Li, L. Zhao and Y. Shen, *European Journal of Inorganic Chemistry*, 2018, **2018**, 1224-1228.

200. S. Dong, C. Li, X. Ge, Z. Li, X. Miao and L. Yin, *ACS Nano*, 2017, **11**, 6474-6482.
201. S. Wang, S. Liu, X. Li, C. Li, R. Zang, Z. Man, Y. Wu, P. Li and G. Wang, *Chemistry-A European Journal*, 2018, **24**, 3873-3881.
202. Z. Zhang, J. Zhao, M. Xu, H. Wang, Y. Gong and J. Xu, *Nanotechnology*, 2018, **29**, 335401.
203. J. Ni, X. Bi, Y. Jiang, L. Li and J. Lu, *Nano Energy*, 2017, **34**, 356-366.
204. W. Sun, X. Rui, D. Zhang, Y. Jiang, Z. Sun, H. Liu and S. Dou, *Journal of Power Sources*, 2016, **309**, 135-140.
205. W. Yang, H. Wang, T. Liu and L. Gao, *Materials Letters*, 2016, **167**, 102-105.
206. B. Long, Z. Qiao, J. Zhang, S. Zhang, M.-S. Balogun, J. Lu, S. Song and Y. Tong, *Journal of Materials Chemistry A*, 2019, **7**, 11370-11378.
207. C. Lu, Z. Li, L. Yu, L. Zhang, Z. Xia, T. Jiang, W. Yin, S. Dou, Z. Liu and J. Sun, *Nano Research*, 2018, **11**, 4614-4626.
208. H. Liang, J. Ni and L. Li, *Nano Energy*, 2017, **33**, 213-220.
209. H. Wang, X. Lan, D. Jiang, Y. Zhang, H. Zhong, Z. Zhang and Y. Jiang, *Journal of Power Sources*, 2015, **283**, 187-194.
210. J. Morales, J. Santos and J. Tirado, *Solid State Ionics*, 1996, **83**, 57-64.
211. S. H. Choi and Y. C. Kang, *Nanoscale*, 2016, **8**, 4209-4216.
212. Y. N. Ko, S. Choi, S. Park and Y. C. Kang, *Nanoscale*, 2014, **6**, 10511-10515.
213. H. Wang, L. Wang, X. Wang, J. Quan, L. Mi, L. Yuan, G. Li, B. Zhang, H. Zhong and Y. Jiang, *Journal of The Electrochemical Society*, 2016, **163**, A1627-A1632.
214. Z. Zhang, Y. Fu, X. Yang, Y. Qu and Z. Zhang, *ChemNanoMat*, 2015, **1**, 409-414.
215. D. Xie, W. Tang, Y. Wang, X. Xia, Y. Zhong, D. Zhou, D. Wang, X. Wang and J. Tu, *Nano Research*, 2016, **9**, 1618-1629.
216. F. Niu, J. Yang, N. Wang, D. Zhang, W. Fan, J. Yang and Y. Qian, *Advanced Functional Materials*, 2017, **27**, 1700522.
217. L. B. Tang, B. Zhang, C. S. An, H. Li, B. Xiao, J. H. Li, Z. J. He and J. C. Zheng, *Inorganic Chemistry*, 2019, **58**, 8169-8178.
218. H. Liu, H. Guo, B. Liu, M. Liang, Z. Lv, K. R. Adair and X. Sun, *Advanced Functional Materials*, 2018, **28**, 1707480.
219. D. Xie, X. Xia, Y. Zhong, Y. Wang, D. Wang, X. Wang and J. Tu, *Advanced Energy Materials*, 2017, **7**, 1601804.
220. Q. Wang, Y. Wang, X. Zhang, G. Wang, P. Ji and F. Yin, *Journal of The Electrochemical Society*, 2018, **165**, A3642-A3647.
221. W. Yang, J. Wang, C. Si, Z. Peng and Z. Zhang, *Nano Research*, 2017, **10**, 2584-2598.
222. T. R. Juran and M. Smeu, *Journal of Power Sources*, 2019, **436**, 226813.
223. D. Zhang, G. Zhao, P. Li, Y. Zhang, W. Qiu, J. Shu, Y. Jiang, S. X. Dou and W. Sun, *Chemistry-A European Journal*, 2018, **24**, 1193-1197.
224. X. Lv, W. Wei, Q. Sun, B. Huang and Y. Dai, *Journal of Physics D: Applied Physics*, 2017, **50**, 235501.

225. Y. Subramanian, G. K. Veerasubramani, M.-S. Park and D.-W. Kim, *Journal of The Electrochemical Society*, 2019, **166**, A598-A604.
226. X. Wei, C. Tang, Q. An, M. Yan, X. Wang, P. Hu, X. Cai and L. Mai, *Nano Research*, 2017, **10**, 3202-3211.
227. K. Zhang, Z. Hu, X. Liu, Z. Tao and J. Chen, *Advanced Materials*, 2015, **27**, 3305-3309.
228. F. Zhao, S. Shen, L. Cheng, L. Ma, J. Zhou, H. Ye, N. Han, T. Wu, Y. Li and J. Lu, *Nano Letters*, 2017, **17**, 4137-4142.
229. H. Fan, H. Yu, Y. Zhang, J. Guo, Z. Wang, H. Wang, N. Zhao, Y. Zheng, C. Du and Z. Dai, *Energy Storage Materials*, 2018, **10**, 48-55.
230. P. Ge, H. Hou, S. Li, L. Yang and X. Ji, *Advanced Functional Materials*, 2018, **28**, 1801765.
231. C. An, Y. Yuan, B. Zhang, L. Tang, B. Xiao, Z. He, J. Zheng and J. Lu, *Advanced Energy Materials*, 2019, **9**, 1900356.
232. H. Yin, H.-Q. Qu, Z. Liu, R.-Z. Jiang, C. Li and M.-Q. Zhu, *Nano Energy*, 2019, **58**, 715-723.
233. Y. Zhang, A. Pan, L. Ding, Z. Zhou, Y. Wang, S. Niu, S. Liang and G. Cao, *ACS Applied Materials & Interfaces*, 2017, **9**, 3624-3633.
234. X. Li, W. Zhang, Y. Feng, W. Li, P. Peng, J. Yao, M. Li and C. Jiang, *Electrochimica Acta*, 2019, **294**, 173-182.
235. K. Zhang, M. Park, L. Zhou, G. H. Lee, W. Li, Y. M. Kang and J. Chen, *Advanced Functional Materials*, 2016, **26**, 6728-6735.
236. C. Cui, Z. Wei, G. Zhou, W. Wei, J. Ma, L. Chen and C. Li, *Journal of Materials Chemistry A*, 2018, **6**, 7088-7098.
237. Y. Fang, X. Y. Yu and X. W. Lou, *Advanced Materials*, 2018, **30**, 1706668.
238. X. Hu, X. Liu, K. Chen, G. Wang and H. Wang, *Journal of Materials Chemistry A*, 2019, **7**, 11016-11037.
239. P. Ge, S. Li, L. Xu, K. Zou, X. Gao, X. Cao, G. Zou, H. Hou and X. Ji, *Advanced Energy Materials*, 2019, **9**, 1803035.
240. J. S. Cho, S. Y. Lee and Y. C. Kang, *Scientific Reports*, 2016, **6**, 23338.
241. S. Zhu, Q. Li, Q. Wei, R. Sun, X. Liu, Q. An and L. Mai, *ACS Applied Materials & Interfaces*, 2016, **9**, 311-316.
242. S. Liu, D. Li, G. Zhang, D. Sun, J. Zhou and H. Song, *ACS Applied Materials & Interfaces*, 2018, **10**, 34193-34201.
243. X. Yang, R. Zhang, N. Chen, X. Meng, P. Yang, C. Wang, Y. Zhang, Y. Wei, G. Chen and F. Du, *Chemistry-A European Journal*, 2016, **22**, 1445-1451.
244. S. Yuan, Y. H. Zhu, W. Li, S. Wang, D. Xu, L. Li, Y. Zhang and X. B. Zhang, *Advanced Materials*, 2017, **29**, 1602469.
245. F. Zhang, C. Xia, J. Zhu, B. Ahmed, H. Liang, D. B. Velusamy, U. Schwingenschlögl and H. N. Alshareef, *Advanced Energy Materials*, 2016, **6**, 1601188.
246. X. Ren, J. Wang, D. Zhu, Q. Li, W. Tian, L. Wang, J. Zhang, L. Miao, P. K. Chu and K. Huo, *Nano Energy*, 2018, **54**, 322-330.

247. W. Li, M. Zhou, H. Li, K. Wang, S. Cheng and K. Jiang, *Electrochemistry Communications*, 2015, **60**, 74-77.
248. W. Luo, A. Calas, C. Tang, F. Li, L. Zhou and L. Mai, *ACS Applied Materials & Interfaces*, 2016, **8**, 35219-35226.
249. X. Ou, C. Yang, X. Xiong, F. Zheng, Q. Pan, C. Jin, M. Liu and K. Huang, *Advanced Functional Materials*, 2017, **27**, 1606242.
250. Y. Fang, X. Y. Yu and X. W. Lou, *Angewandte Chemie International Edition*, 2018, **57**, 9859-9863.
251. L. Xie, Z. Yang, J. Sun, H. Zhou, X. Chi, H. Chen, A. X. Li, Y. Yao and S. Chen, *Nano-micro Letters*, 2018, **10**, 50.
252. D. Li, J. Zhou, X. Chen and H. Song, *ACS Applied Materials & Interfaces*, 2018, **10**, 30379-30387.
253. Y. Kim, Y. Kim, A. Choi, S. Woo, D. Mok, N. S. Choi, Y. S. Jung, J. H. Ryu, S. M. Oh and K. T. Lee, *Advanced Materials*, 2014, **26**, 4139-4144.
254. J. Liu, P. Kopold, C. Wu, P. A. van Aken, J. Maier and Y. Yu, *Energy & Environmental Science*, 2015, **8**, 3531-3538.
255. Q. Li, Z. Li, Z. Zhang, C. Li, J. Ma, C. Wang, X. Ge, S. Dong and L. Yin, *Advanced Energy Materials*, 2016, **6**, 1600376.
256. W. Wang, J. Zhang, Y. Denis and Q. Li, *Journal of Power Sources*, 2017, **364**, 420-425.
257. J. Y. Jang, Y. Lee, Y. Kim, J. Lee, S.-M. Lee, K. T. Lee and N.-S. Choi, *Journal of Materials Chemistry A*, 2015, **3**, 8332-8338.
258. W.-J. Li, S.-L. Chou, J.-Z. Wang, H.-K. Liu and S.-X. Dou, *Chemical Communications*, 2015, **51**, 3682-3685.
259. Y. Wang, C. Wu, Z. Wu, G. Cui, F. Xie, X. Guo and X. Sun, *Chemical Communications*, 2018, **54**, 9341-9344.
260. Z. Li, L. Zhang, X. Ge, C. Li, S. Dong, C. Wang and L. Yin, *Nano Energy*, 2017, **32**, 494-502.
261. J. Zhang, K. Zhang, J. Yang, G. H. Lee, J. Shin, V. Wing‐hei Lau and Y. M. Kang, *Advanced Energy Materials*, 2018, **8**, 1800283.
262. F. Zhao, N. Han, W. Huang, J. Li, H. Ye, F. Chen and Y. Li, *Journal of Materials Chemistry A*, 2015, **3**, 21754-21759.
263. S. Chen, F. Wu, L. Shen, Y. Huang, S. K. Sinha, V. Srot, P. A. van Aken, J. Maier and Y. Yu, *ACS Nano*, 2018, **12**, 7018-7027.
264. Y. Zhang, G. Wang, L. Wang, L. Tang, M. Zhu, C. Wu, S.-X. Dou and M. Wu, *Nano Letters*, 2019, **19**, 2575-2582.
265. J.-Y. Hwang, S.-T. Myung and Y.-K. Sun, *Chemical Society Reviews*, 2017, **46**, 3529-3614.
266. N. Yabuuchi, K. Kubota, M. Dahbi and S. Komaba, *Chemical Reviews*, 2014, **114**, 11636-11682.
267. D. Kundu, E. Talaie, V. Duffort and L. F. Nazar, *Angewandte Chemie International Edition*, 2015, **54**, 3431-3448.
268. Q. Wang, J. Xu, W. Zhang, M. Mao, Z. Wei, L. Wang, C. Cui, Y. Zhu and J. Ma, *Journal of Materials Chemistry A,* 2018, **6**, 8815-8838.

269. M. Mao, F. Yan, C. Cui, J. Ma, M. Zhang, T. Wang and C. Wang, *Nano Letter*, 2017, **17**, 3830-3836.
270. F. Li, Z. Wei, A. Manthiram, Y. Feng, J. Ma and L. Mai, *Journal of Materials Chemistry A,* 2019, **7**, 9406-9431.
271. H. Hou, L. Shao, Y. Zhang, G. Zou, J. Chen and X. Ji, *Advanced Science*, 2017, **4**, 1600243.
272. F. Niu, J. Yang, N. Wang, D. Zhang, W. Fan, J. Yang and Y. Qian, *Advanced Functional Materials,* 2017, **27**, 1700522.
273. H. Tang, D. Yan, T. Lu and L. Pan, *Electrochimica Acta,* 2017, **241**, 63-72.
274. J. Yang, X. Zhou, D. Wu, X. Zhao and Z. Zhou, *Advanced Materials* 2017, **29**, 1604108.
275. Y. Yang, M. Qiu, L. Liu, D. Su, Y. Pi and G. Yan, *Nano,* 2016, **11**, 1650124.
276. W. Chen, C. Chen, X. Xiong, P. Hu, Z. Hao and Y. Huang, *Advanced Science*, 2017, **4**, 1600500.
277. J. Qian, F. Wu, Y. Ye, M. Zhang, Y. Huang, Y. Xing, W. Qu, L. Li and R. Chen, *Advanced Energy Materials*, 2018, **8**, 1703159.
278. B. Farbod, K. Cui, W. P. Kalisvaart, M. Kupsta, B. Zahiri, A. Kohandehghan, E. M. Lotfabad, Z. Li, E. J. Luber and D. Mitlin, *ACS Nano,* 2014, **8**, 4415-4429.
279. H. Xie, W. P. Kalisvaart, B. C. Olsen, E. J. Luber, D. Mitlin and J. M. Buriak, *Journal of Materials Chemistry A,* 2017, **5**, 9661-9670.
280. Y. Kim, Y. Kim, A. Choi, S. Woo, D. Mok, N. S. Choi, Y. S. Jung, J. H. Ryu, S. M. Oh and K. T. Lee, *Advanced Materials,* 2014, **26**, 4139-4144.
281. M.-S. Balogun, Y. Luo, W. Qiu, P. Liu and Y. Tong, *Carbon*, 2016, **98**, 162-178.
282. M. Lao, Y. Zhang, W. Luo, Q. Yan, W. Sun and S. X. Dou, *Advanced Materials,* 2017, **29**, 1700622.
283. Z. Hu, Q. Liu, S. L. Chou and S. X. Dou, *Advanced Materials,* 2017, **29**, 1700606.
284. Y. Zhao, L. P. Wang, M. T. Sougrati, Z. Feng, Y. Leconte, A. Fisher, M. Srinivasan and Z. Xu, *Advanced Energy Materials*, 2017, **7**, 1601424.
285. Y. Xiao, S. H. Lee and Y. K. Sun, *Advanced Energy Materials*, 2017, **7**, 1601329.
286. S. Qi, D. Wu, Y. Dong, J. Liao, C. W. Foster, C. O'Dwyer, Y. Feng, C. Liu and J. Ma, *Chemical Engineering Journal*, 2019, **370**, 185-207.
287. S. Peng, X. Han, L. Li, Z. Zhu, F. Cheng, M. Srinivansan, S. Adams and S. Ramakrishna, *Small,* 2016, **12**, 1359-1368.
288. Q. Wang, W. Zhang, C. Guo, Y. Liu, C. Wang and Z. Guo, *Advanced Functional Materials*, 2017, **27**, 1703390.
289. Y. Liu, A. Zhang, C. Shen, Q. Liu, X. Cao, Y. Ma, L. Chen, C. Lau, T.-C. Chen and F. Wei, *ACS Nano*, 2017, **11**, 5530-5537.
290. H. Hou, X. Qiu, W. Wei, Y. Zhang and X. Ji, *Advanced Energy Materials*, 2017, **7**, 1602898.

291. I. Hasa, X. Dou, D. Buchholz, Y. Shao-Horn, J. Hassoun, S. Passerini and B. Scrosati, *Journal of Power Sources*, 2016, **310**, 26-31.
292. B. Jache, J. O. Binder, T. Abe and P. Adelhelm, *Physical Chemistry Chemical Physics,* 2016, **18**, 14299-14316.
293. J. Rodríguez-García, I. Cameán, A. Ramos, E. Rodríguez and A. B. García, *Electrochimica Acta,* 2018, **270**, 236-244.
294. S. Y. Cho, M. Kang, J. Choi, M. E. Lee, H. J. Yoon, H. J. Kim, C. Leal, S. Lee, H. J. Jin and Y. S. Yun, *Small,* 2018, **14**, 1703043.
295. C. Jo, Y. Park, J. Jeong, K. T. Lee, J. Lee, *ACS Applied Materials & Interfaces*, 2015, **7**, 11748-11754.
296. Y. Tan, K.-W. Wong, Z. Zhang and K. M. Ng, *Nanoscale,* 2017, **9**, 19408-19414.
297. W. Shi, Y. Zhang, Z. Q. Tian, Z. Pan, J. Key and P. K. Shen, *Journal of Power Sources*, 2018, **398**, 149-158.
298. W. Xiong, Z. Wang, J. Zhang, C. Shang, M. Yang, L. He and Z. Lu, *Energy Storage Materials*, 2017, **7**, 229-235.
299. W. Li, M. Zhou, H. Li, K. Wang, S. Cheng, K. Jiang, *Energy & Environmental Science*, 2015, **8**, 2916-2921.
300. Y. M. Xing, X. H. Zhang, D. H. Liu, W. H. Li, L. N. Sun, H. B. Geng, J. P. Zhang, H. Y. Guan and X. L. Wu, *ChemElectroChem,* 2017, **4**, 1395-1401.
301. L. Qie, W. Chen, X. Xiong, C. Hu, F. Zou, P. Hu and Y. Huang, *Advanced Science.* 2015, **2**, 1500195.
302. P. Simon, Y. Gogotsi and B. Dunn, *Science,* 2014, **343**, 1210-1211.
303. L. Qie, W. M. Chen, Z. H. Wang, Q. G. Shao, X. Li, L. X. Yuan, X. L. Hu, W. X. Zhang and Y. H. Huang, *Advanced Materials*, 2012, **24**, 2047-2050.
304. C. Chen, G. Li, J. Zhu, Y. Lu, M. Jiang, Y. Hu, Z. Shen and X. Zhang, *Carbon*, 2017, **120**, 380-391.
305. Y. Bao, Y. Huang, X. Song, J. Long, S. Wang, L.-X. Ding and H. Wang, *Electrochimica Acta*, 2018, **276**, 304-310.
306. L. Li, Z. Chen and M. Zhang, *Solid State Ionics*, 2018, **323**, 151-156.
307. L. Wang, Y. Wang, M. Wu, Z. Wei, C. Cui, M. Mao, J. Zhang, X. Han, Q. Liu and J. Ma, *Small*, 2018, **14**, 1800737.
308. H.-g. Wang, C. Jiang, C. Yuan, Q. Wu, Q. Li and Q. Duan, *Chemical Engineering Journal*, 2018, **332**, 237-244.
309. G. Kresse and J. Hafner, *Physics Review B Condensed Materials*, 1993, **47**, 558.
310. J. Liang, Z. Wei, C. Wang and J. Ma, *Electrochimica Acta*, 2018, **285**, 301-308.
311. P. Blockl, *Physics Review B Condensed Materials,* 1994, **50**, 17953.
312. G. Kresse and D. Joubert, *Physics Review B Condensed Materials,* 1999, **59**, 1758.
313. Z. Wei, Y. Zhang, S. Wang, C. Wang and J. M. Ma, *Journal of Materials Chemistry A,* 2018, **6**, 13790-13796.

314. D. Xu, C. Chen, J. Xie, B. Zhang, L. Miao, J. Cai, Y. Huang and L. Zhang, *Advanced Energy Materials*, 2016, **6**, 1501929.
315. C. Sun, Y. Zhang, P. Wang, Y. Yang, Y. Wang, J. Xu, Y. Wang and W. Y. William, *Nanoscale Research Letter,* 2016, **11**, 110.
316. J. Xu, M. Wang, N. P. Wickramaratne, M. Jaroniec, S. Dou and L. Dai, *Advanced Materials* 2015, **27**, 2042-2048.
317. Z.-Q. Zhao, P.-W. Xiao, L. Zhao, Y. Liu and B.-H. Han, *RSC Advances*, 2015, **5**, 73980-73988.
318. Y. Li, K.-H. Wu, N. Huang, S. Dalapati, B.-J. Su, L.-Y. Jang, I. R. Gentle, D. Jiang and D.-W. Wang, *Energy Storage Materials*, 2018, **12**, 30-36.
319. T. H. Hwang, D. S. Jung, J.-S. Kim, B. G. Kim and J. W. Choi, *Nano Letter*, 2013, **13**, 4532-4538.
320. J. S. Lee, W. Kim, J. Jang and A. Manthiram, *Advanced Energy Materials*, 2017, **7**, 1601943.
321. N. A. Kaskhedikar and J. Maier, *Advanced Materials*, 2009, **21**, 2664-2680.
322. A. Manthiram and X. Yu, *Small,* 2015, **11**, 2108-2114.
323. G. Ning, X. Ma, X. Zhu, Y. Cao, Y. Sun, C. Qi, Z. Fan, Y. Li, X. Zhang, X. Lan, *ACS Applied Materials & Interfaces*, 2014, **6**, 15950-15958.
324. J. Li, W. Qin, J. Xie, H. Lei, Y. Zhu, W. Huang, X. Xu, Z. Zhao and W. Mai, *Nano Energy*, 2018, **53**, 415-424.
325. J. Wang, J. Polleux, J. Lim and B. J. T. Dunn, *The Journal of Physical Chemistry C,* 2007, **111**, 14925-14931.
326. S. Huang, Z. Li, B. Wang, J. Zhang, Z. Peng, R. Qi, J. Wang and Y. Zhao, *Advanced Functional Materials,* 2018, **28**, 1706294.
327. W. Tang, B.-M. Goh, M. Y. Hu, C. Wan, B. Tian, X. Deng, C. Peng, M. Lin, J. Z. Hu and K. P. J. T. Loh, *The Journal of Physical Chemistry C,* 2016, **120**, 2600-2608.
328. N. Yabuuchi, K. Kubota, M. Dahbi and S. Komaba, *Chemical Review*, 2014, **114**, 11636-11682.
329. D. B. Christoph Vaalma, Marcel Weil and Stefano Passerini, *Nature Reviews Materials*, 2018, **3**, 18013.
330. Y. Fang, X.-Y. Yu and X. W. Lou, *Matter*, 2019, **1**, 90-114.
331. P. K. Nayak, L. Yang, W. Brehm and P. Adelhelm, *Angewandte Chemie, International Edition in English*, 2018, **57**, 102-120.
332. X. Li, X. Hu, L. Zhou, R. Wen, X. Xu, S. Chou, L. Chen, A.-M. Cao and S. Dou, *Journal of Materials Chemistry A*, 2019, **7**, 11976-11984.
333. Y. Cao, L. Xiao, M. L. Sushko, W. Wang, B. Schwenzer, J. Xiao, Z. Nie, L. V. Saraf, Z. Yang and J. Liu, *Nano Letter*, 2012, **12**, 3783-3787.
334. H. Hou, C. E. Banks, M. Jing, Y. Zhang and X. Ji, *Advanced Materials*, 2015, **27**, 7861-7866.
335. P. Lu, Y. Sun, H. Xiang, X. Liang and Y. Yu, *Advanced Energy Materials*, 2018, **8**, 1702434.
336. W. Ma, J. Wang, H. Gao, J. Niu, F. Luo, Z. Peng and Z. Zhang, *Energy Storage Materials*, 2018, **13**, 247-256.

337. M. Sheng, F. Zhang, B. Ji, X. Tong and Y. Tang, *Advanced Energy Materials*, 2017, **7**, 1601963.
338. H. Yang, R. Xu, Y. Yao, S. Ye, X. Zhou and Y. Yu, *Advanced Functional Materials*, 2019, **29**,1809195.
339. Y. Zhao and A. Manthiram, *Chemistry of Materials*, 2015, **27**, 3096-3101.
340. C. Chen, Y. Wen, X. Hu, X. Ji, M. Yan, L. Mai, P. Hu, B. Shan and Y. Huang, *Nature Communication*, 2015, **6**, 6929.
341. Y. Zheng, T. Zhou, C. Zhang, J. Mao, H. Liu and Z. Guo, *Angewandte Chemie, International Edition in English*, 2016, **55**, 3408-3413.
342. D. Chen, L. Peng, Y. Yuan, Y. Zhu, Z. Fang, C. Yan, G. Chen, R. Shahbazian-Yassar, J. Lu, K. Amine and G. Yu, *Nano Letter*, 2017, **17**, 3907-3913.
343. K. Zhang, M. Park, L. Zhou, G.-H. Lee, W. Li, Y.-M. Kang and J. Chen, *Advanced Functional Materials*, 2016, **26**, 6728-6735.
344. Y. Wang, Y. Wang, W. Kang, D. Cao, C. Li, D. Cao, Z. Kang, D. Sun, R. Wang and Y. Cao, *Advanced Science (Weinh)*, 2019, **6**, 1801222.
345. F. Zhang, C. Xia, J. Zhu, B. Ahmed, H. Liang, D. B. Velusamy, U. Schwingenschlögl and H. N. Alshareef, *Advanced Energy Materials*, 2016, **6**, 1601188.
346. S. Wang, L. Xia, L. Yu, L. Zhang, H. Wang and X. W. D. Lou, *Advanced Energy Materials*, 2016, **6**, 1502217.
347. W. Li, M. Zhou, H. Li, K. Wang, S. Cheng and K. Jiang, *Energy & Environmental Science*, 2015, **8**, 2916-2921.
348. J. Yang, X. Zhou, D. Wu, X. Zhao and Z. Zhou, *Advanced Materials*, 2017, **29**, 1604108.
349. Z. Li, J. Ding and D. Mitlin, *Accounts of Chemical Research*, 2015, **48**, 1657-1665.
350. J. Ni, X. Bi, Y. Jiang, L. Li and J. Lu, *Nano Energy*, 2017, **34**, 356-366.
351. Z. Hu, Q. Liu, S. L. Chou and S. X. Dou, *Advanced Materials*, 2017, **29**, 1700606.
352. D. Yang, W. Chen, X. Zhang, L. Mi, C. Liu, L. Chen, X. Guan, Y. Cao and C. Shen, *Journal of Materials Chemistry A*, 2019, **7**, 19709-19718.
353. Y. Fang, X.-Y. Yu and X. W. D. Lou, *Angewandte Chemie International Edition*, 2019, **58**, 7744-7748.
354. Y. Zhang, Q. Zhou, J. Zhu, Q. Yan, S. X. Dou and W. Sun, *Advanced Functional. Materials*, 2017, **27**, 1702317.
355. Q. Yun, Q. Lu, X. Zhang, C. Tan and H. Zhang, *Angewandte Chemie International Edition,* 2018, **57**, 626-646.
356. J. Huang, Z. Wei, J. Liao, W. Ni, C. Wang and J. Ma, *Journal of Energy Chemistry*, 2019, **33**, 100-124.
357. Y. V. Lim, Y. Wang, D. Kong, L. Guo, J. I. Wong, L. K. Ang and H. Y. Yang, *Journal of Materials Chemistry A*, 2017, **5**, 10406-10415.
358. Y. Song, J. Liao, C. Chen, J. Yang, J. Chen, F. Gong, S. Wang, Z. Xu and M. Wu, *Carbon*, 2019, **142**, 697-706.

359. Y. Wang, D. Kong, S. Huang, Y. Shi, M. Ding, Y. Von Lim, T. Xu, F. Chen, X. Li and H. Y. Yang, *Journal of Materials Chemistry A*, 2018, **6**, 10813-10824.
360. Y. Wang, D. Kong, W. Shi, B. Liu, G. J. Sim, Q. Ge and H. Y. Yang, *Advanced Energy Materials*, 2016, **6**, 1601057.
361. S. H. Choi and Y. C. Kang, *Nanoscale*, 2015, **7**, 3965-3970.
362. D. Su, S. Dou and G. Wang, *Chemical Communications (Camb)*, 2014, **50**, 4192-4195.
363. Y. Song, S. Bai, L. Zhu, M. Zhao, D. Han, S. Jiang and Y. N. Zhou, *ACS Applied Materials & Interfaces*, 2018, **10**, 13606-13613.
364. X. Wang, J. Huang, J. Li, L. Cao, W. Hao and Z. Xu, *ACS Applied Materials & Interfaces*, 2016, **8**, 23899-23908.
365. X. Zeng, Z. Ding, C. Ma, L. Wu, J. Liu, L. Chen, D. G. Ivey and W. Wei, *Applied Materials & Interfaces*, 2016, **8**, 18841-18848.
366. Q. Pang, Y. Gao, Y. Zhao, Y. Ju, H. Qiu, Y. Wei, B. Liu, B. Zou, F. Du and G. Chen, *Chemistry*, 2017, **23**, 7074-7080.
367. X. D. Xu, X. J. Li, J. Q. Zhang, K. Qiao, D. Z. Han, S. T. Wei, W. Xing and Z. F. Yan, *Electrochimica Acta*, 2019, **302**, 259-269.
368. J. Liang, Z. Wei, C. Wang and J. Ma, *Electrochimica Acta*, 2018, **285**, 301-308.
369. C. Wu, X. Zeng, P. He, L. Chen and W. Wei, *Advanced Materials Interfaces*, 2018, **5**, 1701080.
370. S. Zhou, J. Chen, L. Gan, Q. Zhang, Z. Zheng, H. Li and T. Zhai, *Science Bulletin*, 2016, **61**, 227-235.
371. X. Yu, C. Pei, W. Chen and L. Feng, *Electrochimica Acta*, 2018, **272**, 119-126.
372. J. Ma, J. Zhang, S. Wang, T. Wang, J. Lian, X. Duan and W. Zheng, *The Journal of Physical Chemistry C*, 2011, **115**, 18157-18163.
373. Z. Wei, Y. Zhang, S. Wang, C. Wang and J. Ma, *Journal of Materials Chemistry A*, 2018, **6**, 13790-13796.
374. G. Kresse and J. Hafner, *Physics Review B Condensed Materials*, 1993, **47**, 558-561.
375. K. B. John P. Perdew, and M. Ernzerhof, *Physical Review Letters*, 1996, **77**, 3865.
376. P. E. Blochl, *Physics Review B Condensed Materials*, 1994, **50**, 17953-17979.
377. G. Kresse, D. Joubert, *Physical Review B*, 1999, **59**, 1758.
378. L. M. Malard, M. A. Pimenta, G. Dresselhaus and M. S. Dresselhaus, *Physics Reports*, 2009, **473**, 51-87.
379. X.-G. Yu, J.-Y. Xie, J. Yang, H.-j. Huang, K. Wang and Z.-S. Wen, *Journal of Electroanalytical Chemistry*, 2004, **573**, 121-128.
380. C. C. P. Piaggio, G. Dellepiane, E. Campani, G. Gorini, G. Masetti, M. and N. A. G. Petrillo, *Spectrochimica. Acta*, 1989., **45A**, 347.
381. R. Ma, L. Fan, J. Wang and B. Lu, *Electrochimica Acta*, 2019, **293**, 191-198.

382. H. Tan, J. Tang, X. Zhou, D. Golberg, S. K. Bhatia, Y. Sugahara and Y. Yamauchi, *Chemical Communications (Camb)*, 2018, **54**, 9494-9497.
383. L. Fu, K. Tang, K. Song, P. A. van Aken, Y. Yu and J. Maier, *Nanoscale*, 2014, **6**, 1384-1389.
384. X. Xia, D. Chao, Y. Zhang, J. Zhan, Y. Zhong, X. Wang, Y. Wang, Z. X. Shen, J. Tu and H. J. Fan, *Small*, 2016, **12**, 3048-3058.
385. V. Augustyn, P. Simon and B. Dunn, *Energy & Environmental Science*, 2014, **7**, 1597-1614.
386. W. Lei, W. Xiao, J. Li, G. Li, Z. Wu, C. Xuan, D. Luo, Y. P. Deng, D. Wang and Z. Chen, *ACS Applied Materials & Interfaces*, 2017, **9**, 28604-28611.
387. Y. Yao, R. Xu, M. Chen, X. Cheng, S. Zeng, D. Li, X. Zhou, X. Wu and Y. Yu, *ACS Nano*, 2019, **13**, 4695-4704.
388. J. Cui, S. Yao, M. Ihsan-Ul-Haq, J. Wu and J.-K. Kim, *Advanced Energy Materials*, 2019, **9**, 1802777.
389. T. Jin, H. X. Li, Y. Li, L. F. Jiao and J. Chen, *Nano Energy*, 2018, **50**, 462-467.
390. Y. Wu, S. Hu, R. Xu, J. Wang, Z. Peng, Q. Zhang and Y. Yu, *Nano Letter*, 2019, **19**, 1351-1358.
391. L. Wang, X. Xie, K. N. Dinh, Q. Y. Yan and J. M. Ma, *Coordination Chemistry Reviews*, 2019, **397**, 138-167.
392. D. Wu, C. Wang, M. Wu, Y. Chao, P. He and J. Ma, *Journal of Energy Chemistry*, 2020, **43**, 24-32.
393. P. Lu, Y. Sun, H. F. Xiang, X. Liang and Y. Yu, *Advanced Energy Materials*, 2018, **8**, 1702434.
394. Z. Wang, N. Zhang, M. Yu, J. Liu, S. Wang and J. Qiu, *Journal of Energy Chemistry*, 2019, **37**, 183-191.
395. H. S. Hou, X. Q. Qiu, W. F. Wei, Y. Zhang and X. B. Ji, *Advanced Energy Materials,* 2017, **7**, 1602898.
396. J. T. Xu, M. Wang, N. P. Wickramaratne, M. Jaroniec, S. X. Dou and L. M. Dai, *Advanced Materials*, 2015, **27**, 2042-2048.
397. Y. Ding, C. K. Zhang, L. Y. Zhang, Y. E. Zhou and G. H. Yu, *Chemical Society Reviews*, 2018, **47**, 69-103.
398. W. J. Lu, X. F. Li and H. M. Zhang, *Physical Chemistry Chemical Physics*, 2018, **20**, 23-35.
399. B. H. She, L. T. Shan, H. J. Chen, J. Zhou, X. Gun, G. Z. Fang, X. X. Cao and S. Q. Liang, *Journal of Energy Chemistry,* 2019, **37**, 172-175.
400. Y. X. Zeng, X. Y. Zhang, R. F. Qin, X. Q. Liu, P. P. Fang, D. Z. Zheng, Y. X. Tong and X. H. Lu, *Advanced Materials*, 2019, **31,** 1903675.
401. C. Y. Yang, J. Chen, X. Ji, T. P. Pollard, X. J. Lu, C. J. Sun, S. Hou, Q. Liu, C. M. Liu, T. T. Qing, Y. Q. Wang, O. Borodin, Y. Ren, K. Xu and C. S. Wang, *Nature*, 2019, **569**, 245.
402. F. Wang, E. Y. Hu, W. Sun, T. Gao, X. Ji, X. L. Fan, F. D. Han, X. Q. Yang, K. Xu and C. S. Wang, *Energy & Environmental Science*, 2018, **11**, 3168-3175.

403. Y. Sun, S. H. Guo and H. S. Zhou, *Advanced Energy Materials*, 2019, **9**, 1800212.
404. Y. X. Huang, L. Z. Zhao, L. Li, M. Xie, F. Wu and R. J. Chen, *Advanced Materials*, 2019, **31,** 1808393.
405. M. Wu, B. Xu, Y. Zhang, S. Qi, W. Ni, J. Hu and J. Ma, *Chemical Engineering Journal*, 2020, **381**, 122558.
406. X. Xie, M. Mao, S. Qi and J. Ma, *CrystEngComm*, 2019, **21**, 3755-3769.
407. B. Jache and P. Adelhelm, *Angewandte Chemie-International Edition*, 2014, **53**, 10169-10173.
408. H. Kim, J. Hong, Y. U. Park, J. Kim, I. Hwang and K. Kang, *Advanced Functional Materials*, 2015, **25**, 534-541.
409. Z. Q. Zhu, F. Y. Cheng, Z. Hu, Z. Q. Niu and J. Chen, *Journal of Power Sources*, 2015, **293**, 626-634.
410. M. Cabello, X. Bai, T. Chyrka, G. F. Ortiz, P. Lavela, R. Alcantara and J. L. Tirado, *Journal of the Electrochemical Society*, 2017, **164**, A3804-A3813.
411. N. Zhang, X. Han, Y. Liu, X. Hu, Q. Zhao and J. Chen, *Advanced Energy Materials*, 2015, **5**, 1401123.
412. S. Qi, D. Wu, Y. Dong, J. Liao, C. W. Foster, C. O'Dwyer, Y. Feng, C. Liu and J. Ma, *Chemical Engineering Journal,* 2019, **370**, 185-207.
413. S. Qi, B. Xu, V. T. Tiong, J. Hu and J. Ma, *Chemical Engineering Journal,* 2020, **379**, 122261.
414. Y. J. Fang, Z. X. Chen, L. F. Xiao, X. P. Ai, Y. L. Cao and H. X. Yang, *Small*, 2018, **14**, 1703116.
415. X. Wei, W. H. Li, J. A. Shi, L. Gu and Y. Yu, *ACS Applied Materials & Interfaces*, 2015, **7**, 27804-27809.
416. D. H. Li, Y. Y. Sun, S. Chen, J. Y. Yao, Y. H. Zhang, Y. Z. Xia and D. J. Yang, *ACS Applied Materials & Interfaces*, 2018, **10**, 17175-17182.
417. Q. H. Wang, W. C. Zhang, C. Guo, Y. J. Liu, C. Wang and Z. P. Guo, *Advanced Functional Materials*, 2017, **27**, 1703390.
418. S. Y. Lee and Y. C. Kang, *Chemical Engineering Journal*, 2016, **22**, 2769-2774.
419. A. Jin, M. J. Kim, K. S. Lee, S. H. Yu and Y. E. Sung, *Nano Research*, 2019, **12**, 695-700.
420. Z. M. Liu, F. Hu, J. Xiang, C. Yue, D. Lee and T. Song, *Particle & Particle Systems Characterization*, 2018, **35**, 1800163.
421. W. H. Chen, X. X. Zhang, L. W. Mi, C. T. Liu, J. M. Zhang, S. Z. Cui, X. M. Feng, Y. L. Cao and C. Y. Shen, *Advanced Materials*, 2019, **31**, 1806664.
422. M. J. Choi, J. Kim, J. K. Yoo, S. Yim, J. Jeon and Y. S. Jung, *Small*, 2018, **14**, 1702816.
423. H. Zhang, Q. M. Gao, X. H. Tian, Z. Y. Li, P. Xu and H. Xiao, *Electrochimica Acta*, 2019, **319**, 472-480.
424. L. D. Shi, D. Z. Li, J. L. Yu, H. C. Liu, Y. Zhao, H. L. Xin, Y. M. Lin, C. D. Lin, C. H. Li and C. Z. Zhu, *Journal of Materials Chemistry A*, 2018, **6**, 7967-7976.

425. Q. D. Li, Q. L. Wei, W. B. Zuo, L. Huang, W. Luo, Q. Y. An, V. O. Pelenovich, L. Q. Mai and Q. J. Zhang, *Chemical Science*, 2017, **8**, 160-164.
426. Q. S. Liu, J. L. Gao, C. T. Cao, G. P. Yin, Z. X. Jiang, M. Y. Ge, X. H. Xiao, W. K. Lee and J. J. Wang, *Nano Energy*, 2019, **62**, 384-392.
427. K. Zhang, M. Park, L. M. Zhou, G. H. Lee, J. Shin, Z. Hu, S. L. Chou, J. Chen and Y. M. Kang, *Angewandte Chemie-International Edition*, 2016, **55**, 12822-12826.
428. L. Mai, J. Sheng, L. Xu, S. Tan and J. Meng, *Accounts of Chemical Research*, 2018, **51**, 950-959.
429. A. Singh and V. Kalra, *Journal of Materials Chemistry A*, 2019, **7**, 11613-11650.
430. J. M. Ma, J. B. Lian, X. C. Duan, X. D. Liu and W. J. Zheng, *Journal of Physical Chemistry C*, 2010, **114**, 10671-10676.
431. L. M. Malard, M. A. Pimenta, G. Dresselhaus and M. S. Dresselhaus, *Physics Reports-Review Section of Physics Letters*, 2009, **473**, 51-87.
432. H. L. Wu, L. A. Huff and A. A. Gewirth, *ACS Applied Materials & Interfaces*, 2015, **7**, 1709-1719.
433. P. Zhang, X. Zhao, Z. Liu, F. Wang, Y. Huang, H. Li, Y. Li, J. Wang, Z. Su and G. Wei, *NPG Asia Materials*, 2018, **10**, 429-440.
434. Q. M. He, K. Rui, J. H. Yang and Z. Y. Wen, *ACS Applied Materials & Interfaces*, 2018, **10**, 29476-29485.
435. P. X. Xiong, X. X. Zhao and Y. H. Xu, *Chemsuschem*, 2018, **11**, 202-208.
436. M. J. Choi, J. Kim, J. K. Yoo, S. Yim, J. Jeon and Y. S. Jung. *Small*, 2018, **14**, 1702816.
437. Q. M. He, K. Rui, J. H. Yang and Z. Y. Wen, *ACS Applied Materials & Interfaces*, 2018, **10**, 29476-29485.
438. F. Y. Jiang, Q. Wang, R. Du, X. S. Yan and Y. L. Zhou. *Chemical Physics Letters*, 2018, **706**, 273-279.
439. Z. M. Liu, F. Hu, J. Xiang, C. Yue, D. Lee and T. Song. *Particle & Particle Systems Characterization*, 2018, **35**, 1800163.
440. L. D. Shi, D. Z. Li, J. L. Yu, H. C. Liu, Y. Zhao, H. L. Xin, Y. M. Lin, C. D. Lin, C. H. Li and C. Z. Zhu, *Journal of Materials Chemistry A*, 2018, **6**, 7967-7976.
441. Y. M. Guo, L. J. Zhang, J. T. Wang, J. M. Liang, L. Xi, *Electrochimica Acta*, 2019, **322**, 134763.
442. S. Y. Li, B. H. Qu, H. Huang, P. Deng, C. H. Xu, Q. H. Li and T. H. Wang, *Electrochimica Acta*, 2017, **247**, 1080-1087.
443. W. Huang, H. Y. Sun, H. H. Shangguan, X. Y. Cao, X. X. Xiao, F. Shen, K. Mølhave, L. J. Ci, P. C. Si and J. D. Zhang, *Nanoscale*, 2018, **10**, 7851-7859.
444. X. L. Wu，H. Q. Zhao，J. M. Xu，Z. F. Zhang，W. X. Sheng，S. G. Dai，T. T. Xu，S. Zhang，X. C. Wang，Y. Wang and X.J. Li, *Applied Surface Science*, 2019, **492**, 504-512.
445. W. S. Weng，J. Y. Xu，C. L. Lai，Z. H. Xu，Y. C. Du，J. Lin and X. S. Zhou, *Journal of Alloys and Compounds*, 2019: 152732.

446. A. H. Jin, M. J. Kim, K. S. Lee, S. H. Yu and Y. E. Sung, *Nano Research*, 2019, **12**, 695-700.
447. B. H. Hou, Y. Y. Wang, J. Z. Guo, Y. Zhang, Q. L. Ning, Y. Yang, W. H. Li, J. P. Zhang, X. L. Wang and X. L. Wu, *ACS Applied Materials & Interfaces,* 2018, **10**, 3581-3589.
448. H. Yang, R. Xu, Y. Yao, S. F. Ye, X. F. Zhou and Y. Yu, *Advanced Functional Materials*, 2019, **29**, 1809195.

APPENDIX A: LIST OF PUBLICATIONS

1. **X. Li**, X. C. Hu, L. Zhou, R. Wen, X. Xu, S. L. Chou, L. B. Chen, A.-M. Cao and S. X. Dou, S/N-Doped High-Capacity Mesoporous Carbon Anode for Na-ion Batteries. Journal of Materials Chemistry A, 2019, **7**, 11976-11984.

2. **X. Li**, Y. G. Sun, X. Xu, Y. X. Wang, S. L. Chou, A.-M. Cao , L. B. Chen and S. X. Dou, Lotus rhizome-like S/N-C with embedded WS_2 for superior sodium storage. Journal of Materials Chemistry A, 2019, **7**, 25932-25943.

3. **X. Li**, X. Xu, S. L. Chou, A.-M. Cao and L. B Chen, S/N-doped Carbon Nanofibers Affording Fe_7S_8 Particles with Superior Sodium Storage. Journal of Power Sources, 2020, **451**, 227790.